VILNIUS UNIVERSITY

PATRIK ŠČAJEV

INVESTIGATION OF WIDE-BAND-GAP SEMICONDUCTOR PHOTOELECTRIC PROPERTIES BY USING OPTICAL TECHNIQUES WITH TEMPORAL AND SPATIAL RESOLUTION

Doctoral thesis

Physical Sciences, Physics (02 P), Semiconductor Physics (P 265)

Vilnius, 2013

The research has been carried out in 2009-2013 at the Institute of Applied Research, Vilnius University.

Scientific supervisor:

Prof. habil. dr. Kęstutis Jarašiūnas (Vilnius University, Physical Sciences, Physics – 02 P, Semiconductor Physics – P 265).

VILNIAUS UNIVERSITETAS

PATRIK ŠČAJEV

PLAČIATARPIŲ PUSLAIDININKIŲ FOTOELEKTRINIŲ SAVYBIŲ OPTINĖ DIAGNOSTIKA SU LAIKINE IR ERDVINE SKYRA

Daktaro disertacija

Fiziniai mokslai, fizika (02 P), puslaidininkių fizika (P 265)

Vilnius, 2013

Disertacija parengta Vilniaus universitete, Taikomųjų mokslų institute 2009-2013 metais.

Mokslinis vadovas:

Prof. habil. dr. Kęstutis Jarašiūnas (Vilniaus universitetas, fiziniai mokslai, fizika – 02 P, puslaidininkių fizika – P 265).

Santrauka

Silicio karbidas (SiC), galio nitridas (GaN) ir deimantas – tai plačiatarpiai puslaidininkiai, pasižymintys unikaliomis savybėmis ir turintys plačias taikymo galimybes aukštų temperatūrų, didelių galių elektronikoje bei optoelektronikoje. Todėl šių medžiagų elektrinės bei optinės savybės pastaruoju metu yra intensyviai tiriamos. Dinaminių gardelių (DG), diferencinio pralaidumo (DP), diferencinio atspindžio (DA), fotoliuminescencijos (FL) optinės nesąlytinės metodikos tinka tirti krūvininkų dinamiką, kuri yra nulemta fundamentinių bei defektinių medžiagos savybių.

Pagrindiniai darbo tikslai buvo gauti naujų žinių apie krūvininkų rekombinacijos ir difuzijos procesus plačiatarpiuose puslaidininkiuose (SiC, GaN, deimantas), kompleksiškai panaudojant optinius metodus. Siekta ištirti nepusiausvirųjų procesų ypatumus tankioje plazmoje skirtingo defektiškumo medžiagose, skaitmeniškai modeliuojant krūvininkų dinamiką, nustatyti dominuojančius krūvininkų rekombinacijos mechanizmus bei pagrindinių fotoelektrinių parametrų - krūvininkų gyvavimo trukmės, difuzijos koeficiento ir difuzijos nuotolio priklausomybes nuo sužadinimo ir temperatūros.

Darbe DG metodas buvo pritaikytas tarpjuostinių sugerties koeficientų verčių nustatymui storuose SiC ir deimanto kristaluose naudojamomis eksperimentinėmis sąlygomis (80-800 K temperatūrų intervale ties 351 ir 213 nm sužadinimo bangos ilgiais). Šis tikslas buvo pasiektas matuojant santykinį difrakcijos efektyvumą, priklausantį nuo gardelės storio, ir savo ruožtu nuo sugerties koeficiento.

Sukurta nauja eksperimentinė metodika gyvavimo trukmių pasiskirstymo matavimui DP pagrindu, kur vietoj fotodetektoriaus panaudota CCD kamera. Šios metodikos dėka pagerėjusi erdvinė skyra (~5 μm) leido parodyti, kad GaN kristalai yra nevienalyčiai ir patvirtinti, jog nespindulinės rekombinacijos sparta yra ribojama difuzinės krūvininkų pernašos į tarpkristalitines ribas, o tūrinės rekombinacijos įtaka pasireiškia tik didelių kristalitų centruose.

Krūvininkų difuzijos koeficiento matavimai parodė, kad SiC ir GaN difuzijos koeficiento priklausomybei nuo sužadinimo lemiamą įtaką turi juostų

renormalizacija, fononų sąveikos su krūvininkais ekranavimas, bei elektron-skylinės plazmos išsigimimas. Tuo tarpu deimantuose daug stipresnis difuzijos koeficiento mažėjimas nuo sužadinimo (nuo 50 cm^2/s iki 7 cm^2/s, 300 K) buvo paaiškintas elektron-skyline sklaida ir eksitonų įtaka, o žemose temperatūrose ($T < 150$ K) – papildoma bieksitonų ir elektron-skylinių lašų įtaka.

Netiesiatarpiuose SiC ir deimanto puslaidininkiuose esant mažiems sužadinimams rekombinacija yra ribota nespinduliniais defektais (gyvavimo trukmės iki 700 ns kambario temperatūroje) ir paviršine rekombinacija (jos sparta $S = 10^3$-10^5 cm/s). Panaudojus tikslius krūvininkų dinamikos modeliavimus su nustatytais sugerties bei difuzijos koeficientais, priklausančiais nuo krūvininkų tankio ir temperatūros, gauta netiesinės rekombinacijos sparta. 4H-SiC ji buvo nulemta fononiniu Ože rekombinacijos procesu (su koeficientu $C_0=(5\pm1)\times10^{-31}$ cm^6/s), kuris prie žemų sužadinimų buvo sustiprintas kulonine sąveika iki 10 kartų, bei susilpnintas prie didelių dėl elektron-fononinės sąveikos ekranavimo. Deimante esant žemoms temperatūroms netiesinė rekombinacija buvo sąlygota eksitonų, bieksitonų bei elektron-skylinių lašų sustiprintos Ože rekombinacijos. Aukštose temperatūrose stebėtas nespindulinės rekombinacijos sustiprinimas su E_{th} = 560 meV slenksčiu. Pastarasis efektas priskirtas defektų įtakotam eksitoniniam Ože procesui.

FL efektyvumo ir DP matavimai parodė, kad GaN spindulinės rekombinacijos sparta yra žymiai mažesnė už nespindulinę. Savo ruožtu 3C-SiC bimolekulinės rekombinacijos koeficientas nuo krūvininkų tankio nepriklausė ($B_{rad} = 2.05\times10^{-15}$ cm^3/s) bei sutapo su teoriškai apskaičiuotu.

Kompensuojančių defektų (aliuminio SiC ir boro deimante) koncentracijos ir aktyvacijos energijos nustatytos stebint jų sąlygotos defektinės sugerties padidėjimo dėl jų perkrovimo nepusiausviraisiais krūvininkais. Perkrautų defektų sugerties signalo įsisotinimas leido nustatyti jų koncentraciją (~10^{16}-10^{18} cm^{-3} SiC, ~10^{14}-10^{16} cm^{-3} deimante), o signalo relaksacijos spartos priklausomybė nuo temperatūros – jų aktyvacijos energiją (~200 meV SiC, 340 meV deimante).

Acknowledgements

Firstly, I would like to give my special thanks to my scientific supervisor prof. Kęstutis Jarašiūnas for his encouragement, knowledge share and versatile support of the research.

I acknowledge doctors Saulius Nargelas, Tadas Malinauskas, Ramūnas Aleksiejūnas, Arūnas Kadys, Jūras Mickevičius, Vytautas Grivickas, Vytautas Gudelis, prof. Edmundas Kuokštis and Mindaugas Karaliūnas for sharing their experience and support on measurement equipment and experimental techniques at Vilnius University.

Also I acknowledge foreign collaborators for sharing the samples and performing measurements of absorption, photoluminescence and structural properties.

The work has been partially supported by the Lithuanian State Study Foundation, the Research Council of Lithuania, and international collaboration projects: Eureka, FP6, FP7, etc.

Table of Contents

List of abbreviations

BBA	band-to-band absorption
BEL	band-edge luminescence
BGR	band gap renormalization
CCD	charge-coupled device
CL	cathodoluminescence
CVD	chemical vapor deposition
CW	continuous wave
DAP	donor-acceptor pair
DR	differential reflectivity
DT	differential transmittivity
EBIC	electron beam induced current
EHD	electron-hole droplets
EHP	electron-hole plasma
FCA	free carrier absorption
FTG	Fourier transient grating
FWM	four wave mixing
FWHM	full width at half maximum
HPHT	high-pressure high-temperature
HVPE	hydride vapor phase epitaxy
IR	infrared
LED	light-emitting diode/device
LITG	light-induced transient grating
LT	low-temperature
MPCD	microwave photoconductivity decay
NBEL	near-band-edge luminescence
PL	photoluminescence
PVT	physical vapor transport
RT	room temperature
SE	sublimation epitaxy
SPA	single-photon absorption
SRH	Shockley-Read-Hall
TAAR	trap assisted Auger recombination
TOF	time of flight (technique)
TPA	two-photon absorption
TRFCA	time resolved free carrier absorption
TRPL	time resolved photoluminescence
UV	ultraviolet
VIS	visible
VLS	vapor–liquid–solid

List of commonly used symbols

b	TPA absorption factor (cm/J)
B	quadratic recombination coefficient (cm^3/s)
B_{rad}	radiative recombination coefficient (cm^3/s)
B_{nonr}	nonradiative quadratic recombination coefficient (cm^3/s)
C	Auger coefficient (cm^6/s)
d	sample thickness (μm)
d^*	effective excitation depth (μm)
D	diffusion coefficient (cm^2/s)
D_a, D_e, D_h	ambipolar, electron, hole diffusion coefficient (cm^2/s)
E	carrier (photon) energy (eV)
E_{ex}	exciton binding energy (eV)
E_g	bandgap (eV)
E_{ph}	phonon energy (eV)
f_F	Fermi distribution function
$h\nu$ ($\hbar\omega$)	photon (phonon) energy (eV)
I_0	excitation fluence (mJ/cm^2)
L_D	diffusion length (μm)
m_e^*	effective electron mass (kg)
m_h^*	effective hole mass (kg)
m_{eh}	reduced (optical) mass (kg)
n	refractive index
n_B	Bose-Einstein phonon population factor
n_{eh}	refractive index change by one electron-hole pair (cm^3)
n_0, p_0	electron, hole equilibrium density (cm^{-3})
N_A, N_D	acceptor, donor concentration (cm^{-3})
N_{TD}	threading dislocation density (cm^{-2})
S, S_{inter}	surface, interface recombination velocity (cm/s)
T	temperature (K)
α	band-to-band absorption coefficient (cm^{-1})
α_R	reabsorption coefficient (cm^{-1})
β	two-photon absorption coefficient (cm/GW)
γ	slope of a curve in log-log scale
Δn	refractive index change
ΔN	nonequilibrium carrier density (cm^{-3})
ΔN_0	nonequilibrium carrier density on the front excited surface (cm^{-3})
ΔN_{02}	nonequilibrium carrier density on the front excited surface at TPA excitation conditions (cm^{-3})

ΔN_{av}	depth-averaged carrier density (cm^{-3})
ΔN_e, ΔN_h	electron, hole nonequilibrium density (cm^{-3})
ΔN_{ex}	exciton density (cm^{-3})
ΔN_{FC}	nonequilibrium free carrier density (cm^{-3})
ΔN_s	depth integrated carrier density (cm^{-2})
η	diffraction efficiency
λ	wavelength (m)
Λ	LITG period (μm)
μ	mobility (cm^2/Vs)
μ_a, μ_e, μ_h	ambipolar, electron, hole mobility (cm^2/Vs)
ν	frequency (Hz)
σ_{eh}	free carrier absorption cross section (cm^2)
σ_e, σ_h	electron, hole absorption cross section (cm^2)
σ_n, σ_p	electron, hole capture cross section of a defect (cm^2)
τ_D	LITG diffusive erasure time (s)
τ_{DAP}	donor-acceptor pair recombination time (s)
τ_e, τ_h	electron, hole recombination time (s)
τ_{ex}	exciton recombination time (s)
τ_G	LITG decay time (s)
τ_L	laser pulse width at FWHM (s)
τ_m	momentum relaxation time (s)
τ_R	carrier lifetime (s)
τ_{RBULK}	bulk recombination time (s)
τ_S	surface recombination time (s)
τ_{SRH}	Shockley-Read-Hall lifetime (s)
ω	circular frequency (s^{-1})

Introduction

Silicon carbide (SiC), gallium nitride (GaN), and diamond are extremely promising wide band gap semiconductor materials for optoelectronics and high temperature, high power electronics. SiC and diamond are the indirect bandgap semiconductors, being more suitable for electronic devices and optoelectronics, while GaN is a direct-bandgap semiconductor being also important in lighting applications.

Among the over 200 SiC polytypes that have been identified, only three of them are the most common: the only one cubic (3C-SiC) and the other two hexagonal (4H- and 6H-SiC). Up to now, research and industry are mostly focused on the hexagonal SiC polytypes. Although 3C-SiC is expected to have superior properties than those of the hexagonal polytypes, its growth is encumbered due to inclusions of hexagonal islands. Less expensive growth on lattice-mismatched silicon substrates is complicated by generation of large structural defect density.

GaN achievements are still limited by an absence of suitable substrates for GaN layers as there is no bulk GaN single crystals commercially available. Therefore, the whole technological development of GaN based devices relies on heteroepitaxy. Most of the current device structures are grown on sapphire or 6H-SiC. Since the substrate lattice parameters and thermal expansion coefficients are not well matched to GaN, the epitaxial growth generates huge densities of structural defects, with threading dislocations being the most prevalent (up to 10^{10} cm^{-2}). Actually this large density of defects in GaN drastically limits the performance and operating lifetime of the devices. Growth of thicker layers improves structural quality, but it is not a commercially feasible solution due to expensiveness. Therefore, new solutions as growth masks and amonothermal method have been developed.

The defect-free diamond is known to exhibit the largest values of hardness, heat conductivity and carrier mobility of all the wide-bandgap semiconductors. This makes the material attractive for production of high

power devices and detectors for ultraviolet and ionizing radiation that could operate under harsh environmental conditions. However, the development of diamond electronics is hampered by several obstacles, such as a lack of shallow dopants, relatively small single crystals, low crystalline quality of heteroepitaxial synthetic diamonds. Synthetic diamonds are usually produced by high-pressure high-temperature (HPHT) and more recently by chemical vapor deposition (CVD) growth techniques. The latter technique for high quality homoepitaxial diamond is not well established and suffers from slow deposition rate, inclusion of impurities (mainly nitrogen, boron, silicon), large dislocation density. Thus the deposition of synthetic diamond free from morphological defects and impurities is still one of the major technological challenges, which the scientific community has to face.

Due to growth-dependent parameters of the semiconductors, characterization techniques are needed to evaluate the material suitability for device applications and for optimization of the growth processes of the layers and heterostructures. Numerous techniques are used to analyze structural quality of SiC, GaN and diamonds, such as electron microscopy, atomic force microscopy, X-ray diffraction, Raman spectroscopy. Optical and electrical properties are studied by photoluminescence (PL), cathodoluminescence (CL), electron beam induced current (EBIC), time of flight (TOF), and charge collection techniques. Time resolved optical techniques, such as light induced transient grating technique (LITG), differential transmittivity (DT), differential reflectivity (DT), time-resolved photoluminescence (TRPL) have been shown as versatile nondestructive tools for investigation of semiconductor wafers, as these techniques provide straightforward information on carrier dynamics as well as important parameters such as carrier/exciton lifetime, diffusion coefficient and diffusion length.

The carrier recombination and diffusion is governed by defect density in a material and also by intrinsic properties. Therefore, knowledge of carrier dynamics enables characterization of samples in terms of growth technology optimization and fundamental phenomena. The lifetime of nonequilibrium

carriers is very sensitive to the existence of point, extended and surface defects in the material bulk and its surface. It may also reach intrinsic limit, which can not be improved by technological means (for example, nonlinear Auger recombination process).

The recombination processes can be either radiative or nonradiative. The ratio between the radiative and nonradiative recombination rates determines the internal quantum efficiency of GaN and, therefore, has a key importance for light emitting devices efficiency. The carrier diffusion coefficient and diffusion length are crucial electronic parameters for operation of optoelectronic devices.

The experimental part in this thesis is based on the known and modified optical characterization methods. The combination of several experimental techniques (LITG, DT, DR, PL) enabled investigation of carrier diffusion coefficient and lifetime in wide nonequilibrium carrier density and temperature ranges under precisely controlled generated carrier density and its in-depth profile. Deeper insight into the carrier dynamics in these materials was obtained by numerical modeling of the excess carrier transport.

Main goals

The thesis is aimed at gaining new knowledge on exciton and carrier dynamics in SiC, GaN and diamond crystals and improvement of the experimental techniques. The experimental studies that were performed by means of contactless optical techniques: light-induced transient grating (LITG), differential transmittivity (DT), differential reflectivity (DR) and photoluminescence (PL) techniques are targeted at extracting important parameters, characterizing carrier/exciton dynamics in the investigated materials in wide excess carrier density and temperature ranges.

Main objectives

1. To investigate carrier diffusion and recombination processes by monitoring their spatial and temporal dynamics in a wide temperature and nonequilibrium carrier density range for GaN, SiC, and diamond, exploring a single- and two-photon carrier photoexcitation.

2. To develop advanced experimental tools for contactless characterization of wide bandgap semiconductors in a wide temporal range - from ps to ms - and with few micrometer spatial resolution, using different mechanisms of light induced refractive and absorptive index modulation. In particularly, to develop novel techniques for diffraction-based absorption coefficient measurement, free carrier lifetime microscopy, and photorecharged trap recovery.

3. To model the excitation- and temperature- dependent carrier diffusion coefficient as well as linear and nonlinear recombination rates in SiC, GaN and diamond, describing simultaneous impact of surface, bulk, linear and nonlinear recombination processes.

Novelty and importance of the thesis

Even though there are already commercially available devices based on wide-bandgap semiconductors: SiC, GaN and diamond, the interest in these materials is continuously increasing. The processes taking place in these materials are poorly analyzed and understood, in particularly due to a limited amount of techniques applied for study of carrier dynamics.

Combination of various characterization techniques (light induced transient grating, differential transmittivity, differential reflectivity, photoluminescence) and high-quality materials (thick epilayers and bulk crystals) provided by world-wide leading companies and universities, ensured an extensive basis for this study. Further development of the time- and spatially-resolved optical techniques was performed.

Nonequilibrium carrier density and temperature are the most important parameters, describing device operation. Therefore, these parameters were varied in very wide ranges of carrier density (10^{15}-10^{20} cm^{-3}), and temperature (80-800 K). Wide nonequilibrium carrier density range was obtained by using combined single- and two-photon absorption regimes. Precise control of the nonequilibrium carrier density was performed by measurement of interband carrier absorption coefficient by newly modified light induced transient grating technique, while the absolute values of diffraction efficiency, differential transmittivity and differential reflectivity were used for carrier density determination.

High temporal resolution and wide delay range was obtained by combining optical and electronic delay of the probe beam. This allowed investigating both slow and fast recombination processes and their excitation dependences by DT technique. Such measurements have not been performed up to now in GaN. Comparison of photoluminescence efficiency with the obtained differential transmittivity decay time provided radiative and nonradiative lifetime dependences on nonequilibrium carrier density in GaN. These features could not be obtained by time resolved photoluminescence due to impact of carrier in-depth redistribution and reabsorption. The measurements of absolute integrated photoluminescence efficiency provided radiative recombination coefficient in 3C-SiC.

Carrier lifetime inhomogenity was revealed using either conventional lifetime mapping technique or newly developed CCD camera based device for carrier lifetime microscopy. Modeling of the lifetime inhomogenity together with an inverse correlation between carrier lifetime and diffusion coefficient temperature dependences allowed proving that the carrier recombination in GaN is mainly limited by their diffusive flow to grain boundaries.

Carrier density and temperature dependent lifetime and diffusion coefficient in SiC and diamond provided a new insight into the Auger recombination and exciton/carrier interaction processes. Coulomb enhancement and screening of Auger recombination was observed.

Compensating acceptor density and their activation energy in 3C-SiC and diamond was obtained by a newly proposed method: a full trap photo-recharge, leading to differential absorption signal saturation, provided the acceptor concentration, while the temperature dependences of recharged acceptor recovery rate – the acceptor activation energy. Much lower carrier diffusion coefficient at excess carrier density below the acceptor concentration was explained by impact of internal space charge field between the immobile recharged acceptors and electrons.

The points to be maintained

1. Ambipolar diffusion coefficient reduction at carrier densities above 10^{17}-10^{18} cm^{-3} (depending on T) in SiC and GaN is dominated by bandgap renormalization, while diffusion coefficient increase at further increase of carrier densities (10^{18}-10^{19} cm^{-3}) is determined by carrier plasma degeneracy and screening of carrier-phonon interactions.

2. In diamond, diffusion coefficient reduction (at carrier densities $\geq 10^{15}$ cm^{-3}) is dominated by exciton formation (leading to 6.5 times lower diffusion coefficient), electron-hole scattering, biexciton and electron-hole droplet formation (at T <150 K), while the diffusion coefficient increase at higher excitations ($\geq 10^{19}$ cm^{-3}) is caused by screening of Coulomb interaction and carrier plasma degeneracy.

3. Carrier lifetime values in the 0.4-60 ns range for GaN layers with low dislocation density are of nonradiative origin and determined by diffusive carrier flow to grain boundaries and recombination there, while in SiC, mono- and poly-crystalline diamonds the low-excitation lifetime is limited by point defects.

4. Nonlinear recombination in 4H-SiC is dominated by phonon assisted Auger process, being Coulombically enhanced at low ($\leq 5\times10^{18}$ cm^{-3}) and screened at high ($\geq 10^{19}$ cm^{-3}) carrier densities.

5. Compensating trap density in 3C-SiC and diamond can be determined by

using their full photoneutralization by UV pump and subsequent monitoring of their photoionization transitions by IR probe. Temperature dependences of the recharged acceptor recovery time provided the aluminum (3C-SiC) and boron (diamond) acceptor activation energies.

Layout of the thesis

The thesis is organized as follows. In chapter 1, an overview of some basic SiC, GaN and diamond properties is presented. Some more advanced issues, such as band structure, effective mass, absorption and refraction coefficients, carrier mobility and recombination, are discussed in more detail.

In chapter 2, the experimental setups, used for optical characterization of the samples under study, are described. These include light induced transient grating, differential transmittivity, differential reflectivity, and photoluminescence techniques.

Chapter 3 deals with precise determination of nonequilibrium carrier density and its in-depth profile in the investigated bulk samples by means of single- and two-photon excitation used in the work.

In chapter 4, the study of carrier diffusion coefficient in wide excitation and temperature range is provided. Its dependences on carrier density and temperature are modeled by means of electron, hole, exciton and phonon interactions.

Chapter 5 deals with the study of carrier recombination. Photoexcitation and temperature dependences of lifetime provide surface, bulk and nonlinear recombination rates, the latter being of radiative or nonradiative origin. Screening and exciton impact on these recombination processes is evaluated. Also the modeling of carrier in-plane and in-depth profiles is investigated.

In chapter 6, the investigation of compensating trap recharge impact on carrier relaxation and diffusion coefficient is provided. Compensating trap densities and activation energies are determined. The thesis is finalized with a concluding summary.

Author's contribution

The most of the results presented in the thesis were obtained in the Optoelectronics Division of the Institute of Applied Research at Vilnius University. The author performed all measurements by LITG, DR and DT techniques. Measurements of spectrally resolved PL were performed by M. Karaliūnas, J. Jurkevičius and J. Mickevičius. Measurements of time resolved PL were performed by S. Okur (USA) and J. Hassan (Sweden). Calibration of PL efficiency in SiC was performed by the author of the thesis. Absorption spectra in diamonds were obtained by the coauthors from Belarus (Minsk). Structural characterization of diamonds was performed by Belgian (Hasselt, Diepenbeek) and French (Paris, Versailles) partners. The investigations were performed on the samples provided by many leading SiC, GaN and diamond growing companies and universities from Belgium, France, Japan, Russia, S. Korea, Sweden, Ukraine and USA.

The numerical analysis of the experimental results was done by the author. The interpretations of the observed phenomena were discussed with the thesis advisor K. Jarašiūnas. Most of the papers manuscripts were prepared by the author of the thesis. All the obtained results were presented at national and international conferences, and later published in conference proceedings and/or international journals.

List of publications

List of papers related to the thesis

P1. **P. Ščajev**, V. Gudelis, K. Jarašiūnas and P. B. Klein, "Fast and slow carrier recombination transients in highly excited 4H- and 3C-SiC crystals at room temperature", J. Appl. Phys. **108**, 023705 (2010).

P2. K. Jarašiūnas, **P. Ščajev**, V. Gudelis, P. B. Klein and M. Kato, "Nonequilibrium carrier recombination in highly excited bulk SiC crystals", Mater. Sci. Forum **645-648**, 215-218 (2010).

P3. A. Kadys, **P. Ščajev**, G. Manolis, V. Gudelis, K. Jarašiūnas, P. Abramov, S. Lebedev and A. Lebedev, "On the correlation of the structural perfection and nonequilibrium carrier parameters in 3C SiC heterostructures", Mater. Sci. Forum **645-648**, 219-222 (2010).

P4. **P. Ščajev**, K. Jarašiūnas, A. Kadys, J. Storasta, P. L. Abramov, S. P. Lebedev and A. A. Lebedev, "Impact of Nonintentional Al Impurity to Carrier Lifetime and Diffusion in Sublimation Grown 3C Heterostructures", AIP Conference Proceedings **1292,** 107-110 (2010).

P5. **P. Ščajev**, J. Hassan, K. Jarašiūnas, M. Kato, A. Henry and J. P. Bergman, "Comparative Studies of Carrier Dynamics in 3C-SiC Layers Grown on Si and 4H-SiC Substrates", J. Electron. Mater. **40**, 394-399 (2011).

P6. **P. Ščajev**, T. Malinauskas, L. Lubys, E. Ivakin, M. Nesladek, K. Haenen and K. Jarašiūnas, "Optical monitoring of nonequilibrium carrier diffusion in single crystalline CVD and HPHT diamonds under high optical excitation", Phys. Status Solidi RRL **5**, 193–195 (2011).

P7. **P. Ščajev**, A. Mekys, P. Malinovskis, J. Storasta, M. Kato and Jarašiūnas, "Electrical parameters of bulk 3C-SiC crystals determined by Hall effect, magnetoresistivity, and contactless time-resolved optical techniques", Mater. Sci. Forum **679-680**, 157-160 (2011).

P8. J. Hassan, **P. Ščajev**, Jarašiūnas and J. P. Bergman, "Optically detected temperature dependences of carrier lifetime and diffusion coefficient in 4H- and 3C-SiC", Mater. Sci. Forum **679-680**, 205-208 (2011).

P9. **P. Ščajev**, A. Usikov, V. Soukhoveev, R. Aleksiejūnas and K. Jarašiūnas, "Diffusion-limited nonradiative recombination at extended defects in hydride vapor phase epitaxy GaN layers", Appl. Phys. Lett. **98**, 202105 (2011).

P10. **P. Ščajev**, V. Gudelis, E. Ivakin and K. Jarašiūnas, "Nonequilibrium carrier dynamics in bulk HPHT diamond at two-photon carrier generation", Phys. Status Solidi A **208**, 2067–2072 (2011).

P11. **P. Ščajev,** M. Kato and K. Jarašiūnas, "A diffraction-based technique for determination of interband absorption coefficients in bulk 3C-, 4H- and 6H-SiC crystals", J. Phys. D: Appl. Phys. **44**, 365402 (2011).

P12. **P. Ščajev**, K. Jarašiūnas, S. Okur, Ü. Özgür and H. Morkoç, "Nonequilibrium carrier dynamics in bulk GaN under two photon carrier excitation", Phys. Status Solidi B, **249**, 503-506 (2012).

P13. **P. Ščajev**, K. Jarašiūnas, S. Okur, Ü. Özgür and H. Morkoç, "Carrier dynamics in bulk GaN", J. Appl. Phys. **111**, 023702 (2012).

P14. **P. Ščajev**, K. Jarašiūnas, Ü. Özgür, H. Morkoç, J. Leach and T. Paskova, "Anisotropy of free-carrier absorption and diffusivity in m-plane GaN", Appl. Phys. Lett. **100**, 022112 (2012).

P15. **P. Ščajev,** V. Gudelis, K. Jarašiūnas, I. Kisialiou, E. Ivakin, M. Nesládek and K. Haenen, "Carrier recombination and diffusivity in microcrystalline CVD-grown and single-crystalline HPHT diamonds", Phys. Status Solidi A **209**, 1744–1749 (2012).

P16. **P. Ščajev**, P. Onufrijevs, G. Manolis, M. Karaliūnas, S. Nargelas, N. Jegenyes**,** J. Lorenzzi, G. Ferro, M. Beshkova, R. Vasiliauskas, M. Syväjärvi, R. Yakimova, M. Kato and K. Jarašiūnas, "On applicability of time-resolved optical techniques for characterization of differently grown 3C-SiC crystals and heterostructures", Mater. Sci. Forum **711**, 159-163 (2012).

P17. K. Jarašiūnas, R. Aleksiejūnas, T. Malinauskas, S. Nargelas and **P. Ščajev**, "Nonlinear Optical Techniques for Characterization of Wide Band Gap Semiconductor Electronic Properties: III-Nitrides, SiC, and Diamonds", MRS Proceedings **1396** (2012), DOI: 10.1557/opl.2012.497.

P18. K. Jarašiūnas, **P. Ščajev**, S. Nargelas, R. Aleksiejūnas, J. Leach, T. Paskova, S. Okur, Ü. Özgür and H. Morkoç, "Recombination and diffusion processes in polar and nonpolar bulk GaN investigated by time-resolved photoluminescence and nonlinear optical techniques", Proc. of SPIE **8262**, 82620G (2012).

P19. K. Jarašiūnas, **P. Ščajev**, T. Malinauskas, M. Kato, E. Ivakin, M. Nesládek, K. Haenen, Ü. Özgür and H. Morkoç, "Carrier Diffusivity in Highly Excited Bulk SiC, GaN, and Diamond Crystals by Optical Probes", Mater. Sci. Forum **717-720**, 309-312 (2012).

P20. **P. Ščajev,** M. Karaliūnas, E. Kuokštis and K. Jarašiūnas, "Radiative and nonradiative recombination rates in cubic SiC", J. Lumin. **134**, 588-593 (2013).

P21. **P. Ščajev**, K. Jarašiūnas, P. L. Abramov, S. P. Lebedev and A. A. Lebedev, "Optical characterization of compensating defects in cubic SiC", Mater. Sci. Forum **740-742**, 401-404 (2013).

P22. **P. Ščajev**, L. Trinkler, B. Berzina, E. Ivakin and K. Jarašiūnas, "Influence of boron on donor–acceptor pair recombination in type IIa HPHT diamonds", Diamond Relat. Mater. **36**, 35-43 (2013).

P23. R. Aleksiejūnas, **P. Ščajev**, S. Nargelas, T. Malinauskas, A. Kadys and K. Jarašiūnas, "Impact of Diffusivity to Carrier Recombination Rate in Nitride Semiconductors: from Bulk GaN to (In,Ga)N Quantum Wells", Jpn. J. Appl. Phys. **52**, 08JK01 (2013).

P24. **P. Ščajev** and K. Jarašiūnas, "Temperature- and excitation-dependent carrier diffusivity and recombination rate in 4H-SiC", J. Phys. D: Appl. Phys. **46**, 265304 (2013).

P25. **P. Ščajev**, S. Nargelas and K. Jarašiūnas, "Time-resolved free carrier lifetime microscopy in bulk GaN", Phys. Status Solidi RRL **7**, 647-650 (2013).

P26. **P. Ščajev**, V. Gudelis, A. Tallaire, J. Barjon and K. Jarašiūnas, "Injection and temperature dependent carrier recombination rate and diffusion length in freestanding CVD diamond", Phys. Status Solidi A (2013), DOI 10.1002/pssa.201300045.

P27. **P. Ščajev**, S. Nargelas, K. Jarašiūnas, I. Kisialiou, E. Ivakin, W. Deferme, J. D'Haen and K. Haenen, "Crystallite size dependent carrier recombination rate and thermal diffusivity in undoped and boron doped CVD diamond layers", Phys. Status Solidi A (2013), DOI 10.1002/pssa.201300046.

P28. **P. Ščajev**, "Application of excite-probe techniques for determination of surface, bulk and nonlinear recombination rates in cubic SiC", submitted to Mater. Sci. Eng. B.

P29. G. Liaugaudas, **P. Ščajev** and K. Jarašiūnas, "Evaluation of photoelectrical parameters of highly compensated 3C-SiC epilayers by nonlinear optical techniques", submitted to Semicond. Sci. Technol.

List of papers not included in the thesis

P30. P. Bogdanovich and **P. Ščajev**, "Estimation of LS-coupling validity within configuration interaction approach", Lith. J. Phys. **48**, 17-23 (2008).

P31. **P. Ščajev** and K. Jarašiūnas, "Application of a time-resolved four-wave mixing technique for the determination of thermal properties of 4H-SiC crystals", J. Phys. D: Appl. Phys. **42,** 055413 (2009).

P32. **P. Ščajev**, A. Kadys and K. Jarašiūnas, "Investigation of Thermal Properties of Heavily Doped 4H-SiC Crystals by a Picosecond Transient Grating Technique", Mater. Sci. Forum **615-617**, 319-322 (2009).

P33. P. Onufrijevs, T. Serevičius, **P. Ščajev**, G. Manolis, A. Medvids, L. Chernyak, E. Kuokštis, C. C. Yang and K. Jarašiūnas, "Characterization of Optical and Photoelectrical Properties of ZnO Crystals", Acta Physica Polonica A **119**, 274-276 (2011).

P34. R. Aleksiejūnas, **P. Ščajev**, S. Nargelas, S. Miasojedovas, K. Jarašiūnas, L. Trinkler, J. Grigorjeva, B. Berzina, K. H. Chen, Y. T. Chen, M. W. Chen and L. C. Chen, „Carrier dynamics in nanostructures of ternary AlGaN with tunable bandgap", IOP Conf. Series: Materials Science and Engineering **38**, 012054 (2012).

List of conference contributions related to the thesis

C1. K. Jarašiūnas, T. Malinauskas, R. Aleksiejūnas, S. Nargelas, **P. Ščajev**, G. Manolis, V. Gudelis, "Optical characterization of wide bandgap semiconductors at excitation conditions approaching a power device operation", Workshop on Advanced Semiconductor Materials and devices for Power Electronics applications (WASMPE 2009), 5.6-8, Catania, Italy, 2009.

C2. **P. Ščajev**, V. Gudelis, K. Jarašiūnas, and P. B. Klein, "Nonequilibrium carrier recombination peculiarities in highly excited bulk SiC crystals", 38th Lithuanian National Physics Conference (LNFK-38), 6.8-10, Vilnius, Lithuania, 2009 (Conference Abstracts, page 156).

C3. A. Kadys, G. Manolis, **P. Ščajev**, V. Gudelis, K. Jarašiūnas, P. Abramov, S. Lebedev, and A. Lebedev, "On correlation of the structural perfection and nonequilibrium carrier parameters in 3C SiC heterostructures", 13th International Conference on Silicon Carbide and Related Materials (ICSCRM 2009), 10.11-16, Nürnberg, Germany, 2009.

C4. K. Jarašiūnas, **P. Ščajev**, V. Gudelis, P. B. Klein, M. Kato, "Nonequilibrium carrier recombination in highly excited bulk SiC crystals", 13th International Conference on Silicon Carbide and Related Materials (ICSCRM 2009), 10.11-16, Nürnberg Germany, 2009.

C5. M. Karaliūnas, **P. Ščajev** and K. Jarašiūnas, "Room temperature photoluminescence spectra in bulk 3C-SiC crystals", The 11th International Conference-School Advanced Materials and Technologies, 8.27-31, Palanga, Lithuania, 2009.

C6. **P. Ščajev** and M. Kato, "Monitoring of fast and slow carrier recombination transients in 3C-SiC by time-resolved FCA techniques", Winter School "SiC epitaxial growth: from thin layers to bulk material", 1.25-29, Linkoping, Sweden, 2010.

C7. **P. Ščajev**, K. Jarašiūnas, A. Kadys, J. Storasta, P. L. Abramov, S. P. Lebedev, and A. A. Lebedev, "Role of twin defects to carrier mobility and lifetime in sublimation grown 3C heterostructures", E-MRS 2010 F: Wide bandgap cubic semiconductors: from growth to devices, Spring Meeting, 6.7-11, Strasbourg, France, 2010.

C8. J. Hassan, **P. Ščajev**, K. Jarašiūnas, M. Kato, A. Henry, P. Bergman, "Comparative Studies of Carrier Dynamics in 3C-SiC Layers Grown on Si and 4H-SiC Substrates", Electronic Materials Conference 2010, 6.23-25, Notre Dame, Indiana, USA, 2010.

C9. **P. Ščajev,** A. Mekys**,** P. Malinovskis**,** J. Storasta**,** M. Kato, and K. Jarašiūnas, "Electrical parameters of bulk 3C crystals determined by Hall effect, magnetoresistivity, and contactless time-resolved optical techniques", The 8th European Conference on Silicon Carbide and Related Materials (ECSCRM 2010), 8.29-9.2, Oslo, Norway, 2010.

C10. J. Hassan, **P. Ščajev**, J. P. Bergman and K. Jarašiūnas, "Optically detected temperature and injection dependent carrier lifetime and diffusion in SiC", ECSCRM 2010, 8.29-9.2, Oslo, Norway, 2010.

C11. P. Onufrijevs, **P. Ščajev,** M. Kato, G. Manolis, M. Karaliūnas, S. Miasojedovas, and K. Jarašiūnas, "Study of optical and photoelectrical properties of 3C-SiC single crystals and heterostructures", VIII International Science and Technology Conference "Quantum electronics", 11.22-25, Minsk, Belarus, 2010.

C12. **P. Ščajev**, V. Gudelis, E. Ivakin, K. Jarašiūnas, "Investigation of carrier recombination rate in high-pressure high-temperature diamond by time-resolved free carrier absorption", Hasselt Diamond Workshop 2011 (SBDD XVI), 1.21-23, Hasselt, Belgium, 2011.

C13. **P. Ščajev**, V. Gudelis, E. Ivakin, and K. Jarašiūnas, "Development and implementation of time-resolved nonlinear optical techniques for monitoring of carrier dynamics in SiC and diamond crystals", XIX Belarussian – Lithuanian seminar "Lasers and optical nonlinearity", 05.16-18, Minsk, Belarus, 2011.

C14. **P. Ščajev,** P. Onufrijevs, G. Manolis, M. Karaliūnas, N. Jegenyes, J. Lorenzzi, M. Beshkova, R. Vasiliauskas, M. Kato and K. Jarašiūnas, "Metrological potential of time-resolved optical techniques for characterization of differently grown 3C-SiC crystals and heterostructures", HeteroSiC-WASMPE 2011, 6.27-30, Tours, France, 2011.

C15. **P. Ščajev**, K. Jarašiūnas, U. Ozgur, H. Morkoc, "Nonequilibrium carrier dynamics in bulk GaN under two photon carrier excitation", 9th International Conference on Nitride Semiconductors (ICNS-9), 7.10-15, Glasgow, United Kingdom, 2011.

C16. K. Jarašiūnas, **P. Ščajev**, T. Malinauskas, M. Kato, M. Nesladek, K. Haenen, Ü. Özgür, and H. Morkoç, "Optical Study of Carrier Diffusivity in Highly Excited Bulk SiC, GaN, and Diamond Crystals", International Conference on Silicon Carbide and Related Materials 2011 (ICSCRM 2011), 9.11-16, Cleveland, Ohio, USA, 2011.

C17. **P. Ščajev**, V. Gudelis, S. Nargelas, Z. Vaitonis, M. Kato, E. Ivakin, Ü. Özgür, H. Morkoç, and K. Jarašiūnas, "Implementation of time-resolved nonlinear optical techniques for carrier diffusivity and lifetime investigation in SiC, GaN, and diamond crystals", 39th Lithuanian National Physics Conference (LNFK-39), 10.6-8, Vilnius, Lithuania, 2011.

C18. K. Jarašiūnas, R. Aleksiejūnas, T. Malinauskas, S. Nargelas and **P. Ščajev**, "Nonlinear Optical Techniques for Characterization of Wide Band Gap Semiconductor Electronic Properties: III-Nitrides, SiC, and Diamonds", 2011 MRS Fall Meeting & Exhibit, 11.28-12.2, Boston, Massachusetts, USA, 2011 (invited presentation).

C19. K. Jarašiūnas, **P. Ščajev**, S. Nargelas, R. Aleksiejūnas, J. Leach, T. Paskova, S. Okur, Ü. Özgür, H. Morkoç, "Recombination and diffusion

processes in polar and nonpolar bulk GaN investigated by time-resolved photoluminescence and nonlinear optical techniques", OPTO SPIE Photonics West, 1.21-26, 2012, San Francisco, California, USA, 2012.

C20. **P. Ščajev**, V. Gudelis, K. Jarašiūnas, I. Kisialiou, E. Ivakin, M. Nesládek, K. Haenen, "Carrier recombination and diffusivity in microcrystalline CVD-grown and single crystalline HPHT diamonds", Hasselt Diamond Workshop 2012 (SBDD XVII), 3.14-16, Hasselt, Belgium, 2012.

C21. K. Jarašiūnas, **P. Ščajev**, S. Nargelas, A. Kadys, P. L. Abramov, S. P. Lebedev, A. A. Lebedev, "Optical characterization of compensation in cubic SiC", European Conference on Silicon Carbide and Related Materials 2012 (ECSCRM 2012), 9.2-6, Saint-Petersburg, Russia, 2012.

C22. R. Aleksiejūnas, **P. Ščajev**, S. Nargelas, T. Malinauskas, A. Kadys, and K. Jarašiūnas, "Impact of diffusivity to carrier recombination rate in nitride semiconductors: from bulk GaN to (In,Ga)N quantum wells", International Workshop on Nitride Semiconductors 2012 (IWN2012), 10.14-19, Sapporo, Japan, 2012.

C23. **P. Ščajev**, S. Nargelas, K. Jarašiūnas, I. Kisialiou, E. Ivakin, W. Deferme, and K. Haenen, "Crystallite size dependent carrier recombination rate and thermal diffusivity in undoped and boron doped CVD diamonds", Hasselt Diamond Workshop 2013 (SBDD XVIII), 2.27-3.1, Hasselt, Belgium, 2013.

C24. **P. Ščajev**, V. Gudelis, A. Tallaire, J. Barjon, and K. Jarašiūnas, "Injection and temperature dependent carrier recombination rate and diffusion length in freestanding CVD diamond", Hasselt Diamond Workshop 2013 (SBDD XVIII), 2.27-3.1, Hasselt, Belgium, 2013.

C25. K. Jarašiūnas, **P. Ščajev**, R. Aleksiejūnas, S. Nargelas, V. Gudelis, T. Malinauskas, A. Kadys, M. Vengris, K. Gelžinyte, K. Nomeika, "Nitridinių junginių *ex-situ* optinė diagnostika su laikine, erdvine ir spektrine skyra", 40-oji Lietuvos nacionalinė fizikos konferencija (LNFK-40), 6.10-12, Vilnius, 2013.

C26. K. Jarašiūnas, **P. Ščajev**, "Carrier diffusivity and scattering mechanisms in highly-excited diamonds investigated by light-induced transient grating technique", International Conference on Diamond and Carbon Materials, 9.2-5, Riva del Garda, Italy, 2013 (invited presentation).

C27. **P. Ščajev**, M. Karaliūnas, E. Kuokštis, V. Grivickas, and K. Jarašiūnas, "Radiative and nonradiative recombination in 3C-SiC", International Conference on Silicon Carbide and Related Materials 2013 (ICSCRM 2013), 9.29-10.4, Miyazaki, Japan, 2013.

C28. **P. Ščajev**, K. Jarašiūnas, and P. B. Klein, "Injection and temperature dependent diffusivity and Auger recombination in 4H-SiC", International Conference on Silicon Carbide and Related Materials 2011 (ICSCRM 2011), 9.29-10.4, Miyazaki, Japan, 2013.

1. Properties of SiC, GaN and diamond

In this chapter basic properties of investigated semiconductors are reviewed (crystal structure, electronic band structure, effective masses, density of states, phonon energies). Absorption, carrier mobility, diffusion coefficient, linear and nonlinear lifetimes, and carrier dynamics follow afterwards. These more advanced properties, being investigated in this work, are described in more detail. Appropriate formulae are provided. Finally, results from previous experimental studies of carrier mobility, diffusion coefficient, and recombination are presented.

1.1. Basic properties of wide bandgap semiconductors

Wide bandgap semiconductors are superior versus commonly used semiconductors with much lower bandgaps (Si, GaAs) in terms of much higher operating temperatures, critical electric fields, saturation drift velocity, thermal conductivity and other parameters (see comparison in Table 1.1, where data were compiled from different references [1-9]). However, their growth techniques and processing are much more complicated due to higher growth temperatures and hardness. The most advanced techniques for SiC GaN, and diamond growth are: chemical vapor deposition (CVD) [10,11], hydride vapor phase epitaxy (HVPE) [12], high pressure and high temperature growth (HPHT) [13]. Also other techniques (frequently used for conventional semiconductors) such as growth from melt, vapor liquid solid deposition (VLS) [14], sublimation epitaxy (SE) [15], physical vapor transport (PVT) [16] are applied for growth occasionally.

Table 1.1. Properties of some wide bandgap semiconductors at 300 K [1-9]. Conventional semiconductors, such as Si and GaAs, are included for comparison.

Property	Si	GaAs	3C-SiC	4H-SiC	6H-SiC	2H-GaN	3C diamond
Bandgap (eV)	1.12	1.4	2.36	3.26	3.02	3.452	5.45
Breakdown field (MV/cm)	0.25	0.4	1.2	2.2	2.5	5	10
Saturation drift velocity (10^7 cm/s)	1	2	1.2	2	2.5	2.5	2.7
Max. operating temperature (˚C)	350	460	1200	1200	1200	600	1100
Melting point (˚C)	1410	1511	2830	2830	2830	2500	4373
Electron mobility ($cm^2/V{\cdot}s$)	1350	8500	900	1000	400	1200	2200
Hole mobility ($cm^2/V{\cdot}s$)	480	400	90	120	100	30	1800
Static dielectric constant	11.8	12.8	9.7	10	10	8.9	5.5
Lattice constants (Å)	5.43	5.65	4.36	a = 3.08 c = 10.08	a = 3.08 c = 15.12	a = 3.19 c = 5.19	3.57
Density (g/cm^3)	2.3	5.3	3.2	3.2	3.2	6.15	3.5
Mohs hardness	7	4-5	≥9	9.2-9.3	≥9	≥9	10
Heat capacity (J/g·K)	0.71	0.327	0.69	0.69	0.69	0.49	0.52
Thermal conductivity (W/cm·K)	1.5	0.5	3.6	3.7	4.9	1.3	20
Thermal diffusivity (cm^2/s)	0.9	0.3	1.6	1.7	2.2	0.4	11

1.1.1. The crystal structure

The investigated SiC, GaN and diamond semiconductors can crystallize in the different crystalline structures, where different order of Si-C, Ga-N and C-C biatomic element stacking sequence can occur [17-19]. These crystal structures, having the same atomic composition, are called polytypes. The stacking sequence (of biatomic layers) of most simple polytypes, aligned in c- axis direction, is shown in Fig. 1.1.

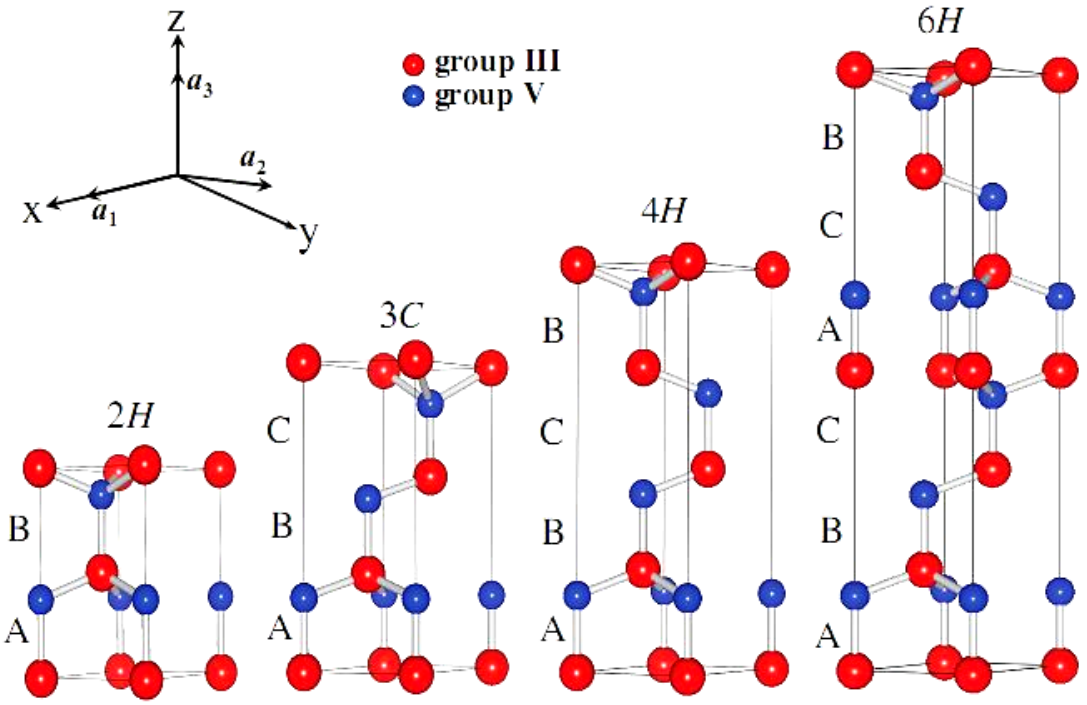

Fig. 1.1. Stick-and-ball models in the four simplest polytypes [18]. Cations: red spheres, anions: blue spheres. The stacking sequence of the cation-anion bilayers are indicated by the symbols A, B or C. The primitive basis vectors a_i (i = 1, 2, 3) are also shown. The cubic (c) or hexagonal (h) character of a bilayer is defined by the nonparallel bond in this plane.

However not all polytypes are thermodynamically stable and often single polytype can grow only under special growth conditions. When few polytypes grow simultaneously, structural defects as stacking faults will appear (different polytypes can also be generated by mechanical deformation). As different polytypes have different electronic properties, stacking faults strongly deteriorate device quality. Such problem is the most important in SiC [17]. The most stable and easily grown are 2H-, 3C-, 4H- and 6H-SiC polytypes. Letter

”H” indicates for hexagonal polytype, while “C” for cubic one. Hexagonal polytypes have wurtzite structure (characterized by two lattice constants, *a* and *c*), while the only one cubic (3C) has the zinc-blende structure. At this time commercially available and applicable SiC polytypes are: 3C-SiC, 4H-SiC, and 6H-SiC, GaN polytypes: 2H-GaN, 3C-GaN [20,21], and cubic diamond polytype 3C-C (2H diamond (lonsdaleite) was also obtained [22]). In this work 3C-SiC, 4H-SiC, 6H-SiC, 2H-GaN, and 3C diamond polytypes will be investigated.

1.1.2. Electronic band structure

Different polytypes have different electronic band structure, i. e. the dependence of carrier energy (*E*) on its momentum (*k*). The band structure of the most common polytypes is provided in Fig. 1.2.

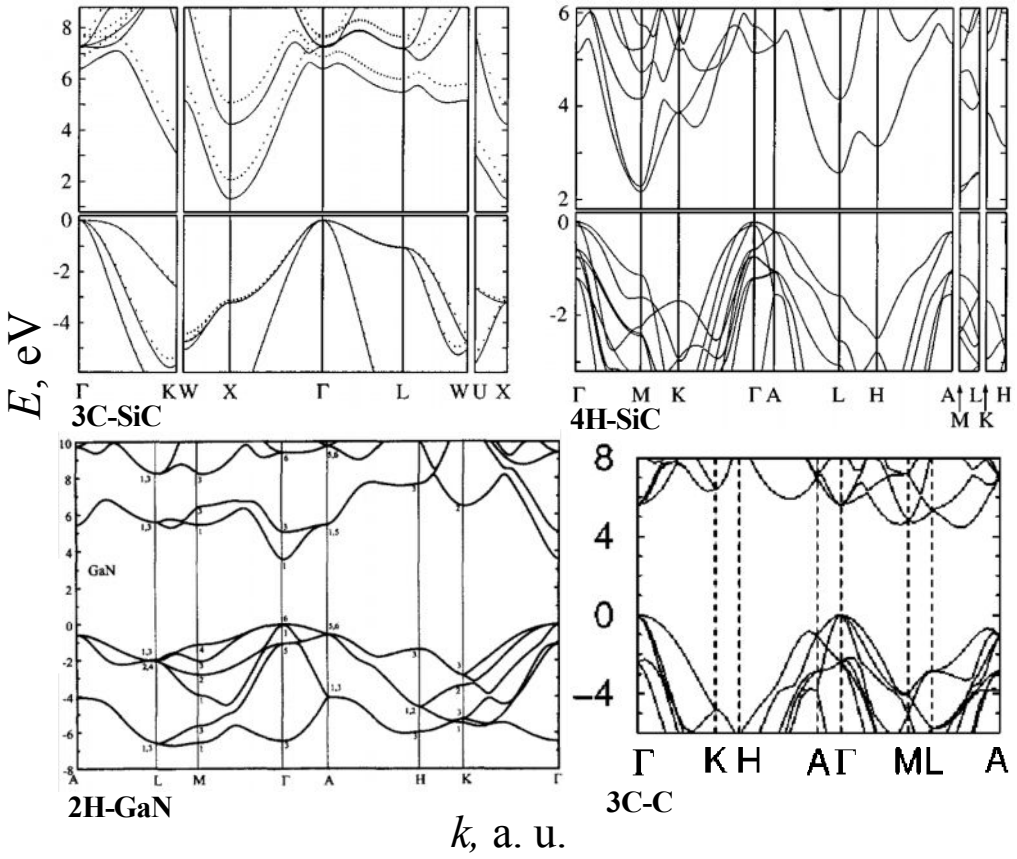

Fig. 1.2. Band structures of the most important polytypes according to [19,23,24]. Letters indicate Brillouin zone symmetry points.

Different band structure leads to different bandgaps, masses, mobility, exciton

binding energies and so on (Table 1.2). The band structures also indicate that SiC and diamond are indirect semiconductors as valence band maximum and conduction band minimum are in different *k* positions. In GaN these extrema are in the same position, leading to its direct bandgap. This favors direct (phonon-less) valence to conduction band transitions and more effective radiative recombination.

1.1.3. Effective masses and density of states

Many electrical semiconductor parameters, such as mobility, density of states, exciton binding energy, are determined by electron and hole effective masses. The effective masses for different materials [2,9,23-26] are provided in Table 1.2. Using their values, the density of states in conduction and valence bands and exciton binding energies were calculated. The latter values were very close to the experimental ones [27-29].

Table 1.2. Effective masses, density of states [2,9,23-26] and exciton binding energies E_{ex} [27-29].

Property	3C-SiC	4H-SiC	6H-SiC	2H-GaN	3C diamond
m_e^*	0.30	0.35	0.50	0.2	0.48
m_h^*	1.11	0.63	0.61	1.5	0.31
m_{eh}	0.24	0.23	0.27	0.18	0.19
m_{cd}^*	0.73	0.77	2.3	0.2	1.9
m_{vd}^*	1.4	0.94	0.92	1.5	0.8
N_{cd}, 10^{19} cm^{-3}	1.6	1.7	8.7	0.22	6.5
N_{vd}, 10^{19} cm^{-3}	4.1	2.3	2.2	4.6	1.8
E_{ex}, meV calculated	32	31	37	31	85
E_{ex}, meV experimental	27	20	78	28	80

Here $m_{cd}^* = \left(N_b^2 m_x m_y m_z\right)^{1/3}$ is the density of states mass, where N_b is the number of equivalent minima in conduction band, $m_c^* = \left(m_x m_y m_z\right)^{1/3}$ is the one conduction valley density of states mass (m_x, m_y, m_z are mass tensor

components); m_e^* and m_h^* are electron and hole effective masses [30]. Here m_e^* is the isotropic effective conduction mass, which is calculated using mass tensor components [31]:

$$1/m_e^* = \left(1/m_x + 1/m_y + 1/m_z\right)/3 . \quad (1.1)$$

Analogically it is calculated for holes. Optical mass (reduced mass) is described by a relation:

$$\frac{1}{m_{eh}} = \left(\frac{1}{m_e^*} + \frac{1}{m_h^*}\right). \quad (1.2)$$

Commonly heavy and light hole bands are present with m_{HH} and m_{LH} masses, correspondingly. Then average inverse optical hole mass is described by a relation [31]:

$$1/m_h^* = \left(m_{HH}^{1/2} + m_{LH}^{1/2}\right)/\left(m_{HH}^{3/2} + m_{LH}^{3/2}\right). \quad (1.3)$$

Exciton binding energy in hydrogenic approximation is calculated according to E_{ex} = 13.6 eV$\times m_{eh}/m_0/\varepsilon_s^2$ relation [32]. Density of states are calculated for holes as $N_{vd} = 4/\sqrt{\pi}\left(2\pi m_{vd}^* k_B T/h^2\right)^{3/2}$ (analogically for electrons).

1.2. Absorption processes

A large variety of energy states may occur in semiconductors, both in the form of bands or in the form of discrete energy levels [31]. Pure semiconductors of perfect crystallinity are characterized by a set of broad valence and conduction electron bands and an abundance of phonon modes; discrete states occur in the presence of impurities and lattice defects, and at low temperatures owing to the possible binding of electrons and holes to excitons and excitonic complexes. Various transitions are thus possible between these states, they are depicted by arrows in Fig. 1.3. These include valence-to-conduction band transitions (which lead to free carrier generation) (a), free carrier transitions (inter-valence-band (b), inter-conduction-band (c) and intraband transitions between the electronic levels of impurities (d), between impurity levels and conduction bands (e), and between valence band and impurity (f) or excitonic levels (g).

Also in the transparency range two-photon absorption can take place at high fluences. In the latter case one photon transfers an electron to virtual level in the bandgap, while other photon transfers the electron to conduction band from the virtual level [33]. In this case two photons are needed to generate one electron-hole pair. The transitions (a-g) can be either "direct" when vertical transitions occur or "indirect", when momentum conservation law needs phonons.

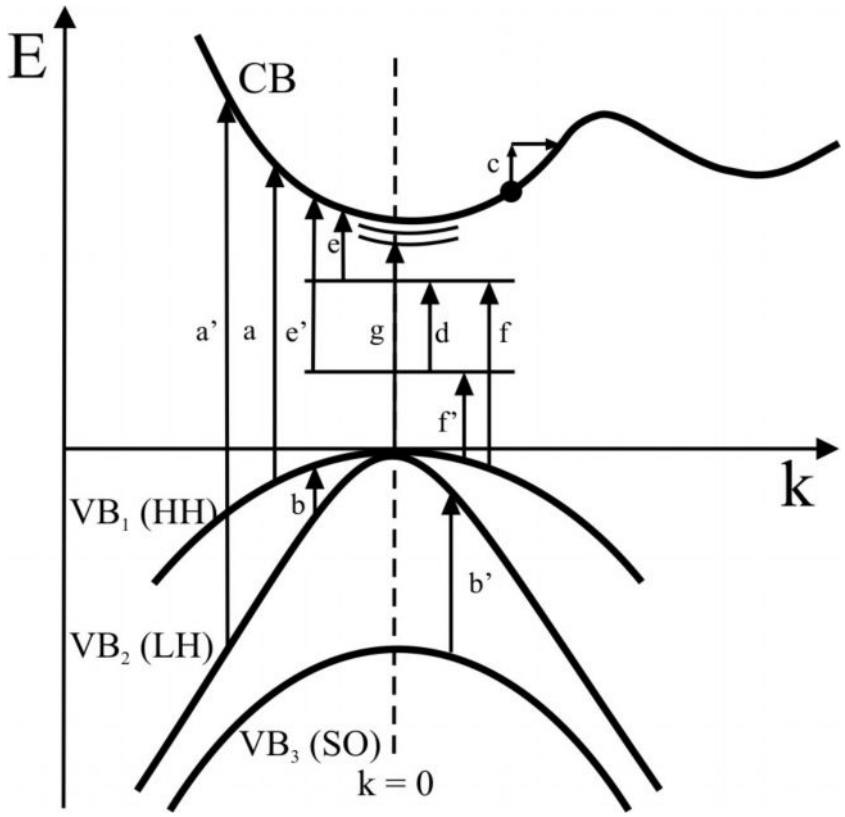

Fig. 1.3. Various optical transitions in semiconductors [31]. See explanations in the text.

The term "interband absorption" refers to an optical transition in which an electron from the valence band is excited to 1) the conduction band or 2) an excitonic state. In this work absorption processes will be studied in direct- (GaN) and indirect-bandgap (SiC, diamond) semiconductors, in particularly related to the experimental studies of the temperature dependences of absorption coefficient in the spectral region above the bandgap.

The absorption spectra of GaN and diamond are provided on Fig. 1.4. It is clearly observed that in direct-bandgap GaN the absorption coefficient, α, increases very sharply near the absorption edge (a), while due to lower probability of the phonon assisted processes, the absorption coefficient increases much slower in diamond (b).

The optical excitation mechanisms can be separated to intrinsic interband electron-hole pair/exciton generation, when absorbed quantum energy is higher than the bandgap E_g, while for lower excitation quanta absorption by defects dominates.

The absorption coefficient in direct bandgap semiconductor is dominated by direct electron-hole pair and exciton generation and can be expressed for photons below, and above the bandgap as follows [32]:

$$\begin{aligned}
&\alpha(\omega) = \Pi \times |d_{cv}(0)|^2 \left[E_{ex} \sum_{i=1}^{\infty} \frac{4\pi}{i^3} \delta\left(\hbar\omega - E_g + E_{ex}/i^2\right) \right], \ \hbar\omega < E_g; \\
&\alpha(\omega) = \Pi \times \left[\pi \frac{\exp(Z)}{\sinh(Z)} |d_{cv}(0)|^2 + \frac{2\varepsilon_0}{m_0^2 \omega^2} \left[\hbar\omega - E_g\right]^{1/2} |p_{cv}(0)|^2 \right], \ \hbar\omega > E_g.
\end{aligned} \tag{1.4}$$

Here $\Pi = \left(2m_{eh} e\omega/\hbar^2\right)^2 / \left(n_g c\omega\varepsilon_0\right)$, $Z = \pi\sqrt{E_{ex}/\left(\hbar\omega - E_g\right)}$, $p_{cv}(0)$ is the interband matrix element for electron valence to conduction band transitions at k =0. $d_{cv}(0)$ is the interband matrix element corresponding to transitions to the electron-hole states, that make the exciton packet.

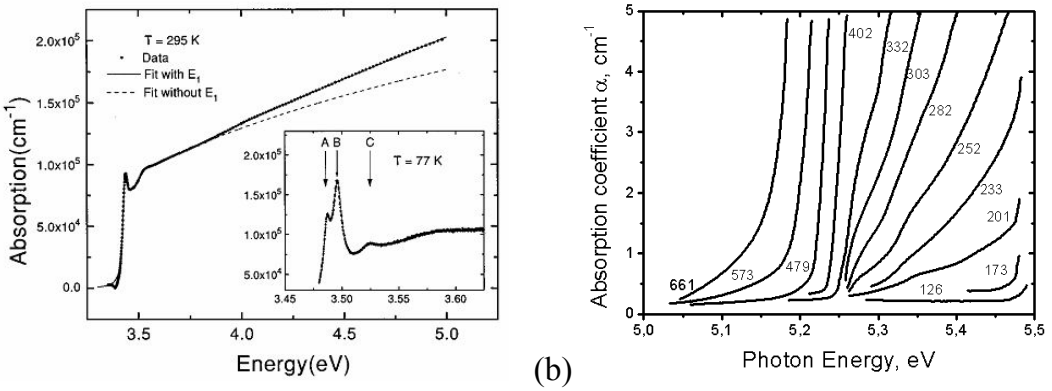

Fig. 1.4. Absorption spectra of GaN [34] (a) and diamond [35] (b) at different temperatures. At low temperatures A, B, and C exciton peaks are observed in GaN.

At $\hbar\omega < E_g$ only absorption to bound exciton states takes place, while at $\hbar\omega > E_g$ absorption to excitonic continuum and to conduction band appears at the same time. Near the bandgap, due to absorption to excitonic continuum, α is strongly enhanced as compared to the valence-conduction band transitions of electrons [36], which is proportional to $\alpha_{free} \sim [\hbar\omega - E_g]^{1/2}$. This leads to so called Coulomb enhancement as $\alpha_{continuum}(\omega) = \alpha_{free}(\omega)C(\omega)$, where the enhancement factor is $C(\omega) = 2Z/[1-\exp(-2Z)]$. Namely, this situation is observed for GaN case (Fig. 1.4). The exciton peaks are broadened due to exciton-phonon and exciton-defect interactions. For example, in GaN, E_{ex}=24 meV leads to ~6 times Coulomb enhancement at RT.

Temperature and quantum energy E (in electronvolts, eV) dependence of intrinsic band-to-band absorption (BBA) coefficient in indirect-gap semiconductor can be approximated using temperature dependent excitonic bandgap $E_{GX}(T)$, excitonic and interband absorption strengths (A_{ex} and A_{IB}), exciton binding energy E_{ex} and phonon energy E_{ph} [33]:

$$\alpha_{BBA}(T) = \frac{n_B + 1/2 \pm 1/2}{E} \left[\begin{array}{l} \sum_i A_{ex,i} \left(E - \left(E_{GX}(T) \pm iE_{ph} \right) \right)^{1/2} + \\ A_{IB} \left(E - \left(E_{GX}(T) \pm E_{ph} + E_{ex} \right) \right)^2 \end{array} \right]. \quad (1.5)$$

Here "+" sign corresponds to phonon emission, the "–" sign for absorption, $n_B = 1/[\exp(E_{ph}/k_BT) - 1]$ is the Bose-Einstein phonon population factor. The first term in the brackets corresponds to excitonic, while the second one for free carrier interband generation.

Strong absorption coefficient temperature and quantum energy dependence in SiC and diamond well above bandgap can be approximated using temperature dependent energy gap $E_g(T)$ (see figure Fig. 1.5), absorption strength A, and phonon energy E_{ph} [37]:

$$\alpha(T) = A \left[\frac{\left(h\nu - E_g(T) - E_{ph} \right)^2}{1 - \exp\left(-E_{ph}/kT \right)} + \frac{\left(h\nu - E_g(T) + E_{ph} \right)^2}{\exp\left(E_{ph}/kT \right) - 1} \right]. \quad (1.6)$$

The bandgap temperature dependence can be described by Passler formula [38,39]:

$$E_{g\,P}(T) = E_{g0} - \left(\varepsilon\Theta_p / 2\right)\left(\sqrt[p]{1 + \left(2T/\Theta_p\right)^p} - 1\right). \tag{1.7}$$

Here $\varepsilon = 3\times10^{-4}$ eV/K, $\Theta_p = 450$ K and $p = 2.9$ for both 4H- and 6H-SiC. The formula is valid in 77-450 K range [39,40]. The same temperature dependence of bandgap can be used for all SiC polytypes (different bandgaps must be taken into account). In diamond, the bandgap temperature dependence is {5.476 – 0.64×exp(–1200K/T)} eV [35]. The temperature dependence of bandgap can be also precisely fitted by vibrational energy function $E_{g\,D}(T)$ [41]:

$$\begin{aligned} E_{g\,D}(T) &= E_{g0} - a_D f_D(\Theta_D / T), \\ f_D(\Theta_D / T) &= 18 k_B T^4 / \Theta_D^3 \int_0^{\Theta_D / T} \left(\exp(x) - 1\right)^{-1} x^3 dx. \end{aligned} \tag{1.8}$$

Here a_D accounts for atomic oscillator interaction (if a_D=1 there is no interaction), Θ_D = 1000 ± 50 K is the Debye temperature and $E_{g\,0}$ is the bandgap at zero temperature, the same as in Passler formula [39].

The spectral dependence of absorption coefficient can be obtained by [39]:

$$\alpha(T) = \frac{A_1}{\hbar\omega}\left[\hbar\omega - E_g - E_{ph}\right]^2 + \frac{A_2}{\hbar\omega}\left[\hbar\omega - E_g + E_{ph}\right]^2. \tag{1.9}$$

The given above formulas can be used for approximations of bandgap and absorption coefficient temperature dependences.

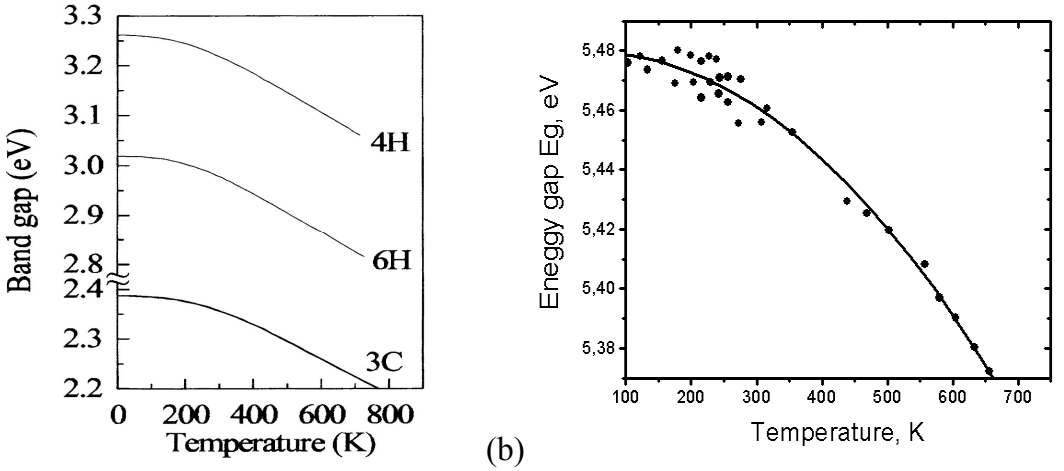

Fig. 1.5. The bandgap temperature dependences of SiC polytypes [40] and diamond [35].

The incident light can be *s*-polarized if its electric field is perpendicular to the plane containing the perpendicular to the sample surface and the incident beam. The light is *p*-polarized if its electric field is parallel to the plane. Reflectivity for air-semiconductor interface is described by Fresnel's equations for *s*- and *p*- polarizations. Corresponding equations are as follows [42]:

$$R_s(\Theta,n)=\left[\frac{\cos(\Theta)-\left(n^2-\sin^2(\Theta)\right)^{1/2}}{\cos(\Theta)+\left(n^2-\sin^2(\Theta)\right)^{1/2}}\right]^2, \quad (1.10a)$$

$$R_p(\Theta,n)=\left[\frac{-n^2\cos(\Theta)+\left(n^2-\sin^2(\Theta)\right)^{1/2}}{n^2\cos(\Theta)+\left(n^2-\sin^2(\Theta)\right)^{1/2}}\right]^2. \quad (1.10b)$$

Here, Θ and n are the incidence angle and the semiconductor refractive index for the incident beam wavelength, respectively.

Sample absorption coefficient near absorption edge can be determined from sample transmission spectra (in normal geometry, $\Theta = 0$), T, according to the relationships following from the Fresnel's equations:

$$P=(-(1-R)^2R^{-2}T^{-1}+\sqrt{(1-R)^4R^{-4}T^{-2}+4R^{-2}})/2,\ R=\frac{(n-1)^2}{(n+1)^2}, \quad (1.11)$$

here $P=\exp(-\alpha d)$ is directly related to sample thickness d and absorption coefficient α. The photon energy dependent refractive index n determines reflection coefficient R. Ordinary refractive index must be used for hexagonal SiC polytypes (4H-, 6H-), as the absorption edge measurements are being performed in the E⊥c geometry (the c axis is almost perpendicular to the surface of the wafers). In a wide spectral range n can be described as: $n^2=1+5.49/\left(1-(E(eV)/E_\Gamma)^2\right)$ according to [43]. Here E_Γ is the energy of the effective direct gap (its values are 7.3 eV, 3.4e V and 7.3-7.4 eV for SiC, GaN and diamond, respectively [9]). Refractive index of 3C-SiC has very similar value and spectral dependence [9] and weakly depends on temperature: $dn/dT = 3.6\times10^{-5}$ K^{-1} at RT [9,41]. In GaN and diamond similar refractive index spectral dependences can be found in [44,45].

1.3. Carrier mobility

An important material parameter is carrier (electron or hole) **mobility**, which in a nondegenerate semiconductor can be expressed as [30]:

$$\mu = \frac{e}{m^*}\langle \tau_m \rangle,\ \langle \tau_m \rangle = \int_0^\infty f_F \left(\sum\nolimits_i \tau_i^{-1}(x,T) \right)^{-1} x^{3/2} dx \Big/ \int_0^\infty f_F x^{3/2} dx\,. \tag{1.12}$$

Here e is the elementary charge, m^* is the carrier effective mass, $x=E/k_BT$, k_B is the Boltzmann constant, τ_m is the carrier momentum relaxation time, which is different for different carrier scattering mechanisms, with carrier energy (E) and lattice temperature (T) dependent relaxation times $\tau_i(x,T)$. $f_F = [\exp(x-x_F) -1]^{-1}$ is the Fermi distribution function ($x_F=E_F/k_BT$). There are different scattering mechanisms: scattering by ionized impurities (1), neutral impurities (2), acoustic phonons (3), polar optical phonons (4), and nonpolar optical phonons (5).

● **Scattering by ionized impurities**

The scattering by ionized impurities (ii) is described in [46] for the case of electrons in the conduction band. The relaxation time is simply adjusted to the case of the valence band by taking into account the p-type symmetry of wave functions in place of the s-type wave functions, as discussed elsewhere [47]. As a consequence, with respect to the conduction band, the relaxation time of the valence band is multiplied by a factor of 1.5. The inverse relaxation time is then:

$$\frac{1}{\tau_{ii}} = \frac{2}{3}\frac{N_I e^4 \left[\ln(\varsigma+1) - \varsigma/(\varsigma+1)\right]}{16\sqrt{2}\pi(\varepsilon_0\varepsilon_s)^2 m_i^{*1/2} E^{3/2}},\ \varsigma = (2k\lambda_s)^2, \tag{1.13}$$

where i runs over light holes and heavy holes, $N_I=p_0+2N_D$ is the density of charged ions in the p-type material, ε_s is the relative static dielectric constant, ε_0 is the vacuum permittivity, λ_s is the screening length (the reciprocal screening length is being designated by q_0) and k is the electron wave vector. λ_s can be calculated for arbitrary degeneracy but, for nondegenerate case, it is:

$$\frac{1}{\lambda_s^2} = \frac{e^2}{\varepsilon_0\varepsilon_s k_B T}\left[p_0 + \frac{(N_A - N_D - p_0)(p_0 + N_D)}{N_A} \right], \tag{1.14}$$

where N_A and N_D are the total densities of acceptors and donors, respectively. $\hbar = h/2\pi$ is the reduced Planck constant.

● Scattering by neutral impurities

The scattering by neutral impurities (ni) is very important in wide bandgap semiconductors. This is because the donor binding energy is i) sufficiently large so that, at low temperature, the majority of impurities are neutral, and ii) not too large, so that the Bohr radius of the bound electron allows scattering of the electrons in the conduction band. The relaxation time can be calculated with the simple approach of Erginsoy (in analogy with atomic physics) [48], or more complete and reliable approach of Meyer and Bartoli [49]. The corresponding relaxation times are then:

$$\frac{1}{\tau_{ni}} = \frac{20 N_n 4\pi\varepsilon_0\varepsilon_s\hbar^3}{m_i^{*2}e^2}, \quad \frac{1}{\tau_{ni}} = \frac{A(\omega)N_n 4\pi\varepsilon_0\varepsilon_s\hbar^3}{m_i^{*2}e^2},$$

$$A(\omega) = \frac{35.2\left(1+\exp(-50\omega)\right)\left(1+80.6\omega+23.7\omega^2\right)}{\omega^{1/2}\left(1+41.3\omega+133\omega^2\right)} \times\left[\frac{\ln(1+\omega)}{\omega} - \frac{1+0.5\omega-0.1667\omega^2}{1+\omega^3}\right], \tag{1.15}$$

where i runs over light holes and heavy holes, $N_n = N_A - N_D - p_0$ is the number of neutral impurities, $\omega = E/E_B$, where E_B is the impurity activation energy.

● Scattering by acoustic phonons

The relaxation time due to the scattering by acoustic phonons (ac) is reviewed, for instance, in the work [30]. Because the acoustic phonons have a small, but finite, wave vector and because the valence band is (almost) degenerate at k=0 both intra- and interband processes can occur. The total density of states, into which a free hole can be scattered, is then proportional to $(m_h^{*3/2} + m_l^{*3/2})$. Taking this into account, the scattering rate can be expressed as [50]:

$$\frac{1}{\tau_{ac}} = \frac{\sqrt{2}\left[m_h^{*3/2} + m_l^{*3/2}\right]C_a^2 k_B T}{\pi\hbar^4\rho v_{\|}^2} E^{1/2}, \tag{1.16}$$

where ρ is the crystal mass density, $v_{\|}$ is the velocity of longitudinal acoustic phonons, and C_a is the acoustic deformation potential.

● **Scattering by polar optical phonons**

For the polar optical phonon (pop) scattering the relaxation time calculated by Callen (cf. Ridley) is being used [30]. The standard expression of relaxation time for the conduction band is multiplied by 2 for the same reason as previously mentioned for the ii scattering. The inverse relaxation time for holes is then:

$$\frac{1}{\tau_{pop}} = \frac{1}{2}\frac{e^2\omega_{op}}{4\pi\varepsilon_0\varepsilon_p\hbar\left(2E/m_d^*\right)^{1/2}}\left[n_B\left(\omega_{op}\right)\left(1+\frac{\hbar\omega_{op}}{E}\right)^{1/2} + \left\{n_B\left(\omega_{op}\right)+1\right\}\left(1-\frac{\hbar\omega_{op}}{E}\right)^{1/2}\right.$$
$$\left. + \frac{\hbar\omega_{op}}{E}\left[-n_B\left(\omega_{op}\right)\sinh^{-1}\left(\frac{E}{\hbar\omega_{op}}\right)^{1/2} + \left\{n_B\left(\omega_{op}\right)+1\right\}\sinh^{-1}\left(\frac{E}{\hbar\omega_{op}}-1\right)^{1/2}\right]\right], \tag{1.17}$$

where $1/\varepsilon_p = 1/\varepsilon_\infty - 1/\varepsilon_s$, $\hbar\omega_{op}$ is the polar optical-phonon energy, and $n_B(\omega_{op}) = 1/[\exp(\hbar\omega_{op}/k_BT) - 1]$ is the phonon occupation factor. The phonon emission terms $n_B(\omega_{op}) + 1$ contribute only for $E \geq \hbar\omega_{op}$, otherwise they vanish. The interband scattering is neglected for this mode [47].

● **Scattering by nonpolar optical phonons**

The scattering due to nonpolar optical phonons (npo) is either intra- or interband [51]. In calculations, combined relaxation time of intra- and interband scattering should be used [52]:

$$\frac{1}{\tau_{npo}} = \frac{1}{\tau_{npo,ii}} + \frac{1}{\tau_{npo,ij}} = \frac{\left(D_{ii}+D_{ij}\right)^2\left[m_h+m_l\right]^{3/2}}{\sqrt{2}\pi\rho\hbar^3\omega_0}$$
$$\times\left[n_B\left(\omega_0\right)\left(E+\hbar\omega_0\right)^{1/2} + \left[n_B\left(\omega_0\right)+1\right]\left(E-\hbar\omega_0\right)^{1/2}\right]. \tag{1.18}$$

where $n_B(\omega_0) = 1/[\exp(\hbar\omega_0/(k_BT)) - 1]$ is the phonon occupation factor and $\tau_{npo,ii}$ and $\tau_{npo,ij}$ are the intra- (ii) and interband (ij) relaxation times due to nonpolar optical phonons. The phonon emission terms $n_B(\omega_0) + 1$ contribute only for $E \geq \hbar\omega_0$, otherwise they vanish. In this approach, the summation over all possible initial and final states is represented by an effective coupling constant ($D_{ii}+D_{ij}$) which takes into account the intraband scattering (D_{ii}) and the interband scattering (D_{ji}). It should be emphasized that these coupling constants have a

rather “effective” meaning since they cannot be distinguished by comparison with experimental results.

● **Screening of carrier-phonon interactions**

At high carrier densities pop and npo are subject to screening. This effect will be stronger at low temperatures, as scattering includes smaller and smaller phonon wave vectors, q. Therefore for non-polar (acoustic and nonpolar optical) and polar phonon scattering processes coupling parameters become, respectively [30]:

$$C^2_{non-polar}(q) \sim \frac{q^2}{\left[1+q_0^2/q^2\right]^2},\ C^2_{polar}(q) \sim \frac{1}{\left[1+q_0^2/q^2\right]^2}. \tag{1.19}$$

For arbitrary degeneracy, the inverse screening length q_0 is calculated according to:

$$q_0^2 = -\frac{e^2}{\varepsilon_0\varepsilon_s}\sum_i N_i \frac{df_F(E_i)}{dE_i} = -\frac{e^2}{\varepsilon_0\varepsilon_s}\int_0^\infty N(E)\frac{df_F(E)}{dE}dE, \tag{1.20}$$

where summation over conduction and valence band states is performed, where $N(E)$ is the density of states per energy interval. In degenerate carrier plasma $q_0^2 = e^2/\varepsilon_0\varepsilon_s N(E_F)$ can be obtained. That corresponds to electron-phonon coupling strength reduction with nonequilibrium carrier density as $\Delta N^{-4/3}$.

1.4. Carrier diffusion coefficient

An important parameter in carrier transport analysis is a diffusion coefficient, D. It describes a number of carriers, going through a unit of area per unit of time [53]. Electron (ΔN_e) and hole (ΔN_h) diffusion takes place when the generated electron-hole plasma is spatially inhomogeneous. Bipolar carrier diffusion is determined by internal electric field between electrons and holes, leading to ambipolar diffusion coefficient [53]:

$$D_a = \frac{n_0 + \Delta N_e + p_0 + \Delta N_h}{(n_0 + \Delta N_e)/D_h + (p_0 + \Delta N_h)/D_e}, \tag{1.21}$$

Here D_e ir D_h are electron and hole diffusion coefficients, respectively. The diffusion coefficients D are related to carrier mobilities μ via Einstein's relationship [53]:

$$D_i = \mu_i k_B T / |e|, \tag{1.22}$$

where μ_i are electron or hole mobilities. Typically, hole mobility is much lower than electron one. In that case (nonequilibrium carrier density also satisfies a relation $\Delta N = \Delta N_e = \Delta N_h >> n_0,\ p_0$) ambipolar diffusion coefficient is related to hole diffusion coefficient as:

$$D = \frac{2D_h D_e}{D_h + D_e} \approx 2D_h \tag{1.23}$$

In case of *n*- or *p*-type semiconductors, at low injections monopolar minority carrier (i.e. hole or electron) diffusion coefficient can be obtained.

Temperature and carrier density dependent hole diffusion coefficient can be described by basic relations including scattering rate calculation [54]:

$$\begin{aligned} &D_h(\Delta N) = D_{h0}\left(\frac{F_{1/2}}{\partial F_{1/2}/\partial x_F} + \frac{\Delta N}{kT}\frac{\partial \Delta E_v}{\partial \Delta N}\right),\ F_{1/2} = \int_0^\infty f_F x^{1/2} dx, \\ &D_{h0} = \frac{kT}{m_h^*}\int_0^\infty f_F\left(\sum\nolimits_i \tau_i^{-1}(x,T,\Delta N)\right)^{-1} x^{3/2} dx \Big/ \int_0^\infty f_F x^{3/2} dx. \end{aligned} \tag{1.24}$$

Here $x=E/k_BT$, $x_F=E_F(\Delta N)/k_BT$, and $E_F(\Delta N)$ is the carrier density dependent Fermi level, which can obtained by Nilsson approximation [55] with few percent precision according to the relation:

$$x_F = \frac{-\ln(w)}{w-1} + \left(3/4\sqrt{\pi w}\right)^{2/3} + \frac{3/2\sqrt{\pi w}}{\left(3+3/4\sqrt{\pi w}\right)^2},\ w = \frac{\Delta N}{N_{vd}}, \tag{1.25}$$

where density of states $N_{vd} = 4/\sqrt{\pi}\left(2\pi m_{vd}^* k_B T/h^2\right)^{3/2}$ is the main parameter and τ_i are the appropriate carrier relaxation times as described above. The $\Delta E_v(\Delta N)$ dependence corresponds to valence band renormalization due to free holes [56].

In bipolar plasma electrons and holes are present simultaneously. Therefore, their interactions such as mutual scattering [30,57] (electron-electron

scattering in heavily doped, e.g. *n*-type, sample can also take place) and binding to excitons (which can also lead to scattering processes [58,59]) must be taken into account. In the case of excitons, the exciton scattering time, τ_{EST}, is expressed as [59]:

$$\frac{1}{\tau_{EST}} = \frac{1}{\tau_{ex-ph}} + \frac{1}{\tau_{ex-carr}} + \frac{1}{\tau_{ex-ex}}. \tag{1.26}$$

Here different scattering mechanisms are taken into account: exiton-phonon scattering ($\tau_{ex\text{-}ph}$), exciton-hole/electron scattering ($\tau_{ex\text{-}carr}$), and exciton-exciton scattering ($\tau_{ex\text{-}ex}$).

1.5. Carrier recombination processes

Free carrier lifetime is one of the main physical quantities, which sensitively reveals the fundamental and defect related material properties at various temperatures and photoexcitation levels. This section describes the basic recombination mechanisms and their relative importance at different excitation intensities.

Instantaneous carrier recombination time (the annihilation time of one electron-hole pair per unit of time) can be obtained taking time derivative of carrier density ΔN as [60]:

$$\tau_R(\Delta N) = -\Delta N(t)/(d\Delta N(t)/dt). \tag{1.27}$$

The corresponding carrier recombination rate, with inclusion of classical recombination mechanisms, can be written as [61]:

$$\tau_R^{-1}(\Delta N) = \tau_{SRH}^{-1} + B\Delta N(x,z,t) + C\Delta N(x,z,t)^2. \tag{1.28}$$

Here τ_{SRH} is the bulk trap related Shockley-Read-Hall (SRH) lifetime [62,63], $B = B_{rad} + B_{nonr}$ is the quadratic recombination coefficient (consisting of radiative, B_{rad}, and usually larger nonradiative, B_{nonr}, (it can be trap-assisted [64] or Coulombically enhanced Auger process [65])), C is the Auger recombination coefficient [61]. In Fig. 1.6 carrier transition for each recombination process is depicted. The first term in Eq. (1.28) corresponds to linear recombination, while the other two are nonlinear ones.

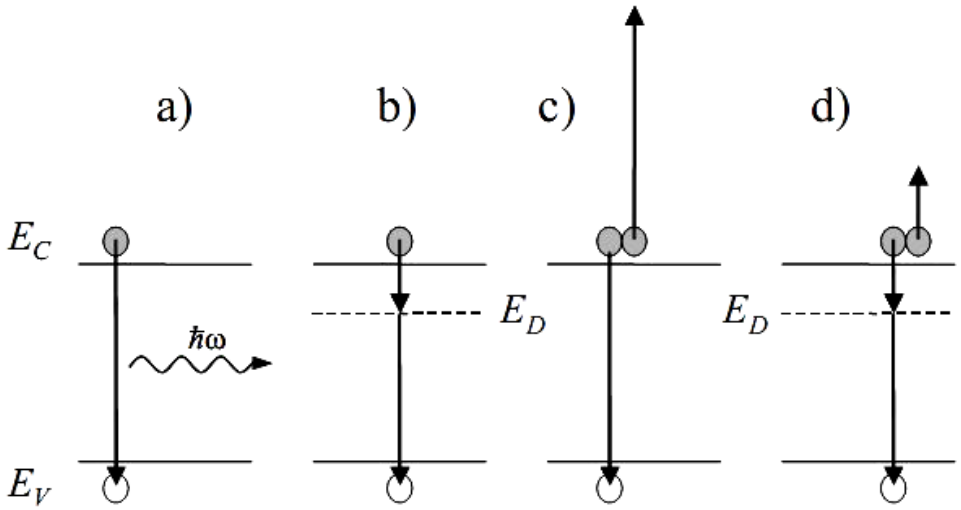

Fig. 1.6. Schematic representation of the classical recombination mechanisms: a) radiative (B_{rad}), b) SRH (τ_{SRH}), c) Auger (C) and d) trap assisted Auger (B_{nonr}) according [61]. E_C, E_V, and E_D specify conduction, valence band edges and defect levels, respectively.

The Shockley-Read-Hall (SRH) model describes electron-hole pair lifetime, when they recombine through a defect level E_D [62,63]. Defects can be either extrinsic (impurity atoms) or intrinsic (point defects, dislocations). The defect firstly captures one type carrier, then the another one. In this way the electron-hole pair annihilates and the defect restores to its initial state. During the capture processes the energy is transferred to phonons. Below, the model is provided for the case when defect concentration is much lower than the nonequilibrium carrier density, i.e. $\Delta N_e \sim \Delta N_h \sim \Delta N$. Then the lifetime formula is [62]:

$$\tau_{SRH} = \left(\tau_h\left(n_0 + n_{1d} + \Delta N\right) + \tau_e\left(p_0 + p_{1d} + \Delta N\right)\right)/\left(n_0 + p_0 + \Delta N\right). \qquad (1.29)$$

Here, $\tau_e = 1/\left(N_T \sigma_p v_{th\,e}\right)$, $\tau_h = 1/\left(N_T \sigma_n v_{th\,h}\right)$, $v_{th\,e} = \sqrt{8/\pi kT/m_e^*}$, and $v_{th\,h} = \sqrt{8/\pi kT/m_h^*}$ are electron and hole lifetimes and thermal velocities, respectively. For electrons (analogically for holes) the capture cross section is described as: $\sigma_n = \int_{E_c}^{\infty} \sigma_n(E) v_{th\,e}(E) g(E) f_F(E) dE / \left(v_{th\,e} N_c\right)$, where $\sigma_n(E)$ is the probability of transition from band level E to the defect level E_D per second, $g(E)$ – is the density of states in conduction band. n_0 and p_0 are equilibrium

electron and hole concentrations, respectively. $n_{1d} = N_{cd} \exp\left(\left(E_T - E_c\right)/kT\right)$ is the electron concentration in conduction band when Fermi level is equal to E_D. $p_{1d} = N_{vd} \exp\left(\left(E_v - E_T\right)/kT\right)$ is the hole concentration in the valence band when Fermi level is equal to E_D. In *n*-type semiconductor, $\tau_{SRH} = \tau_h$, while in *p*-type – $\tau_{SRH} = \tau_e$. This model predicts, that recombination on traps, which are closer to the conduction band centre, is more effective as electron and hole capture rates are similar in that case. In SiC and GaN such defects are known to dominate. In SiC, the defects are carbon vacancies, which provide a discrete level at ~0.7 eV below the conduction band [66], while in diamond the dominating recombination center is nitrogen, being 1.7 eV below E_C [67]. In GaN structural defects, such as dislocations, are considered to be dominant [68].

Under high injection conditions for deep traps, the Eq. (1.29) can be simplified to $\tau_{SRH} = \tau_h + \tau_e$, while for the minority carriers simple form as $\tau_{SRH} = \left(\tau_h n_0 + \tau_e p_0\right)/\left(n_0 + p_0\right)$ can be obtained.

The radiative electron-hole pair or exciton recombination occurs with photon emission. In direct bandgap semiconductors the process can be phononless, while in indirect bandgap ones it can be only phonon-assisted. The process is described by radiative coefficient, B_{rad}, with ~10^{-14} cm^3/s values in indirect [69] and up to ~10^{-10} cm^3/s [70] in direct bandgap semiconductors, respectively.

In direct-gap semiconductors, the radiative band to band free carrier radiative recombination coefficient is [71]:

$$B_{rad\,bb}(T) = \frac{\pi n_g^2 \hbar^3 \alpha_0' \sqrt{\pi}}{c^2 \left(m_{cd} m_{pd}\right)^{3/2}} E_g^{3/2} kT^{-3/2},\ \alpha(h\nu) = \alpha_0' \frac{\left(h\nu - E_g\right)^{1/2}}{E_g^{1/2}}. \qquad (1.30)$$

Here n_g is the refractive index value for $h\nu = E_g$ photon energy. For example α_0'(GaAs) = 2×10^4 cm^{-1}, α_0'(GaN) =~ 1-2×10^5 cm^{-1} (300 K), and, thus, the B_{rad} value for GaAs is 1.4×10^{-10} cm^3/s, and for GaN: 8×10^{-11} cm^3/s.

For indirect-gap semiconductors [69]:

$$B_{radbb}(T)=\frac{4\pi m_g^2\hbar^3\alpha_0^{/}}{c^2\left(m_{cd}m_{pd}\right)^{3/2}}A_{ph},\ \alpha(h\nu)=\alpha_0^{/}\frac{\left(h\nu-E_g\right)^2}{E_g^2}. \quad (1.31)$$

Here $A_{ph}=\left[\exp\left(E_{ph}/kT\right)+1\right]/\left[\exp\left(E_{ph}/kT\right)-1\right]$. The Eqs. (1.30,1.31) can be simplified as:

$$B_{radbb}=2.3\times10^{-18}\alpha_0 n_g^2(E_g/1\text{eV})^{3/2}(300\text{K}/T)^{3/2}(m_{cd}m_{vd}/m_0^2)^{-3/2}. \quad (1.32a)$$

$$B_{radbb}=2.2\times10^{-20}\alpha_0 n_g^2(m_{cd}m_{vd}/m_0^2)^{-3/2}A_{ph}. \quad (1.32b)$$

These equations elucidate, that radiative recombination coefficient in direct semiconductor depends on temperature as $T^{-3/2}$, while in indirect ones it is almost temperature independent. Experimentally few phonon replicas can be observed, then $A_{ph}=\left[n_B/\left(1-n_Bq\right)+\left(n_B+1\right)/\left(1-\left(n_B+1\right)q\right)\right]$. The phonon replicas obey the sum of geometrical progressions, with n_Bq and $(n_B+1)q < 1$ factors (here n_B and n_B+1 are the factors for phonon absorption and emission, respectively, and the $(n_B+1)q$ factor indicates how much the first phonon replica is weaker than the dominant one phonon band).

PL intensity (I_{PL}) in carrier plasma is proportional to $\Delta N_h(\Delta N_e + n_0) \approx \Delta N^2$. Nevertheless, exciton luminescence can not be neglected at lower excitations. The exciton density is $\Delta N_{ex} = \Delta N_h(\Delta N_e + n_0)/n^*$ and determines the exciton luminescence as $I_{PL\,EX} \propto \Delta N_{ex}$. Here $n^* = N_{DOS\,ex}\exp(-E_{ex}(\Delta N)/k_BT)$, $N_{DOS\,ex} = 2(2\pi m_{eh}k_BT/h^2)^{3/2}$ is the exciton density of states [32], $E_{ex}(\Delta N) = E_{ex\,0} - a_{BR}/2[\Delta N^{1/4} + (n_0+\Delta N)^{1/4}]$ and $E_{ex\,0} = 13.6\ \text{eV}\times m_{red}/m_0/\varepsilon_s^2$ [30] are the nonequilibrium carrier density dependent and unscreened ground state exciton binding energies, a_{BR} is the bandgap renormalisation coefficient, m_{eh} is the reduced exciton mass. E_{ex} reduces due to screeening [32] (at the same rate as band gap renormalization in 3D case). Energies of higher bound exciton states are $E_{ex\,i} = -E_{ex}/i^2$, where i is the exciton level number.

The Auger coefficient, C, arises due to a recombination process, when electron and hole recombines, providing their energy to other carrier (electron or hole, which are called Auger electrons (holes)). The Auger process can be either direct (phononless) or indirect, i.e. phonon assisted [72]. The latter one is more probable as phonons compensate the Auger electron (hole) momentum,

which absolute value has to be equal to the recombined electron-hole pair momentum. Direct process can occur, when for the Auger electron higher conduction bands are available, as carrier transitions in the same conduction and valence bands have very small probability in wide-bandgap semiconductors.

Trap assisted Auger recombination (TAAR) has similar recombination rate carrier density dependence as in the case of radiative process, as nonequilibrium carrier density is replaced by a constant concentration of defects [64]:

$$B_{TAAR} = C_{TAAR} \times N_{TAAR} \,. \tag{1.33}$$

Here C_{TAAR} is the TAAR recombination coefficient, while B_{TAAR} is the effective quadratic nonradiative recombination coefficient, N_{TAAR} is the concentration of the traps participating in this process. Also the nonradiative quadratic recombination may arise from Coulombic (excitonic) enhancement of Auger recombination [65], which can be described by B_{enh} coefficient.

By solving a balance equation (1.34) [73], and taking into account the temperature and excitation dependent ambipolar diffusion coefficient $D_a(T,\Delta N)$ and various recombination mechanisms, excess carrier profiles $\Delta N(z,t)$ in the epitaxial layer can be calculated.

$$\begin{aligned} &\frac{\partial \Delta N(z,t)}{\partial t} = \frac{\partial}{\partial z}\left[D_a\left(T,\Delta N\right)\frac{\partial \Delta N(z,t)}{\partial z}\right] \\ &-\frac{\Delta N(z,t)}{\tau_{SRH}\left(T\right)} - B\Delta N(z,t)^2 - C\left(T,\Delta N\right)\Delta N(z,t)^3 + G(z,t) \,. \end{aligned} \tag{1.34}$$

Here carrier generation by the laser pulse is given by the term $G(z,t) = [\alpha I_0 f(t)/h\nu] \times \exp(-\alpha z)$, $\int_{-\infty}^{+\infty} f\left(t\right)dt = 1$. $f(t)$ is the Gaussian pulse temporal dependence, being determined by laser pulse full width at half maximum (FWHM), τ_L:

$$f\left(t\right) = \frac{2}{\tau_L}\sqrt{\frac{\ln\left(2\right)}{\pi}}\exp\left(-4\ln\left(2\right)\frac{t^2}{\tau_L^2}\right). \tag{1.35}$$

The boundary conditons at the epilayer front surface and at the epilayer-substrate interface are as follows [60]: $\partial\Delta N(0,t)/\partial z = S\Delta N(0,t)/D_a(T,\Delta N)$ and $\partial\Delta N(d,t)/\partial z = -S_{inter}\Delta N(d,t)/D_a(T,\Delta N)$, where S is the surface recombination velocity and S_{inter} is the interface recombination velocity.

1.6. Carrier dynamics in SiC, GaN and diamond

Carrier dynamics studies in semiconductors provide information about carrier mobility, diffusion coefficient, various electronic transitions and recombination rate of the nonequilibrium carriers [60]. These studies are important and give information for fundamental materials science as well as for practical use of materials in semiconductor industry, since the determined quantities correlate with material quality, purity, doping level, etc.

Carrier mobility (for electrons and holes) is commonly obtained by Hall measurements [74] in conductive materials (such as SiC, GaN, *p*-type diamonds) and time of flight technique (TOF) [75] in semi insulating ones (such as *n*-type diamonds).

In SiC and GaN Hall measurements were extensively performed on *n*- and *p*-type material [76-82]. Commonly, donors have smaller activation energies than acceptors, therefore, electron mobilities are measured in lightly doped samples. On the other hand, hole mobility, measured in heavily doped *p*-type samples, exhibits impact of impurities to carrier scattering, which complicates discrimination of phonon scattering processes.

In Fig. 1.7 electron and hole mobilities of 3C-SiC are provided, while in 4H-SiC electron and hole mobilities are shown for comparison in Fig. 1.8. It is clearly observed that mobilities in these polytypes have similar temperature dependences and values, but in 3C-SiC, due to wide abundance of structural defects leading to formation of potential barriers, the mobility is strongly decreased. The mobilities in GaN are shown in Fig. 1.9. Similarly as in SiC, hole mobility is also by order of magnitude smaller than electron mobility due to large hole mass. The simulations of the mobility temperature dependences indicate that acoustic phonon scattering, intervalley optical and polar optical

phonon scattering are dominant in intrinsic SiC and GaN.

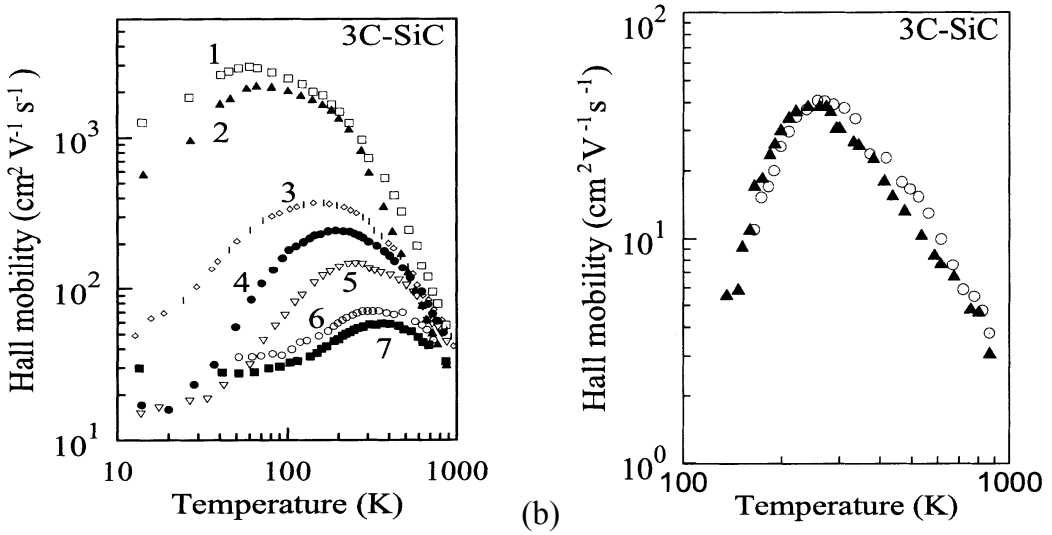

(a) (b)

Fig. 1.7. Electron and hole mobilities in *n*-type (a) and *p*-type (b) 3C-SiC [76-78]. In *n*-type, different doping levels and different levels of Al compensation are shown (curves 1;2 correspond to n_0=1;5×10^{16} cm^{-3}, curves 3-7 correspond to N_D = (1.8-10)×10^{18} cm^{-3}, N_A =(1.1-3)×10^{18} cm^{-3}). In *p*-type: circles – N_D ~ 3.5×10^{18} cm^{-3}, N_A ~ 5.5×10^{18} cm^{-3}, triangles – N_D ~ 5.0×10^{18} cm^{-3}, N_A ~ 2.0×10^{19} cm^{-3}.

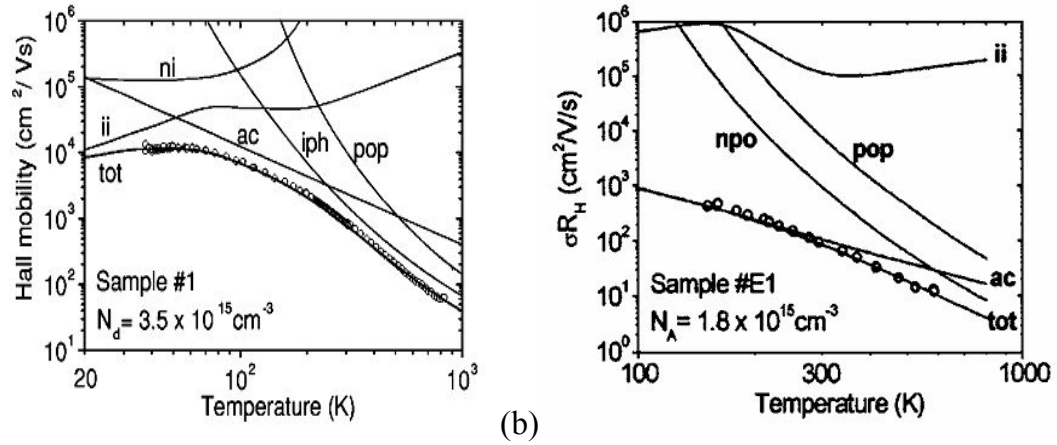

(a) (b)

Fig. 1.8. Electron and hole mobilities in nitrogen (a) and aluminum (b) doped 4H-SiC with theoretical approximations [79,80].

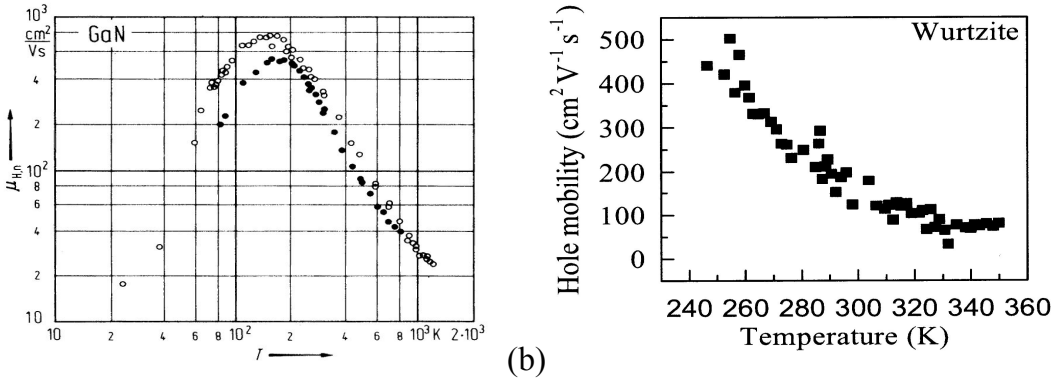

(a) (b)

Fig. 1.9. Electron mobility in silicon doped *n*-type (a) and hole mobility in magnesium doped *p*-type 2H-GaN (b) [81,82].

In diamonds, Hall measurements are quite reliable only in heavily doped *p*-type samples [25,51] (boron *p*-type dopant has 370 meV activation energy [83]), as in *n*-type diamonds donors are very deep (phosphorus is the shallowest dopant with ~600 meV activation energy [84,85]). Also weak acceptor impurity activation prohibits mobility measurements at low temperatures. More reliable technique to investigate mobility at low doping in diamonds is TOF, where optically generated carriers are separated and drift in electric field [25,75,86-88]. Hole and electron TOF mobility measurements are provided in Fig. 1.10.

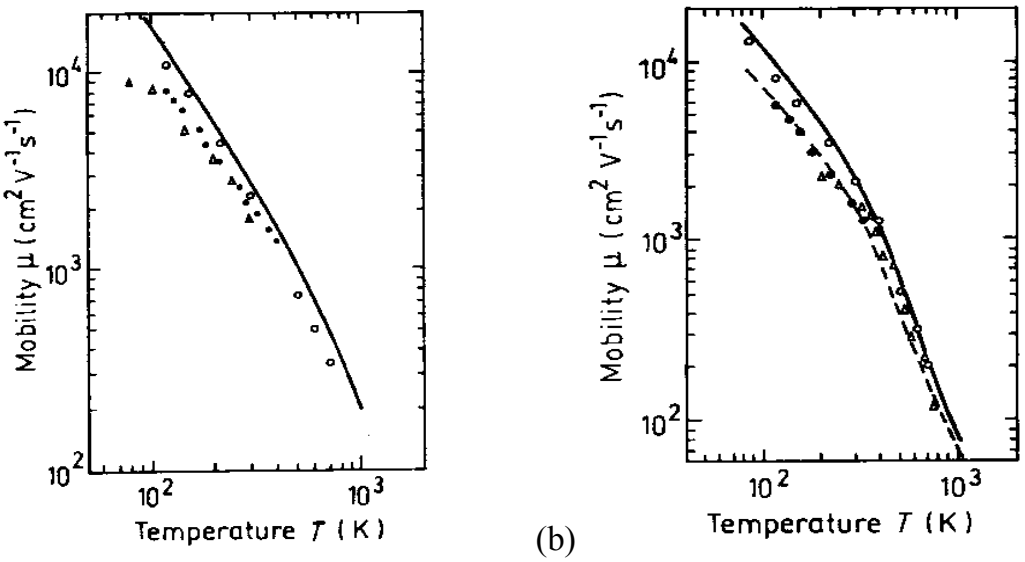

Fig. 1.10. Electron (a) and hole (b) mobilities in natural diamond [25,86]. Curves show the results of calculations of drift mobility (solid line) and Hall mobility (dashed line). Open circles are experimental data for drift mobility. Triangles and closed circles are experimental data for Hall mobility.

In diamonds, only acoustic phonon, and intra/inter-valley optical phonon scattering are possible as diamond is a nonpolar semiconductor (while SiC and GaN are polar ones).

Carrier diffusion coefficient can be studied in a contactless way by LITG technique [89], Fourier transient grating (FTG) [90], electron-beam-induced current (EBIC) and spatially resolved photoluminescence [91]. Carrier diffusion coefficient studies in SiC were performed by FTG and LITG techniques in 10-550 K temperature interval [90,92]. In GaN LITG studies provided diffusion coefficient in 10-300 K range at variable nonequilibrium carrier density [93,94] (see Fig. 1.11).

In diamonds, diffusion coefficient by LITG was studied only at high excitation conditions at 213 nm wavelength [95]. The diffusion coefficient, according Einstein relationship, led to 5 fold smaller ambipolar mobility in comparison to that calculated from TOF mobilities. This effect was ascribed to band-gap renormalization and electron-hole scattering and electron-hole droplet formation at low temperatures. Recently the diffusion coefficient was measured by photoluminescence technique and revealed increased values (~40 cm^2/s) at low excitations [96].

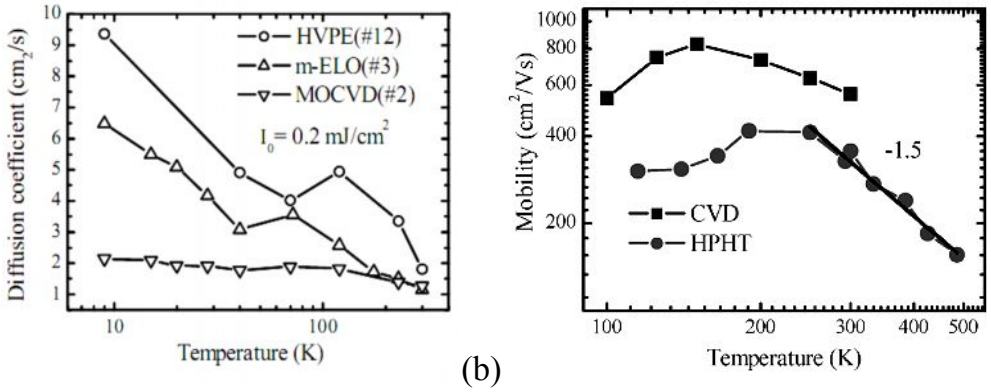

(a) (b)

Fig. 1.11. Carrier diffusion coefficient in GaN (a) and ambipolar carrier mobility, calculated from ambipolar diffusion coefficient in diamonds at $\Delta N \sim 10^{18}$ cm^{-3} (b) [93,95].

Carrier recombination can be either linear (SRH) or nonlinear (quadratic and Auger). Determination of carrier lifetime can be obtained through excitation of a high excess carrier density using a picosecond laser pulse and subsequent monitoring of the temporal and spatial carrier dynamics. The nonlinear time-resolved optical techniques, such as light-induced transient grating (LITG) [89], time resolved free carrier absorption (TRFCA) [61], microwave photoconductivity decay (MPCD) [97], time of flight [75] and time-resolved photoluminescence (TRPL) [98], have been shown to be the valuable tools for determination of carrier recombination rates.

Linear nonradiative SRH recombination in SiC was extensively studied by time resolved free carrier absorption decay (TRFCA) [99,100], microwave photoconductivity decay [101] and time resolved photoluminescence (TRPL) [100,102]. In 4H-SiC lifetime increase with temperature was observed [100]

(Fig. 1.12a), which was attributed to change of charge states of the $Z_{1/2}$ lifetime limiting defects, which are carbon vacancies [66,103]. Their density reduction by post-growth annealing drastically increased lifetime up to 33 μs [103].

In GaN, lifetime measurements were performed basically only by TRPL and LITG under band-to-band [36,104,105] and two photon absorption (TPA) excitation [106,107]. At TPA conditions lifetime exhibited strong increase with temperature (from few ns to ~20 ns [106]). This increase was attributed to exciton radiative recombination suppression with temperature.

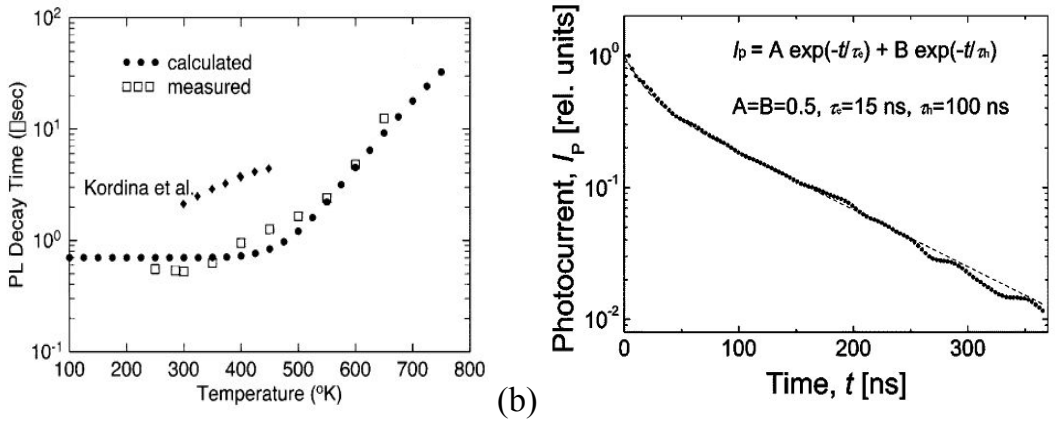

(a) (b)

Fig. 1.12. Temperature dependence of carrier lifetime in 4H-SiC [100,102] (a) and photoconductivity decay in undoped diamond [109] (b).

In diamonds, lifetime was studied by LITG [95,108] and TOF [87,109,110]. LITG provided rather short lifetimes in 0.1-5 ns range (higher lifetimes could not be determined due to carrier diffusion, surface recombination and limited delay range). On the other hand, TOF measurements provided lifetimes of ~100 ns [109,110] (see Fig. 1.12b) and even ~2 μs [87]. In heavily nitrogen doped samples, lifetime strongly reduced (to ~10 ps) as nitrogen is ~1.7 eV deep lifetime limiting defect in diamond [67,111]. Electron capture to the defect is much faster than the hole capture [67,109] (in Fig. 1.12b electron and hole photoconductivity components are distinguished).

Nonlinear recombination studies in literature are not so abundant due to complicated evaluation of nonequilibrium carrier density and a need of precise control of excitation energy density. In 4H-SiC Auger and bimolecular coefficients were reported in [112]. Their values at RT were 7×10^{-31} cm^6/s and

1.2×10^{-12} cm^3/s, respectively. Strong reduction of the Auger coefficient with temperature (Fig. 1.13a) in that work was attributed to a direct phononless Auger recombination process, having a temperature dependent threshold (see inset in 1.13a for details). Bimolecular recombination coefficient was considered to be related both to nonradiative TAAR and radiative processes.

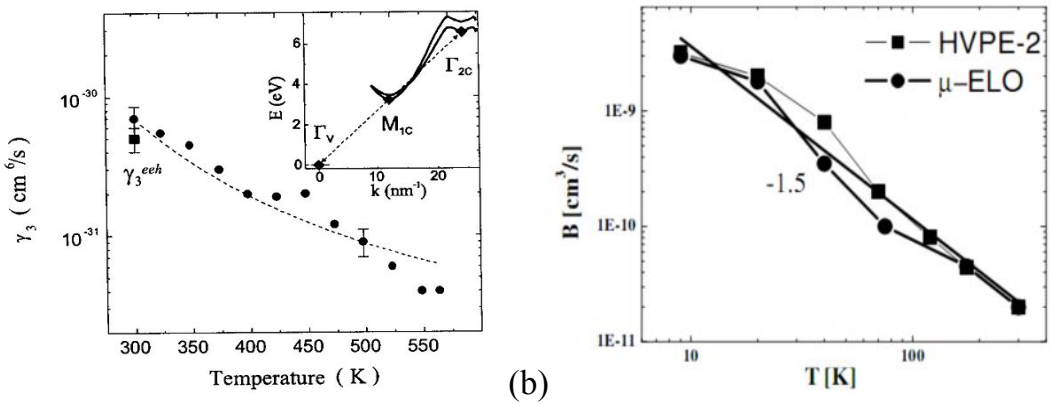

Fig. 1.13. Nonlinear Auger recombination coefficient in 4H-SiC [112] and bimolecular recombination coefficient in 2H-GaN [93].

In GaN, strong recombination nonlinearity may arise due to bimolecular and Auger recombination. B_{rad} was calculated theoretically to be 5×10^{-11} cm^3/s [70]. Similar values of B_{rad} ~2×10^{-11} cm^3/s were obtained experimentally by LITG [93] and PL [36]. Therein, B_{rad} exhibited $T^{-3/2}$ temperature dependence as predicted theoretically for direct-gap semiconductors (see Fig. 1.13b). On the other hand, saturation of radiative recombination rate in GaN was not investigated, while in InGaN alloys it was observed by PL technique at $\Delta N > 10^{18}$ cm^{-3} with rate: ~2×10^7 s^{-1} [113] and explained by momentum space filling [114] and screening of electron-hole interaction [113]. Auger recombination coefficient in GaN was predicted theoretically to be very small [115], $C < 10^{-32}$ cm^6/s. Study of nonlinear recombination in diamonds have not been carried out up to now.

2. Samples and experimental optical techniques

In this chapter the sample information and applied experimental techniques are described. In the first section, a list of samples is given in Table 2.1, where their parameters are indicated. In the following sections light-induced transient grating, differential transmittivity and reflectivity techniques, spectrally- and time- resolved photo-luminescence setups are described. The newly developed diffraction-based absorption coefficient measurement technique and time resolved FCA lifetime microscopy are presented.

2.1. Samples under study

For investigation of carrier dynamics, numerous samples (see Table 2.1) were provided by leading research centers world-wide: LiU (Department of Physics, Chemistry and Biology, IFM, Linköping University, Sweden), UCBL (University Claude Bernard Lyon, Villeurbanne Cedex, France), TDI (Technologies and Devices International, Inc. An Oxford Instruments Company, Silver Spring, Maryland, USA), Kyma (Kyma Technologies, North Carolina, USA), IMO (Institute for Materials Research, Hasselt University & IMOMEC, Diepenbeek, Belgium), UP (Université Paris 13, Sorbonne Paris Cité, Laboratoire des Sciences des Procédés et des Matériaux, Villetaneuse, France), HOYA (HOYA CORPORATION, Tokyo, Japan), IPTI (Ioffe Physico-Technical Institute, St. Petersburg, Russia), CREE (Cree, Inc., Durham, North Carolina, USA), ISM (Institute for Superhard Materials of the National Academy of Sciences of Ukraine), SΛMSUNG (Korea).

The samples were grown by different growth techniques, had different doping level and thickness. That allowed to study the intrinsic and defect-related processes of carrier diffusion and recombination. For detailed study of recombination rate and diffusion coefficient temperature and excitation dependences, the thickest and least defected samples were selected: 3C1, 3C2, 3C3, 4H1, GaN6, GaN7, C1 and C4. Compensating trap dynamics were studied in aluminum and boron compensated 3C8-3C12 and C1, C2 samples, respectively.

Table 2.1. Investigated samples parameters, for details see references.

Sample	Growth technique	Grower	Substrate	Thickness, μm	Impurities, cm^{-3}	Refs.
3C1	CVD	HOYA	Si, R.	160	N, ~10^{17}	[116]
3C2	CVD	HOYA	Si, R.	240	N, ~10^{16}	[117]
3C3	CVD	LiU	n^+ 4H	60	N, ~10^{15}	[118]
3C4	SE	UCBL	6H	200	N, 3×10^{16}	[119]
3C5	CVD	UCBL	3C6	6.2	N, 7×10^{17}	[120]
3C6	VLS	UCBL	6H	2	N, ~10^{18}	[121]
3C7	SE	IPTI	6H	42	N, 5×10^{18}	[122, 123]
3C8	SE	IPTI	6H	35	Al, 1.3×10^{18}	[124]
3C9-3C12	SE	IPTI	6H	10,30, 160,180	[N]-[Al], (1-3)×10^{18}	[122, 123]
4H1	CVD	CREE	n^+ 4H	160	N,~4×10^{14}	[100]
4H2	CVD	LiU	n^+ 4H	60	N, ~10^{15}	[118]
4H3	CVD	CREE	HE	360	SI	
6H1	CVD	CREE	HE	400	SI	
GaN1-5	HVPE	TDI	sapph.	9.9,17,41, 90,145	Si, 1-3×10^{16}	
GaN6	HVPE	SΛMSUNG	sapph. R.	200	Si, 1.3×10^{16}	[125]
GaN7	HVPE	Kyma	sapph. R.	450	Si, 9.5×10^{15}	[126]
C1	HPHT	ISM	HE	1000	N, 10^{17}	[127]
C2	HPHT	ISM	HE	1100	N, 10^{17}	[127]
C3	HPHT	ISM	HE	1000	N, $10^{18\text{-}19}$	[127]
C4	CVD	UP	HE	420	N, 4×10^{13} B, 10^{14}	[128]
C5	CVD	IMO	HE	400	N, 5×10^{14}	[129]
C6	CVD	IMO	Si, R.	1000	-	[130]
C7	CVD	IMO	Si. R.	250	B, ~5×10^{18}	

Here R –removed, HE –homoepitaxy, sapph. – sapphire.

2.2. Light-induced transient grating technique (LITG)

LITG technique is used to study dynamics of electronic, thermal, optical, and mechanical properties of materials [131]. The experiments were carried out on large variety of materials including solids, liquids and gases. The different optical nonlinearities were employed for grating recording, such as free-carrier, thermal, electronic polarization, acousto-optic, and others [131]. This work is focused on free-carrier nonlinearities as being the most informative for study of carrier dynamics in wide-bandgap semiconductors [132,133].

The main principle of light-induced transient grating technique is to generate a transient grating in a material using the interference of two pump beams and monitor the decay of the grating by measuring the diffraction efficiency of the third (probe) beam. For the grating recording two coherent Gaussian beams were used. The grating recording beams intersected at angle Θ in the sample plane, creating an interference pattern with a spatial period Λ (see Fig. 2.1):

$$\Lambda = \lambda_3 / \left(2 \sin\left(\Theta / 2\right)\right). \tag{2.1}$$

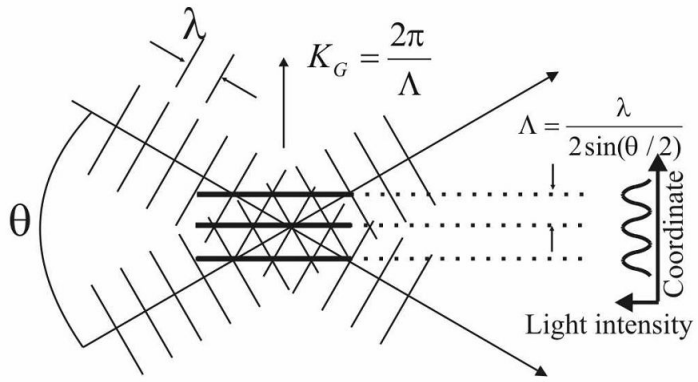

Fig. 2.1. Formation of transient grating by interference of two coherent laser beams [131]. K_G is the grating vector.

The spatially in-plane modulated light intensity is:

$$I(x) = I_0\left(1 + m\cos\left(2\pi x / \Lambda\right)\right), m = 2\sqrt{I_1 I_2} / \left(I_1 + I_2\right). \tag{2.2}$$

It was used to generate nonequilibrium carriers. Here $I_0 = I_1 + I_2$ is the total fluence of the two incident beams, while m is the modulation depth of the

interference pattern, which is commonly equal to unity. Therefore the carrier density profile is as follows:

$$\Delta N(x) = \alpha I_0\left(1+\cos\left(2\pi x/\Lambda\right)\right)/h\nu = \Delta N_0\left(1+\cos\left(2\pi x/\Lambda\right)\right). \quad (2.3)$$

Here I_0 =(1–R)I_{inc} is the total excitation fluence in the sample, α, R are the interband (single-photon) absorption and Fresnel reflection coefficients for excition beam with quantum energy $h\nu$; I_{inc} is the incident excitation fluence and $\Delta N_0 = \alpha I_0/h\nu$ is the nonequilibrium electron-hole concentration near the surface shortly after the excitation. The averaged over sample depth carrier density shortly after single-photon excitation (i.e. at $t << \tau_R$) is [134]:

$$\Delta N_{av} = [1+\exp(-\alpha d)]\times\Delta N_0/2. \quad (2.4)$$

For relatively thick samples ($d >> d^* = 1/\alpha$) investigated in this work, the relation simplifies to $\Delta N_{av} = \Delta N_0/2$. The generated carriers induced a complex refractive index change (temporary modulation of a refractive index and an absorption coefficient), which is proportional to the generated carrier density: $\Delta\tilde{n} = \Delta n_{FC} + i\Delta k \propto \Delta N_0$. The changes can be calculated using the Drude model, which treats electrons and holes classically as quasi-free particles (with effective masses m_e^* and m_h^*) oscillating in the electromagnetic field. Then the refractive index and absorption coefficient changes and their proportionality factors are as follows [42]:

$$\Delta n_{FC} = n_{eh}\Delta N,\ n_{eh} = -\frac{e^2}{2n_p\varepsilon_0 m_{eh}\omega^2}\frac{\omega_\Gamma^2}{\omega_\Gamma^2-\omega^2},\ \frac{1}{m_{eh}} = \left(\frac{1}{m_e^*}+\frac{1}{m_h^*}\right), \quad (2.5)$$

$$\Delta\alpha_{FC} = \sigma_{eh}\Delta N,\ \sigma_{eh} = \sigma_e+\sigma_e;\ \sigma_{e;h} = \frac{e^2}{cn_p\varepsilon_0 m_{e;h}^*}\times\frac{\tau_{m\,e;h}}{1+\omega^2\tau_{m\,e;h}^2}. \quad (2.6)$$

Here, $\omega=2\pi/\lambda_p$ is the probe frequency, ω_Γ is the frequency, corresponding to the effective direct bandgap (E_Γ=7.3 eV for 4H- and 6H-SiC, 3.4 eV for GaN and 7.3-7.4 eV for diamond [9]), n_{eh} is the refractive index change due to one electron-hole pair, m_{eh} is the reduced electron-hole effective mass, and n_p is the refractive index for probe wavelength (for probing 1-st harmonic was used, thus p=1). σ_{eh} =σ_e +σ_h is the free carrier absorption (FCA) cross section,

consisting of electron (σ_e) and hole (σ_h) absorption cross sections [61], τ_m is the momentum relaxation time of carrier, having the probe energy, [30], c is the speed of light in vacuum, ε_0 is the vacuum dielectric constant. When shallow defects are present in a material, $\Delta\alpha$ must be replaced by $\sigma_{eh}\times\Delta N + \sigma_{def}\times N_{def}$, where σ_{def} is the probe beam absorption cross section by a the defect, with density N_{def}. Free carrier absorption cross section temperature and spectral dependences under different carrier scattering mechanisms in virtual level [30] can be expressed as shown in Table 2.2.

Table 2.2. Free carrier absorption cross section temperature and spectral dependences under various scattering mechanisms in virtual level [30].

Scattering mechanism	Dependence
Acoustic phonons	$\sim(kT)^{3/2}/(\hbar\omega)^{3/2}$
Optical phonons	$\sim(kT)^{1/2}/(\hbar\omega)^{3/2}$
Polar optical phonons	$\sim 1/(\hbar\omega)^{5/2}$
Piezoelectric	$\sim(kT)/(\hbar\omega)^{5/2}$
Ionized impurities	$\sim(kT)^{-1/2}/(\hbar\omega)^{5/2}$

A standard experimental setup was used for recording light-induced transient gratings (LITG) [89,135]. The layout of the setup is provided in Fig. 2.2. The spatially modulated structure of non-equilibrium carriers was generated in a semiconductor by two coherent picosecond pulses using the third/fifth harmonic ($\lambda_{3,5} = 351,213$ nm) of a Nd:Yttrium Lithium Fluoride (Nd:YLF) or that of a Nd:Yttrium Aluminum Garnet (Nd:YAG) laser radiation. The grating recording beam passed a diffractive optical element - a permanent diffraction grating with a fixed period, Λ_G, and the two first order diffracted beams were selected by a spatial mask. These beams passed an optical telescope (two lenses with focal lengths of f_1 and f_2) and created refractive index modulation in the sample, called a transient grating with period $\Lambda = \Lambda_G/2\times f_2/f_1$. The diffraction from this grating was monitored by an

optically delayed probe beam at $\lambda_1 = 1053$ nm (1064 nm). The energies of excitation, transmitted and diffracted beams were measured by Si photodetectors. The excitation fluence was changed by an attenuator (A), consisting of a half wave plate (λ/2) for the excitation wavelength and a Beta Barium Borate Glan prism (GP). In this way, the decay kinetics were measured in a wide range of excess carrier density ΔN and temperatures (when sample was placed in a nitrogen-cooled or a closed-cycle helium cryostat). The reflection from a quartz plate provided the excitation energy calibration. For the background scattered light measurements at photodetectors, an electromechanical shutter was used. The diameters of the excitation beams were few times larger than that of probe beams to ensure homogeneous in-plane carrier density.

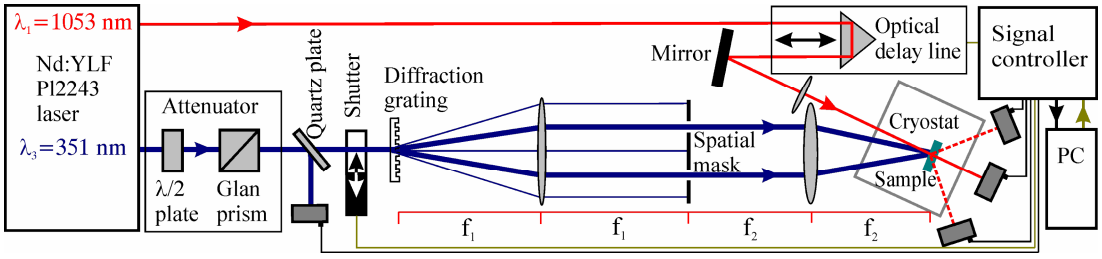

Fig. 2.2. Light induced transient grating setup. [P11]

The diffraction efficiency η of the probe beam primarily depends on a phase modulation Φ of the beam by the grating [131], $\eta \propto \Phi^2 = (2\pi\Delta n d^*/\lambda_1)^2$, and on a parameter $Q = 2\pi\lambda_1 d^* / \left(n_1 \Lambda^2\right)$, which describes the propagation and overlapping of the diffracted beams inside the photoexcited crystal. If the excited layer ($d^* = 1/\alpha$) is thin and the distance between the grating peaks Λ is large ($\Lambda >> d^*$), then $Q << 1$, and multiple symmetric diffraction orders are observed in the far field of diffraction (so called diffraction on a „thin grating“ [131]). If the excited layer thickness increases, and grating period Λ decreases, then the parameter Q may become high enough, $Q > 10$. In that case, only one dominant diffraction order is observed. This corresponds to probe beam diffraction on a “thick Bragg

grating". Light diffraction in the intermediate range of $1 < Q < 10$ corresponds to a transient regime between the thin and thick gratings, and will be further called as an "intermediate grating" and described in section 2.3.". For example in SiC polytypes at common 351 nm wavelength (α = 290 cm^{-1} for 4H-SiC, 2260 cm^{-1} for 3C-SiC, and 1060 cm^{-1} for 6H-SiC [136]), the light penetration depth d^* and the chosen period Λ = 2.85 μm result in Q = 10.84, 1.39, 2.97 values, correspondingly, revealing the "intermediate grating" regime.

Probe beam diffraction efficiency on the thick Bragg grating is described by Eq. (2.7) [131]:

$$\eta_{t=0} = \frac{I_D}{I_T} = \tan^2\left(\frac{\pi\int\Delta n(z)dz}{\lambda_1\cos(\varphi)}\right) = \tan^2\left(\frac{\pi n_{eh} I_0\left(1-\exp(-\alpha d)\right)}{h\nu\lambda_1\cos(\varphi)}\right). \qquad (2.7)$$

Assuming strong interband absorption $\alpha d >> 1$, the carrier excitation depth is small and the probe beam, incident at angle φ, integrates the refractive index change over the depth z (as well it integrates the nonequilibrium carrier density $\Delta N_0(z) \propto I_0(z)/h\nu$).

As light diffraction takes place on a transient free carrier grating which is recorded in a relatively thin surface layer d^*, the grating parameters are changing with time. Firstly, the thickness d^* may increase due to carrier diffusion to the depth. Therefore, evolution of the grating in-depth profile $\Delta N(z)$ must be taken into account. In addition, grating modulation $\Delta n(x,t) \propto \Delta N(x,t)$ decays due to carrier recombination and in-plane diffusion. A solution of the continuity equation in case of linear recombination (Eq. (1.34)) provides the modulated density dynamics $\Delta N(x,z,t)$, seen in the decay of its diffraction efficiency:

$$\begin{aligned} &\Delta N(x,z,t) = \Delta N_0\left(1+\cos\left(\frac{2\pi x}{\Lambda}\right)\exp\left(-\frac{t}{\tau_D}\right)\right)\exp\left(-\frac{t}{\tau_R}\right)\exp(-\alpha z), \\ &\eta(t) = \eta_{t=0}\exp(-2t/\tau_G),\ \frac{1}{\tau_G} = \frac{1}{\tau_R} + \frac{1}{\tau_D},\ \frac{1}{\tau_D} = \frac{4\pi^2 D}{\Lambda^2}. \end{aligned} \qquad (2.8)$$

Here, τ_G is the grating decay time, τ_R is the carrier recombination lifetime, τ_D is the grating diffusive erasure time due to ambipolar diffusion with coefficient

D. In general case, when both refractive index and absorption coefficient changes are substantial, the diffraction efficiency will be:

$$\eta = \left(\frac{4\pi^2 n_{eh}^2}{\lambda_1^2} + \frac{\sigma_{eh}^2}{4} \right) \left| \int_0^{\Lambda} \int_0^{d} \Delta N(x,z,t) dz \cos\left(\frac{2\pi x}{\Lambda} \right) dx \right|^2 ; \tag{2.9}$$

$$\eta = \left(\frac{\pi^2 n_{eh}^2}{\lambda_1^2} + \frac{\sigma_{eh}^2}{16} \right) \left(m \Delta N_0 \frac{(1-\exp(-\alpha d))}{\alpha} \right)^2 \exp\left(-\frac{2t}{\tau_G} \right). \tag{2.10}$$

For determination of *D*, the grating decay rates $1/\tau_G$ must be measured at least at two different grating periods ($1/\tau_1$ for Λ_1 and $1/\tau_2$ for Λ_2) in order to separate the diffusive and the recombinative contributions as:

$$D = \frac{1/\tau_1 - 1/\tau_2}{\left(\frac{2\pi}{\Lambda_1}\right)^2 - \left(\frac{2\pi}{\Lambda_2}\right)^2}, \quad \frac{1}{\tau_R} = \frac{1}{\tau_1} - \left(\frac{2\pi}{\Lambda_1}\right)^2 D. \tag{2.11}$$

The diffusive decay can be dominant at small periods, if bulk carrier lifetime is long enough, i.e. $\tau_R >> \tau_D$. The validity of the equation (2.11) is commonly verified by plotting the dependence of the total grating decay rate, $1/\tau_G$, against the grating period Λ, i.e. $1/\tau_G = f(4\pi^2/\Lambda^2)$. The linear slope of this plot provides *D* value, while the intersection with Y-axis corresponds to recombination rate, $1/\tau_R$.

Under two photon excitation, a value of two-photon absorption coefficient β [cm/GW] and the excitation beam instantaneous power density [33] $P(t) = 2I_0 \exp(-4t^2/\tau_{2h}^2)\pi^{-1/2}\tau_{2h}^{-1}$ [GW/cm^2] determine the generated carrier density $\Delta N_{02} = \int_{-\infty}^{+\infty} \beta P(t)^2 dt / 2h\nu = bI_0^2/2h\nu$. The factor $b = \beta/(\tau_{2h}\sqrt{\pi/2})$ describes a decrease of the incident fluence $I(z)$ during propagation inside the crystal (here τ_{2h} is the excitation pulse full with at 1/e intensity):

$$I(x,z) = \frac{I(x)}{1 + bzI(x)}, \text{ where } I(x) = I_0[1 + \cos(2\pi x/\Lambda)] \tag{2.12}$$

and leads to a slightly decreasing carrier density $\Delta N(z)$ with the penetration depth *z*:

$$\Delta N(x,z) = \frac{\Delta N_{02}\left[1+\cos(2\pi x/\Lambda)\right]^2}{(1+bzI(x))^2}. \qquad (2.13)$$

The above relationships allowed one to calculate an average carrier density $\Delta N_{av} = 1.5\Delta N_{02}/[1+bdI_0]$ for which the diffusion coefficient was measured. The carrier density equals to $1.5\Delta N_{02}$ near the excited surface and the factor 1.5 is due to the nonsinusoidal profile of the grating at TPA excitation.

The refractive index spatial modulation $\Delta n(x)$ creates a phase grating in the crystal, on which the probe beam diffracts with efficiency $\eta(t)$:

$$\eta(t) = \left(\frac{2\pi n_{eh}\Delta N_{02} d}{\lambda_1}\right)^2 \exp\left(-\frac{2t}{\tau_G}\right). \qquad (2.14)$$

Equation (2.14) can overestimate the diffraction efficiency η at high excitation fluences due to the depletion of pump beam (i.e. $I(z)$ and $\Delta N(z) \propto I(z)^2$ vary with depth at two-photon absorption conditions). The exact value of the first order diffraction efficiency at arbitrary modulation profile $\Delta n(x,z,t)$ can be calculated numerically according to [131]:

$$\eta(t) = \left|\frac{2\pi}{\lambda_1}\int_0^{\Lambda}\int_0^{d}\Delta n_{FC}(x,z,t)dz\cos\left(\frac{2\pi x}{\Lambda}\right)dx\right|^2. \qquad (2.15)$$

This equation was used for fitting the measured dependence $\eta(I_0)$. Moreover, the measured η value at a fixed excitation fluence ($\eta \propto \Delta N^2$) allows determination of the two-photon absorption coefficient (see Eqs. (2.14,2.15)). At higher I_0 the depth-averaged carrier density for LITG technique can be calculated using (in analogy with (2.4)):

$$\Delta N_{av} = \int_0^d \Delta N^2(x,z)dz \Big/ \int_0^d \Delta N(x,z)dz \approx 1.5\Delta N_{02}/(1+bdI_0). \qquad (2.16)$$

2.3. Diffraction based absorption coefficient measurement technique

Let us consider laser beam absorption in the media and deduce formulas for the first diffraction orders on the intermediate grating (i.e. for the Bragg and anti-Bragg beams). Approaching the thin grating regime, intensities of both

diffraction orders become equal, while the anti-Bragg beam intensity vanishes at approaching the Bragg diffraction condition.

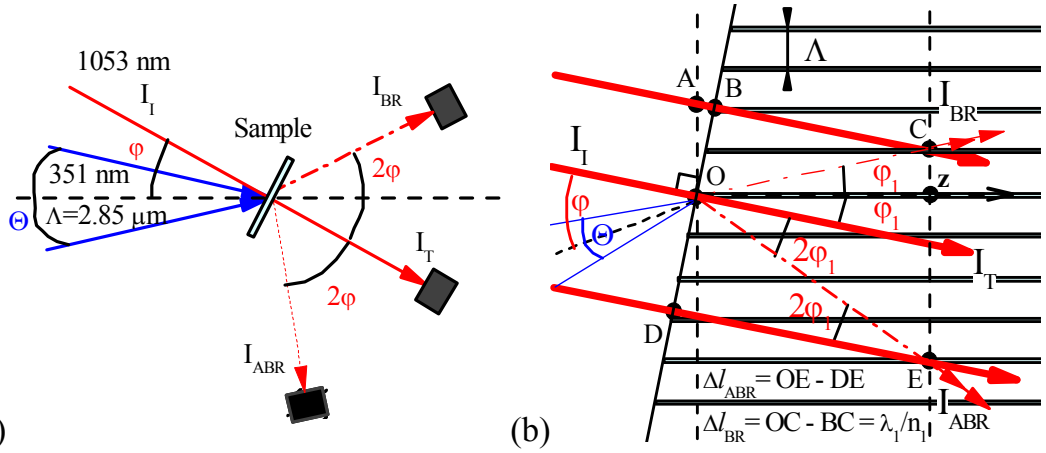

Fig. 2.3. Experimental scheme for diffraction based absorption coefficient measurement (a) and formation of the diffracted Bragg and anti-Bragg beams (b). The sample is positioned normally to the probe beam in order to get equal reflection coefficients for both diffracted beams. [P11]

The Bragg diffraction angle is given by $2\sin(\varphi) = \lambda_1 / \Lambda$ [131]**.** The angle 2φ is between the transmitted probe and the first order diffracted beams (in a typical case $\varphi = 3\Theta/2$ as λ_1=3λ_3). As diffraction on an intermediate grating is being considered, the first order Bragg beam I_{BR} is stronger than the symmetric anti-Bragg beam I_{ABR} (see Fig. 2.3a). Due to the Snell's law, the incident beams inside the crystal propagate with a lower angle $\sin(\varphi_1) = \sin(\varphi)/n_1$ (see Fig. 2.3b).

The Anti-Bragg beam electric vector can be obtained by integrating the electric vectors of diffracted beams on the depth elements [131]. The phase difference $\Delta\varphi(z)$ of the beams, diffracted at the interface (z = 0) and at the depth z varies with z, and is expressed by their path difference $\Delta l_{ABR}(z)$ (see details in Fig. 2.3b):

$$\Delta\varphi(z) = 2\pi n_1 \Delta l_{ABR} / \lambda_1,$$
$$\Delta l_{ABR}(z) = z(1-\cos(2\varphi_1))/\cos(3\varphi_1) \approx 2z\varphi_1^2 / (1-4\varphi_1^2). \quad (2.17)$$

The maximum φ angles are deduced using the limit of internal reflection for the Bragg and anti-Bragg beams as $2\varphi = \pi/2 = \arcsin(\lambda_1/\Lambda)$, which leads to λ_1

= Λ. If using Λ = λ_1 = 1053 nm, $\varphi_1 = \pi/4n_1 \approx 0.3$ rad can be obtained, thus approximation by (2.17) leads to a negligible error of about 0.1 %. Therefore, combining the phase difference from (2.17) and Bragg condition $\varphi_1 \approx \lambda_1 / 2n_1\Lambda$, a relation follows:

$$\Delta\varphi(z) = \pi\lambda_1 / \left(n_1\Lambda^2\left[1-4\varphi_1^2\right]\right)z = qz/2;\ \ q = 2\pi\lambda_1 / \left(n_1\Lambda^2\left[1-4\varphi_1^2\right]\right). \qquad (2.18)$$

Here q is the parameter of phase shift for the Anti-Bragg beam. The phase factor for complex electric vector becomes $\exp(i\Delta\varphi(z))$, and the vector can be expressed as:

$$\dot{E} = E_0 \exp(-\alpha z/2 - i\Delta\varphi(z)). \qquad (2.19)$$

Complex electric vector after averaging over the thickness and neglecting the probe beam intensity losses with depth due to diffraction is expressed as:

$$\dot{E} = E_0 \frac{\int_0^d \exp(-(\alpha/2 + iq/2)z)dz}{\int_0^d \exp(-\alpha z/2)dz}. \qquad (2.20)$$

This equation was integrated analytically. For Bragg beam, q = 0 (all electric vectors are phase matched as phase difference is multiple to wavelength, see Fig. 2.3b) and the electric vector is equal to E_0. The calculations provide:

$$\frac{I_{ABR}}{I_{BR}} = \frac{\dot{E}\dot{E}^*}{E_0^2} = \frac{1}{1+Q^2}\frac{(1-2\cos(qd/2)\exp(-\alpha d/2)+\exp(-\alpha d))}{(1-\exp(-\alpha d/2))^2}. \qquad (2.21)$$

Here $Q=q/\alpha$. At very low absorption coefficients, Eq. (2.21) leads to I_{ABR}/I_{BR} $=\sin^2(qd/4)/(qd/4)^2$. A case of relatively weak absorption of the pump beam can be approximated by condition $\alpha d < 8$, then oscillating function of $\cos(qd/2)$ can be eliminated by using a slightly slanted sample across the probe beam waist (slant of $\Delta d = 4\pi/q$). For strong absorption ($\alpha d > 8$), more simple formula from (2.21) can be obtained, by assuming infinite sample thickness:

$$\frac{I_{ABR}}{I_{BR}} = \frac{\dot{E}\dot{E}^*}{E_0^2} = 1\Big/\left[1+\left(\frac{2\pi\lambda_1}{n_1\Lambda^2\alpha\left[1-4\varphi_1^2\right]}\right)^2\right] = \frac{1}{1+Q^2}. \qquad (2.22)$$

The latter approximation gives an error of ≤5% for α determination at $\alpha d > 8$ condition. For 200-400 μm SiC samples the $\alpha d > 8$ condition is fully satisfied.

The Q value, determined experimentally, enables one to determine the absorption coefficient by Eq. (2.22), as the other parameters are given by experimental conditions. In figure 2.4 dependence of the calculated diffraction efficiency ratio I_{ABR}/I_{BR} versus absorption coefficient values for two grating periods is presented. At very strong absorption, Eq. (2.22) is approximated by $I_{ABR}/I_{BR} = 1 - q^2/\alpha^2$. The upper limit for determination of absorption coefficient is $\alpha_{max} = 3q(\Lambda)$ and it corresponds to $I_{ABR}/I_{BR} = 0.9$. Using $\Lambda = 2.85$ μm, $\lambda_1 = 1053$ nm, α_{max} equals to 10^4 cm^{-1}, while for $\Lambda = 1.3$ μm period the α_{max} value is 5×10^4 cm^{-1}. The lower limit for absorption coefficient is obtained from $\alpha d < 8$ condition, at which the $\alpha_{min} = 8/d \sim 200$ cm^{-1} can be determined for 400 μm thick sample.

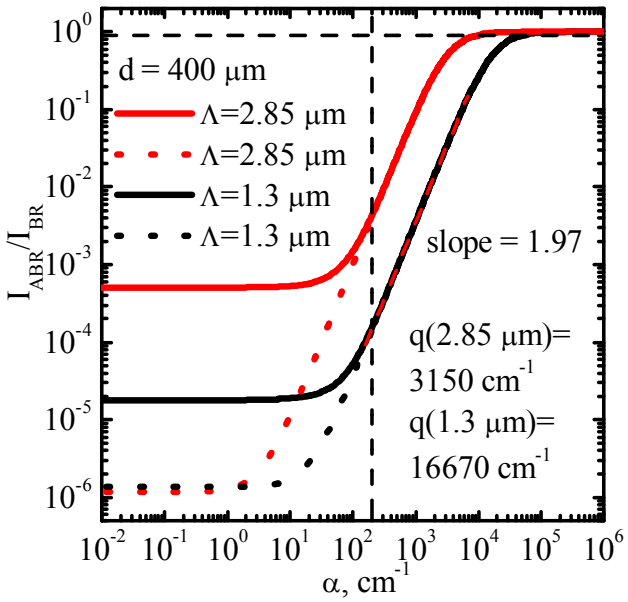

Fig. 2.4. Dependence of the diffraction efficiency ratio I_{ABR}/I_{BR} on absorption coefficient for two grating periods: calculations according equation (2.21) are shown by dotted lines, and with averaged oscillating function – by solid lines. The dashed lines designate lower and upper limits for determination of the absorption coefficient. [P11]

The calculations have shown that the proposed method allows determination of high absorption coefficient using very thick wafers ($\alpha d > 8$), when its value can not be determined by transmission measurements or ellipsometric techniques [43]. On the other hand, lower absorption coefficient ($\alpha d < 8$) can be extracted either by the proposed method or by conventional UV-VIS spectrometry [43], as well by scanning the carrier density in-depth profile

[137]. The method will be used for determination of the temperature-dependent absorption coefficient in investigated thick crystals.

2.4. Differential transmittivity and differential reflectivity techniques

The differential transmittivity (DT) kinetics were used to determine the carrier lifetime values τ_R at various excitations. The DT decay was given by (2.23a) relation, where $\sigma_{eh} = \sigma_e + \sigma_h$ is the free carrier pair absorption (FCA) cross section, consisting of electron (σ_e) and hole (σ_h) absorption cross sections [61] (σ_{eh} was considered to be isotropic as in cubic material). Θ is the incidence angle of the probe beam. The differential reflectivity (DR) kinetics provided decay of the carrier density in the vicinity of the surface (in the depth $d_{obs} \sim \lambda_p / 4\pi n_0$ which is known as the effective observation depth of the material refractive index for the reflected probe radiation [138]) according to the (2.23b,c) relationships. The relationships were obtained using approximate linearized equation: $\mathrm{DR} = -[dR(n)/dn]/R(n_0)\Delta n$ when the refractive index changes are that small that $\Delta R \ll R$ is valid (Fresnel's equations (1.10) were used for *s*- and *p*-polarized probe beams).

$$\mathrm{DT}(t) = \ln\left(\frac{T_0}{T(t)}\right) - \ln\left(\frac{1-R_0}{1-R(t)}\right) = \frac{\sigma_{eh}\int_0^d \Delta N(z,t)\,dz}{\cos\left(\arcsin\left[n_p \sin(\Theta)\right]\right)}, \tag{2.23a}$$

$$\mathrm{DR_s}(t) = \frac{R_0 - R(t)}{R_0} = \frac{4n_p \cos(\Theta)}{\left(n_p^2 - 1\right)\left[n_p^2 - \sin^2(\Theta)\right]^{1/2}} \Delta n(t), \tag{2.23b}$$

$$\mathrm{DR_p}(t) = \frac{R_0 - R(t)}{R_0} = \frac{4n_p \cos(\Theta)}{\left(n_p^2 - 1\right)\left[n_p^2 - \sin^2(\Theta)\right]^{1/2}} \cdot \frac{\left[n_p^2 - 2\sin^2(\Theta)\right]}{\left[\left(n_p^2 + 1\right)\cos^2(\Theta) - 1\right]} \Delta n(t). \tag{2.23c}$$

In (2.23c) strong enhancement of the signal appears near the Brewster's angle ($\Theta_B = \mathrm{atan}(n_0)$) as the factor $\left(n_p^2 + 1\right)\cos^2(\Theta) - 1$ in the denominator approaches zero. $\mathrm{DR_s}$ is always positive, while $\mathrm{DR_p}$ is positive up to Θ_B and becomes negative afterwards. At 0° both equations provide the same DR value. In this work for excitation and probing in most cases both *s*-polarized beams were used. At zero delay after photoexcitation (t=0) the integral in (2.23a) for

infinite sample equals $\sigma_{eh}I_0/h\nu$ in DT case, while $\mathrm{DR}(t=0)=4n_{eh}\Delta N(z=d_{obs},t=0)/(n^2-1)$ for $\Theta\sim 0^\circ$ case.

The average carrier density at single photon excitation is $\Delta N_{av}=\Delta N_0/2$. While depth-averaged carrier density for TPA case is $\Delta N_{av}=\Delta N_{02}/(1+bdI_0)$.

In the measurements, nonequilibrium carriers were excited by an above-gap optical pulse at λ_{ex} =351 nm (or at 355, 266, 213 nm) from a Q-switched Nd:YLF (Nd:YAG) laser, emitting 15 (25) ps duration pulses (see Fig. 2.5). The optically delayed 15 picosecond duration probe pulse at 1053 nm was used to monitor the fast DT and DR decays (up to 4 ns, with ~10 ps resolution), while an electronically delayed 2 ns duration pulse at 1064 nm (from a diode pumped Nd:YAG laser, triggered by the picosecond laser) was used for monitoring of the long relaxation tails of DT (with ~2 ns time resolution).

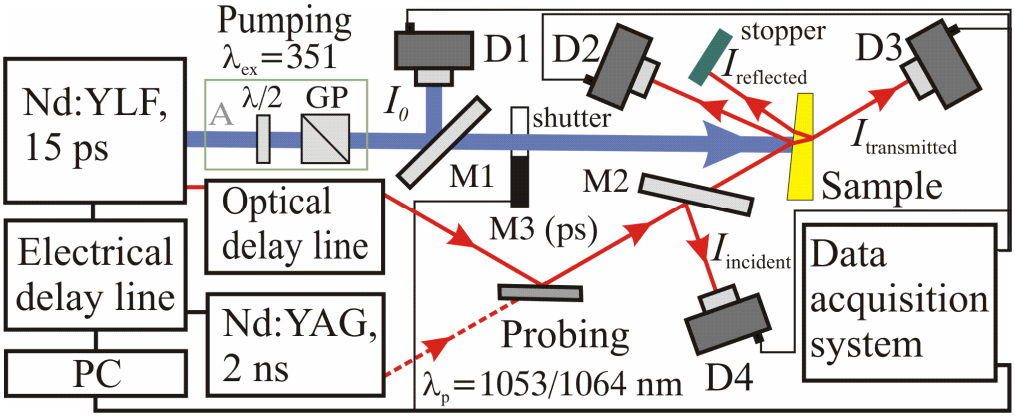

Fig. 2.5. DT and DR experimental setup. [After P1,P2,P28]

Relative probe beam transmission or reflection (only from the excited surface, as the reflection from the back surface was blocked) without excitation is $T_0=I_{\mathrm{transmitted0}}/I_{\mathrm{incident}}$, $R_0=I_{\mathrm{reflected0}}/I_{\mathrm{incident}}$ (when the shutter is closed) and under excitation is $T(t)=I_{\mathrm{transmitted}}(t)/I_{\mathrm{incident}}$, $R(t)=I_{\mathrm{reflected}}(t)/I_{\mathrm{incident}}$ (when the shutter is opened). These coefficients were measured at various delay times of the probe beam, t, using silicon photodiodes as the detectors (D2 – D4). For each data point, the data was filtered by using a calibration detector D1 and taken if the excitation fluence I_0 was in the 1-3 % interval. These normalization and

filtration procedures allowed to eliminate the laser beam energy variations and increase the decay measurement accuracy.

2.5. Time-resolved free carrier lifetime microscopy

The commonly used optical techniques for point by point lifetime mapping, such as time resolved photoluminescence (TRPL) [98,100], free carrier absorption [61,100], and microwave photoconductivity decay [97,100] provide high temporal resolution (<~ns) but are time consuming [61]. CCD camera based photoluminescence lifetime mapping [139,140] has high spatial resolution (~μm) and fast data acquisition, but the carrier lifetime is indirectly determined from PL intensity proportionality to the lifetime assuming a single exponential decay. Therefore a new setup was constructed, combining advantages of temporal and spatial resolution, and using well known relationship between the measured FCA signal and carrier density.

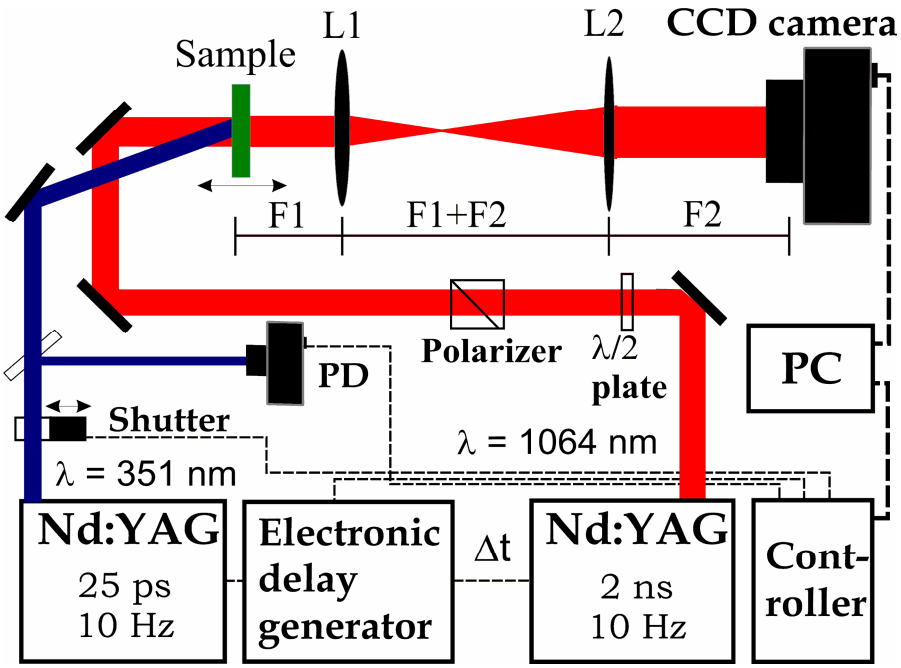

Fig. 2.6. The free carrier lifetime microscopy setup. [P25]

The experimental setup for time-resolved free carrier lifetime microscopy, based on differential transmission (DT), is provided on Fig. 2.6. The picosecond Nd:YAG Ekspla PL2143 (τ_L= 25 ps) laser 3rd harmonic at 355 nm

(pump) generates carriers in a sample, while the 1st harmonic of a nanosecond single mode Ekspla NL303G laser at 1064 nm probes the generated FCA decay. The external synchronization pulse from an electronic delay generator (Highland Technology P400) triggers the picosecond laser, while the same but electronically delayed pulse triggers the nanosecond laser. A photodetector, PD, controls average excitation energy in 1 % interval. The DA data are recorded on a CCD camera (12 bit Thorlabs BC106-UV with 6.5 μm pixel size) at different probe delay time, Δt. For probe beam attenuation, a λ/2 plate and a polarizer were used. The used lenses of F1 =100 mm and F2 =250 mm focal lengths magnify the sample image on the CCD camera by 2.5 times, thus one pixel can provides a 2.6 μm spatial resolution. The actual resolution of 5 μm was determined by measuring two-fold drop of transmitted probe intensity near a thin foil edge. The setup successfully operated at ambient light conditions as 20 dB infrared filter was used on the camera.

For carrier lifetime mapping, few hundreds probe pulses were measured and averaged for each pixel with excitation on (shutter opened, $I_{\mathrm{i,wex}}(\Delta t)$) and off (shutter closed, $I_{\mathrm{i,woex}}(\Delta t)$) at varying probe delay. The time dependent differential transmission (DT) signal on each pixel was calculated according to a relation [61]:

$$\mathrm{DT_i}(\Delta t)=\ln[I_{\mathrm{i,woex}}(\Delta t)/I_{\mathrm{i,wex}}(\Delta t)]=\sigma_{eh}\Delta N_s(\Delta t). \qquad (2.24)$$

$\Delta N_s(\Delta t) = \int_0^d \Delta N(z,\Delta t)dz$ is the integrated over depth nonequilibrium carrier density (in $\mathrm{cm^{-2}}$); $\Delta N(z,\Delta t)$ is the spacio-temporal carrier density profile (in $\mathrm{cm^{-3}}$). The carrier lifetime, τ_R, commonly calculated at 1/e signal drop (the signal is assumed to decay exponentially, $\mathrm{DT_i}(\Delta t) \sim \exp(-\Delta t/\tau_R)$) was determined in each pixel, assuming $\Delta t = \tau$. About 40 seconds were needed to obtain differential absorption image at a fixed delay. Therefore the setup required about 10 minutes per full carrier lifetime image of 1×1 $\mathrm{mm^2}$ area, with good spatial (5 μm) and temporal (~2 ns) resolution.

2.6. Spectrally- and temporally-resolved photoluminescence

The excitation-dependent PL spectra (**time integrated spectrally-resolved PL)** were obtained at Vilnius University by the time-integrated PL measurements in 3C-SiC (see Fig. 2.7a) and GaN. The PL signal was collected with the wide-diameter lens and focused to the double monochromator with focal length of 0.6 m through the vertically adjusted polarizer. The slits of the monochromator were set to 2 mm, resulting in the system resolution of about 5 meV. The PL signal was detected using the photomultiplier tube (PMT) and recorded using boxcar integrator [141].

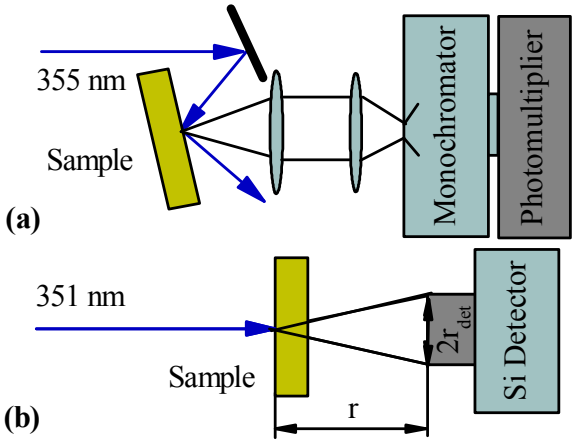

Fig. 2.7. Spectrally-resolved PL (a) and calibration of spectrally integrated PL intensity (b) setups, provided for 3C-SiC case. [P20]

In order to determine the absolute radiative recombination coefficient value in SiC the **PL intensity calibration setup** was employed (Fig. 2.7b). The high gain Si photodetector (HGPD) was positioned behind the sample in order to block the 351 nm excitation beam. The detector spectral response was fitted as $\sim h\nu^{-4.2}$ in 3C-SiC luminescence interval ($h\nu$ is the PL quantum energy), and its calibration constant was 4.9×10^{-14} J/count at 2.36 eV. The generated light penetrated through the sample with tickness d and reached the opposite side, therefore 3 percent of light intensity was lost, as follows from the sample transmission, averaged over the PL band: $T_{abs} = \int I_{PL}(h\nu)\exp(-\alpha(h\nu)d)d\nu/\int I_{PL}(h\nu)d\nu$. The PL emission, transmitted through the sample, reached the detector sensitive area (see Fig. 2.7b), therefore light collection efficiency for the used calibration setup is calculated as [71]:

$$\eta_{coll} = \left[1-\cos^2(\operatorname{atan}(r_{det}/r))\right]/\left[n_g\left(n_g+1\right)^2\right]. \qquad (2.25)$$

Here r_{det} is the detector active area diameter, and r is the distance to it (see Fig. 2.7b). r_{det} = 0.5 cm and r = 2.1 cm were used. The ratio of the detected and generated light intensities is as follows:

$$I_{PL\ detect}/I_{PL\ gener} = T_{abs} \times \eta_{coll}. \quad (2.26)$$

In **SiC time-resolved PL (TRPL)** measurements in Linköping University (Sweden) were performed under relatively low excess carrier densities ΔN = 10^{16} -10^{18} cm^{-3}, and in the temperature range T = 80-500 K. Free carriers were excited using a diode pumped frequency tripled Nd:YAG laser with emission at 355 nm, of 35 ns pulse width and repetition rate of 6 - 16 kHz. The signal from the bandgap region was selected using either interference filters or a monochromator and detected using photon counting setup.

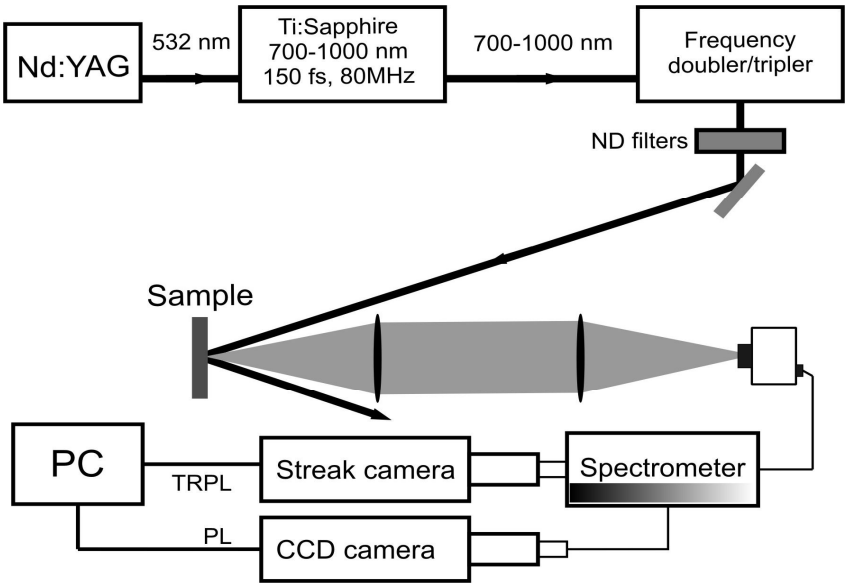

Fig. 2.8. TRPL setup with a streak camera. [P18]

For **GaN TRPL** measurements in VCU (Virginia Commonwealth University, USA), the decay transients were detected by a UV sensitive streak camera system for excess carrier densities in the range from 10^{16} to ~10^{18} cm^{-3} (estimated at the very surface of GaN at the end of the excitation pulse). A standard setup of time-resolved PL spectroscopy was employed using ~150 fs frequency tripled pulses from a Ti-Sapphire laser at λ=266 nm with Hamamatsu streak camera.

3. Carrier generation and absorption mechanisms

The knowledge of nonequilibrium carrier density is crucial for experiments in which excitation and temperature dependences of carrier lifetime and diffusion coefficient are studied. However, in literature the data for absorption coefficients are rather scarce. Therefore, determination of temperature and excitation dependences of absorption coefficients is the primarily task.

In this chapter free carrier, single photon absorption and two photon absorption coefficients are studied by using absolute and relative differential absorption signal and diffraction efficiencies at different excitation fluences and temperatures. The calibrated DR and DT signals provided free carrier absorption cross sections in SiC, GaN and diamond in section 3.1. Original data on absorption coefficients at 351 nm and 213 nm are presented for three SiC polytypes and diamond in section 3.2. Absorption saturation in GaN at 355 nm excitation is observed by DR in section 3.3. In section 3.4 two photon absorption coefficients are calibrated by means of absolute diffraction efficiency to provide the nonequilibrium carrier density and the FCA cross sections. The chapter ends with a short summary.

3.1. Calibration of DT, DR and LITG signals

In this section determination of n_{eh} and σ_{eh} values (which are proportionality coefficients of refractive index and absorption coefficient to the excess carrier density changes, see Eqs. (2.5) and (2.6)) are provided, as determination of the nonequilibrium carrier density in TPA case is based on these calibrated values.

The dependences of Bragg diffraction efficiencies η in SiC at $\Lambda = 2.85$ μm grating period were measured at various excitation fluences, as shown in Fig. 3.1. The quadratic increase of diffraction efficiency with excitation was used for extraction of n_{eh} values for the three SiC polytypes, corresponding n_{eh} values are given on the plot (n_{eh} error is about 0.2×10^{-22} cm^3). The experimental values of n_{eh} in 3C2, 4H3, 6H1 samples were found very similar to the calculated using Eq. (2.5) (n_{eh} = (8.4; 8.8; 7.3)$\times10^{-22}$ cm^3 for 3C, 4H and

6H, respectively; for calculations, m_{eh} = 0.24; 0.23; 0.27 $\times m_0$ were taken from Table 1.2). The DT and DR excitation dependences in 3C-SiC provided σ_{eh} = 5.1×10^{-18} cm^2 and rather the same n_{eh} value. Similarly in 4H-SiC and 6H-SiC σ_{eh}=1.0×10^{-17} cm^2 was obtained at RT. FCA measurements in a 4H-SiC epilayer and its substrate at various temperatures provided temperature-dependent values of σ_{eh} =$(0.79+ 3.9\times10^{-5}\times T^{1.5})\times10^{-17}$ cm^2 (here, temperature independent and dependent FCA components reveal carrier scattering (at probe energy) by polar optical and acoustic phonons, respectively; see Table 2.2 for details).

Knowledge of σ_{eh} and n_{eh} values provided possibility to determine not only the nonequilibrium carrier density at two photon excitation, but two photon absorption coefficient as well (see section 3.4). Let us note again that n_{eh} value can be calculated precisely using electron and hole effective masses using Eq. (2.5).

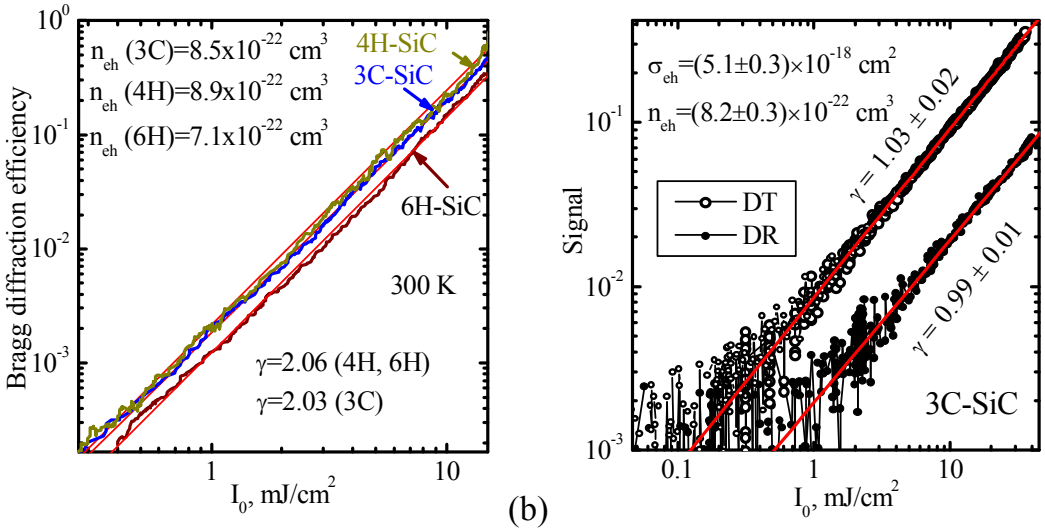

Fig. 3.1. Dependence of Bragg diffraction efficiency (a), and DR and DT signals (b) on excitation fluence at t =0. γ are the slopes of the curves in the log-log plot. [After P11,P28]

3.2. Temperature dependences of absorption coefficients in SiC and diamond

The largest α values, which can be determined from UV-VIS spectrometric measurements in 0.2-1.0 mm thick samples, are of about 300 cm^{-1}. It is clear

that it is not possible to measure much higher α values at 351 nm in 6H- or 3C-SiC due to large sample thickness. Therefore, implementation of a new diffraction based technique was applied for determination of high interband absorption coefficients in SiC (samples 3C2, 4H3, 6H1, correspondingly) and diamond (sample C4) at main excitation wavelengths (351 nm and 213 nm).

The measured ratios of I_{ABR}/I_{BR} diffraction efficiencies for different SiC polytypes at 351 nm were used for extraction of absorption coefficient values and their temperature dependences (Fig. 3.2). The used excitation energy density for α determination was in the 0.1-2 mJ/cm^2 range, thus decrease of the probe beam intensity due to its diffraction was negligible, and α values were calculated according to Eq. (2.22). Due to lower absorption coefficient in 4H-SiC, the α increase with temperature was found the largest among the other studied SiC polytypes, spanning over one order of magnitude (see Fig. 3.2a).

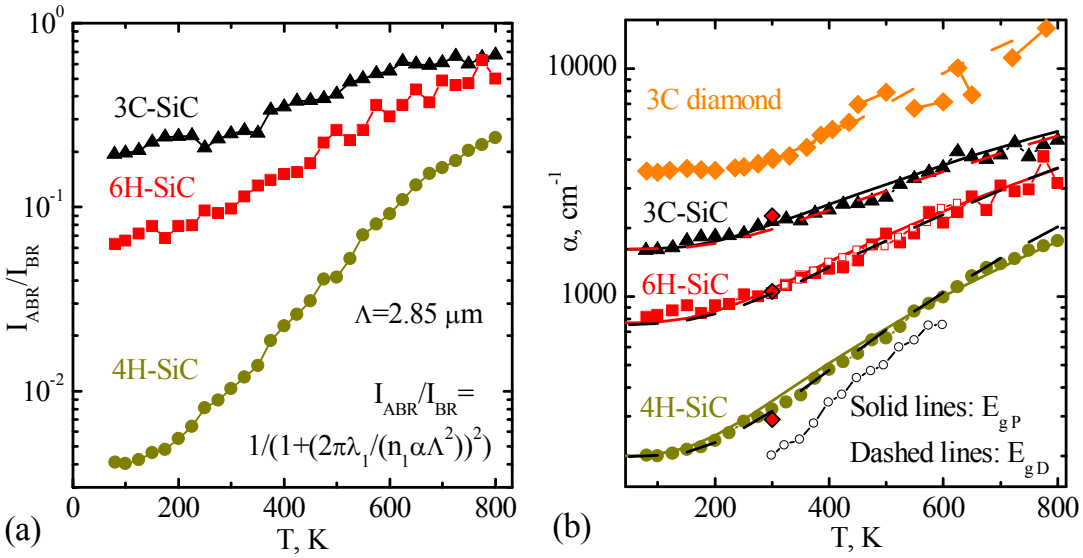

Fig. 3.2. Temperature dependences of I_{ABR}/I_{BR} diffraction efficiency ratio (a) and the determined absorption coefficients in SiC at 351 nm and in diamond at 213 nm (b). Fitting by Passler and Debye approximations for $E_g(T)$ are denoted by solid and dashed curves, respectively. For comparison, data at 351 nm [136] are given as rhombs, while 355 nm data [137] – as open points. [After P11]

The fitting of $\alpha(T)$ dependences in SiC was performed under two different simulation models, based on $E_g(T)$ dependences (Eqs. (1.6-1.8)). Using Passler approximation (Eq. (1.7)) (solid lines in Fig. 3.2b), phonon energies and slope

A values were determined (see Table 3.1). This is consistent with the average acoustic phonon energies and slope A values, obtained from the fitting of absorption edges according to Eq. (1.9) [P11]. A_{ref} values were obtained from [136]. Using Debye approximation (Eq. (1.8)), higher phonon energies (~70-80 meV) and slope A values (Table 3.1) were used (dashed lines) with respect to those determined from the absorption edges. Thus the phonon energy of 60 meV for all studied SiC polytypes gives a reasonably good fit of the absorption edges and temperature dependences of interband absorption coefficients. In 4H-SiC, $\alpha(T) = 190 + 9\times10^{-5}\times T^{2.5}$ cm^{-1} relationship was fitted with ~10% precision in the 80-800 K range.

Table 3.1. SiC absorption coefficient approximation parameters at 3.53 eV.

SiC polytype	$E_{g\,0}$, eV	A_{ref}, cm^{-1}/eV^2	A_{abs}, cm^{-1}/eV^2	Passler $E_g(T)$		Debye $E_g(T)$	
				A, cm^{-1}/eV^2	E_{ph}, meV	A, cm^{-1}/eV^2	E_{ph}, meV
3C-SiC	2.335	1200	1100	1250	63	1250	70
4H-SiC	3.232	3200	3100	3400	59	4300	82
6H-SiC	2.973	2700	4300	3100	63	3400	78

In diamond, temperature dependence of α was fitted, using 160 meV phonon energy [9], bandgap temperature dependence (see Fig. 1.5b) and $A = 1.03\times10^5$ cm^{-1}/eV^2 parameter. The absorption coefficient was rather constant at T <300 K, while at higher temperatures strongly increased due to increase of phonon population.

3.3. Absorption saturation in GaN

In GaN, due to its direct bandgap, absorption at 351/355 nm weakly depends on temperature and is described by rather large coefficient, $\alpha_0 = 1.0\times10^5$ cm^{-1} [34], thus carrier in-depth redistribution after excitation is very important.

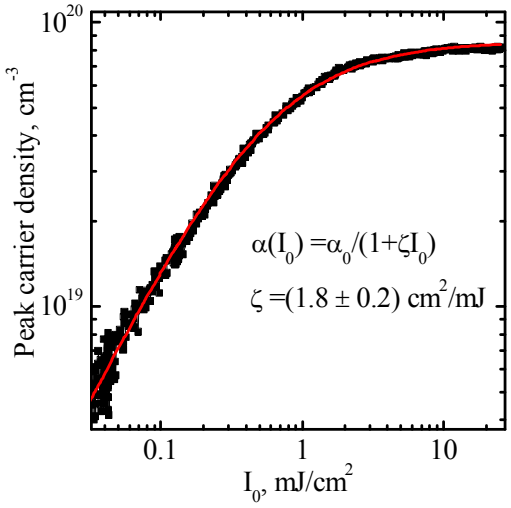

Fig. 3.3. Surface carrier density dependence on excitation fluence at zero delay in GaN7 sample.

In addition, absorption bleaching takes place at high excitations, and this will limit the carrier density at the surface. Onset of the latter effect can be evaluated by monitoring DR signal at different fluences, as the known value of n_{eh} (1.36×10^{-21} cm^3, see next section) allows calculation of the nonequilibrium carrier density at the surface after photoexcitation.

In Fig. 3.3 the near surface carrier density dependence on 355 nm excitation fluence is shown. The DR peak values at different fluences provided the peak carrier density near surface using Eq. (2.23b) and $\Delta n = n_{eh}\Delta N$ relationship. The DR signal value at different delay after photoexcitation will provide average carrier density at that time, which in turn will provide diffusion coefficient excess carrier density dependence (see section 4.2). The generated carrier density near surface was fitted using saturation of the absorption coefficient by analytical relation $\alpha(I_0) = \alpha_0/(1+\zeta I_0)$, where $\zeta = 1.8$ cm^2/mJ was determined. This relation can provide carrier in depth distribution at arbitrary fluences according $\alpha(z) = \alpha_0/(1+\zeta I(z))$.

3.4. Absorption at two photon excitation in GaN and diamond

The two-photon absorption in GaN (GaN6) was confirmed by a nearly quadratic increase of the differential transmission (DT $\propto I_0^2$) associated with the nonlinear carrier generation rate $\Delta N \propto I_0^2$ (see Fig. 3.4a). The grating

diffraction efficiency, η, increased twice steeper than DT with excitation fluence ($\eta \propto I_0^4$). The relationships between DT and η signals and the carrier density (Eqs. (2.15), (2.16), (2.23a)) allowed determination of the free carrier absorption cross-section $\sigma_{eh} = (2.5\pm0.5)\times10^{-17}$ cm^2 at 1053 nm and the two-photon absorption (TPA) coefficient $\beta = 15\pm2$ cm/GW at 527 nm (the factor b (given by Eq. (2.12)) is equal to 0.85 cm/mJ). A similar β value of 17-20 cm/GW at 527 nm was obtained by Z-scan technique [142]. Rotation of the excitation beam polarization provided the β angular dependence (see Fig. 3.4b). The dependence of β was described by a two-photon absorption matrix element angular dependence according Ref. [143]: $\beta(\phi) = \beta_\perp \sin^4(\phi) + \beta_\parallel \cos^4(\phi) + \Psi\cos^2(\phi)\sin^2(\phi)$. The $\beta_\perp = 15$, $\beta_\parallel = 17.8$ and $\Psi = 22$ cm/GW values (with ~15 % error) were determined from fit in Fig. 3.4b.

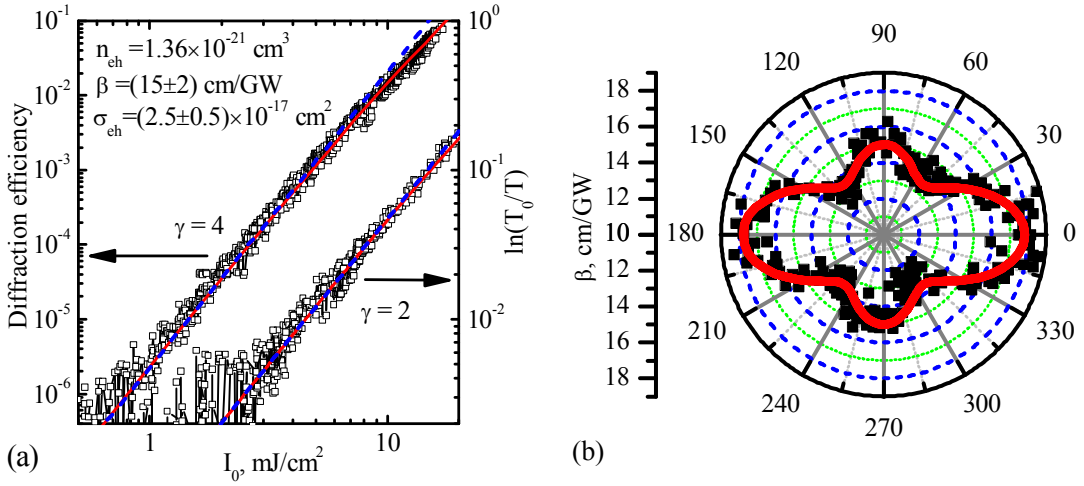

Fig. 3.4. Dependences of light-induced diffraction efficiency, η, and differential transmission DT on excitation energy fluence, I_0, in GaN6 under two-photon carrier excitation (a) and the two photon absorption coefficient angular dependence in GaN7 sample (b). The indices γ are the slopes of the curves in log-log scale: expected ones (γ = 2 and 4, dashed lines) and experimental ($\gamma_{exp} < \gamma$, solid lines). [After P12,P13]

The fitting of dependence $\eta(I_0)$ allowed one to obtain bdI_0=0.34 (at 20 mJ/cm^2), which led to the depth averaged carrier density of $0.77\times1.5\Delta N_{02}$ and $0.77\Delta N_{02}$ for diffraction (LITG) and free carrier absorption, respectively ($\Delta N_{02} = bI_0^2/2h\nu$). Therefore, the depletion of the pump beam (see Eq. (2.12)) with

depth provided the slightly decreased slopes γ with excitation, as seen in the dependences in Fig. 3.4a, for $I_0 \geq$ 5-10 mJ/cm^2. The TPA coefficient was found virtually independent on temperature (within 10% error) as followed from the dependence of diffraction efficiency on T. On the other hand, the FCA cross-section had weak temperature dependence with T^s (s = –0.15) both for SPA and TPA excitations. The small σ_{eh} value points out to carrier scattering predominantly by polar optical phonons according to the relationship $\sigma_{eh} \sim T^0 h\nu^{-2.5}$ (see Table 2.2).

A varying FCA signal strength for different probe beam polarizations implies that the σ_{eh} value is strongly anisotropic (Fig. 3.5a). The FCA cross section in GaN7 sample was fitted by using $\sigma_{eh}(\phi)=\sigma_{eh\perp} - (\sigma_{eh\perp}-\sigma_{eh\parallel})\cos^2(\phi)$. For 1053 nm probe, $\sigma_{eh\perp}=2.2\times10^{-17}$ cm^2, $\sigma_{eh\parallel}=3.4\times10^{-18}$ cm^2, and anisotropy ratio S $=\sigma_\perp/\sigma_\parallel$ = 6.5 were obtained. The same values of σ_{eh} and S were obtained under two photon excitation, i.e. in the carrier density range from 10^{15} to 5×10^{17} cm^{-3} (see Fig. 3.5a). This result can be attributed to the polar optical phonon assisted FCA in valence bands, being excitation-independent at the given probe wavelength of 1053 nm, thus $\sigma_{eh} \approx \sigma_h$ ($\sigma_e << \sigma_h$ [144]).

Polarization-dependent FCA measurements with the 527 nm probe were performed at low and high carrier excitation conditions (i.e. using excitation pulses at 527 nm or 351 nm wavelengths, respectively). At low excess carrier density (~5×10^{17} cm^{-3}) and 527 nm probing, the measurements provided smaller σ_{eh} values compared to those for the 1053 nm probe, and no dependence on polarization: $\sigma_{eh\perp}=\sigma_{eh\parallel}$ = 8×10^{-17} cm^2 (Fig. 3.5b). This is a clear signature that holes, responsible for FCA anisotropy at 1053 nm, do not contribute significantly to FCA in the visible spectral range, or at least at 527 nm. Therefore, the electron-related transitions within the conduction band are not forbidden, in contrary to the calculation-based predictions of $\sigma_e = 4.6\times10^{-19}$ cm^2 [144]. The measured significantly higher value can be ascribed to the isotropic electron cross section σ_e (the isotropy of σ_e at low nonequilibrium carrier density can be explained by isotropic conduction bands of GaN) as the

hole absorption cross sections are smaller and strongly anisotropic: $\sigma_{h\perp}=1.5\times10^{-18}$ cm^2, $\sigma_{h\parallel}=6.2\times10^{-19}$ cm^2 (S= $\sigma_\perp/\sigma_\parallel$ = 2.4) [144]. The contribution of direct inter-valence-band hole transitions at 527 nm cannot be observed due to absence of appropriate valence bands (see Fig. 3.5c). At 351 nm excitation (high excess carrier density, $\Delta N \sim 2.6\times10^{19}$ cm^{-3}), the σ_{eh} value decreased up to 6 times (compare external and internal circles in Fig. 3.5b), which can be attributed to screening of electron interband transitions, band filling and renormalization, while residual absorption is probably related to holes as predicted theoretically [144].

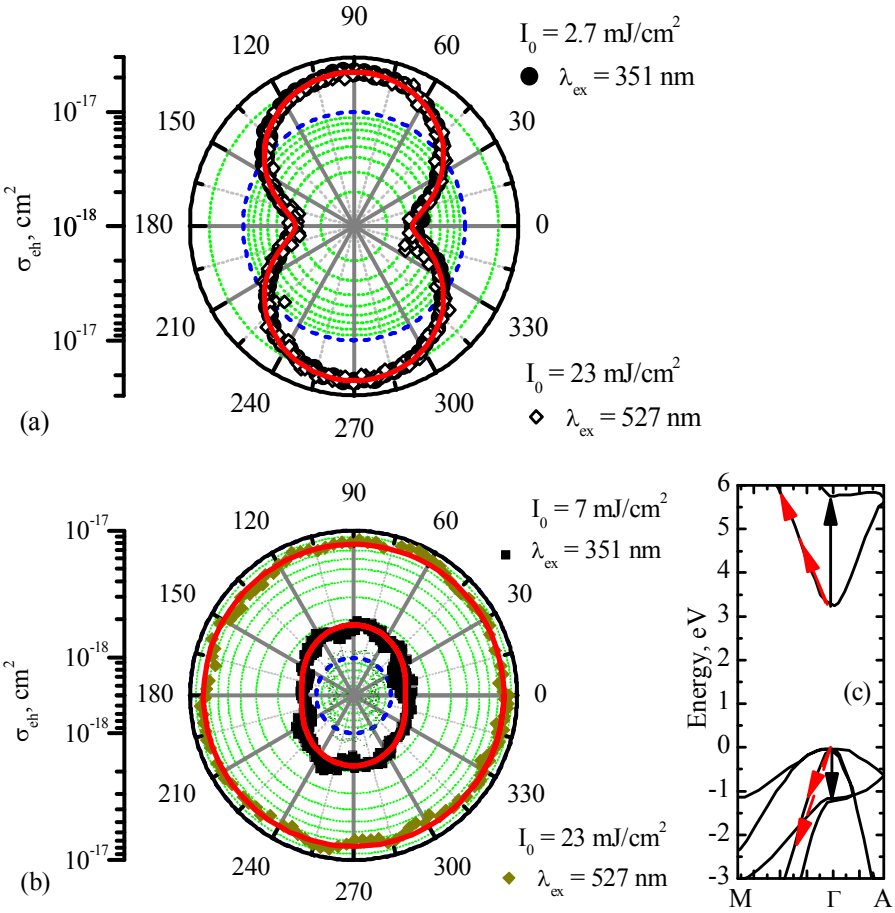

Fig. 3.5. Polarization dependence of FCA cross-section for 1053 nm probe wavelength at SPA (351 nm) and at TPA (527 nm) excitation conditions (a). In (b), FCA anisotropy for 527 nm probe is given at low (external circle) and at high excess carrier density (351 nm excitation, internal circle). In (c) direct (vertical arrows) and indirect phonon assisted (diagonal arrows) transitions are schematically depicted for 1053 and 527 nm in valence and conduction bands, which structure was taken from [144]. [P14]

The experimentally measured dependences of probe beam diffraction efficiency and induced transmission in diamond (sample C1) on excitation fluence are presented on Fig. 3.6a. The nonlinear dependence of LITG signal follows a $\eta \sim I_0^4$ law, while the peak FCA signal depends on excitation fluence quadratically, similarly as in GaN. The slope values in log-log plot were close to expected ones (4 and 2, correspondingly) and thus confirmed two photon carrier generation in diamond at 351 nm excitation.

The diffraction efficiency value of 0.0025 at I_0=24 mJ/cm^2 allowed estimation of the corresponding excess carrier density ΔN_0=1.5×10^{16} cm^{-3}. In turn, the constant b=30 cm/J and two-photon absorption coefficient $\beta = (0.37 \pm 0.07)$ cm/GW were calculated from the relationship given by Eq. (2.14). The determined β value coincides quite well with that reported in [145] (0.3 cm/GW).

The diffraction efficiency was found nearly temperature independent in 80-800 K range, indicating a constant β value in this range. Therefore, from the measured temperature dependence of the FCA signal, the temperature dependence of σ_{eh} was determined. The calculated σ_{eh} value was approximated with σ_{eh} =8×10^{-18}×(T/300K)$^{0.44}$ cm^2 relationship (see Fig. 3.6b). The power factor, being close to 0.5, points out to carrier scattering by nonpolar optical phonons for probe quantum energy (see Table 2.2).

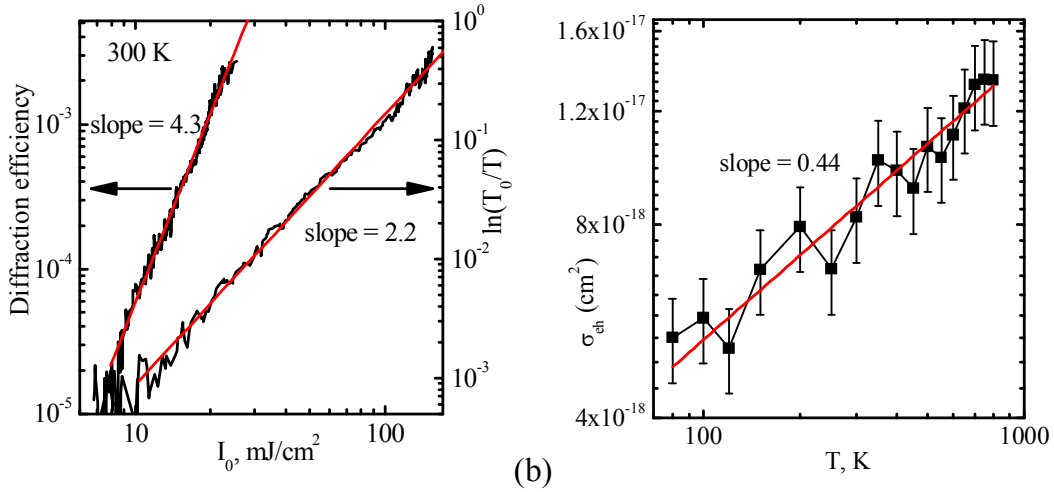

Fig. 3.6. Excitation dependences of diffraction efficiency and free carrier absorption (a) and the temperature dependence of free carrier absorption cross section (b). [P10]

3.5. Short summary

1. A new method, based on light diffraction on a transient free carrier grating, was used for the determination of the interband absorption coefficient at wavelengths well above the bandgap. The absorption coefficient values in the range from 200 to 5000 cm^{-1} were measured for three bulk SiC polytypes and diamond in the 80-800 K range.
2. The significant increase of indirect absorption coefficient with temperature (by order of magnitude in 4H, by 3-5 times in 3C, 6H, and 3 times in diamond) were approximated using corresponding phonon energies (~60 meV/160 meV) and the temperature dependent decrease of the bandgaps.
3. In GaN, saturation of differential reflectivity indicated the absorption bleaching at reaching 1 mJ/cm^2 excitation energy fluence for 355 nm excitation wavelength.
4. Measurements of TG diffraction efficiency provided two-photon absorption coefficients values of 15 cm/GW in GaN at 527 nm and 0.37 cm/GW in diamond at 351 nm. Two photon absorption coefficients were found temperature independent and weakly dependent on polarization in GaN.
5. The free carrier absorption cross sections σ_{eh} in SiC and diamond increased with temperature due to increasing scattering by phonons. In GaN, σ_{eh} was almost constant due to dominance of polar optical phonon scattering.
6. In GaN, the polarization dependence of σ_{eh} at 1053 nm wavelength was rather strong ($\sigma_{\perp}/\sigma_{\parallel} = 6.5$) due to the valence band anisotropy. FCA at 527 nm was isotropic, thus ascribed to electron transitions between the lower and upper conduction bands, while at high nonequilibrium carrier density electron transitions were suppressed due to screening, band filling and renormalization. Under strong blocking of electron transitions, the anisotropic features of hole-related FCA were observed.

4. Carrier diffusion coefficient and mobility excitation and temperature dependences

Carrier mobility and diffusion coefficient are very important for bipolar device operation. However, no extensive studies of latter parameters can be found in literature. Especially strong excitation dependence of carrier diffusion coefficient in diamond was not studied up to now. Carrier diffusion coefficient and mobility in SiC, GaN and diamonds are described in sections 4.1, 4.2, 4.3, respectively. Short summary follows afterwards.

4.1. Carrier diffusion coefficient and mobility in SiC

In order to elucidate strong impact of excess carrier density on diffusion coefficient in 4H-SiC, LITG decay kinetics at small grating periods were measured, when the grating decay is diffusion governed (Fig. 4.1), i.e. $\tau_G \propto \Lambda^2/D$ (measurements at Λ = 11.4 μm provided the τ_R impact to τ_G).

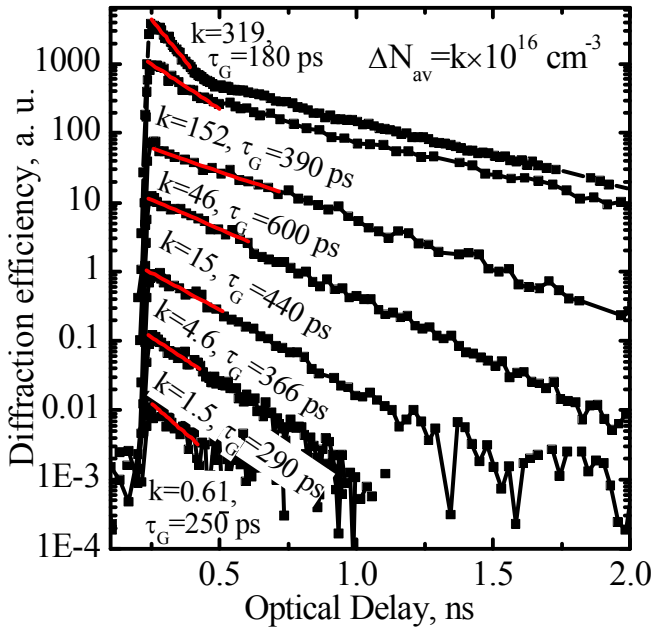

Fig. 4.1. LITG decays for Λ = 2.85 μm period at 80 K at various excess carrier densities from 10^{16} to 10^{18} cm^{-3} (sample 4H1). The small grating period ensures almost purely diffusive grating decay: $\tau_G \approx \tau_D << \tau_R$. [P24]

The grating decay time was determined from the initial part of the decay (Fig. 4.1) to ensure nearly constant nonequilibrium carrier density ΔN_{av} during the measurement time. It was clearly observed that the decay rate becomes slower with increase of the excitation but at the highest excitations it revealed faster transient again. Similar sets of LITG decay measurements at different temperatures provided the excitation

dependences of the ambipolar diffusion coefficient $D_a(T,\Delta N)$ at various temperatures (see Fig. 4.2a). The data from Ref. [146] are shown for comparison. They coincide with present measurements only at low excitations ($\Delta N < 10^{18}$ cm^{-3}), while at high excitations ($\Delta N > 10^{18}$ cm^{-3}) the increase of D_a appears due to incorrect discrimination of diffusion coefficient from the competing decay by Auger recombination, as the authors in [146] used relatively large (~20 μm) grating period.

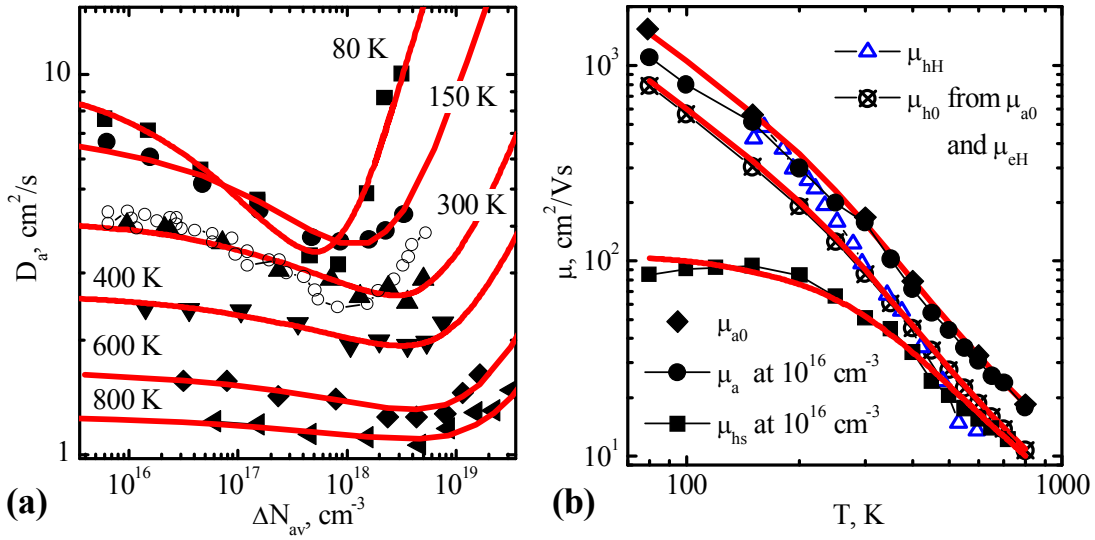

Fig. 4.2. Excitation dependences of ambipolar diffusion coefficient D_a at selected temperatures (a) and temperature dependences of electron, hole, and ambipolar mobilities at ~10^{15} cm^{-3} excitations (b). In (a): filled points are the experimental data, lines are the fits according to equation (4.1), open points show data from Ref. [80] at 296 K. In (b): full points are the experimental data in the *n*-type epilayer (μ_{a0}) and substrate (μ_{hs}); the solid lines are mobility fits using parameters, given in the text. Crossed points are hole mobility in the studied layer (μ_{h0}), as derived from μ_{a0} and μ_{eH}. [P24]

An analytical approximation to $D_a(\Delta N)$ was performed taking into account the contributions of band-gap renormalization (BGR) and plasma degeneracy [54], which can lead to reduction or enhancement of diffusion coefficient, respectively:

$$D_a(T,\Delta N) = D_{a0}(T)\left[\left(1 + a_1(T)\Delta N/10^{18}\right)^{2/3} - a_2(T)\left(\Delta N/10^{18}\right)^{1/3}\right]. \quad (4.1)$$

Here $D_{a0}(T)$ is the low-excitation, phonon-limited ambipolar diffusion coefficient, and the two terms in brackets represent impact of plasma

degeneracy and BGR, respectively. The D_{a0}, a_1, and a_2 are fitting parameters. The a_1 and a_2 coefficients decrease with temperature by a power law, describing quite precisely the impact of degeneracy ($a_1 \propto T^{-1.5}$, because the density of states increases with temperature as $T^{1.5}$) and confirming the vanishing BGR effect at elevated temperatures ($a_2 \propto T^{-1}$, as carriers with increased thermal energy more easily overcome the potential barrier of the decreased bandgap [146]). The temperature dependence of the dimensionless parameters a_1 and a_2 were fitted with 5% precision to the expressions $a_1=135/T^{(1.3-18/T)}$ and $a_2=113/T$. The low-excitation ambipolar diffusion coefficient, D_{a0}, is determined by the electron (D_e) and hole (D_h) diffusion coefficients: $D_{a0}=2D_eD_h/(D_e+D_h)$ (see Eq. (1.23)). The individual diffusivities can be calculated from the relevant ambipolar and monopolar mobilities according to $D_i=\mu_i k_B T/\mathrm{e}$ (where $i=a,e,h$). Therefore, the determined values of $D_{a0}(T)$, if combined with electron Hall mobilities $\mu_{e0}=\mu_{eH}$ [80], provide the low-excitation hole mobility $\mu_{h0}(T)$ in the layer (Fig. 4.2b). In this way, the temperature dependence of all three low-excitation mobilities μ_{i0} was fitted with a simplified equation, $1/\mu_{i0}=1/\mu_{OPi}+1/\mu_{ACi}$, where $\mu_{OPi}=OP_i\times[\exp(E_{ph}/k_BT)-1]$ cm^2/Vs is the optical phonon scattering term, $\mu_{AC}=AC_i\times(T[\mathrm{K}])^{-1.5}$ cm^2/Vs is the acoustic phonon scattering term, and E_{ph} = 120 meV. The fitting parameters for $i=a,e,h$, respectively, are as follows: OP_i=6.5; 18.5; 3.9 and AC_i =1.05; 7.8; 0.6×10^6 (see curves in Fig. 4.2b). These fits led to the approximate relation $\mu_a \approx 1.8\mu_h$. The low-excitation μ_{a0} values (obtained from D_{a0}) are slightly higher than μ_a at $\Delta N_0=10^{16}$ cm^{-3} as they are not influenced by the BGR effect. As the Hall measurements of hole mobility, μ_{hH}, are not very accurate for 4H-SiC [79] due to the complex valence band structure, the electrically and optically measured $\mu_h(T)$ dependences coincide well only in 300-400 K range (Fig. 4.2b). It must be mentioned that the hole mobility in the doped substrate, μ_{hs}, (i.e. of minority carriers, as $\Delta N_0=10^{16}$ cm^{-3} << $n_0=3.5\times10^{18}$ cm^{-3}), was found lower than that in the epilayer because of additional scattering by neutral impurities (μ_{NI}), and the value of μ_{NI}= 125

cm^2/Vs at 300K was determined from the relationship $1/\mu_{hs} = 1/\mu_{h0} + 1/\mu_{NI}$. The latter mechanism becomes dominant at 80-300 K temperatures according to Ref. [79].

Similar temperature dependence of ambipolar diffusion coefficient was observed in 3C-SiC at low excitations (Fig. 4.3a). The diffusion coefficient decrease with nonequilibrium carrier density in 3C-SiC was also revealed (Fig. 4.3b).

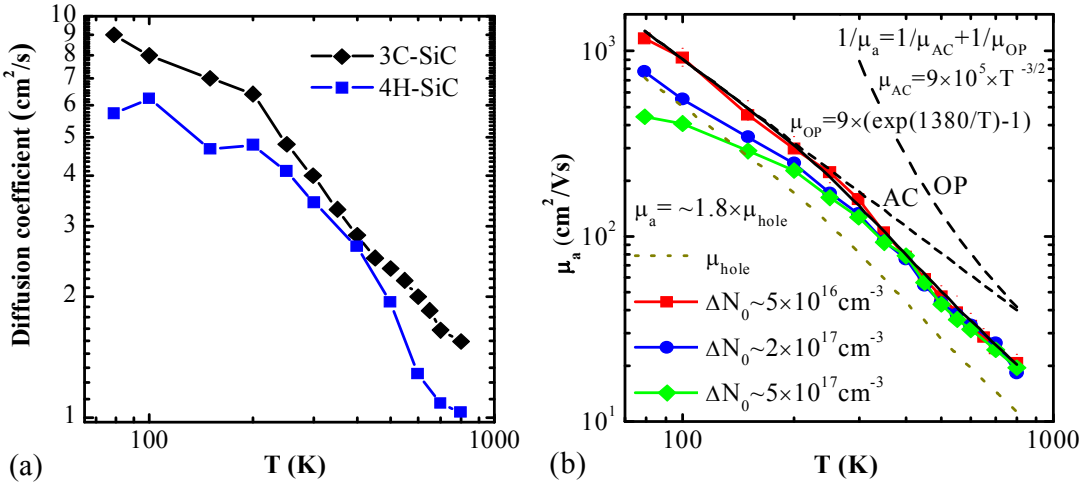

Fig. 4.3. Temperature dependence of ambipolar diffusion coefficient in 3C/SiC and 4H-SiC (samples 3C3 and 4H2) at ~10^{16} cm^{-3} excess carrier density (a), and ambipolar mobility in 3C-SiC (sample 3C2) at different excitations (b). [P8,P7]

Therefore, the optical measurements provided the temperature dependences of ambipolar and hole (μ_h ~100 cm^2/Vs at RT) mobilities, which did not reveal the defect scattering features in lightly doped samples. On the other hand, strong diffusion coefficient reduction at higher doping levels was observed in low temperature wing in heavily doped 4H-SiC substrate.

4.2. Ambipolar and hole diffusion coefficient in GaN

In this section carrier diffusion coefficient studies in low doped free-standing GaN layers (GaN6 and GaN7) were performed. Noting that the hole mobility is much smaller than that of electrons ($\mu_h << \mu_e$), the measurements at the moderate excitation regime ($\Delta N = \Delta N_e = \Delta N_h >> n_0$) may provide an ambipolar diffusion coefficient D_a, while at low excitation conditions ($\Delta N << n_0$), the hole

diffusion coefficient may be determined in GaN. Both cases were realized experimentally, assuming that $n_0 \sim 10^{16}$ cm^{-3} is a standard value for undoped HVPE GaN [125]. The small grating periods, Λ, ensured faster diffusive decay than the recombination governed decay ($\tau_D << \tau_R$), thus a plot of $1/\tau_G$ vs. $1/\Lambda^2$ for different Λ values provided D at various nonequilibrium carrier densities and temperatures. In Fig. 4.4a the exponential decay of the LITG at 2P carrier excitation is plotted for a fixed grating period Λ = 1.74 μm at different sample temperatures. Similar measurements resulted in a set of diffusion coefficient values for various nonequilibrium carrier densities (Fig. 4.4b). The latter data at moderate excitation ($\Delta N_e = \Delta N_h = 10^{17}$ cm^{-3} >> n_0) provided the value $D_a \approx 2D_h$ = 1.6 cm^2/s as well as a hole mobility $\mu_h = eD_a/(2k_BT)$ = 31 cm^2/Vs. On the other hand, deviation from ambipolarity at low excitations ($\Delta N_e = \Delta N_h = 10^{15}$ cm^{-3} < n_0) directly led to the hole mobility in c-GaN. Indeed, in m-GaN diffusion coefficient dropped to very low values due to impact of recharged acceptors with ~10^{15} cm^{-3} density (see explanation in chapter 6).

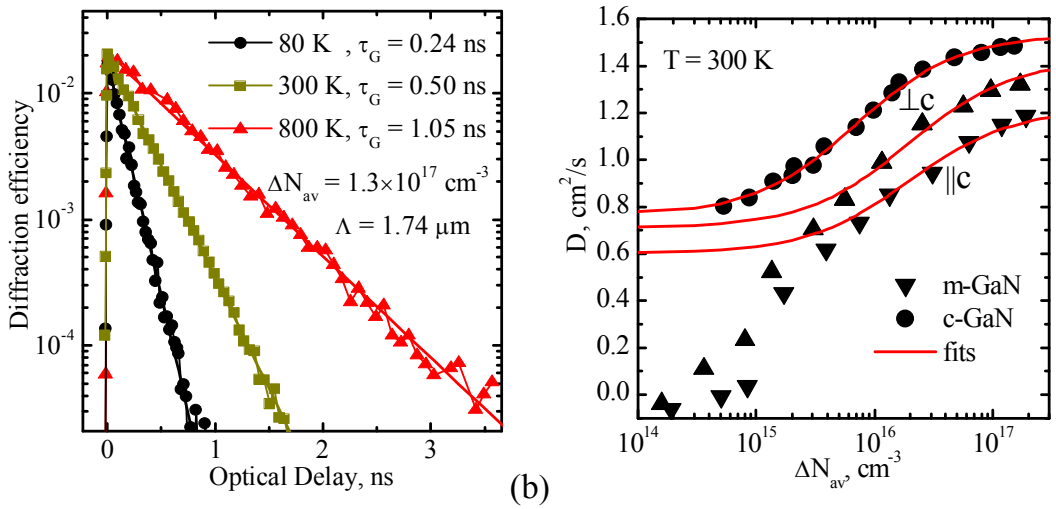

Fig. 4.4. Diffusive decay of LITG kinetics in bulk GaN (GaN6) at two-photon carrier excitation with a grating period of 1.74 μm (a). Anisotropy of diffusion coefficient in bulk m-GaN (b). Various decay times in (a) reveal dependence of diffusion coefficient on temperature. [P13,P14]

Note that the excitation level, at which D_a =1.5D_h, corresponds to the doping concentration n_0 (see Eq. (5.21)), and thus the fitting of $D(\Delta N)$ curve allowed estimation of the equilibrium carrier density $n_0 \approx 8\times10^{15}$ cm^{-3} at RT in

c-plane (sample GaN6) and 2×10^{16} cm^{-3} in m-plane (sample GaN7). Hole diffusion coefficients of $D_{h\perp}$= 0.76 cm^2/s and $D_{h\parallel}$ = 0.65 cm^2/s were determined rotating the sample by 90 degrees to obtain orthogonal or parallel orientations of the grating vector $K_G = 2\pi/\Lambda$ (which is in the plane of grating recording beams) with respect to the c-axis. The slightly higher $D_{h\perp}$= 0.81 cm^2/s value in c-GaN sample is due to lower doping ($n_0 = 8\times10^{15}$ cm^{-3}).

Thus, according to formulas (1.16-1.18) and GaN valence band parameters [24] diffusion coefficient anisotropy $D_\perp/D_\parallel$ = 1.35 was obtained, using the same deformation potentials for all valence bands. The calculated anisotropy value is close to the experimentally obtained one of 1.17. Such small anisotropy is caused by opposite anisotropy of the light- and split-off valence bands.

For modeling of diffusion coefficient dependence on carrier density at different temperatures (Fig. 4.5a), the equilibrium carrier densities are needed. These values were calculated using a previously determined donor concentration of 1.04×10^{16} cm^{-3} and acceptor of 2.4×10^{15} cm^{-3} [147] (with activation energies E_D = 25 meV and E_A = 140 meV). The concentration of free electrons *vs*. T was calculated according [148], revealing its decrease to 3.2×10^{15} cm^{-3} at 80 K and saturation above RT at $n_0 = N_D - N_A = 8\times10^{15}$ cm^{-3}. In order to fit the hole diffusion coefficient temperature dependence (Fig. 4.5b), temperature-dependent scattering rates were used for acoustic (ac), polar and nonpolar optical phonon (pop and npo, respectively) scattering (see Eqs. (1.16-1.18)). Appropriate parameters were used for $D_{h,\ theor}$ calculation: static and optical dielectric constants $\varepsilon_r(0) = 10.4$, $\varepsilon_r(\infty) = 5.43$, density $\rho = 6.1$ g/cm^3, longitudinal velocity $v_\parallel$ = 8 km/s, heavy and light hole density of states effective masses $m_{HH/LH}$ = 1.9/0.33 m_0 [24], polar and nonpolar optical phonon energies 91 meV and 80 meV, respectively [149]. The fitting provided acoustic and optical inter/intra-valley deformation potentials, C_a = 9.6 eV and D_{ii+jj} = 1.34×10^9 eV/cm, respectively. The dependence $D_{h,\ theor}$ was also fitted by the empirical (with 2% precision) relationship $1/D_{h,\ theor} = 1/D_{ap} + 1/D_{op}$, where the

$D_{ap} = 19.1 \times T^{-1/2}$ and $D_{op} = 3.6 \times 10^{-4} \times T[\exp(E_{ph}/k_B T) - 1]$ correspond to the acoustic and optical phonon (E_{ph} = 91 meV) contributions, respectively.

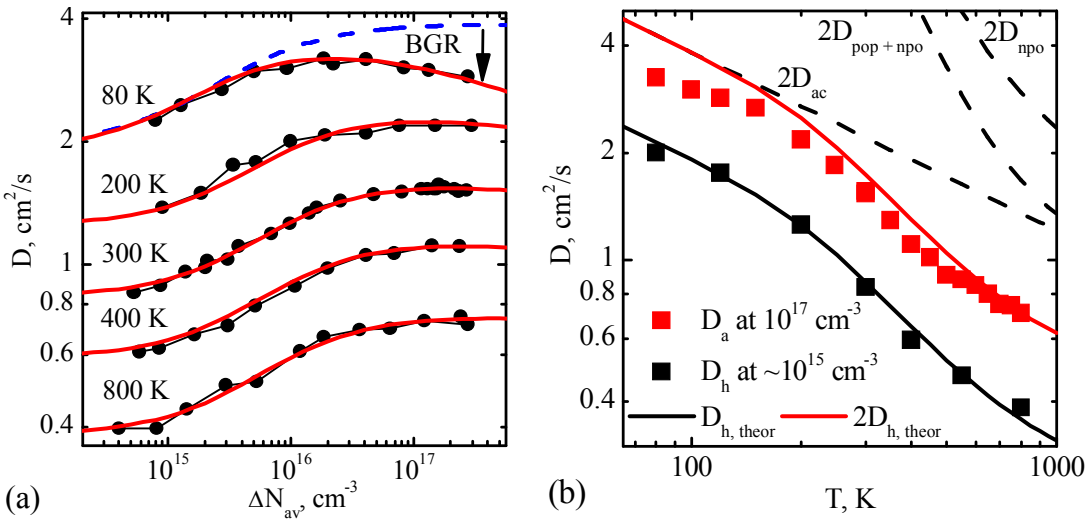

Fig. 4.5. (a) The measured dependences of diffusion coefficient D on nonequilibrium carrier density at different temperatures (symbols) and the modeled data (lines); at 80 K, the modeled curves with/without the impact of band gap renormalization (BGR) are compared. (b) Experimental data compared with theoretically calculated temperature dependence for hole ($D_{h,\ theor}$) and ambipolar ($D_a = 2D_{h,\ theor}$) diffusion coefficient (lower and upper solid curves, respectively), which account for acoustic (ac), polar and nonpolar optical phonon (pop and npo, respectively) scattering (dashed curves). [P13]

The carrier-density dependent ambipolar diffusion coefficient in GaN was calculated using the relationship $\Delta E_v(\Delta N) = \chi \times [3\text{ meV } (\Delta N/10^{18})^{1/3} + 19\text{ meV } (\Delta N/10^{18})^{1/4}]$ [56] for valence band modulation, which takes into account the effect of BGR by adjusting the fitting parameter χ. This factor χ = 0.48 for GaN is lower than that for SiC (χ = 1) probably due to higher density of valence band states as well as the larger static dielectric constant $\varepsilon_r(0)$ = 10.4 in GaN (as opposed to 9.66 in SiC) which reduce the BGR effect [54].

The fundamental relations (1.15, 1,16, 1.18) allowed simulation of temperature and density dependent hole diffusion coefficient in the nondegenerate regime (this approach is valid in the whole temperature range because even at 80 K the density of states in the valence band, $N_{vd} = 5.5 \times 10^{18}$ cm^{-3}, is by an order of magnitude higher than the nonequilibrium carrier density). At lower temperatures the spatial bandgap renormalization hindered

carrier diffusion and thus led to lower than calculated D_a values which manifested itself as decreasing $D(\Delta N)$ with increasing carrier density at 80 K (Fig. 4.5a). Moreover, the difference between $D_a = 2D_{h,\,theor}(T)$ dependence, not accounting for BGR, and the experimentally measured $D_a(T)$ at $T < 150$ K is also caused by BGR (Fig. 4.5b).

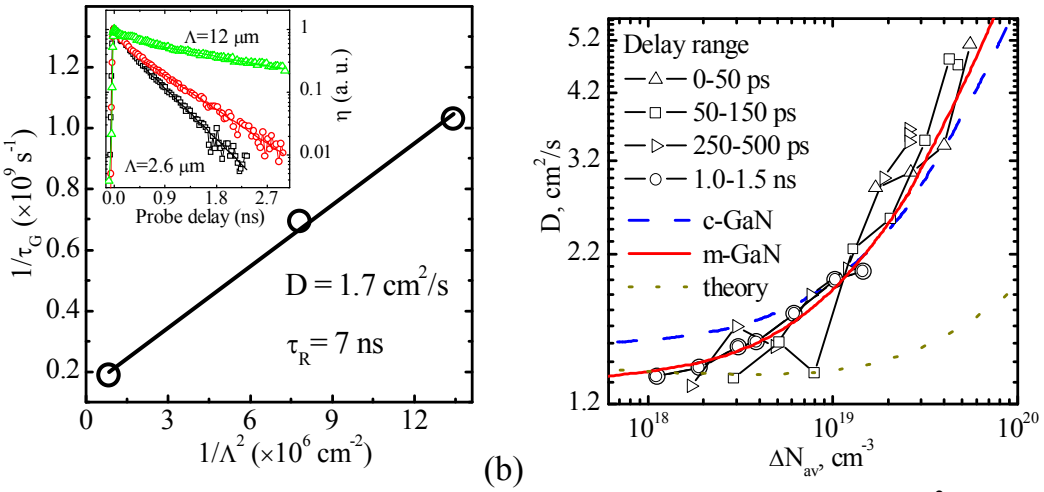

Fig. 4.6. Determination of ambipolar diffusion coefficient by $1/\tau_G = f(1/\Lambda^2)$ plot in 145-μm thick GaN (GaN5) at room temperature and at I_0 ~1 mJ/cm^2 (a), and carrier diffusion coefficient excitation dependences in GaN6 and GaN7 (b). In (a) the inset shows kinetics at different periods. In (b) solid and dashed lines are fits for m- (this work) and for c-plane GaN [94], respectively. Theoretical calculations, assuming carrier density independent interaction with phonons, are provided by dotted curve. [After P23,P19]

The diffusion coefficient dependence on nonequilibrium carrier density in GaN at high 355 nm excitation is provided in Fig. 4.6. In Fig. 4.6a an angular dependence is provided. The diffusion coefficient in m-plane (Fig. 4.6b) was determined from LITG decays at different time intervals, when average carrier density at these time interval centers were determined from DR decays at the same excitation fluences. The rather similar data in c-plane was obtained by numerical carrier transport modeling [94]. The diffusion coefficient value at ~10^{18} cm^{-3} carrier density is rather the same as at two photon excitation (Fig. 4.5), however at higher excitations diffusion coefficient starts to increase quite strongly. The diffusion coefficient dependence on carrier density was fitted by $D(\Delta N) = D_0(1+\Delta N/N_x)$, where $D_0 = 1.5$ (1.3) cm^2/s

and N_x =2.2×10^{19} (1.8×10^{19}) cm^{-3} for c- (m-) plane samples, respectively. Theoretical calculations of ambipolar diffusion coefficient using equation (1.24) provided dotted curve in Fig. 4.6b. This simple model does not fit the diffusion coefficient excitation dependence as density of states in the valence band is very large, N_{vd} =4.6×10^{19} cm^{-3}. The main origin of much stronger diffusion coefficient increase with excitation may be due to screening of hole-phonon interaction by the generated carriers (see Eq. (1.19)).

4.3. Carrier diffusion coefficient and mobility in diamond

The measured grating decay times τ_G for different grating periods Λ (4.2 to 11 μm) were used to evaluate the diffusive grating decay time $\tau_D = \Lambda^2/4\pi^2 D_a$ and determine D_a values from the standard plot $1/\tau_G$ *vs.* $1/\Lambda^2$ (Fig. 4.7). The contribution of recombination to the grating decay was negligible at two-photon excitation ($\tau_R >> \tau_D$, thus $\tau_G \approx \tau_D$), as evidenced by close to zero value of $1/\tau_G$ at large grating periods. The slopes of the curves in Fig. 4.7 indicated the high $D_a \approx$ 51 cm^2/s value at low excitations and its decrease to ~ 20 cm^2/s at moderate ones at room temperature.

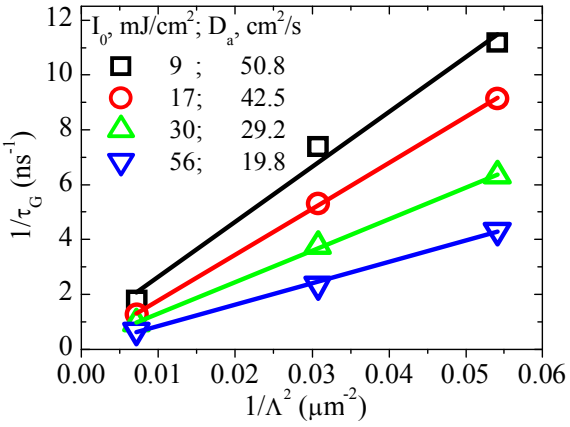

Fig. 4.7. Determination of ambipolar diffusion coefficient in CVD diamond C5 at two-photon carrier excitation. [P6]

The measured dependences of diffusion coefficient on excess carrier density at 300 K (Fig. 4.8a) provided a value of $D_a \approx$ 51 cm^2/s for the CVD layer at $\Delta N = 10^{15}$ cm^{-3} (~ 38 cm^2/s value was obtained for the HPHT sample due to higher doping). Strong decrease of D_a was observed with increase of excess carrier density, down to 6 - 10 cm^2/s at $\Delta N \approx 10^{18}$ cm^{-3}.

The room-temperature D_a value at the lowest excitations was found very close to the D_{ToF} = 55 cm^2/s value, based on ToF electron (2050 cm^2/Vs) and

hole (2250 cm^2/Vs) mobilities in a CVD layer [75], while the mechanisms of nearly tenfold decrease of diffusion coefficient at high excitation required more detailed analysis. Temperature dependence of D_a also confirmed density-dependent effect on ambipolar carrier mobility, especially on low-temperature wing (Fig. 4.8b), thus indicating possible contribution of carrier-carrier scattering, exciton formation and the bandgap renormalization.

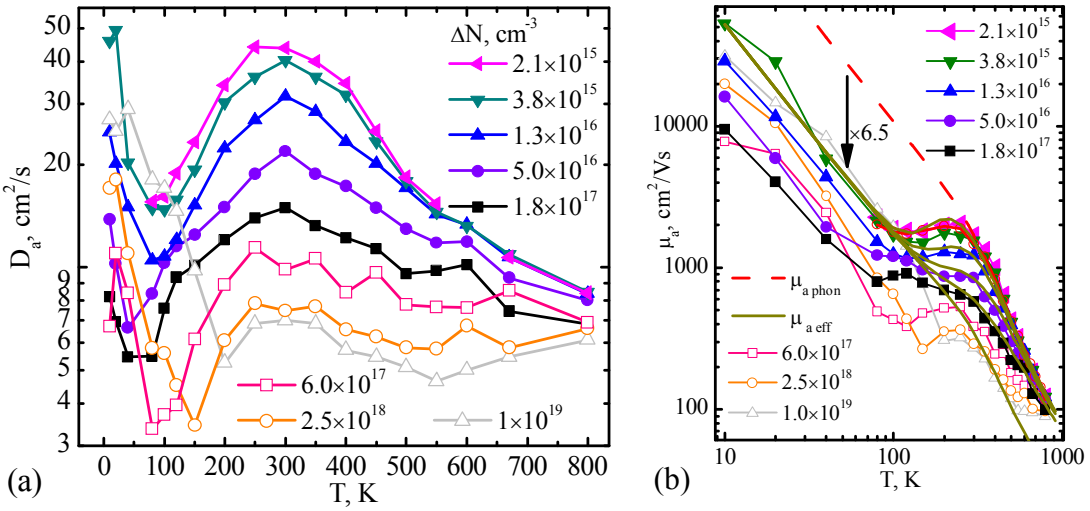

Fig. 4.8. Excitation and temperature dependences of diffusion coefficient (a) and mobility (b) in CVD layer (sample C4). In (b) ambipolar mobility fit ($\mu_{a\ phon}$) is shown by dashed line. Solid lines, showing effective mobility ($\mu_{a\ eff}$), were calculated using nonequilibrium carrier density dependent exciton concentration and 6.5 times lower exciton mobility than ambipolar one. [After P26,C26]

In order to fit the low excitation phonon mobility, carrier energy and temperature dependent scattering rates were used, taking into account for acoustic, and optical phonon scattering. The equations (1.16), (1.18) and parameters [84]: static dielectric constant $\varepsilon_s = 5.7$, density $\rho = 3.515$ g/cm^3, longitudinal speed velocity $v\| = 17.5$ km/s, optical phonon energy $\hbar\omega_0 = 165$ meV were used in the calculations. Acoustic deformation potential C_a = 4.95 eV, optical inter/intra-valley deformation potential D_{ii+jj} = 1.5×10^9 eV/cm were obtained by assuming electron/hole masses equal to m_0.

As diamond has very large exciton binding energy (80 meV), exciton formation at high excitations and low temperatures will provide not free carrier, but exciton diffusion coefficient. In Fig. 4.9 the calculated relative exciton density is shown. Exciton binding energy carrier density dependence was calculated using BGN coefficients of SiC [56], i.e. $E_{ex}(\Delta N) \approx 80 - 19\times2\times(\Delta N/10^{18}\ \mathrm{cm}^{-3})^{1/4}$ meV. It is observed, that at lowest temperatures ($T <$ 200 K) and at used excitations all carriers are bound to excitons (see Fig. 4.9), thus only exciton diffusion coefficient could be determined. At low temperatures acoustic phonon scattering prevails, thus excitons will be also subject to acoustic phonon scattering. Comparison of exciton and ambipolar free carrier mobility, $\mu_{a\ phon}$, (Fig. 4.8b) provided 6.5 times lower exciton mobility, $\mu_{a\ ex}$, value ($\mu_{a\ phon}$ was calculated using electron [25] and hole [86] drift mobilities; resultant mobility was divided by 1.2 factor). This peculiarity can be explained by higher exciton translational mass ($m_{tr}=m_e^*+m_h^*$) and thus more effective interaction with phonons as $\mu_{ac} \sim m_{tr}^{-5/2}$ (see Eqs. (1.16), (1.18)), leading to ~5.6 times lower exciton diffusion coefficient, if assuming $m_e^* \approx m_h^*$. The exciton model also accurately described the kink of mobility around ~120 K.

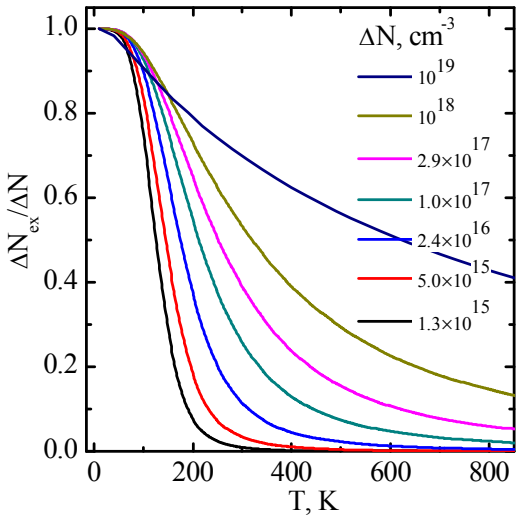

Fig. 4.9. Calculated relative exciton density temperature and carrier density dependences.

Average mobility calculations were performed at different excitations, using equation $\mu_{a\ eff}=1/[(\Delta N - \Delta N_{ex})/\Delta N/\mu_{a\ phon} + \Delta N_{ex}/\Delta N/\mu_{a\ ex}]$, where scattering rate additivity was used (see Fig. 4.8b). Further mobility decrease at even higher excitations and at $T <$ 300 K can be attributed to exciton-exciton scattering rate increase and formation of heavier biexcitons and electron-hole droplets (at 80 K $\mu \sim \Delta N^{-0.24}$ was found).

As electron and hole masses are very close, electron-hole scattering (EHS) impact should be rather weak [30]. Nevertheless, at highest excitations it can appear after Mott transition. Finally at the highest carrier densities, bandgap renormalization and degeneracy effects should appear. Due to huge variety of mentioned processes, their identification at high excitations is very complicated and unambiguous. Moreover, contribution of electron hole droplet formation below 173 K in ~10^{18}-10^{19} cm^{-3} excitation range [150] should be present. As droplets consist of few electron-hole pairs, their diffusion coefficient will be rather low and excitation independent. Indeed, that effect was observed – after ~300 ps delay after excitation. At such delays drops were formed and their diffusion coefficient was ~7 cm^2/s, while in the initial stage diffusion coefficient was ~6 times larger due to carrier plasma degeneracy (in confirmation to that, diffusion coefficient increase with carrier density as $\sim \Delta N^{2/3}$ was observed).

In polycrystalline diamond sample (C6), the grating decay was diffusion-governed on the growth side and recombination governed on the nucleation side of the undoped layer. Dependence of D_a on carrier density in the U-CVD is shown on Fig. 4.10. Excitation-dependent diffusion coefficient was observed: its gradual decrease up to 10^{19} cm^{-3} of excess carrier density and subsequent increase, similarly as in monocrystalline diamonds. Hence, the impact of structural and point defects is practically insignificant on the growth side. In contrary, the diffusion coefficient on the nucleation side was rather low and difficult to extract due to short carrier lifetimes (~100 ps). The low value can be explained

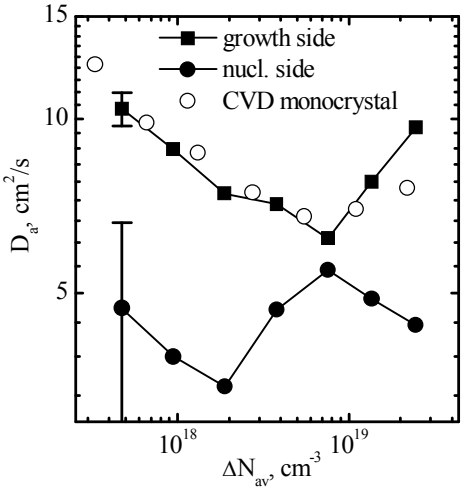

Fig. 4.10. Nonequilibrium carrier density dependences of ambipolar diffusion coefficient in the C6 sample on the growth and nucleation sides with large and small crystallite sizes, respectively. Open points are data for undoped CVD diamond (C5). [P27]

by additional scattering of carriers on grain boundaries [151] and more abundant defect density in crystallites.

4.4. Short summary

1. The light-induced transient grating technique was demonstrated as a powerful tool for determination of excitation-and temperature dependent carrier diffusion coefficient (ambipolar mobility) at single- and two-photon excitation conditions.
2. In undoped SiC, GaN, and diamond, temperature dependence of ambipolar mobility, $\mu(T) \sim T^{-(1.5\text{-}3)}$, at low excitations was governed by acoustic and optical phonon scattering, while in doped 4H-SiC, impurity scattering at low temperatures contributed, leading to saturation of hole mobility at 100 cm^2/Vs. At low excess carrier densities, transition from monopolar (D_h =0.8 cm^2/s) to bipolar (D_a =1.5 cm^2/s) regime allowed determination of the doping level in GaN, namely n_0 =8×10^{15} cm^{-3} and 2×10^{16} cm^{-3} in the used crystals.
3. Small anisotropy of hole and ambipolar diffusion coefficient (up to 17 %) was explained by the effective valence band parameters and opposite anisotropy of the light- and split-off hole masses.
4. At high (>10^{17} cm^{-3}) nonequilibrium carrier density many body effects, such as exciton, biexciton formation, electron-hole scattering, bandgap renormalization and degeneracy contributed to mobility value. These effects were strongest in diamond, weaker in SiC, and the weakest in GaN, leading to 7-fold, 2-fold and 1.1-fold reduction of the ambipolar diffusion coefficient with respect to the low excitation value at RT.
5. The drastic decrease of carrier diffusion coefficient from 50 cm^2/s to 7 cm^2/s in diamond with increase of carrier density from 10^{15} to 10^{18} cm^{-3} at 300 K was explained by 6.5 times lower exciton diffusion coefficient, due to twice larger exciton translational mass. Additional scattering on grain boundaries of micrometer size crystallites on the nucleation side of polycrystalline diamond resulted in D reduction up to two times.

5. Carrier dynamics in SiC, GaN and diamond at high photoexcitations

Carrier dynamics, or, in other words, their redistribution and annihilation after photoexcitation, is an important issue for material characterization and its suitability for device applications. SiC, GaN and diamond are prospective wide bandgap semiconductors, being very promising for high power, high temperature device applications. Therefore, their recombination features should be extensively studied in order to forward their application and quality improvement. The most important parameter of semicoductor material to be investigated is the carrier lifetime, with its carrier density and temperature dependences.

In this chapter, dependences of carrier recombination rate on temperature and carrier density are described. Nonequilibrium carrier in-depth redistribution due to their diffusion is considered using temperature and excitation dependent carrier diffusion coefficient from previous chapter. In section 5.1 carrier surface recombination impact is considered both analytically (a new formula for surface recombination lifetime was derived) and numerically. In sections 5.2, 5.3, 5.4, investigations of linear and nonlinear recombination rate in SiC, GaN and diamond are presented, respectively. In section 5.5, the ambipolar diffusion length is calculated using the determined carrier density and temperature dependent carrier recombination rate and diffusion coefficient. Carrier spatial lifetime distributions in structurally inhomogeneous GaN and polycrystal diamonds are provided in section 5.6. Finally, in section 5.7, the measurements of radiative recombination rate in 3C-SiC and GaN are described using spectrally- and time-resolved photoluminescence. The chapter ends with a short summary.

5.1. Surface recombination and modeling of carrier in-depth profiles

The effect of surface recombination on the carrier lifetime in wide-bandgap semiconductors is rather important since quite long carrier lifetimes can be

achieved in these materials. The surface contribution can be described by surface-limited or diffusion-limited recombination pathways [152], which are valid at stationary conditions, i.e. when the carrier density profile $\Delta N(z,t)$ in a layer of thickness d becomes independent of time (in this case, the partial derivative by z of the carrier density profile is time-independent: $\partial^2 \Delta N(z,t)/\partial z \partial t = 0$).

Upon reaching stationary conditions, the FCA decay kinetics becomes a single exponential. In this case, bulk and surface recombination govern the carrier decay with τ_{SRH} and τ_S lifetimes, respectively:

$$1/\tau = 1/\tau_{SRH} + 1/\tau_S, \qquad \tau_S = d_{eff}/2S + \left(d_{eff}/\pi\right)^2/D. \tag{5.1}$$

Sproul [152] has shown that the latter equation is valid for non-zero surface recombination on only one surface (S_1=0, S_2=S or S_2=0, S_1=S, with d_{eff} = 2d) or on both surfaces (S_1=S_2=S, then d_{eff} = d). Here, surface-limited or diffusion-limited recombination may take place, if the first term in Eq. (5.1) or the second one dominates, respectively. It was assumed that the stationary conditions are satisfied, and the generated carriers fill the entire layer thickness (see Fig. 5.1). Nevertheless, in most experimental cases the carriers are excited on the front side of an epilayer, and the subsequent carrier in-depth redistribution takes place. Therefore, Eq. (5.1) is not applicable until the carriers redistribute spatially and reach the stationary conditions. Moreover, excess carrier leakage from an epilayer to the substrate may take place upon

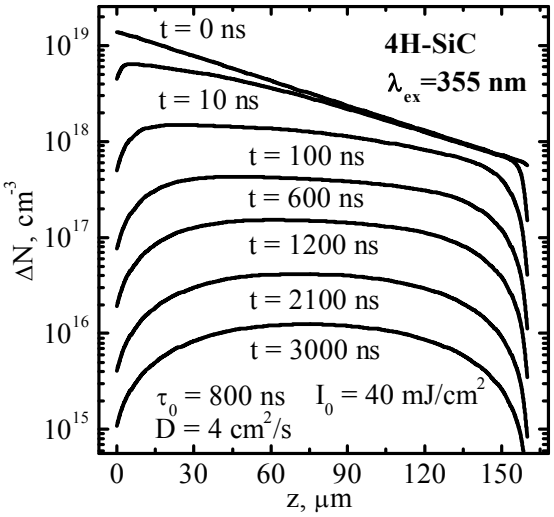

Fig. 5.1. Numerical simulation of carrier density profile evolution in 160 μm thick 4H-SiC epilayer at 355 nm excitation. For modeling, typical 4H-SiC parameters were used: $S_1 = 10^4$ cm/s, $S_2 = 4\times10^4$ cm/s, $B = 1.2\times10^{-12}$ cm^3/s, $C = 7\times10^{-31}$ cm^6/s [112] and τ_{SRH} = 800 ns [100]. [P1]

reaching the stationary conditions, as the SiC epitaxial structures are usually grown on heavily doped substrates with short carrier lifetimes. Escape of excess carriers from the epilayer to the substrate can be taken into account by taking a larger interface recombination velocity (IRV) value S_2 at the epilayer-substrate interface than the SRV at the front surface. Alas, carrier lifetimes cannot be modeled by Eq. (5.1) in the case of different S_1 and S_2 values. Latter drawback may be eliminated by using a newly modified relationship for τ_S evaluation.

The analytical approach is derived from Eq. (5.1) by dividing the stationary carrier profile of the layer of thickness d into two sublayers of thickness d_1 and d_2, which are treated as separate films (d_1 from $z_1 = 0$ to x_m and d_2 from $z_2 = x_m$ to d; here x_m is the position of the maximum in the carrier depth profile). Then the thicknesses of the sub-layers are $d_1=x_m$ and $d_2=d-x_m$, respectively. Setting the SRV to zero at the imaginary interface at $z=x_m$ and applying Eq. (5.1) to each sublayer ($d_{eff1} = 2d_1$ and $d_{eff2} = 2d_2$), the surface lifetimes τ_1 and τ_2 in the two sublayers were obtained, respectively. Due to profile stability at reaching the stationary conditions, there is only one common lifetime (carrier density at $z=x_m$ must be equal in both regions at any time: $\Delta N(z \to x_m - 0, t) = \Delta N(z \to x_m + 0, t)$, thus $\tau_1 = \tau_2$), therefore:

$$\tau_S = \tau_1 = \tau_2 = x_m / S_1 + (2x_m / \pi)^2 / D, \qquad x_m = \frac{\tau_D + \tau_{S2}}{\tau_{S1} + \tau_{S2} + 2\tau_{DL}} d. \qquad (5.2)$$

Here $\tau_{DL}=d^2/\pi^2 D$ is the diffusion limited surface recombination time (on both surfaces), $\tau_{S1}=d/4S_1$ and $\tau_{S2}=d/4S_2$ are the surface-limited surface recombination times on the front and back sides of the epilayer. The x_m position was calculated from the condition $\tau_1 = \tau_2$. This formula can be rewritten in a symmetrical form and provides 5 % accuracy (same as for Eq. (5.1)) with respect to more strict numerical modeling at stationary conditions:

$$\tau_S = (\tau_{DL} + \tau_{S1} + \tau_{S2})(\tau_{DL} + \tau_{S1})(\tau_{DL} + \tau_{S2}) / (\tau_{DL} + (\tau_{S1} + \tau_{S2})/2)^2. \qquad (5.3)$$

To calculate the surface recombination time τ_S for various epilayer thicknesses and different SRV values (Fig. 5.2) the modified relationship (5.3) was used. Three cases are given in the figure. The S_1=S_2 case corresponds to a similar quality of both surfaces (e.g. for quasi-bulk free-standing 3C layers); the case of S_2=10 cm/s stands for a negligible impact of the second interface (e.g. acting as a *p-n* junction); while the S_2=4×10^4 cm/s is the case of a huge impact of the second interface (e.g. for an epilayer grown on heavily doped substrate). At low values of S_1 and $S_2 < S_1$, the surface lifetime τ_S in a thin layer is inversely proportional to S_1 and corresponds to the surface-limited recombination case, while at high S_1 values the diffusion-limited case takes place and leads to τ_S independent of S.

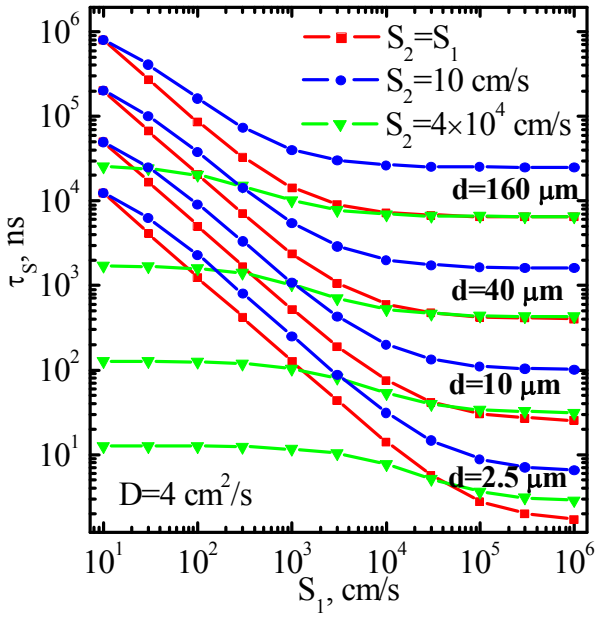

Fig. 5.2. The calculated surface recombination time for different epilayer thicknesses and varying S_1 and S_2. The dashed line is guide to the eye for separating the surface-limited surface recombination ($\tau_S \sim 1/S_1$) from diffusion-limited surface recombination ($\tau_S \approx$ const). [P1]

Using typical values: $S_1 = 10^4$ cm/s and $S_2 = 4\times10^4$ cm/s [112], the surface recombination times of 10-100 ns for thin 4H layers (2.5-10 μm) were obtained. For the thicker layers used in this study (40-160 μm), the diffusion limited surface recombination provides surface lifetimes τ_S from 400 to 7000 ns. This result leads to an important conclusion that bulk carrier lifetimes of microsecond duration in SiC (or diamond) can be accurately determined only for the ≥100 μm thick layers, since only for thick enough layers the condition $\tau_S > \tau_R$ is satisfied. Therefore, in this work very thick layers were used for investigation of carrier recombination rate.

As noted above, the analytical relationships (5.1) and (5.3) are not applicable for the analysis of the carrier depth redistribution after short pulse excitation. Calculations show, that carrier profile stabilization occurs only at times, t > 2000 ns. Therefore, time-dependent carrier depth profiles for the epitaxial layers must be calculated numerically by using Eq. (1.34) at picosecond pulse excitation and varying the carrier generation conditions (excitation wavelength, energy fluence, and layer thicknesses).

5.2. Excitation and temperature dependent carrier lifetime in SiC

FCA decay kinetics in the 4H1 epilayer were measured in a range of excess carrier density from 10^{16} up to 5×10^{19} cm^{-3}. Therefore, the condition for a bipolar plasma was satisfied ($\Delta N_0 >> n_0$). Carrier excitation in ~30 μm depth of the 160 μm thick epilayer resulted in their nonhomogeneous in-depth profile; therefore a numerical modeling of temporal and spatial carrier dynamics with boundary conditions was required. By solving a balance equation (1.34), excess carrier profiles $\Delta N(z,t)$ in the epitaxial layer was calculated, taking into account the temperature and excitation dependent ambipolar diffusion coefficient $D_a(T,\Delta N)$ and various recombination mechanisms, both linear and nonlinear. In the boundary conditions at the epilayer front surface and at the epilayer-substrate interface (Eq. (1.34)) the surface recombination velocity, S, was a fitting paramter, while the interface recombination velocity was fixed at S_{inter} ~4×10^4 cm/s [112]. In calculations τ_{SRH} was the nonradiative trap-related Shockley-Read-Hall (SRH) lifetime, $\tau_{SRH} = \tau_h + \tau_e$ (when $\Delta N >> N_{trap}$ ~10^{13} cm^{-3} in the layer [100]), τ_h and τ_e are the corresponding hole and electron lifetimes.

In Fig. 5.3a the calculated evolution of carrier density profile at T =700 K is plotted (similar calculations were performed for all temperatures). At the initial stage of decay, the nonlinear and surface recombination reduce the carrier density at the front surface, while the diffusion after few microseconds brings them up to the substrate, where their lifetime is much shorter. The latter

was confirmed by direct measurement of carrier lifetime in the substrate, using excitation from the backside (in this case the carriers do not reach the epilayer because of their rather short diffusion length). A stationary carrier profile evolves at ~15 μs, and its subsequent decay is determined by the bulk and surface recombination.

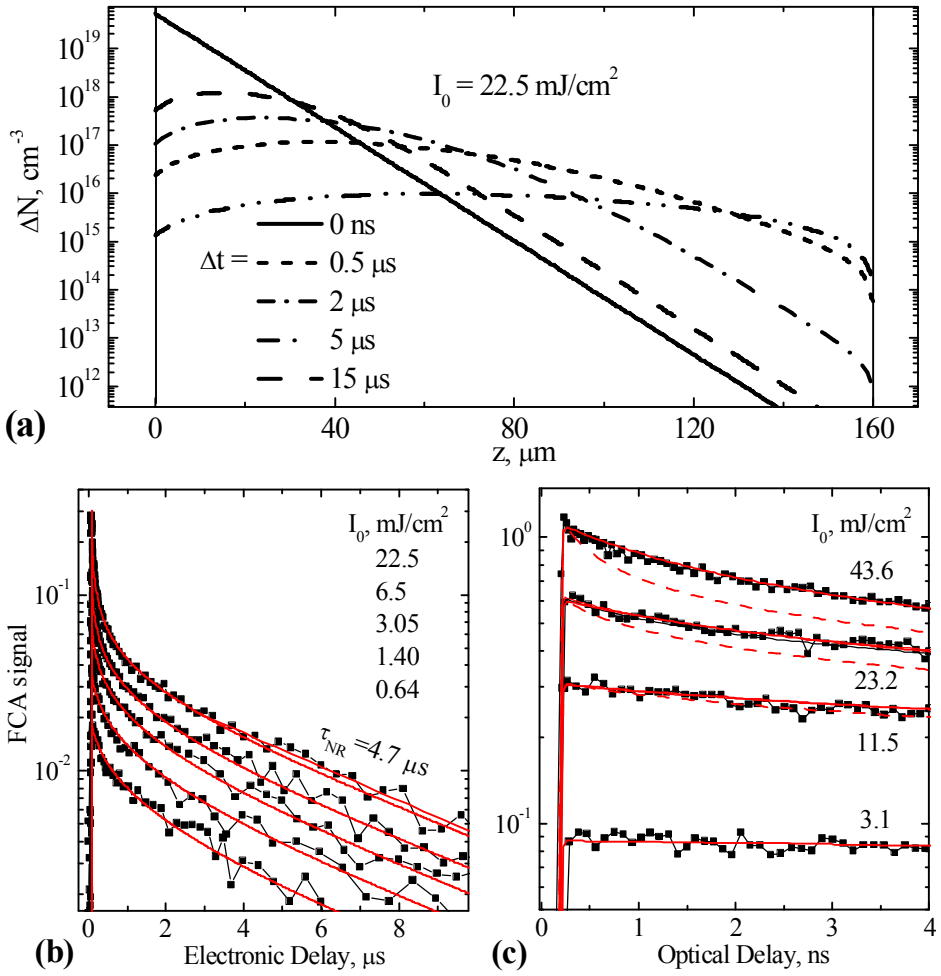

Fig. 5.3. Evolution of excess carrier density profile at 700 K in 4H-SiC (a). The slow (b) and fast (c) transients of FCA decay in the epilayer at 700 K for different excitation fluences I_0. The solid curves are the numerical fits with excitation dependent Auger coefficient C, while the dashed curves in (c) correspond to unscreened Auger coefficient value, C_0. [P24]

The experimental kinetics of FCA decay kinetics in the 4H1 epilayer at various excitation energy densities I_0 are presented in Fig. 5.3b,c. The low excitation kinetics (Fig. 5.3b) were fitted by using S =(3±1)×10^3 cm/s and τ_{SRH} =6700 ns in the bulk. The surface recombination rate in the epilayer was found

to be temperature independent, what means that the capture cross section of the surface traps does not change significantly with temperature. At higher carrier densities, contribution of nonlinear Auger recombination leads to fast transients of few ns duration (Fig. 5.3c).

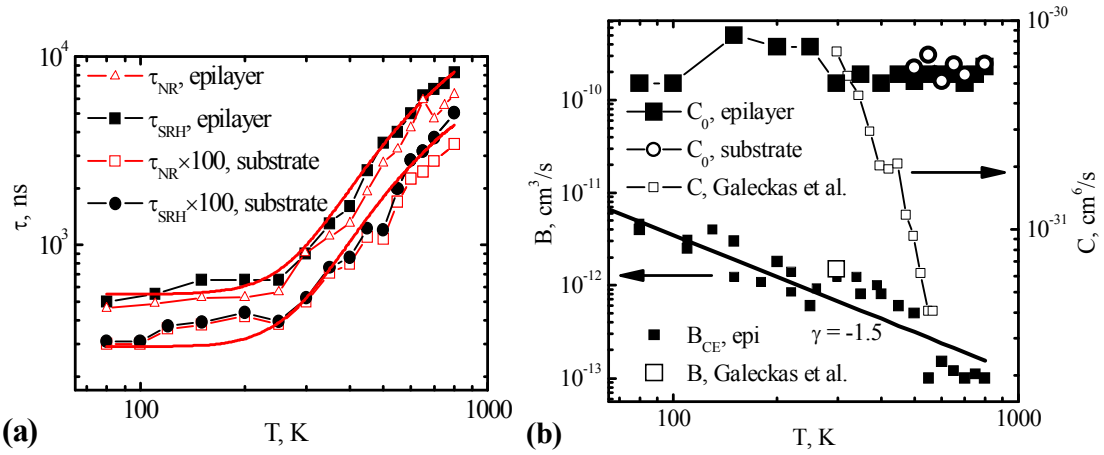

Fig. 5.4. (a) Temperature dependence of exponential decay tail nonradiative (τ_{NR}) and bulk defect related (τ_{SRH}) recombination times at low excitation level (ΔN_0 ~10^{17} cm^{-3}) and (b) temperature dependences of Auger coefficient (unscreened value of C_0 with its Coulomb enhancement factor $B_{CE} \sim T^{-\gamma}$). Open squares in (b) show $C(T)$ dependence and B value at 300K according to Ref. [112]. [P24]

The low-excitation lifetimes (τ_{NR} is determined from the exponential decay tails, while τ_{SRH} accounts only for impact of bulk traps as determined by modeling) both in the epilayer and substrate increase with temperature (Fig. 5.4a), thus confirming the dominant role of $Z_{1/2}$ defect, related to carbon vacancies [66,100]. The defect-related lifetime τ_{SRH} in the substrate was almost carrier density independent, indicating that $\tau_e << \tau_h$ and leading to approximation $\tau_{SRH} \sim \tau_h$ (as $\Delta N << n_0$). In addition, the substrate doping (n_0) leads to Auger lifetime τ_A ~110 ns (as calculated from relationship $1/\tau_A \sim C_{subs} n_0^2$, where C_{subs} =5×10^{-31} cm^6/s [112]). Therefore the determined nonradiative lifetime, $1/\tau_{NR} = 1/\tau_{SRH} + 1/\tau_{AUG}$, was used to analyze the temperature-dependent defect-related SRH lifetime, $\tau_{SRH}(T)$, in the substrate. The latter dependence (open squares in Fig. 5.3a) was found identical to one in the epilayer. Consequently, ~190 times lower SRH lifetime in the substrate than in the epilayer (Fig. 5.4a) clearly indicates that the hole recombination

rate both in the layer and in the substrate is governed by the same defects (therefore, in the substrate N_{trap} ~2×10^{15} cm^{-3} was evaluated).

Finally, the lifetime was fitted with a simplified formula: $\tau_{SRH} = \tau_0\times[1+100/\{1+\exp(E_{a\tau}/k_BT)\}]$ with $E_{a\tau}$ =125 meV activation energy, where τ_0=550 ns and τ_0=2.9 ns are the defect-related lifetimes in the layer and substrate, respectively. The $E_{a\tau}$ energy reflects the thermal emission of electrons from $Z_{1/2}$ defect and reduction of the recombination rate at higher temperatures.

The excitation dependence of Auger coefficient was derived from the variation of the nonlinear carrier recombination rate with excitation, as obtained from modeling by equation (1.34). At relatively low excitations (<5×10^{18} cm^{-3}), the Auger recombination follows a trend of a nonradiative bimolecular recombination with a Coulomb (excitonic) enhancement coefficient (B_{CE}) [65]. At high excitations (>10^{19} cm^{-3}) the Auger recombination coefficient decreased, what was attributed to screening of the carrier-phonon interaction by free carriers [30]. Therefore the resultant formula for the Auger coefficient is as follows:

$$C(T,\Delta N) = \left(C_0 + B_{CE}(T)/\Delta N\right)/\left(1+\Delta N/\left(a_{SC}\times T\right)\right)^2. \qquad (5.4)$$

Here C_0=(5±1)$\times10^{-31}$ cm^6/s is the temperature-independent unscreened phonon-assisted Auger recombination coefficient [72], $B_{CE}(T)$ =$3.5\times10^{-9}/T^{1.5}$ cm^3/s is the Coulomb enhancement coefficient of the Auger recombination, a_{SC} =7.8×10^{16} cm^{-3}/K is the screening parameter ($a_{SC}=\varepsilon_0\varepsilon_r k_B K_{ph}/e^2$ [30], where ε_0, ε_r=10, k_B, e are the static dielectric, relative dielectric, Boltzmann constants and elementary charge, respectively; K_{ph}=1.3 nm^{-1} is the obtained phonon wavevector). Coulomb-enhancement decreases with temperature as $T^{-1.5}$, following the temperature dependence of the density of exciton states [65]. Similar reduction of Coulomb enhancement was observed in silicon [65]. The temperature dependences of B_{CE} and C_0 coefficients are presented in Fig. 5.4b. These coefficients at 300 K coincide rather well with data of Galeckas et al. [112], while they reported a very strong decrease of C_0 with temperature. The

obtained data pointed out to almost temperature independent C_0. This discrepancy is probably caused by the strongly increasing with temperature carrier density and its varying in-depth profile, what was not taken into account in Ref. [112] because of limited temporal resolution used. Moreover, a strong reduction of the Auger coefficient with temperature in [112] was attributed to a direct phononless Auger recombination process, having a temperature dependent threshold. Present measurements indicate that only in the 100-250 K range (see C_0 peak in Fig. 5.4b) the direct Auger process may have a small impact, while phonon assisted processes are dominant due to C_0 temperature independence.

A possible transition scheme for direct and phonon-assisted Auger processes is shown in Fig. 5.5. A direct process requires precise carrier wavector matching, thus is less probable than the phonon-assisted process, when carrier wavectors (K) and phonon wavector (K_{PH}) are superimposed.

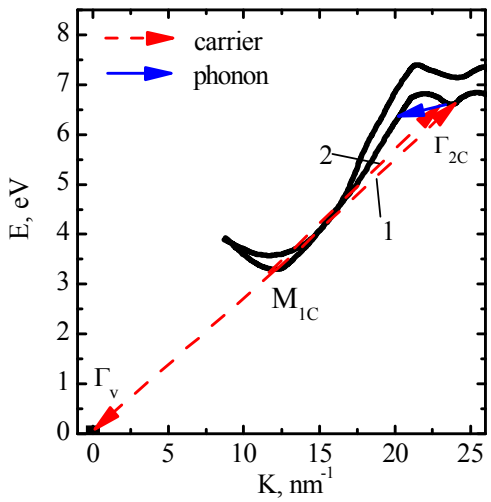

Fig. 5.5. A scheme of phononless (1) and phonon-assisted (2) Auger processes in 4H-SiC. The band structure scheme from Ref. [112] was modified assuming more strong impact of phonon-assisted transitions. [P24]

On the other hand, 3C-SiC exhibited much shorter lifetime due to lower quality and higher defect density. Also strong lifetime inhomogenity was observed. Using the $D(\Delta N)$ fits and I_0 values, the DT and DR decays were numerically fitted by equations (1.34) in order to obtain the τ_{SRH}, S, B, and C values. For this purpose all the measured decays were combined: optical delay DR and DT and electrical delay DT decays (the latter provided large τ_{SRH} values, Fig. 5.7). The resultant numerical fits are provided in the figures 5.6 and 5.7 by solid lines. From these fits the bulk lifetimes τ_{SRH} ~180 ns and ~60 ns were determined on the layer polished and as-grown sides, respectively, while the surface recombination velocities

were $S = (4\pm1)\times10^4$ and $(4\pm1)\times10^3$ cm/s. The determined $B <\sim10^{-13}$ cm^3/s was very small and did not affect the modeled decay within the experimental error bar. The same Auger coefficient, $C=(4\pm1)\times10^{-32}$ cm^6/s, was determined on both sample sides, using either DT or DR technique. The determined Auger and bimolecular coefficients are by order magnitude lower than in 4H-SiC [112], indicating that 3C-SiC is more suitable for devices working at high injections.

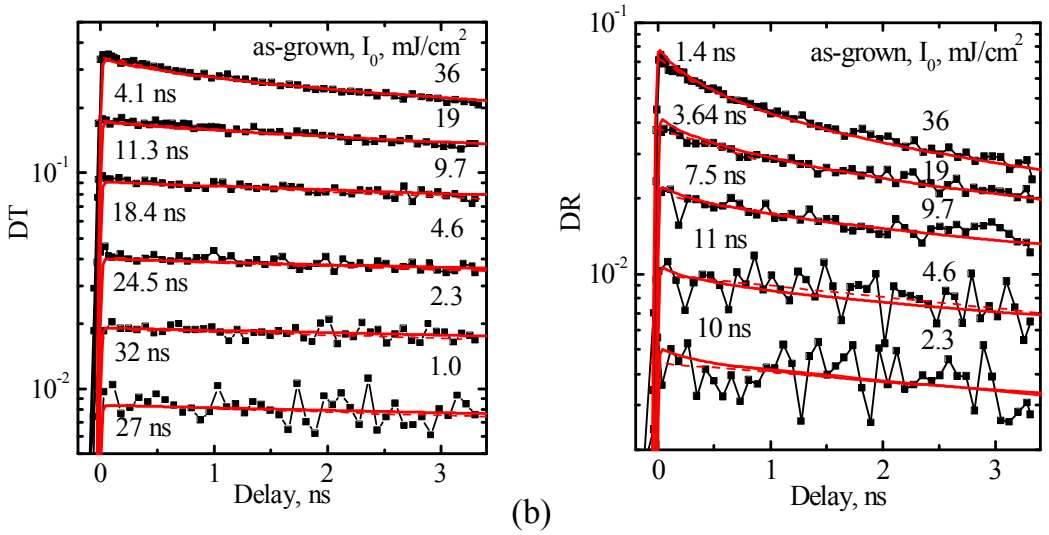

Fig. 5.6. Excitation dependent fast decay transients on as-grown side of 3C1 sample, measured by DT (a) and DR (b) techniques. Relevant initial lifetimes and excitation fluences, I_0, are provided. [P28]

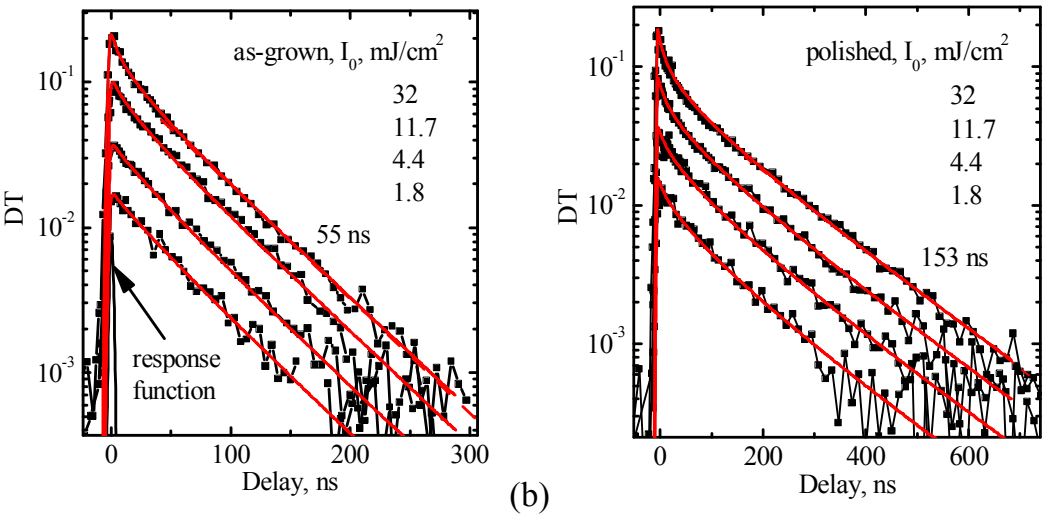

Fig. 5.7. Excitation dependent slow DT decay components on as-grown (a) and on polished (b) sides of 3C1 sample. [P28]

The surface recombination velocity in 3C-SiC was 10 times smaller on the as-grown face in comparison to the polished surface due to polishing

induced defects. Moreover, three times smaller τ_{SRH} value on the as-grown side reveals higher defect concentration in the strained near surface region. This pecularity indicates that the strain on the as-grown side possibly induces the increase of the nonradiative recombination center concentration (nonradiative centers are probably carbon vacancies [66]). Lifetime reduction with strain increase recently was also observed by microwave photoconductivity in similar sample [153].

Lifetime temperature dependences were nearly the same (see Fig. 5.8) in different 3C-SiC layers, indicating presence of the same recombination defect but with different density.

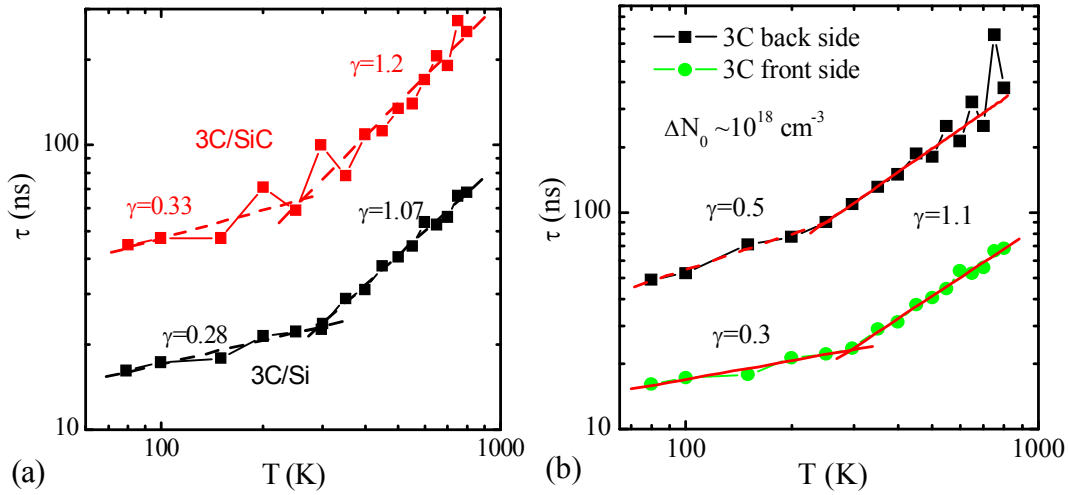

Fig. 5.8. (a) Temperature dependences of carrier lifetime in 3C/Si (sample 3C2) and 3C/SiC (sample 3C3) layers in 80-800 K range. γ are the slope indices of the linear fits to the curves in the log-log plot. (b) Temperature dependences of carrier lifetimes, τ, on the front and back sides of the 3C2 sample, measured by the time-resolved DT technique. [P5,P7]

5.3. Excitation and temperature dependent carrier lifetime in GaN

Carrier lifetimes in different thickness GaN layers and bulk samples are presented in this section. Firstly, relatively thin layers (GaN1-5) are analyzed at interband excitation conditions, while 200 μm-thick c-GaN (GaN6) and 450 μm-thick m-GaN (GaN7) are investigated at two photon carrier generation. Explanations of lifetime increase with layer thickness are provided.

In Fig. 5.9 the FCA decay kinetics are presented, from which the carrier lifetimes, τ_R, in the thinnest and thickest GaN layers were determined. The

carrier lifetime consists of radiative τ_{rad} and nonradiative τ_{nonr} components: $1/\tau_R = 1/\tau_{rad} + 1/\tau_{nonr}$. A contribution of radiative lifetime $\tau_{rad}(T, \Delta N) = (B_{rad}(T)\,\Delta N)^{-1}$ (where $B_{rad}(T) = 2\times10^{-11}\times(\mathrm{T}/300\ \mathrm{K})^{-1.5}$ cm^3/s is the bimolecular recombination coefficient according [93]) to the measured τ_R value can be evaluated by modeling the temporal carrier in-depth distribution, governed by the carrier diffusion to the depth. The modeling showed that the exponential tails of the FCA decay (see Fig. 5.9) provide the $\tau_R \approx \tau_{nonr}$ values, as carrier density substantially decreases with time to validate condition $\tau_{nonr} << \tau_{rad}$ (i.e. ΔN drops to 5×10^{18} cm^{-3} for probe beam delay time t above 0.8 ns (Fig. 5.9a) and to 1×10^{17} cm^{-3} for t = 60 ns (Fig. 5.9b), leading to corresponding τ_{rad} values of 10 ns and 500 ns at RT). Similar evaluation of τ_{rad} by $\Delta N(z,t)$ modeling was performed at different temperatures for experimental conditions and allowed to attribute the measured τ_R values (Fig. 5.9) to the nonradiative origin, $\tau_R \approx \tau_{nonr}$, in all 80 – 800 K range. It is worth noting that presence of the initial nonexponential FCA transients (Fig. 5.9a,b) indicated impact of radiative and surface recombination after generation in the surface layer.

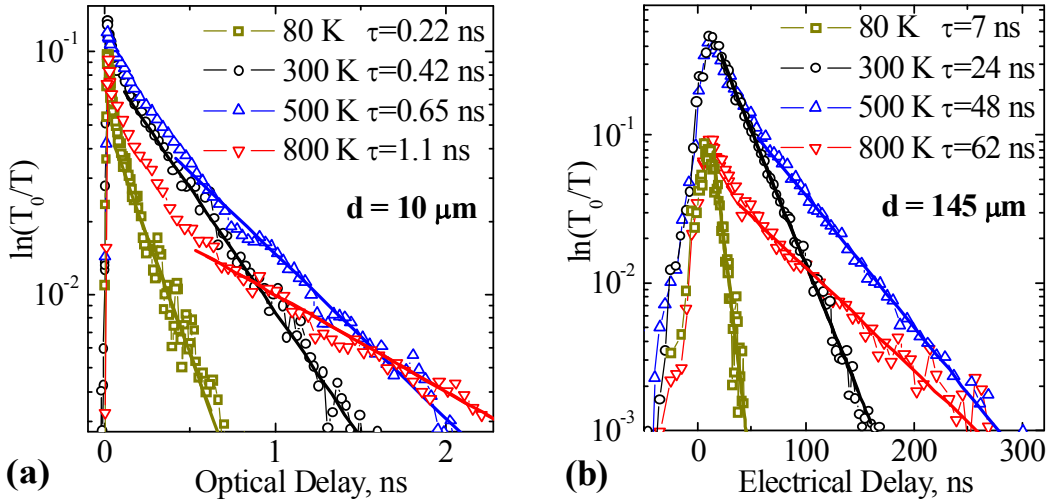

Fig. 5.9. Fast and slow FCA decay components for different thickness HVPE GaN layers (GaN1-5) at various temperatures: d =10 μm (a) and d =145 μm (b). Excitation fluence was ~2 mJ/cm^2 (a) and ~20 mJ/cm^2 (b). [P9]

The temperature dependences of nonradiative carrier lifetime, $\tau_{nonr}(T)$, measured in three GaN layers of different thickness (thus, at different TD

density) revealed monotonous increase of lifetime with increasing temperature in 80-800 K range (Fig. 5.10a). High excitation conditions ($\Delta N > 10^{18}$ cm^{-3}) and high temperatures (up to 800 K) used in the experiments excluded the noticeable contribution of excitonic recombination.

The anticorrelation between the $\tau_{nonr}(T)$ and $D_a(T)$ dependences (Fig. 5.10a,b) resembles a case of diffusion-limited surface recombination in bulk semiconductors. In such a case, the diffusive carrier flow to the surface defects determines the surface lifetime τ_S that is inversely dependent on diffusion coefficient, $\tau_S \propto d^2/D_a$. The presence of electrically active extended and point defects at the grain boundaries of hexagon columns of GaN layers grown on c-plane sapphire [151] must be taken into account, and in particularly the impact of threading dislocations (TDs). Thus the diffusive flow of carriers to the grain boundaries may lead to interface recombination at dislocations or point defects.

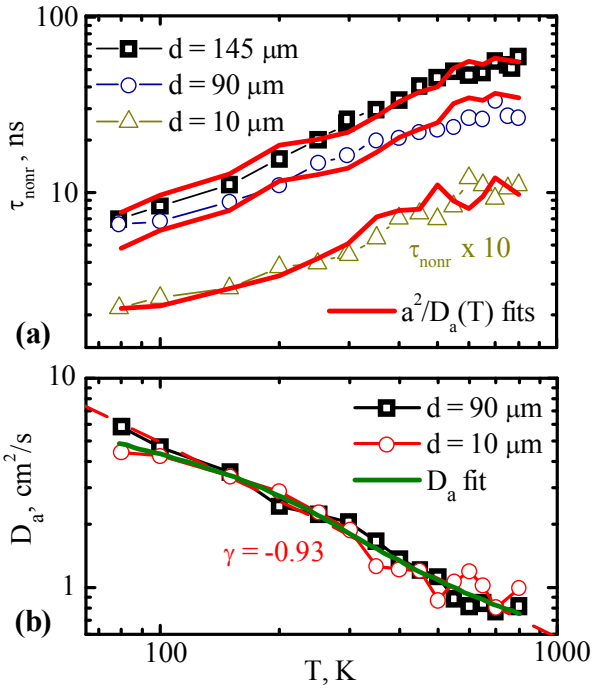

Fig. 5.10. Temperature dependences of nonradiative lifetime (a) and ambipolar diffusion coefficient (b) for different thickness GaN layers. The dashed curve in (b) is a fit by a power function $D_a \sim T^{\gamma}$. [P9]

In order to calculate the carrier diffusion governed nonradiative recombination time, a balance equation in cylindrical coordinates (ρ, z) was solved. The hexagon columns were assumed to be cylinders to simplify the calculations:

$$\frac{\partial \Delta N(\rho,t)}{\partial t} = D_a \frac{1}{\rho}\frac{\partial}{\partial \rho}\left(\rho \frac{\partial \Delta N(\rho,t)}{\partial \rho}\right). \qquad (5.5)$$

Here, the boundary conditions are defined in the hexagon center and its interface, $\partial\Delta N(0,t)/\partial\rho = 0$; $\partial\Delta N(r_{cyl},t)/\partial\rho = -\Delta N(r_{cyl},t)S_{inter}/D_a$, respectively (see inset in Fig. 5.11), and S_{inter} is the interface recombination rate on the cylinder boundary. A numerical solution of this equation provided the interface recombination time analytical approximation (with 5 % precision), τ_{nonr}, for different values of S and grain radii r_{cyl}:

$$\tau_{nonr} = \pi^{-3/2} r_{cyl}^{\,2} / D_a + \pi^{-1/2} r_{cyl} / S_{inter}\,. \qquad (5.6)$$

Eq. (5.6) describes diffusion-limited (the first term) and interface-limited (the second term) recombination times, respectively. Thus, at relatively large r_{cyl} values, the first term in Eq. (5.6) determines the nonradiative lifetime value, being inversely proportional to the diffusion coefficient D_a (as it was observed experimentally, see Fig. 5.10). Using Eq. (5.6), the measured temperature dependences of nonradiative decay times were fitted by function $\tau_{nonr}(T) = a^2/D_a(T)$ in Fig. 5.10a (a=6.71, 5.29 and 0.98 cm for 145, 90 and 10 μm layers, respectively). The lifetime increase with layer thickness was described by $\tau_{nonr} \sim d^{1.54}$ dependence.

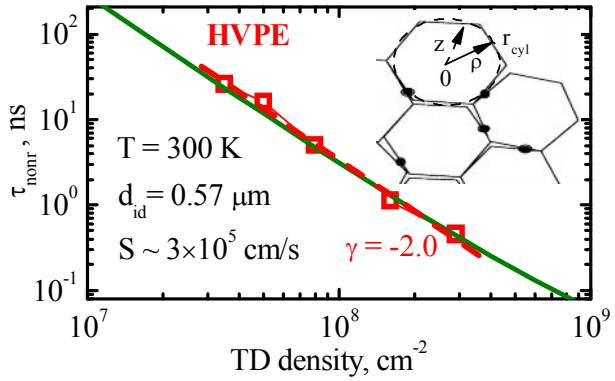

Fig. 5.11. Dependence of nonradiative carrier lifetime on screw TD density in HVPE layers: points - experimental data, line - calculations according to Eq. (5.6). The dashed line is a power fit of the data, $\tau_{nonr} \sim N_{TD}^{\gamma}$. The inset shows the domain structure used for modeling [151] (dots indicate TDs). [P9]

Grain boundary length per surface area is $L_{GL} = (\pi r_{cyl})/(\pi r_{cyl}^{\,2}) = 1/r_{cyl}$ [cm^{-1}] (having in mind that each boundary belongs to two grains) and the average distance between neighboring dislocations on the boundary is $d_{id} = L_{GL}/N_{TD}$. Therefore $r_{cyl} = 1/(N_{TD} d_{id})$ and the Eq. (5.6) for diffusion limited case describes the impact of dislocation density to nonradiative lifetime:

$$\tau_{nonr} = \pi^{-3/2} / \left(N_{TD}^2 d_{id}^2 D_a \right). \quad (5.7)$$

The experimentally measured lifetime dependence on TD density (Fig. 5.11) confirmed the expected $\tau_{nonr} \sim 1/N_{TD}^2$ tendency (Eq. (5.7)). The latter equation provided cylinder radii in the studied layers varying from 0.6 to 5.6 μm for the 10 and 145 μm thick layers. In this way, the model of carrier diffusion governed flow to grain boundaries explained both the inverse correlation between the nonradiative lifetime and diffusion coefficient, as well as the quadratic lifetime decrease with TD density. The influence of S_{inter} was observed to have a minor impact in this case (S_{inter} ~3×10^5 cm/s value was assumed). Decrease of TD density with layer thickness was observed (Fig. 5.12), similarly as in other works.

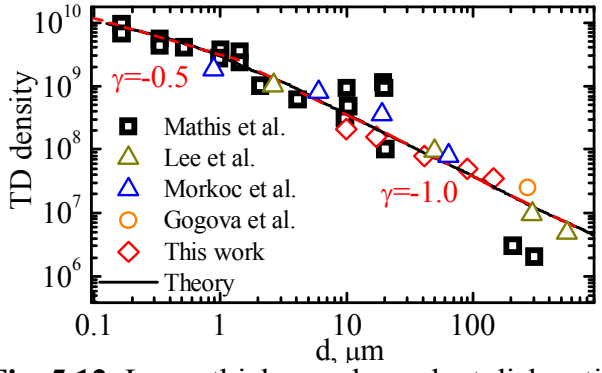

Fig. 5.12. Layer thickness dependent dislocation density in HVPE grown GaN layers. Data from this work are compared with those from different sources [154-157]. [P9]

Under two photon excitation of thick GaN6 sample the FCA decay exhibited single exponential kinetics in the 80-800 K range and led to carrier lifetime τ_R variation from ~10 to 120 ns with temperature (Fig. 5.13). The dislocation density was very low (chemical etching and pit density analysis of similar samples provided N_{TD} =5×10^5 cm^{-2} on the Ga face [125]). The lifetime was found to be independent of the excess carrier density in the range $\Delta N = 3\times10^{16} - 5\times10^{17}$ cm^{-3} achieved at 2P excitation conditions. The contribution of radiative recombination to the total carrier lifetime $1/\tau_R = 1/\tau_{rad} + 1/\tau_{nonr}$, where τ_{rad} and τ_{nonr} are the radiative and nonradiative lifetimes, respectively, was also estimated to be minor. The estimation of diffusion-limited surface recombination for the studied 200 μm-thick c-GaN layer provided value $\tau_S \approx 100$ μs at RT, which is far from the experimental value of ~30 ns (D_a = 1.6 cm^2/s value was used for this estimation according to Eq. (5.1)). Thus, surface impact can be neglected.

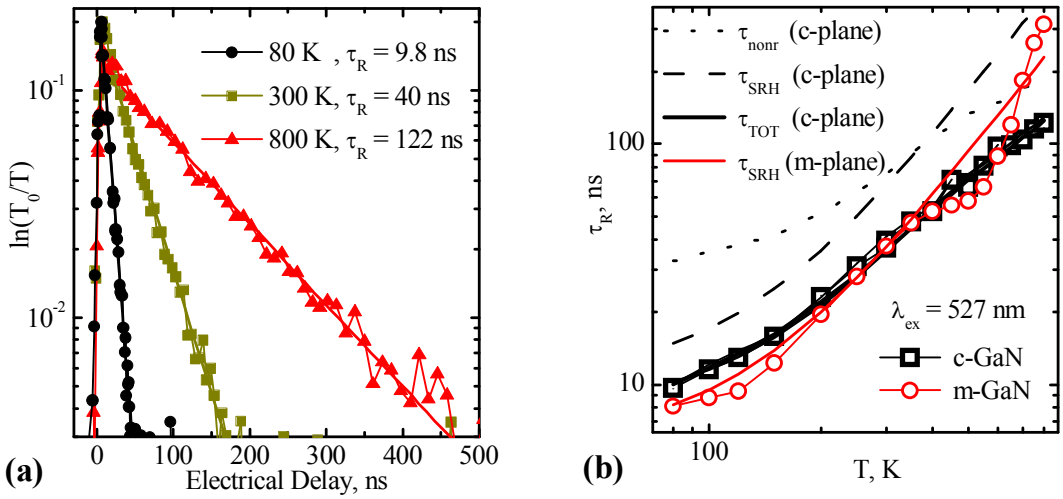

Fig. 5.13. DT kinetics at two-photon carrier excitation in a bulk c-plane GaN sample (a) and comparison of bipolar lifetime temperature dependences in c- and m-GaN. [After P13,P17]

Therefore, recombination on the internal boundaries of GaN hexagonal grains and on deep SRH traps must be considered. The resultant recombination time τ_{TOT}, can be described by a relation $\tau_{TOT}^{-1}=\tau_{SRH}^{-1}+\tau_{nonr}^{-1}$, where τ_{SRH} is the recombination time on point defects, while $\tau_{nonr}=\tau_{inter}+\tau_{diff}=\pi^{-1/2}r_c/S_{inter}+\pi^{-3/2}r_c^2/D_a$ (see Eq. (5.6)). The m-GaN sample contained similar dislocation density (N_{TD} =4×10^5 cm^{-2}) and had similar lifetime (~40 ns at RT), but with steeper temperature dependence (Fig. 5.13b). This may be and indication of much lower S_{inter} value or more probably that the lifetime is determined only by bulk traps. The decays at 355 nm excitation (see Fig. 5.14) provided even higher 60 ns bulk lifetime, influenced only by surface recombination with S =(5±1)×10^3 cm/s. Excitation increase diminishes S influence due to bleaching (see section 3.3) as it is shown by modeled decays in Fig. 5.15. Furthermore, lifetime decrease to ~45 ns was observed in the decay tails (Fig. 5.14b). This is an indication of lifetime transition from bipolar to monopolar regime (see Eq. (1.29)). Indeed, the TPA decay tails also exhibited this effect, with two-fold lifetime reduction in minority carrier (hole) regime. Corresponding carrier density profiles indicate that this occurs at 200 ns delay after 10 mJ/cm^2 photoexcitation when carrier density drops to the doping level of 2×10^{16} cm^{-3}

(see Fig. 5.15). Note that if lifetime was diffusion limited, then it should increase at low carrier densities due to diffusion coefficient decrease.

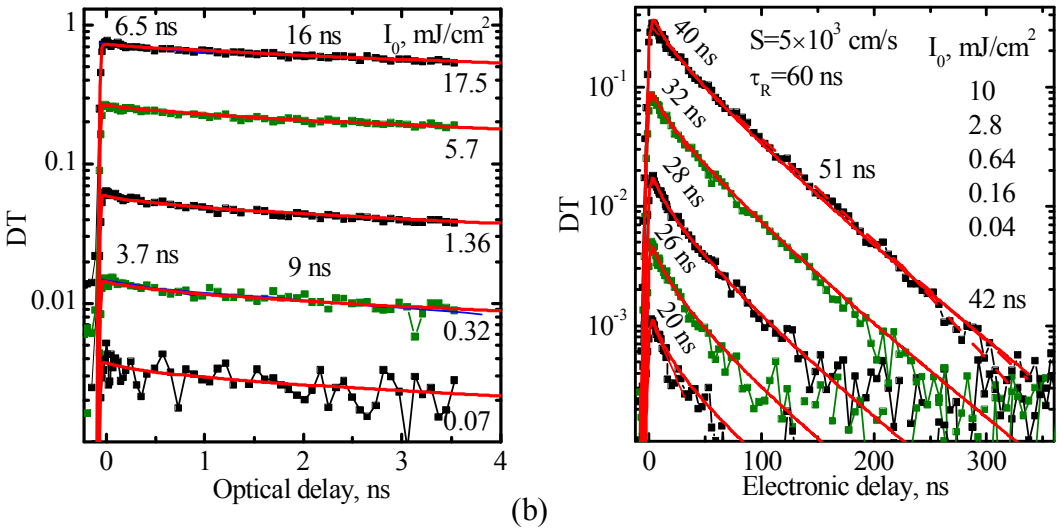

(a) (b)

Fig. 5.14. Fast (a) and slow (b) FCA decay components in m-GaN. Solid curves are numerical fits, obtained using S =(5±1)×10^3 cm/s and τ_R =60±5 ns.

The SRH lifetime temperature dependence in m-GaN (Fig. 5.13b) was fitted with an approximate relation: τ_{SRH}(m-GaN) =(3.5×10^{-4}×T^2 +6) ns. The fit in c-GaN was obtained using average grain size r_c = 7.5 μm, an effective interface recombination velocity of S_{inter} = 4×10^4 cm/s at RT (see section 5.6) and τ_{SRH}(c-GaN) =1.8×τ_{SRH}(m-GaN). The S_{inter} ~$\sigma_c v_{th} N_{tr}$ ~ $T^{-3/2}$ dependence was used, where capture of carriers by charged defects with their cross section strongly dependent on temperature was assumed; σ_c ~T^{-2} [30] was employed, v_{th} ~$T^{1/2}$ is the carrier thermal velocity and N_{tr} is the interface trap density. Lower τ_{SRH} in m-GaN indicates almost two times higher deep trap density than in c-GaN (doping is also ~2 times larger). Such effect of larger point defect density is typical for m-plane GaN [158]. The m-plane sample exhibited strong

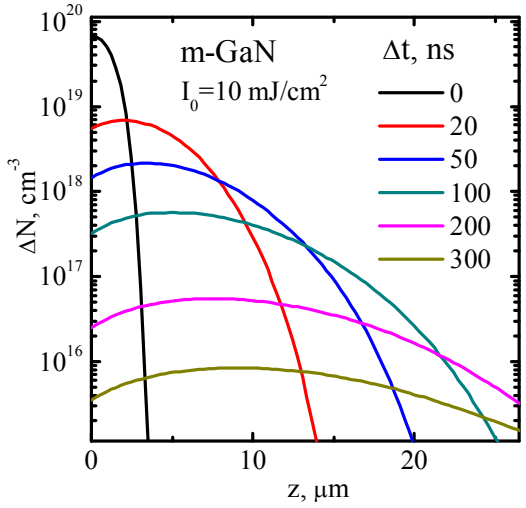

Fig. 5.15. The simulated carrier in-depth profiles in m-GaN.

lifetime variations (in 30-50 ns range) due to inhomogeneous trap distribution, and this led to not so "smooth" $\tau_R(T)$ dependence in Fig. 5.13b. More detail carrier recombination studies on grain boundaries are provided in section 5.6.

5.4. Excitation and temperature dependent carrier lifetime in diamond

In this section carrier recombination in diamond is investigated. Fitting of carrier density decays at two-photon and interband excitations provided insight into the origin of defect-governed and intrinsic recombination rates.

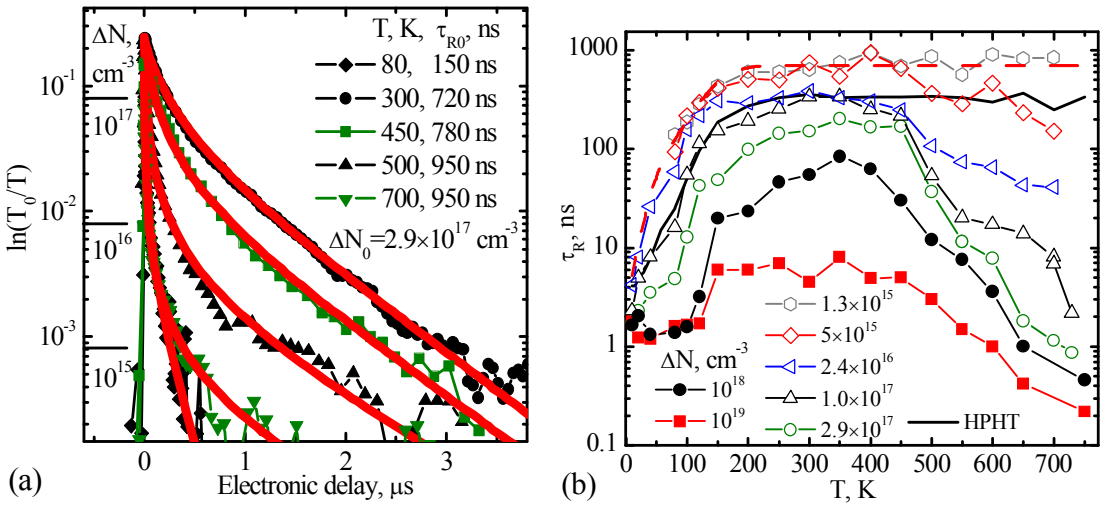

Fig. 5.16. FCA decay kinetics at various temperatures in C4 CVD diamond (a) and the measured temperature dependences of carrier lifetimes at different excitation levels, ΔN (b). In comparison, the results obtained at $\Delta N = 2\times10^{15}$ cm^{-3} on the low nitrogen content HPHT sample C1 are shown. The dashed line in (b) shows effective τ_{eff} carrier-exciton lifetime. [After P26,C26]

FCA decay kinetics at different temperatures under TPA excitation (Fig. 5.16a) were approximated by a function

$$\Delta N(t) = \Delta N_0/[\exp(t/\tau_{R0}) + B_{nonr}\Delta N_0 \tau_{R0}(\exp(t/\tau_{R0}) - 1)], \qquad (5.8)$$

providing the defect-related lifetime τ_{R0} at low excitations and the quadratic coefficient B_{nonr}. As the FCA signal (proportional to instantaneous carrier density value $\Delta N(t)$) and its decay rate varied significantly during the decay, the instantaneous carrier lifetime $\tau_R(\Delta N) = -\Delta N(t)/(d\Delta N(t)/dt)$ was also determined by taking the time derivative of the carrier density at a delay time, when ΔN has fixed values. The obtained $\tau_R(\Delta N,T)$ dependences are plotted in

Fig. 5.16b. It was observed, that at ~1.3×10^{15} cm^{-3} nonequilibrium carrier densities the τ_R values coincide with the defect-related lifetime τ_{R0}, while at high carrier densities τ_R decreases due to B_{nonr} impact. The highest carrier densities (10^{18}-10^{19} cm^{-3}) were achieved using 213 nm excitation.

The low-excitation τ_R =720 ns value at RT is of the same-order of magnitude as that of ~2 μs deduced indirectly from time-of-flight experiments in other high quality and high purity CVD diamond [87], while it clearly exceeds the 100 ns lifetime reported from transient photocurrent measurements in homoepitaxial CVD films, grown on Ib type HPHT substrates [110]. In comparison with HPHT samples, the carrier lifetime of 720 ns is by two orders of magnitude larger than that in heavily nitrogen doped ($[N_S]>10^{18}$ cm^{-3}) HPHT type Ib diamonds (lifetimes in representative C3 sample were found very short, ~20-300 ps, similarly as in [95,108]: ~200-500 ps). Indeed, it is well known that nitrogen defects are efficient lifetime killing defects [67]. In low nitrogen-content HPHT IIa diamond (sample C1) the lifetime of 360 ns was found twice shorter than in the CVD sample (sample C4).

Note that the measured recombination time, τ_{R0}, of the electron-hole pairs can be determined by the hole capture time, τ_h, to the nitrogen related traps (which can be single or aggregated defects [67]), as the electron capture to the defects is much faster ($\tau_e << \tau_h$) according to [67], i.e. $\tau_{R0} = \tau_h + \tau_e \approx \tau_h$. Consequently, using the relationship $1/\tau_{R0}(300K) = \sigma_p v_{th\,p} N_T$, (here $v_{th\,p} = (2.55 k_B T/m_h^*)^{1/2} = 9.1\times10^6$ cm/s and $\sigma_p \approx 10^{-16}$ cm^2 are the hole thermal velocity and hole capture cross section to the defect, respectively [67]) for the measured τ_{R0}(300K) = 720 ns (CVD) and 360 ns (HPHT) values the corresponding densities of tentatively electrically active nitrogen were calculated: $N_T = 1.5\times10^{15}$ cm^{-3} and 3.1×10^{15} cm^{-3}. It should be noted, that the latter N_T value for HPHT crystal C1 is ~10 times lower than the single substitutional nitrogen density determined by optical measurements (N_N $=4.3\times10^{16}$ cm^{-3}). However, the opposite tendency ($N_T >> N_N$) is obtained for the CVD sample, therefore contribution of other kind lifetime limiting defects,

presumably dislocations, cannot be excluded. Similar temperature dependences of lifetimes in CVD and HPHT diamonds point out to an impact of the same recombination center of unknown origin (Fig. 5.16b). Thus, the role of nitrogen related defects seems to be negligible.

The temperature dependence of τ_{R0} (Fig. 5.16b) pointed out that in the high temperature region the unknown trap capture cross section σ_p is rather constant while at low temperatures it is enhanced by an order of magnitude. Consequently, other recombination mechanisms come into play, for example, defect (the same as for FC) assisted recombination of excitons [159] as at T <150 K all carriers are bound to excitons. Therefore at 1.3×10^{15} cm^{-3} excitation the effective lifetime can be described as

$$\tau_{eff}=1/[(1-\Delta N_{ex}/\Delta N)/\tau_{FC}+\Delta N_{ex}/\Delta N/\tau_{ex\,LT}], \qquad (5.9)$$

where constant free carrier τ_{FC} =700 ns, and temperature dependent exciton $\tau_{ex\,LT}=0.17\times T^{3/2}$ ns lifetimes were used for fit in Fig. 5.16b.

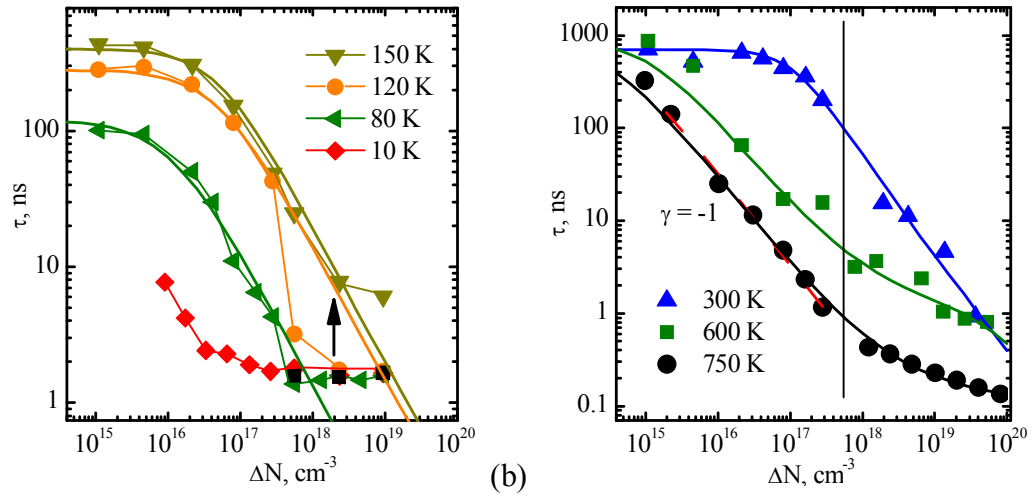

Fig. 5.17. Lifetime dependences on nonequilibrium carrier density at selected temperatures in low (a) and high (b) temperature wings. Vertical bar separates TPA and SPA excitation regimes. [After P26]

Analysis of $\tau_R(T)$ dependences (Fig. 5.16b) point out to decreasing with excitation carrier lifetime, especially at low (T <150 K) and high temperature (T > 450K) wings. These tendencies are shown in Fig. 5.17 for some temperatures. At two photon excitation conditions (ΔN <3×10^{17} cm^{-3}) the

dependences can be simulated with effective nonradiative quadratic recombination coefficient B_{nonr} (see curves in Fig. 5.16a). Indeed, the B_{nonr} values at low and high T are essentially higher than those at 300 K. The temperature dependence of B_{nonr} (Fig. 5.18a) was plotted, adding data for other diamonds (monocrystalline HPHT (sample C1) and microcrystalline CVD (sample C6)). The B_{nonr} value was found strongly increasing at high temperatures with 560 meV activation energy, while in the low temperature wing (250 to 80 K) the B_{nonr} value increased with cooling, providing the 42 meV deactivation energy. The B_{nonr} coefficient was fitted by the following relationship:

$$B_{nonr}\,[\mathrm{cm}^{-3}] = 4\times10^{-5}\times\exp(-E_1/k_BT) + 0.3\times10^{-11}\times\exp(E_2/k_BT), \qquad (5.10)$$

where E_1=560±30 meV, E_2=42±2 meV. It should be underlined, that the same B_{nonr} (T) tendencies were observed in diamond samples of completely different technology (HPHT and microcrystalline CVD), indicating that these recombination features probably are caused by the intrinsic diamond properties or commonly abundant unidentified defects.

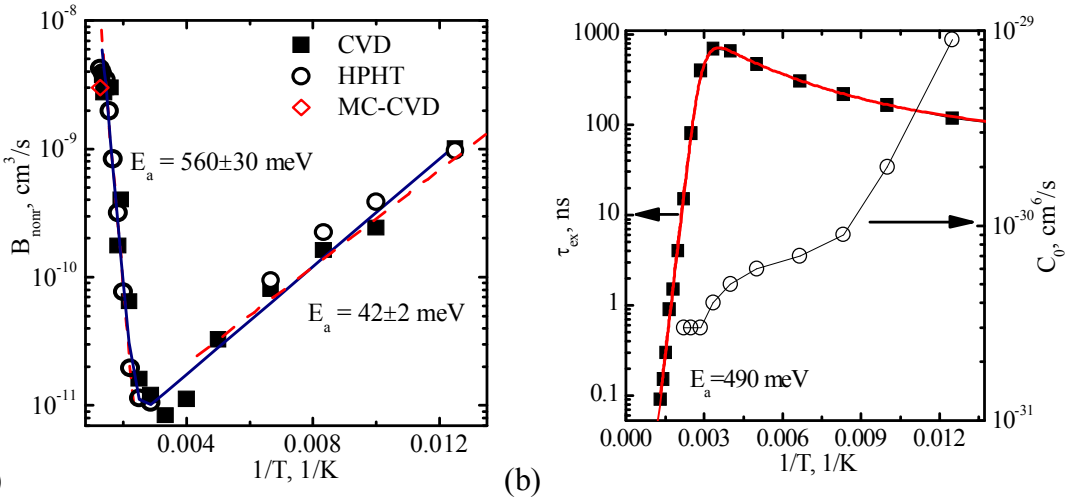

Fig. 5.18. Temperature dependence of an effective nonlinear recombination coefficient in differently grown diamonds (a). Here, data for HPHT and MC-CVD (samples C1,C6) are provided for comparison. In (b), temperature dependences of exciton lifetime and effective Auger coefficient are given. Solid lines are fits to the dependences. [After P26,C26]

The fitting of lifetime in full excitation range was obtained using effective Auger coefficient, C_0, at low temperatures and activatedly reducing with

temperature exciton lifetime, $\tau_{ex\,HT}$, at high ones. They were found from equations (5.11a) and (5.11b), respectively:

$$\frac{1}{\tau(\Delta N)} = C_0\left[N_{loc}\left(\Delta N_{ex}{}^2 + \Delta N_{ex}\Delta N_{FC}\right) + \Delta N_{FC}{}^3\right]/\Delta N + \frac{1}{\tau_{eff}(\Delta N)}, \qquad (5.11a)$$

$$\frac{1}{\tau_{ex}(\Delta N)} = \frac{1}{\tau_{ex\,LT}} + \frac{1}{\tau_{ex\,HT}}. \qquad (5.11b)$$

Here N_{loc}=8.4×10^{19} cm^{-3} is the average local electron-hole pair density in the diamond exciton. Exciton density calculations were provided in section 4.3. High temperature exciton lifetime was fitted with an equation: $\tau_{ex\,HT}$=5×10^{-5}×exp(490meV/$k_B T$) ns.

Strong increase of Auger coefficient at low T (see Fig. 5.18b) can be explained by formation of biexcitons and electron-hole droplets, having 1.5 ns lifetime (see Fig. 5.17a). Room temperature C_0 value and the carrier density in droplets, ~10^{20} cm^{-3} [160], provided 0.25 ns lifetime, being 6 times lower than the observed in droplets. This can be a consequence of local modification of the band structure by the droplets (strong renormalization and screening).

At high temperature wing exciton lifetime activatedly decreased with temperature with 490 meV threshold (see Fig. 5.18b). Such short exciton lifetime probably indicates for some kind of nonlinear excitonic Auger process of unknown origin or impact of trap assisted Auger recombination process [64]. Latter is under question as large concentration of some type of traps must be present in quite pure CVD diamond.

Kinetics of FCA decay at 213 excitation are provided in Fig. 5.19. They were modeled using the nonlinear recombination parameters and surface redombination velocity, S ~10^5 cm/s. The fast FCA decay components slow down with dealy due to carrier density dilution and their redistribution much further from the surface. The S value is quite large, indicating for huge surface trap density, which probably arises due to mechanically damaged subsurface layer [161]. Therefore special treatment of surfaces is very needed for applications, requiring thin diamond layers.

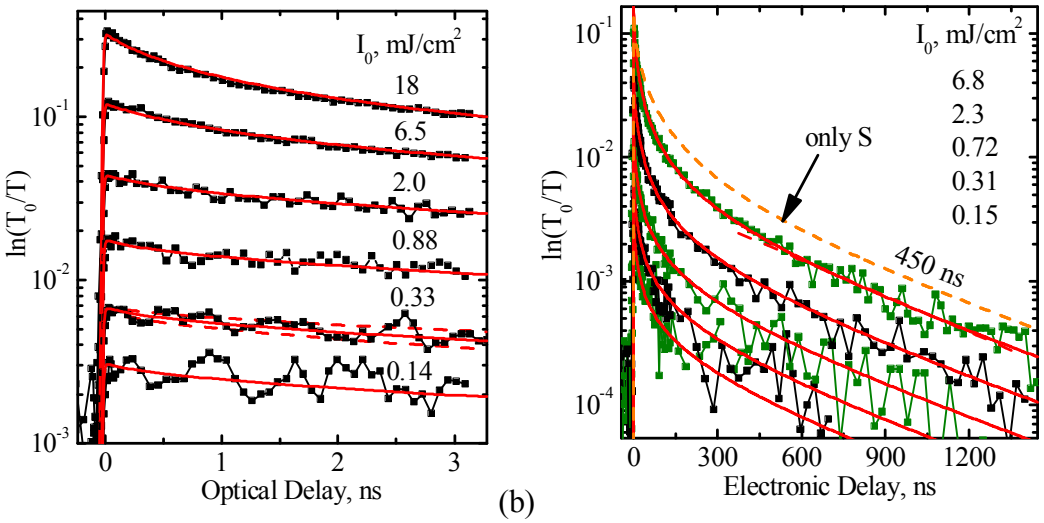

Fig. 5.19. Fast (a) and slow (b) FCA decay components at 300 K and 213 nm excitation. Numerical fits, obtained using C_0 =4×10^{-31} cm^6/s, τ_{R0} =650 ns and S =10^5 cm/s, are shown by solid lines. The dashed lines in (a) were obtained using S =0.5×10^5 (upper curve) and S =2×10^5 cm/s (lower curve) at 0.33 mJ/cm^2. [After C26]

5.5. Carrier diffusion length in SiC, GaN and diamond

Using the excitation-dependent recombination rate [$\tau_R(T,\Delta N)^{-1} = \tau_{SRH}^{-1} + C(T,\Delta N)\times\Delta N^2$] and excitation-dependent diffusion coefficient $D_a(T,\Delta N)$ approximations, the ambipolar diffusion length, $L_D(T,\Delta N) = [D_a(T,\Delta N)\times\tau_R(T,\Delta N)]^{1/2}$ was obtained at selected temperatures (see Fig. 5.20).

The diffusion length in 4H-SiC (sample 4H1) of 20-30 μm remains almost constant up to 10^{17} cm^{-3} excess carrier densities and weakly depends on T. At higher excitations, a significant drop is observed due to nonlinear Auger recombination which is partly compensated later on by degeneracy. To obtain the corresponding plots for hole and electron diffusion lengths, the data in Fig. 5.20 should be scaled by 1.34 and ~2.5, respectively.

In CVD 3C-SiC (sample C1) ~2.5 times shorter diffusion length at carrier densities below 10^{19} cm^{-3} was obtained near the surface of the as-grown side versus the central part due to larger nitrogen and nonradiative point defect concentrations. At higher carrier densities, decrease of L_D is due to nonlinear recombination. In comparison, EBIC technique provided hole diffusion length

of 1.5 μm in sublimation grown sample [162]. This indicates much better quality (mainly in terms of lifetime) of CVD 3C-SiC.

In HVPE GaN (GaN6), the diffusion length was found very long (2-3 μm) in comparison to the published data (< 1 μm [163,164]). The observed L_D increase is due to diffusion coefficient transition from monopolar to bipolar regime.

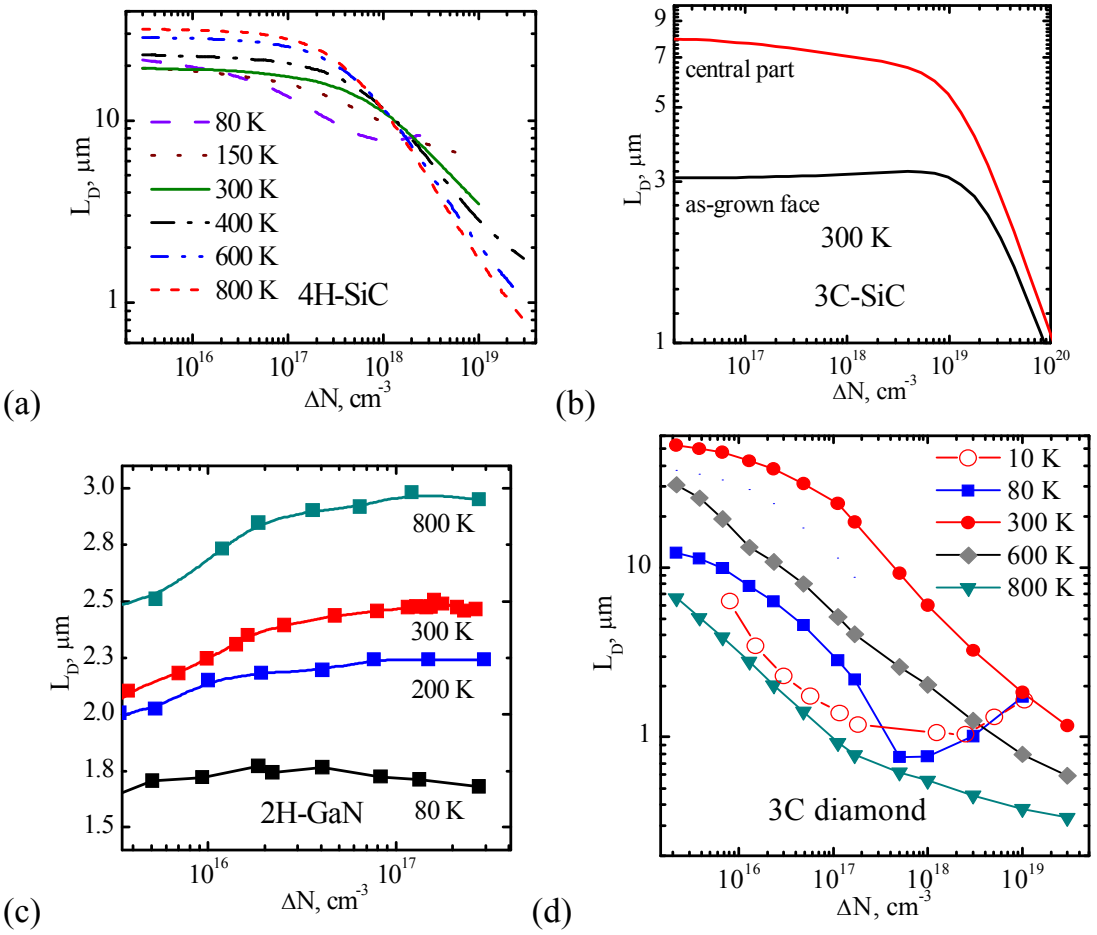

Fig. 5.20. Temperature and carrier density dependences of diffusion length in 4H-SiC (a), 3C-SiC (b), GaN (c) and CVD diamond (d). [After P24,P28,P13,P26]

In diamond (sample C4), L_D value peaked at 50 μm for 10^{15} cm^{-3} carrier densities and T ≈300 K, while at higher ΔN and temperatures the L_D value drastically decreased to 1 μm due to nonlinear recombination. The low injection value of diffusion length, L_D = 8 μm at 10 K, determined by cathodoluminescence technique [165] and L_D = 30 μm at 300 K, determined by photoluminescence [96], are in good agreement with the determined ones by

LITG. Therefore, the strongly carrier density dependent intrinsic lifetime and diffusion length can have adverse impact on diamond devices working at high temperatures and injections.

To summarize, the diffusion length at low carrier densities is determined by nonradiative defects and intrinsic carrier scattering phenomena, while decrease of L_D at high carrier densities is governed by increase of nonlinear recombination rate (as observed in SiC and diamond). On the other hand, the opposite effect was observed in highly excited GaN due to rather weak nonlinear recombination rate, relatively high doping and quite strong increase of diffusion coefficient due to screening of hole-phonon interactions. In SiC and diamond, increase of L_D can be also observed at the highest excitations and lowest temperatures, when carrier plasma degeneracy takes place. In 4H-SiC and diamond, L_D is by order larger than in 3C-SiC and GaN mainly due to much larger lifetime and diffusion coefficient. Therefore, 4H-SiC and diamond are the most mature for production of bipolar devices.

5.6. Spatially resolved carrier dynamics in GaN and diamond

In this section, spatially resolved carrier dynamics are presented for bulk 200 μm thick GaN sample (GaN6) and 1.0 mm thick polycrystalline CVD diamond (C4). Numerical simulations reveal impact of recombination on grain boundaries and in the grains.

The DT images for bulk GaN (sample GaN6) are shown in Fig. 5.21 at three fixed delay times. At small delay (2 ns), the signal spatial distribution is quite homogeneous due to position independent carrier generation, while at longer delays the ongoing recombination discloses the carrier lifetime inhomogeneity. The inhomogeneity factor (i.e. a ratio of spatially-averaged standard deviation to an average signal) increases with time and equals to 0.1, 0.3 and 1.0 at 2, 30 and 70 ns delay times, respectively. The carrier lifetime τ was determined for each pixel assuming the exponential decay of the DT signal ($DT_i(\Delta t) \sim \exp(-\Delta t/\tau_R)$) and taking the time interval $\Delta t = \tau_R$. Of about 40 seconds were needed to obtain the DT image at a fixed delay, and of 10

minutes per full carrier lifetime image, with good spatial (5 μm) and temporal (~2 ns) resolution.

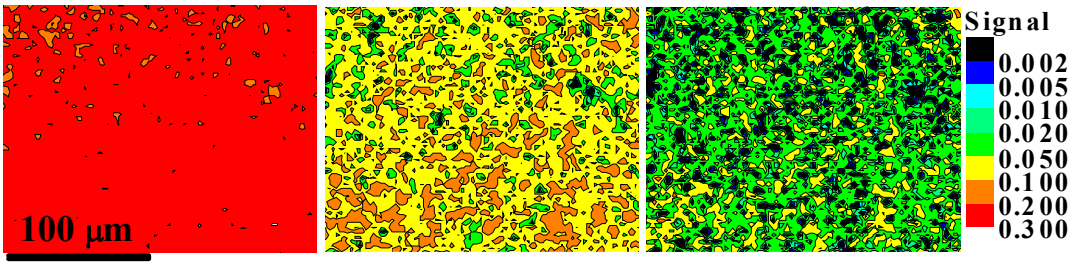

Δt = 2 ns Δt = 30 ns Δt = 70 ns

Fig. 5.21. Images of differential absorption signal in GaN, i.e. DT(Δ*t*) at different relative pump and probe delays, Δ*t*. [P25]

The measurements of DT images at various delay times provided the lifetime mapping (Fig. 5.22a) with τ_R values varying in a wide range (from 10 to 70 ns). Moreover, the spatial distribution of lifetimes resembled islands of long lifetime (50-70 ns), surrounded by regions of reduced lifetime (20-40 ns); in some areas, the lifetime dropped even to 10 ns (see enlarged view in Fig. 5.22a with points 1-3). Lifetime maps did not depend significantly (±20%) on the excitation fluence in a range from 1.0 to 6.4 mJ/cm^2.

In Fig 5.22b, the spatially-resolved FCA decays were compared for selected pixels. It was found that the decay rate varies with time in areas of lifetime maxima (point 1) and surrounding rings (point 2). In the maxima, the initial decay is slow (~70 ns) but becomes twice faster at longer delays, while in the rings the opposite tendency was observed (it increases from 20 to 40 ns). Note that in the regions with the shortest lifetime the decay is almost exponential (point 3). On the other hand, spatially-averaged lifetime over the full area (85×70 pixels, Fig. 5.22c) has shown very similar lifetime value of 40 ns, as those in the decay tails of points 1 and 2.

To explain the FCA decay rate peculiarities, a model of diffusion-limited recombination on grain boundaries was used (see section 5.3). In order to precisely calculate the carrier diffusion governed nonradiative recombination decay rate at various lateral positions, a modified balance equation (5.5)

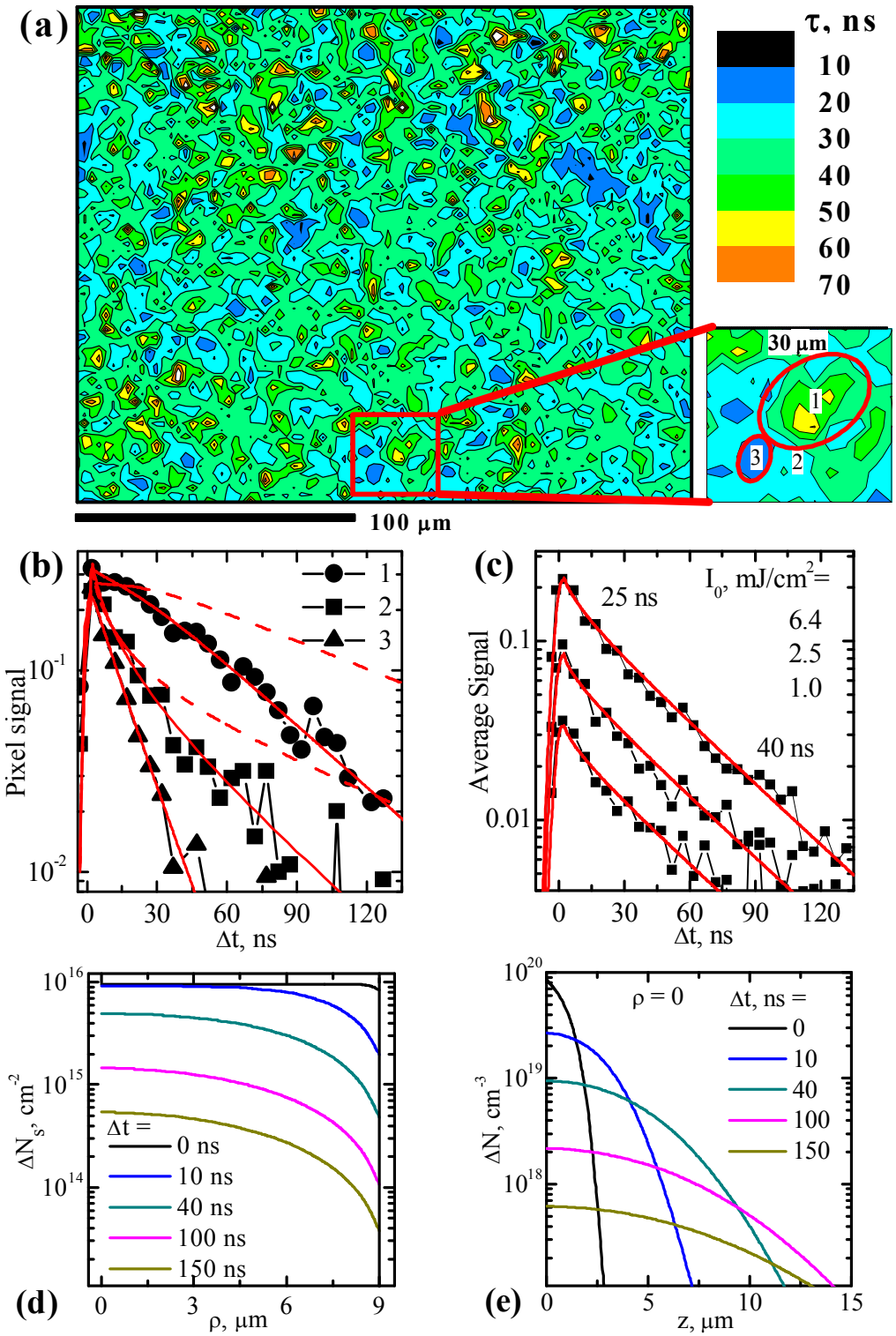

Fig. 5.22. FCA carrier lifetime map at I_0 =6.4 mJ/cm^2 (a), decays at selected points (b) as well as spatially averaged decays over whole investigated area (c). In (d) and (e) the modelled depth-integrated lateral and depth-resolved carrier profiles are shown. The modelling provided fits (solid lines) for the experimental curves (b,c), while the dashed curves in (b) do not take into account the contribution of τ_{RBULK}. [P25]

in cylindrical coordinates was solved, including a term with bulk lifetime in grains ($\tau_{RBULK}^{-1}=\tau_{SRH}^{-1}+\tau_{rad}^{-1}$) and carrier density dependent diffusion coefficient, $D(\Delta N)$ (see section 4.2):

$$\frac{\partial \Delta N(\rho,z,\Delta t)}{\partial \Delta t}=\frac{1}{\rho}\frac{\partial}{\partial \rho}\left(D_{\mathrm{a}}(\Delta N)\rho\frac{\partial \Delta N}{\partial \rho}\right)+ \frac{\partial}{\partial z}\left(D(\Delta N)\frac{\partial \Delta N}{\partial z}\right)+\frac{\Delta N}{\tau_{RBULK}}. \tag{5.12}$$

The photogenerated carrier density in-depth profile was described by a relation $\Delta N(z,t=0) = \alpha(z)I(z)/h\nu$, where $\alpha(z)= \alpha_0/(1+\zeta I(z))$ is the excitation dependent absorption coefficient, described in section 3.3. A numerical solution of Eq. (5.12) provided dynamics of spatial carrier redistribution within the grains and on the grain boundaries. Consequently, the total lifetime is an average of all contributing processes: $1/\tau_{TOT}= 1/\tau_{nonr}+ 1/\tau_{RBULK}$.

The numerical modeling confirmed that the decay time increase in point 1 is due to the fact that the carriers must be delivered to the grain boundaries (point 2) by diffusion from more distant and less defective regions. To simulate the recombination processes in these areas, the equation (5.12), was solved for a 18 μm- large grain (r_{cyl} =9 μm). The calculated lateral carrier profiles are shown in Fig. 5.22d for various times after photoexcitation, while the corresponding carrier in-depth profiles are given in Fig. 5.22e. Using the carrier density profiles, the decay kinetics in the near grain boundary (point 2) and defect free area (point 1) were calculated by Eq. (5.12), neglecting the bulk term and using large interface recombination velocity, S =4×10^4 cm/s (Fig. 5.22b, dashed curves). In such a case, the calculated curves are slower than the experimental ones: the initial part of the measured decay of 58 ns (in point 1) does not correspond to the solely diffusion-limited 300 ns time. Therefore, in order to obtain a good fit to the experimental data in the central part of the grain, the impact of bulk recombination (τ_{RBULK} =70 ns) in the crystallites was added, in addition to the diffusion-limited recombination on the grain boundaries, and the latter calculations (see solid curves in Fig. 5.22b) fitted

well the experimental data. The fast exponential decay of τ_{nonr} ~12 ns (in the point 3) was attributed to ~6 μm grain size (the same *S* value was used).

Spatially-averaged FCA decays were simulated (Fig. 5.22c), and their decay tails of 40 ns provided an average effective grain size of about 15 μm (the grain coalescence probably leads to different interface trap density on different grain edges, thus randomizing the lifetime pattern). Note that the latter decay time remains constant at Δt > 30 ns, in spite of that the carrier density in this time interval varies in the 10^{18}-10^{19} cm^{-3} range (according to Fig. 5.22e). Therefore, not dependent on excitation the total lifetime τ_R points to constant values of diffusion- limited recombination time (τ_{nonr} =const) and bulk recombination time (τ_{RBULK}=const).

The τ_{RBULK} lifetime is probably related to the intragrain nonradiative traps, as photon emission to the air does not effectively contributes to the carrier density reduction. This peculiarity can be explained by large minimal effective radiative recombination time according [166]: $\tau_{rad}^{*}=\tau_{sat}\phi_{reabs}\phi_{extr}\phi_{enh}$, where τ_{sat}~25 ns is the saturated radiative lifetime (see next chapter for its evaluation), ϕ_{reabs} is the reabsorption factor ($\phi_{reabs}= d_{ph}/d^{*}\times[1-\exp(-d^{*}/d_{ph})]$, d_{ph} =2 μm [105] is the photon mean free path, d^{*} is the carrier distribution thickness), $\phi_{extr}=1/(4n_{GaN}^{2})=0.037$ is the light extraction efficiency factor [113] from GaN to air (n_{GaN}=2.6 is the refractive index for 3.4 eV GaN PL peak [113]), and ϕ_{enh} ~$1/(1+\tau_{sat}/\tau_{nonr})$ is the inverse number of times the photon reabsorption process occurs. Finally, calculations led to τ_{rad}^{*} >~400 ns value, being much larger than the determined experimentally. In confirmation to the above explanation ~40 ns carrier density independent (in 10^{16}-10^{17} cm^{-3} range) average lifetime was observed in the sample at two photon excitation conditions (see Fig. 5.13a). Therefore, recombination rate on the nonradiative traps in the grain bulk and on their edges is carrier density independent in 10^{16}-10^{19} cm^{-3} range.

Carrier dynamics under interband carrier excitation (213 nm) was studied in two freestanding microcrystalline CVD diamond layers: an undoped C6 and

B-doped C7. The average grain size, determined by scanning electron microscopy (Fig. 5.23), varied from d_{grain} ~1-2 μm to ~130 μm on the nucleation and growth sides of the undoped layer, while in the B-doped layer the grain size at the growth side was ~40 μm (the average grain area, $\sim\pi d_{grain}^2/4$, was obtained dividing the total investigated area by number of grains in it).

For carrier excitation, a Nd:YAG laser was used. Its 5-th harmonic pulse λ_5=213 nm generated the carriers in the bulk via interband transitions, providing their density in 5×10^{17} - 3×10^{19} cm^{-3} range. Interband carrier generation at λ_5 in a δ =1/α_5 =3.1-μm thick surface region (here α_5 = 3200 cm^{-1}, section 3.1), provided free carriers, and their lifetimes and diffusivities were measured on the both sides of the studied samples.

(a) 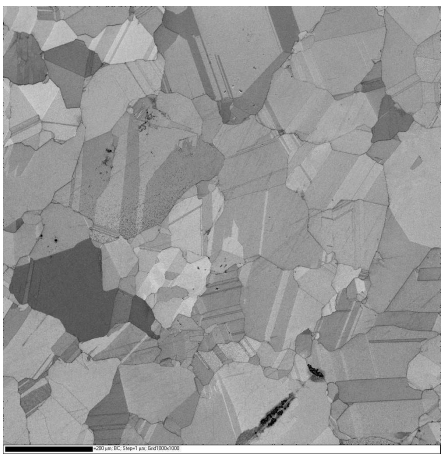 (b) 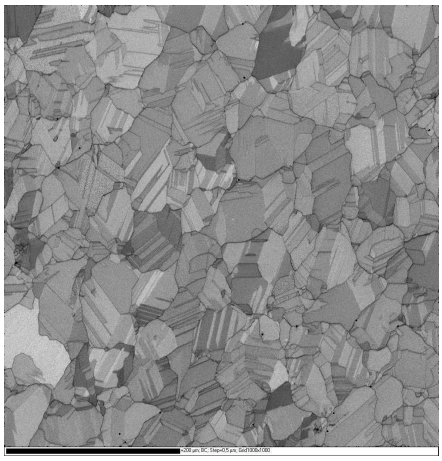

Fig. 5.23. Microcrystalline structures on the growth side of the undoped (a) and B-doped CVD layers (b). The bars on the figures indicate a 200 μm length. [P27]

Differential transmittivity and reflectivity signals exhibited linear excitation dependences, thus the signal decay time directly reflected carrier lifetime. Decay kinetics for the undoped CVD sample are shown on Fig. 5.24a,b. Decay time on the growth side exhibited very strong position dependence, while such dependence on the nucleation side was much weaker. This effect is probably due to more pronounced variation of grain size on the growth side, as can be seen in Fig. 5.23a. Lifetime dependence on excitation, if measured in the selected place with the longest lifetime, was rather weak (Fig.

5.24b), thus the decay of 3-5 ns is determined by nonradiative recombination, consisting of recombination on structural, point defects, and surface.

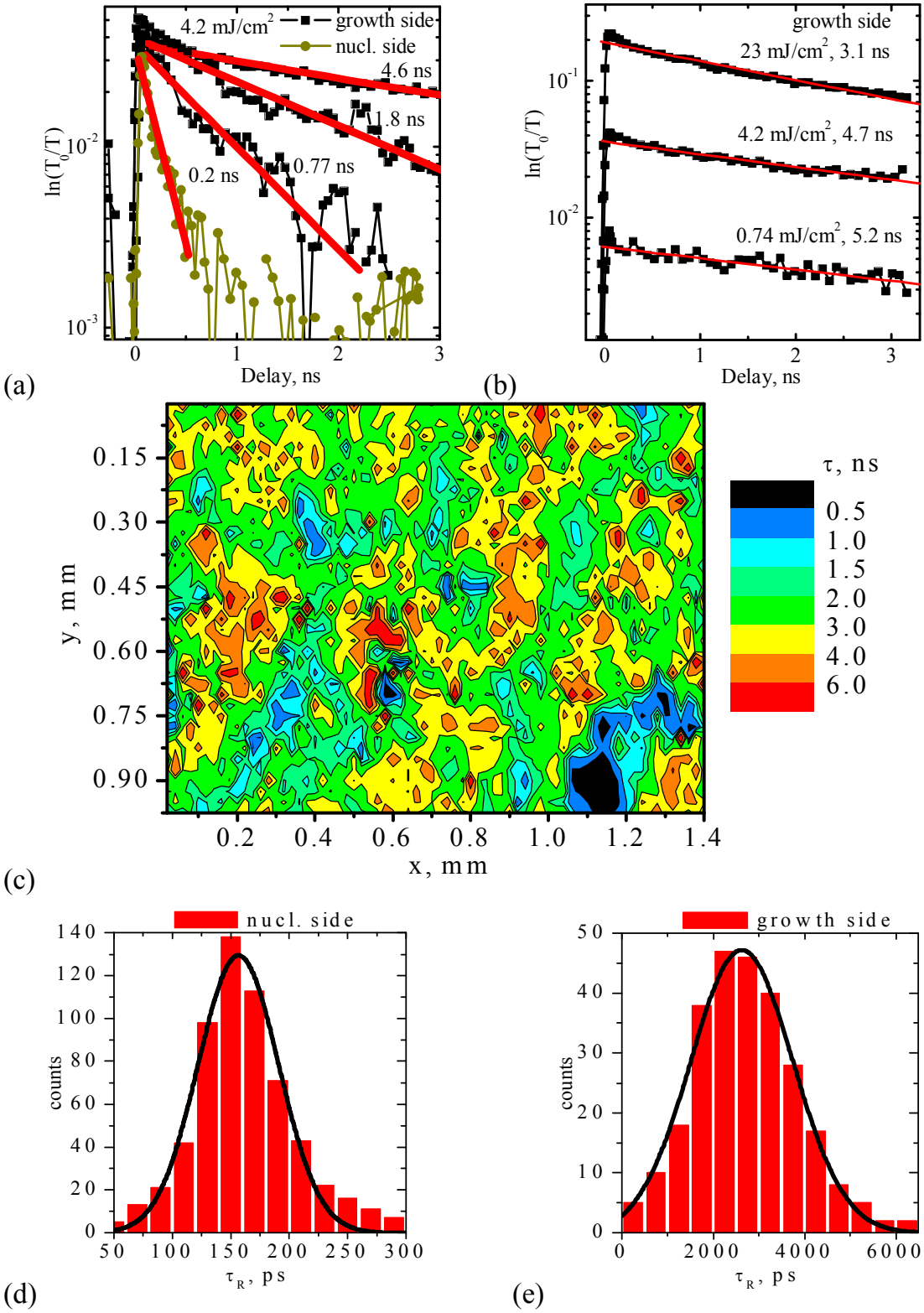

Fig. 5.24. Carrier lifetimes on the growth and the nucleation sides of the undoped layer C6, measured at I_0 =10 mJ/cm^2 excitation fluence (a), DT kinetics at different I_0 values (b), lifetime spatial variations on growth side with 40 μm resolution (c) and lifetime statistics on the opposite sides of the layer (d,e). [P27]

Initial slightly faster decay can be a consequence of some different grain sizes (and consequently, lifetimes) as well of surface defects. Note that the impact of surface defects leads to the decreased lifetimes, as revealed by DR kinetics.

To evaluate the statistical distribution of lifetimes (the average value of lifetime is needed to correlate it with average grain size), it was measured in 280 points. For this purpose in each point the DT values were measured at two different delay times (0.5 ns and 2.5 ns for the growth side and 0.1 ns and 0.4 ns for the nucleation side, respectively), thus providing a simple way for carrier lifetime determination. An almost Gaussian lifetime distribution was determined on the nucleation and growth sides (see Fig. 5.24d,e), with the average lifetime values, τ_{av}, of 160 ps and 2600 ps, respectively (the lifetime fitting as $A\times\exp[-2\times((\tau - \tau_{av})/\sigma)^2]$ was used, here σ=70 ps and 2200 ps, respectively). Consequently, the average lifetime on the nucleation side is ~15 times smaller than that on the growth side, while the grain size on the nucleation side is about ~100 times smaller (few μm with respect to few hundred μm on the growth side). It can be concluded that in the case of large grains the recombination is governed by bulk non-radiative traps, as the carrier diffusion time to grain boundaries ($\tau_D = d_{grain}^2/(22\times D_a)$) is much larger (~0.1 μs and ~1 μs, respectively), while on the nucleation side an impact of diffusion-limited recombination on grain boundaries is possible, as τ_D =100-400 ps. Indeed, lifetimes up to 100 ns were observed in ~100 μm large grains of purified CVD diamond at 266 nm excitation wavelength [110]. For comparison, in bulk HPHT diamonds lifetimes were in 150-330 ns range. The large variation of lifetime values (especially on the growth side) might be a consequence of different growth orientation of the grains and consequently different point defect incorporation probability [84].

In the boron-doped diamond sample (B-CVD), the lifetime values exhibited a rather narrow distribution on both sides. Lifetime value on the nucleation side was 3 times smaller partially due to smaller grains there when

compared to the growth side. However, by order of magnitude shorter lifetime on growth side of the B-CVD in comparison to the U-CVD indicates for much higher defect density in the B-CVD (i.e. dislocations, other diamond phases), which is caused by high boron concentration [167]. For DT measurements (Fig. 5.25a) in this sample a 523 nm probe was used, as the layer transmission for the 1064 nm probe was not detectable due to a relatively high boron concentration. DR measurements (Fig. 5.25b) provided 97 ps on the growth and <10 ps on the nucleation side. Note that DR decay in the undoped layer provided lifetimes of 250 ps on the growth and <10 ps on the nucleation sides. The growth surface lifetimes are comparable for both samples, but are much shorter than the bulk lifetime, probably due to similar but large surface trap densities.

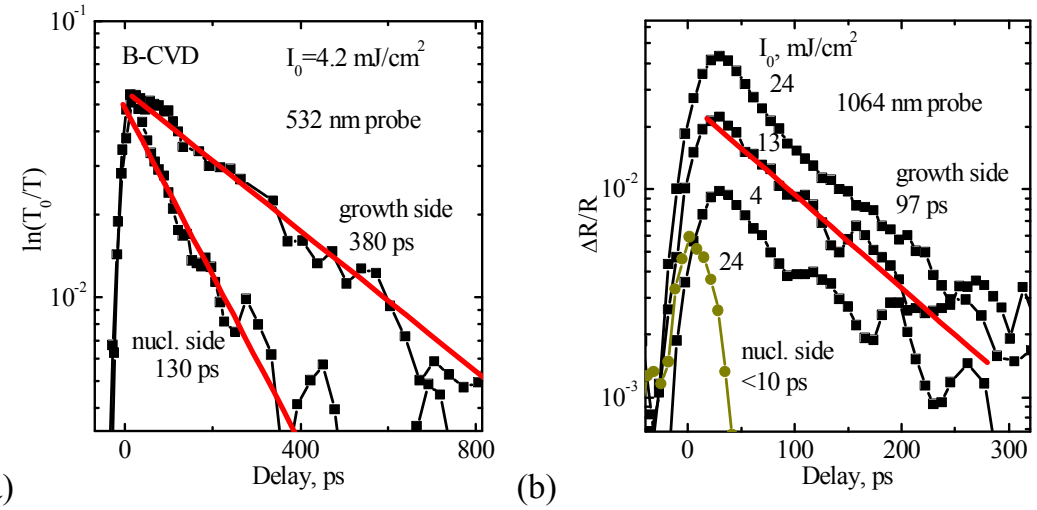

Fig. 5.25. Differential transmittivity (a) and differential reflectivity (b) decays on the growth and nucleation sides of B-doped CVD layer C7. [P27]

5.7. Radiative recombination in 3C-SiC and GaN

In this section, measurements of radiative recombination rate in indirect-gap 3C-SiC (3C1,3C2) and direct-gap GaN (GaN7) samples are presented. In 3C-SiC the radiative recombination coefficient was found to be constant, while in GaN it was strongly dependent on carrier density. Saturation of radiative recombination rate in GaN was observed.

The PL intensity measured in 3C-SiC by the photodiode or PMT at different excitation levels is shown in Fig. 5.26a.

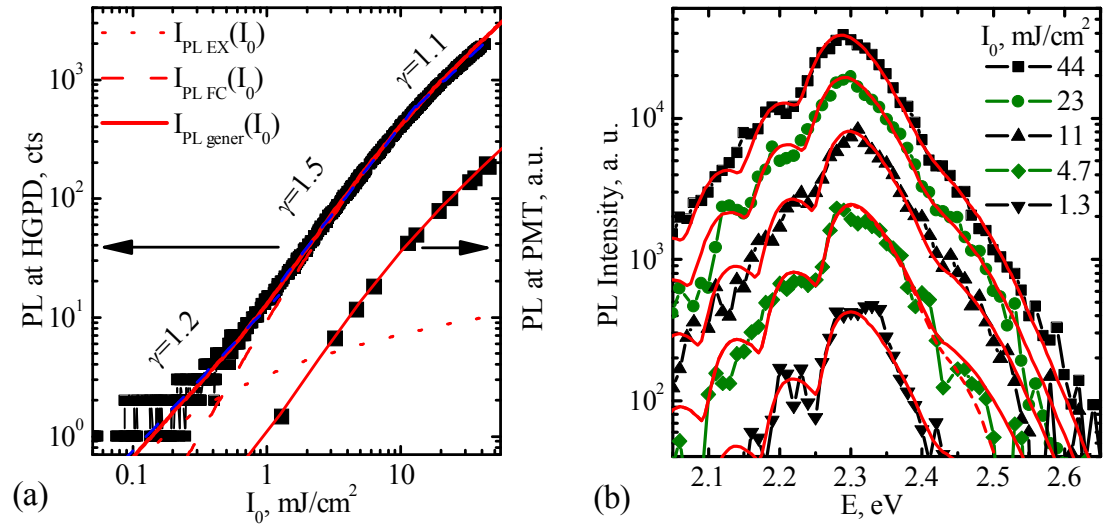

Fig. 5.26. Integrated PL intensity measured by the photodiode or PMT (a) and integrated PL spectra at different excitation fluences (b). The points indicate experimental data, and the solid lines show numerical fitting, whereas the dashed lines in (a) correspond to the linear fits in log-log scale. The dashed curve ($I_{PL\ FC}$) in (a) was calculated neglecting exciton impact ($I_{PL\ EX}$), which is shown by dotted curve. [P20]

The integrated over depth time-dependent PL intensity decay (Fig. 5.26b) was calculated at RT as [36]:

$$I_{PL}(I_0,t) = B_{rad} h\nu_{PL} \times \int_0^d \left[1 + N_{loc}/n^*\right] \Delta N_h(z,t)\left(\Delta N_e(z,t) + n_0\right) dz \,. \qquad (5.13)$$

The unity in square brackets corresponds to free carrier luminescence case, while N_{loc}/n^* corresponds to exciton one at thermal equilibrium [36,168]. Here $N_{loc}(\Delta N) = 1/(\pi a_B^3) \times (E_{ex}(\Delta N)/E_{ex0})^{3/2}$ [168] is the average local electron-hole pair density in the exciton, $a_B = \varepsilon_s m_0/m_{eh} \times 0.53\text{Å} = 2.2$ nm is the exciton Bohr radius ($\varepsilon_s = 10$, $N_{loc}(0) = 2.9\times10^{19}$ cm^{-3}). The time-integrated PL intensity in the central part of Gaussian excitation beam was calculated as $I_{PL}(I_0) = \int_0^\infty I_{PL}(I_0,t)dt$. The integration was performed numerically up to 900 ns, when signal drops more than two orders of magnitude, leading to less than one percent error. The $I_{PL}(I_0)$ approximate relation (fitted in 0.1 to 55 mJ/cm^2 excitation interval), averaged over radial coordinate, provided generated PL energy, $I_{PL\ gener}(I_0)$:

$$I_{PL}(I_0) = B_{rad} h\nu_{PL} A \times 10^{a\cdot\zeta + b\zeta\cdot\zeta + c\zeta\zeta\zeta},\ \zeta = \log(I_0),$$
$$I_{PL\ gener}(I_0) = \int_0^\infty I_{PL}\left(I_0 \exp\left(-r^2/r_0^2\right)\right) 2\pi r \mathrm{d}r. \tag{5.14}$$

Here the fit parameters are: a = 1.47, b = -0.011, c = -0.069 and the integration constant is $A = 2.00\times10^{26}$ s/cm^5. Excitation beam radius of 220 μm was used.

The absolute $I_{PL\,gener}(I_0)$ integral (Eq. (5.14)) approximated the experimental PL dependence recorded by HGPD (while the $I_{PL\ gener}(I_0)$ curve recorded by PMT was normalised). It was observed that at high excitations, the slope (γ) of the PL dependenses decreases due to nonlinear recombination. If latter was absent, the slope would be close to 2. The relationship (5.14) together with Eq. (2.26) were used to calculate B_{rad}. From the numerical fits of experimental dependences, $B_{rad} = 2.05\times10^{-15}$ cm^3/s value was obtained, being very close to the theoretical one, namely 2.38×10^{-15} cm^3/s [P20].

In order to fit the PL spectra dependences on excitation (Fig. 5.26b), BGR and band filling (BF) were taken into account (here exciton impact was neglected due to high carrier densities). An average phonon energy E_{ph} = 80 meV was used to calculate the spectra following Ref. [33]:

$$I_{PL}(\chi_\nu, \Delta N) = \int_0^{\chi_\nu - x_g} x^{1/2}\left(\chi_\nu - x_g - x\right)^{1/2} f_{FN} f_{FP} dx / \Delta N^2,\ \chi_\nu - x_g > 0,$$
$$f_{FN} = 1/\left(\exp\left(x - x_{FN}\right)+1\right),\ f_{FP} = 1/\left(\exp\left(\chi_\nu - x_g - x - x_{FP}\right)+1\right), \tag{5.15}$$
$$S_{PL}(x_\nu, \Delta N) = \sum_{n=1}^{\infty} I_{PL}\left(x_\nu \mp n\cdot x_{ph}, \Delta N\right)\cdot\left(n_B + 1/2 \pm 1/2\right)^n q^{n-1}.$$

The spectrum depends on carrier density and normalised quantum energy, $x_\nu = h\nu/k_BT$. The upper sign in the sum provides phonon emission terms, while the lower ones correspond to the phonon absorption. f_{FN} and f_{FP} are electron and hole distribution functions with electron and hole concentration dependent quasi Fermi levels, $x_{FN}(\Delta N)=E_{FN}(\Delta N)/k_BT$ and $x_{FP}(\Delta N)=E_{FP}(\Delta N)/k_BT$, respectively. They were approximated by Nilsson approximation [55], taking corresponding 3C density of states for conduction and valence bands [23] at RT. $x_g = E_g/k_BT$, $x_{ph} = E_{ph}/k_BT$ are the normalised bandgap and phonon energy, respectively. The integration of spectrum S_{PL} (which is normalised by carrier density squared, see Eq. (5.15)) over emitted quanta energy gives the same

integral value at different excitation levels despite the spectrum broadening, which justifies an assumption of a constant B_{rad} value at different carrier density. It was assumed that the same phonons participate at different carrier energy, as well carrier masses and bandgap values do not change significantly. However, the increase of carrier masses and hence the density-of-states at high carrier densities [169] may cause decrease of B_{rad} at high carrier densities.

It was found that the PL peak shifts due to BGR and simultaneously broadens due to BF (see Fig. 5.26b, where fitted PL spectra correspond to average 2.8×10^{19}, 1.9×10^{19}, 6.9×10^{18}, 3.4×10^{18} and 1.0×10^{18} cm^{-3} carrier densities from top to botom). The PL spectrum broadens at high excitations up to 20 % and bandgap reduces by 40 meV. This indicates that the PL peak at high carrier densities may lead to incorrect bandgap value. Broadening of the one phonon assisted band, measured at FWHM, was compared to the theoretical calculations. Finally, the low $E_{g\,0}$= 2.374 ± 0.01 eV and its BGR coefficient a_{BR} = (1.23 ± 0.15)×10^{-6} eV$cm^{3/4}$ were determined. The determined bandgap renormalisation coefficient confirmed the theoretically calculated one: a_{BR} = 1.20×10^{-6} eV·$cm^{3/4}$ [56]. The determined bandgap value agreed rather well with the obtained from absorption spectrum: $E_{g\,0}$ = 2.36 eV [170].

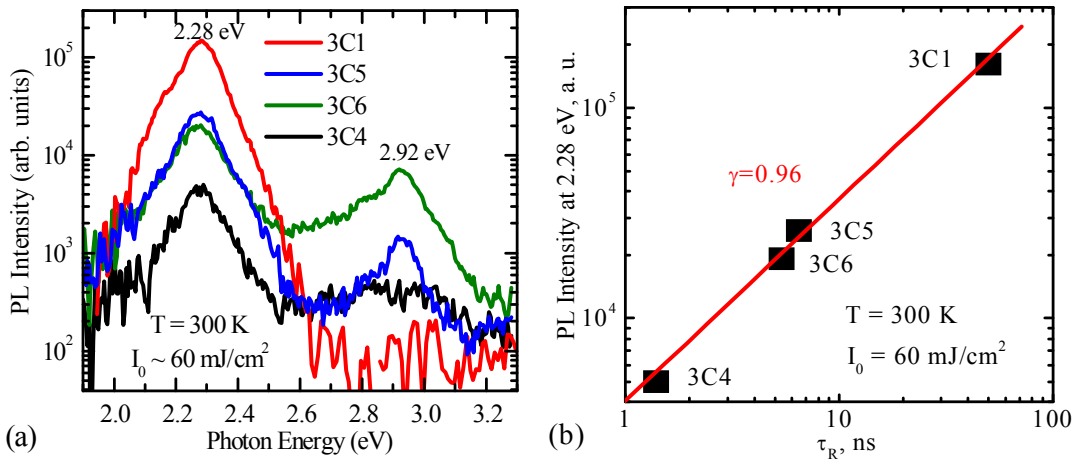

Fig. 5.27. Room temperature photoluminescence spectra in differently grown 3C-SiC layers at carrier excitation by 355 nm (a) and correlation of the band edge emission intensity in 3C-SiC with FCA lifetime (b). [After P16]

The PL spectra in different 3C-SiC layers (see Fig. 5.27a) at RT revealed the same band edge emission peak at 2.28 eV and much weaker signal at 2.92

eV from the underlying 6H-SiC substrate (the latter spectral component was found strongest in the thinnest 3C6 layer and absent in bulk 3C1). The PL spectra in 3C1 CVD layer, measured on both sides and different areas of the wafer, confirmed its good homogeneity. On the other hand, the PL intensity varied strongly for the layers grown by different epitaxial techniques. This feature was analyzed by comparing the PL intensity of a sample with its carrier lifetime value, determined by DT technique. A linear correlation between these parameters was found (Fig. 5.27b) because:

$$I_{PL} \sim \int_0^{\infty} B_{rad} N_0^2 \exp(-2t/\tau_R) dt \sim \tau_R. \quad (5.16)$$

The ratio of 6H-SiC and 3C-SiC PL peaks (see Fig. 5.27a) can be approximated by $R_{6H/3C} = \tau_{6H}/\tau_{3C} \times B_{6H}/B_{3C} \times \exp(-\alpha^* d)$ relation, where the effective absorption coefficient is $\alpha^* = \alpha_{355} + \alpha_{425}$. Here α_{355} determines the part of excitation beam penetrated to the substrate, while α_{425} – the absorption of emission from 6H at 2.92 eV, when it propagates throught the 3C-SiC layer towards the detector. In 3C, light penetration depth, $1/\alpha$, is ~5 μm at 355 nm and ~20 μm at 425 nm [136]. From $R_{6H/3C}$ values SiC polytype dependent B_{rad} coefficients can be determined. The $R_{6H/3C}$ value (according to data in Fig. 5.27a) is 0.051 for CVD layer (3C5) on VLS seed (3C6). Using the total layer thickness of 8.2 μm (see Table 1), the lifetime value in the layer, τ_{3C} = 6.5 ns, lifetime in the 6H-SiC substrate, τ_{6H} = 1.1 ns, and $R_{6H/3C}$ value, the B_{6H}/B_{3C} = 2.2 ratio was calculated. It well agrees with one obtained using theoretical B_{rad} coefficients, B_{6Hth}/B_{3Cth} = 1.6 (B_{rad}(3C) = 2.38×10^{-15} cm^3/s, B_{rad}(6H) = 3.8×10^{-15} cm^3/s, B_{rad}(4H) = 14×10^{-15} cm^3/s values at RT were calcualted using effective masses (see section 1.1.3), absorption parameters 9800 cm^{-1} for 3C and 48920 cm^{-1} for 6H [P11] in equation (1.31), where E_{ph} and q values were equal to 80 meV and 0.32 for 3C, 90 meV and 0.27 for 6H [P11]). Therefore, the PL origin and intensity of the peaks were verified.

The measured time resolved photoluminescence decays (Fig. 5.28a) were two times faster in 4H-SiC as predicted by bimolecular recombination law (Eq.

(5.13)). In 3C due to large lifetime inhomogenity, the latter correlation was difficult to obtain and thus similar lifetimes were obtained (Fig. 5.28b).

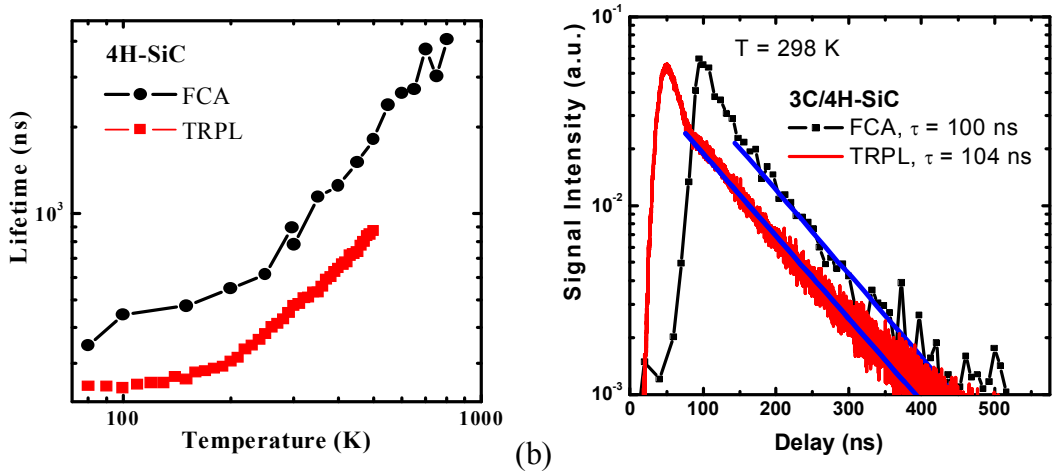

Fig. 5.28. Temperature dependences of FCA and TRPL decay times in 4H-SiC (4H2) at $\Delta N \sim 10^{17}$ cm^{-3} (a), PL and FCA decay kinetics in 3C/4H-SiC layer (3C3) at $\Delta N \sim 10^{18}$ cm^{-3} (b). [P5,P8]

PL transients and spectra at interband excitation in thick GaN6 sample are shown on Fig. 5.29. The room temperature TRPL kinetics were measured at $\sim 10^{18}$ cm^{-3} carrier density by using ~150 fs pulses at 267 nm wavelength.

For numerical calculation of the PL transients, the intensity of the PL emission was integrated over the excited layer thickness taking into account the reabsorption of light emission α_R [105]:

$$I_{PL}(t) \propto \int_0^d \Delta N_h (\Delta N_e + n_0) \exp(-\alpha_R z) dz \,. \qquad (5.17)$$

It was found that the initial fast PL decay within the first 100-500 ps has its genesis in the carrier diffusion away from the surface deeper into the sample which distributes the carriers over a ~1 μm depth within 1 ns. Ambipolar diffusion reduces the peak value of ΔN by an order of magnitude (from $\sim 10^{17}$ cm^{-3} at the end of laser pulse to $\sim 10^{16}$ cm^{-3} at t =1 ns, see Fig. 5.30a). At later times, when carriers diffuse to the deeper layer, an impact of PL emission reabsorption becomes more pronounced, particularly for the shorter wavelengths (see calculated PL decays using different α_R and S values in Fig. 5.30b). Moreover, the surface recombination also contributes to TRPL decay,

and fitting of the data in Fig. 5.29 revealed S = 1.1×10^4 cm/s (reabsorption coefficients α_R =7000 and 400 cm^{-1} were used in spectral regions 1 and 4, respectively). The recombination-governed LITG decay (grating period Λ = 7.8 μm) at SPA excitation conditions, 2×10^{19} cm^{-3}, leads to carrier density decay instantaneous time of ~3.2 ns (lower dashed line in Fig. 5.29). For comparison, FCA decay at 2P excitation conditions (10^{17} cm^{-3}) indicates a 40 ns bulk lifetime (upper dashed line in Fig. 5.29). Thus, the data reveal the combined effects of PL reabsorption and surface recombination. One can then conclude that the fast diffusion-driven PL decay transient during the initial 1 ns period cannot be avoided, while the subsequent decay transients (up to 10 ns) may be influenced both by PL reabsorption and surface states of GaN. Therefore, the bulk recombination rate in the range of measured PL decay (~1.5 ns) was masked by faster processes of diffusion, surface recombination, and reabsorption.

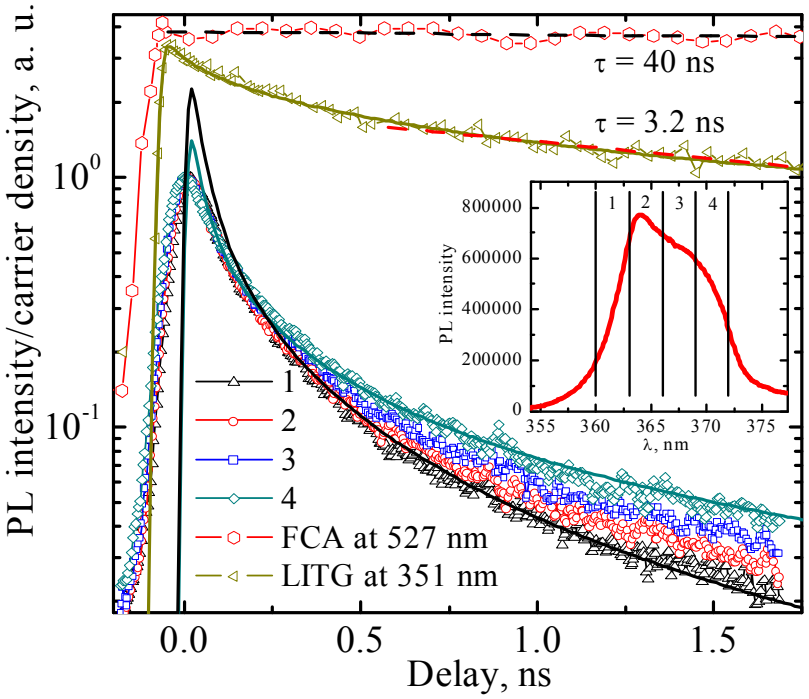

Fig. 5.29. Comparison of carrier decay transients, revealed by various optical techniques at single and two-phonon excitation conditions. TRPL transients were recorded at 267 nm excitation and detected in four spectral ranges (1 to 4). Best fits in the 1 and 4 ranges are provided (solid lines). For comparison, LITG and FCA decays are shown together with their exponential fits (dashed lines). [P13]

The fitting of LITG decay kinetics (in Fig. 5.29) also revealed the impact of surface recombination with $S = 3\times10^4$ cm^{-1}. The three-fold higher S value (with respect to one for PL decay) may be due to an increase of S with carrier density [171]. The rather large S value for the investigated bulk GaN might be explained by the chemical mechanical polishing and subsequent long-term surface self-oxidation. In comparison, in m-plane GaN with much better surface quality, TRPL provided $S = 1.1\times10^3$ cm/s, being even 5 times smaller than that derived from FCA decays ($S = 5\times10^3$ cm^{-1}) in Fig. 5.14a.

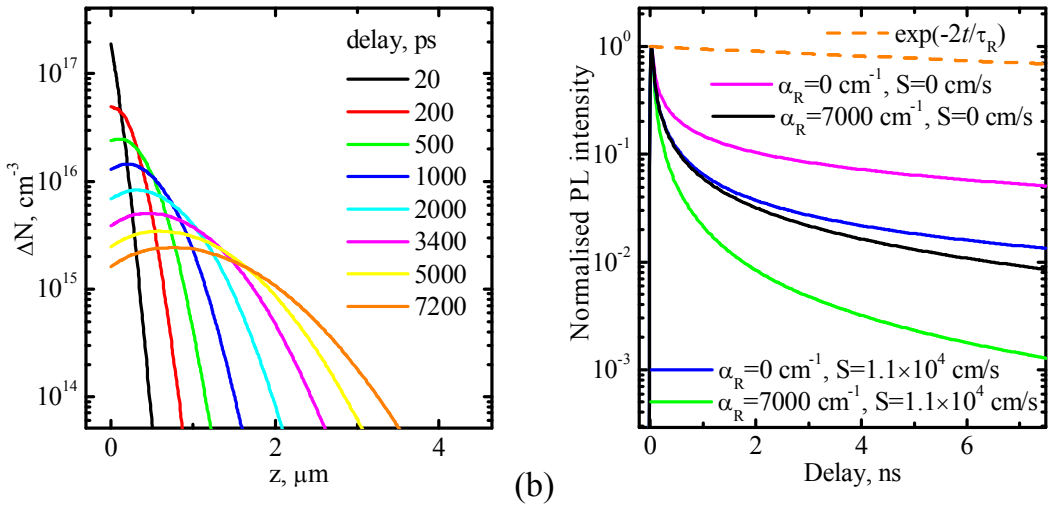

Fig. 5.30. Evolution of carrier depth profiles in bulk GaN after carrier generation at 267 nm wavelength (a) and the calculated TRPL kinetics in different cases: α_R=0, S=0; α_R=0, $S\neq0$; $\alpha_R\neq0$, S=0 and $\alpha_R\neq0$, $S\neq0$ (b). The expected slow PL decay component, governed by bulk recombination only ($I_{PL}\propto \exp(-2t/\tau_R)$ with τ_R= 40 ns), is shown by a dashed line. [P13]

The internal PL efficiency measurements in m-GaN are provided in Fig. 5.31a. Approximate carrier density, corresponding to PL emission, was estimated using $\Delta N_{av} = \Delta N_0/L_D(\Delta N_{av})$ relationship. PL efficiency dependence on excitation fluence was numerically simulated (Eq. (1.34)) using carrier diffusion coefficient (Fig. 4.6b) and lifetime of 40 ns (Fig. 5.13b). Normalized B_{rad} coefficient was fitted by $B_{rad}/B_0 = 1/(1 + 3.5\times[\Delta N/10^{19} + \Delta N^2/3\times10^{39}]^{1.4})$ relationship. Impact of reabsorption was neglected as most PL signal arises below ~3.452 eV bandgap [34]. This peculiarity is a consequence of carrier

interaction with LO phonons. At higher excitations, main PL signal also arose below bandgap, indicating weak reabsorption impact again.

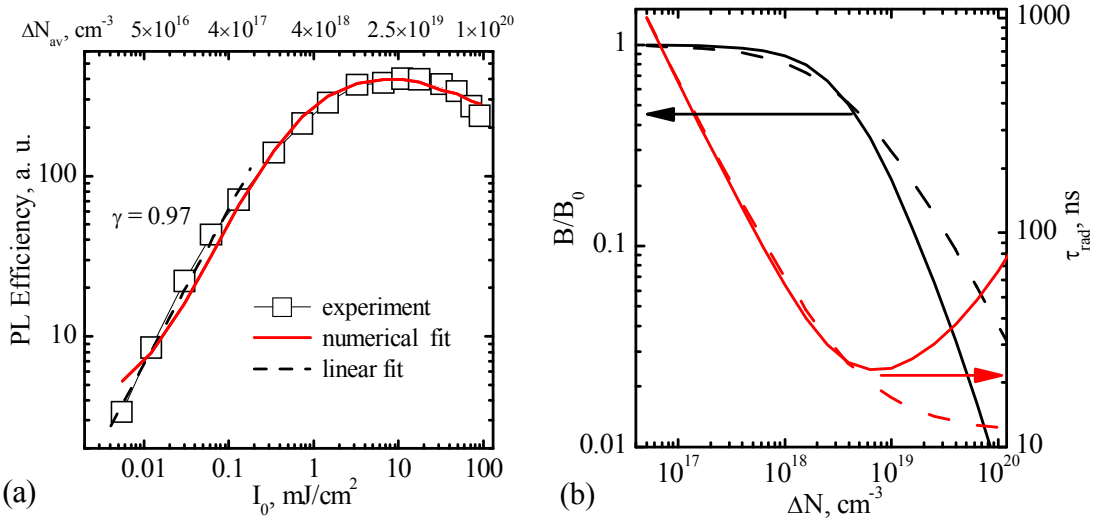

Fig. 5.31. PL efficiency with its numerical fit (a) and the normalized B_{rad} value (b) with corresponding radiative lifetime, obtained using $B_0 = 2\times10^{-11}$ cm^3/s [93]. Dashed curves show results, when reabsorption of 5×10^3 cm^{-1} is included.

The corresponding radiative lifetime for free space, calculated using B_0=2×10^{-11} cm^3/s [93], is provided in Fig 5.31b. It has minimum at about ~30 ns, therefore, the assumption of negligible impact of radiative carrier recombination to it decay proposed in previous section is verified, as light emission extraction efficiency through the excited surface is only ~4%, leading to effective radiative lifetime of ~400 ns. The saturation of B_{rad} can be a consequence of momentum space filling [113,114] as well as screening of carrier-phonon interactions (see Eq. 1.19). In thin InGaN quantum well LED structures the light extraction factors can be eliminated to reach radiative efficiency close to unity with maximum saturated recombination rate of: $1/\tau_{rad}$ =2×10^7 s^{-1} at $\Delta N > 10^{18}$ cm^{-3} [113].

In short, the TRPL and FCA transients at interband excitation conditions in GaN are determined by reabsorption, surface and bulk recombination processes, while radiative recombination impact is rather weak due to weak light extraction efficiency and radiative recombination rate saturation.

5.8. Short summary

1. The low-excitation nonradiative lifetime in 4H-SiC and 3C-SiC gradually increased with temperature due to activation of point defects (carbon vacancies), which capture cross section for holes was found much higher than that for electrons.
2. Lifetime mapping (with ~5 μm resolution) in a bulk HVPE grown GaN together with the inverse correlation of carrier diffusion coefficient and lifetime temperature dependences were in line with the proposed model of diffusion-limited nonradiative recombination on grain boundary defects. The interface recombination velocity on grain boundaries of GaN was found to be $S_{inter} = 4\times10^4$ cm/s and increased with temperature as $T^{3/2}$.
3. In "nitrogen-free" HPHT and CVD diamonds point defect limited free carrier lifetime (approaching 800 ns) was found temperature independent. In polycrystalline CVD diamond few orders of magnitude shorter lifetime indicated for huge point defect density.
4. Impact of surface recombination in SiC was evaluated by newly derived analytical formula, accounting for different surface recombination rate on different sample sides or at internal interface with substrate. High quality SiC and GaN sample surfaces exhibited by order of magnitude lower surface recombination velocity (S =1-5×10^3 cm/s) in comparison to the roughly polished ones (S >3×10^4 cm/s). While in CVD diamond even larger S =10^5 cm/s value was obtained due to strong mechanical subsurface polishing damage.
5. At high excitations (≥ ~10^{18} cm^{-3}) the lifetime decrease in SiC was governed by nonlinear Auger recombination. The temperature dependent Auger recombination rate in 4H-SiC was composed of the almost temperature independent unscreened Auger coefficient (C_0=(5±1)×10^{-31} cm^6/s), which becomes Coulomb-enhanced at low temperatures by coefficient $B_{CE}(T)$ =3.5×$10^{-9}/T^{1.5}$ and decreases at high carrier densities due to screening of carrier-polar optical phonon interaction. In 3C-SiC, the same Auger coefficient, C=(4±1)×10^{-32} cm^6/s, was determined on both

sample sides of a bulk sample by using either DT or DR techniques. The determined Auger and bimolecular coefficients in 3C-SiC were by order magnitude lower than in 4H-SiC, indicating that 3C-SiC is more suitable for power devices.

6. In diamonds, at high excitations strong lifetime reduction in T <300 K and T >300 K wings was observed. At low T it was caused by exciton (with lifetime $\tau_{ex\,LT}$=0.17×$T^{3/2}$ ns), biexciton and electron-hole droplet (with 1.5 ns lifetime) formation. Biexcitons and excitons are subject to strong Auger recombination, which effective coefficient value of C_0=4×10^{-31} cm^6/s was found. At high temperatures the exciton lifetime ($\tau_{ex\,HT}$ =5×10^{-5}×exp(490meV/k_BT) ns) decreased due to presumably trap assisted or Auger process.

7. The subnanosecond decay of PL transients in GaN was strongly affected by carrier diffusion away from the photoexcited thin surface region and by surface recombination, which diminished the emission signal essentially, preventing access to a correct lifetime determination. DT and LITG decays were less sensitive to the surface effects due to deeper carrier generation at 351 nm and independence on the carrier in-depth diffusion.

8. In GaN, saturation of radiative recombination rate and weak light extraction efficiency (~ 4%) indicated that minimal value of radiative lifetime is by order of magnitude larger than the nonradiative one. On the other hand, radiative recombination coefficient B_{rad} = 2.05×10^{-15} cm^3/s in 3C-SiC was determined to be carrier density independent.

6. Carrier trapping and recombination in compensated crystals

Wide-bandgap semiconductors tend to be contaminated by high concentration of deep acceptors, which drastically alter material properties. Commonly determination of latter impurity type and concentration needs destructive methods or weak photoluminescence signal investigations. In this chapter novel time-resolved optical technique based on DT principle has been applied to study the compensating trap density, their activation energy, optical ionization cross section, hole capture parameters. Trap density and their activation energy were determined from saturation of DT signal and recharged acceptor recovery time temperature dependence, respectively. Numerical modeling provided trap capture parameters. Carrier diffusion coefficient studies by LITG revealed strong diffusion coefficient reduction at low carrier densities due to electron electrostatic binding to the recharged acceptors. The numerical modeling description is provided in section 6.1. In sections 6.2 and 6.3 the determined data for 3C-SiC is described, while the diamond studies are provided in section 6.4. The chapter ends with a short summary which is followed by a concluding summary.

6.1. Numerical modelling of recharged acceptor dynamics

The excess carrier dynamics involves processes, which are illustrated in Fig. 6.1 in terms of possible electron transitions. At relatively low temperatures (< 150 K) and at low excitations ($\Delta N_0 < [Al^-]$), (i) all the generated holes will be trapped at Al^- with the capture time τ_c. In this case, the recovery of the equilibrium $[Al^-]$ (or boron $[B^-]$ in case of diamond) is reached through (ii) the donor-acceptor pair (DAP) recombination process and (iii) electron to acceptor recombination (eAl), since some of the nitrogen impurities are ionized. The measured decay time τ_{meas} from the DT kinetics thus gives information on the rates of these two processes, as $1/\tau_0 = 1/\tau_{DAP} + 1/\tau_{eAl}$. Upon raising the temperature, the thermal emission of holes, trapped by Al^0 with time τ_{th} (iv), starts to contribute to the recovery of Al^- and becomes dominant at high

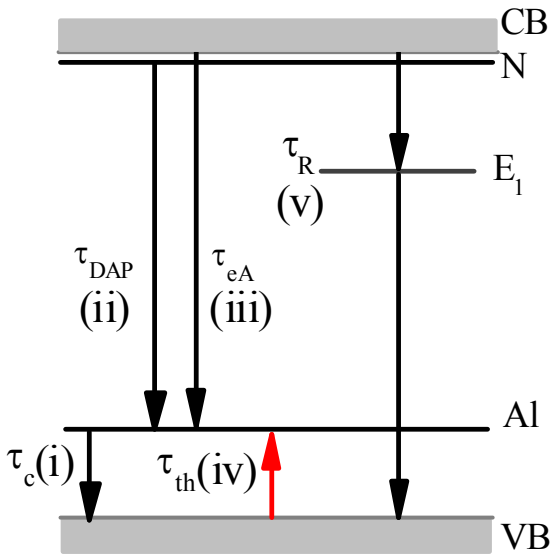

Fig. 6.1. Scheme of possible electron transitions in a compensated semiconductor, doped with the aluminum Al and nitrogen N impurities and containing carbon vacancy (V_c) related defects, E_1. [After P4,P29]

temperatures. The released holes can then recombine through the nonradiative E_1 centres, but also may be re-trapped at Al^-. The rate of re-trapping can be assumed to be much lower than the hole capture rate by E_1 centres, since a decrease of τ_{meas} is observed (as will be shown later). In the trap-saturation regime ($\Delta N_0 > [Al^-]$), contribution of the transition (v) is observed as a pathway of FC recombination. It will emerge as a fast transient in the DT kinetics being governed by recombination via E_1 centres (with recombination time $\tau_{SRH} = \tau_e + \tau_h$).

In order to perform a quantitative analysis of the DT decays, numerical modeling was employed, whereby the excitation-induced changes in the density of holes ΔN_h and neutral aluminum Al^0 were calculated at various temperatures and excess carrier densities. For this purpose the following equation system was used [1,172]:

$$\frac{d\Delta N_h}{dt} = -c_T g \Delta N_h \mathrm{Al}^- + c_T \mathrm{Al}^0 N_{VT} - \frac{\Delta N_h}{\tau_h}, \tag{6.1}$$

$$\frac{d\mathrm{Al}^0}{dt} = c_T g \Delta N_h \mathrm{Al}^- - c_T \mathrm{Al}^0 N_{VT} - \frac{\Delta N_h}{\tau_0}. \tag{6.2}$$

Here $g = 4$ is the degeneracy factor of Al in 3C-SiC [1], $N_{VT} = N_{vd}\exp(-E_a/k_BT)$, $N_{vd} = 2.23\times10^{15}\times T^{3/2}$ (cm^{-3}) [9] and E_a is the activation energy of Al, $c_T = s_h \times v_{th\,h}$ is the thermal capture coefficient of Al^-, with s_h and $v_{th\,h}$ being the hole capture cross section of Al^- and the average hole thermal velocity, respectively. The first term on the right-hand-side of equation (6.1) and

equation (6.2) correspond to the rate of trapping of holes by Al^- (process (i)), the second term describes the rate of thermal emission of holes by Al^0 (process (iv)), the last term of equation (6.1) represents the rate of recombination of free holes through deep traps (process (v)), and the last term of equation (6.2) describes the rate of recovery of the equilibrium [Al^-] (processes (ii) to (iii)).

Solution of the above equations provided approximate fit ($\tau_{TR} > \tau_h$ condition was assumed) for the experimental decays as $\tau_{meas}^{-1} = (\tau_{DAP})^{-1} + (\tau_{eAl})^{-1} + (\tau_{TR})^{-1}$, where

$$\tau_{TR} = \frac{\exp(E_a / k_B T)}{N_{vd}} \left(g\mathrm{Al}^- \tau_h + \frac{1}{c_T} \right) + \tau_h \tag{6.3}$$

is the thermal recombination time of holes, which is defined by the hole thermal emission time from Al^0, $\tau_{th} = \exp(E_a / k_B T) / N_{vd} c_T$, and the subsequent hole capture time by E_1 centres, as well as the possible re-trapping time of holes by Al^-.

Representative modeled decay kinetics of the photo-recharged Al and the hole densities are shown in Fig. 6.2 for different excitation levels and temperatures using parameters from Table 6.1. Process (i) can be seen as the initial rapid decrease of the density of holes with simultaneous increase of Al^0 density.

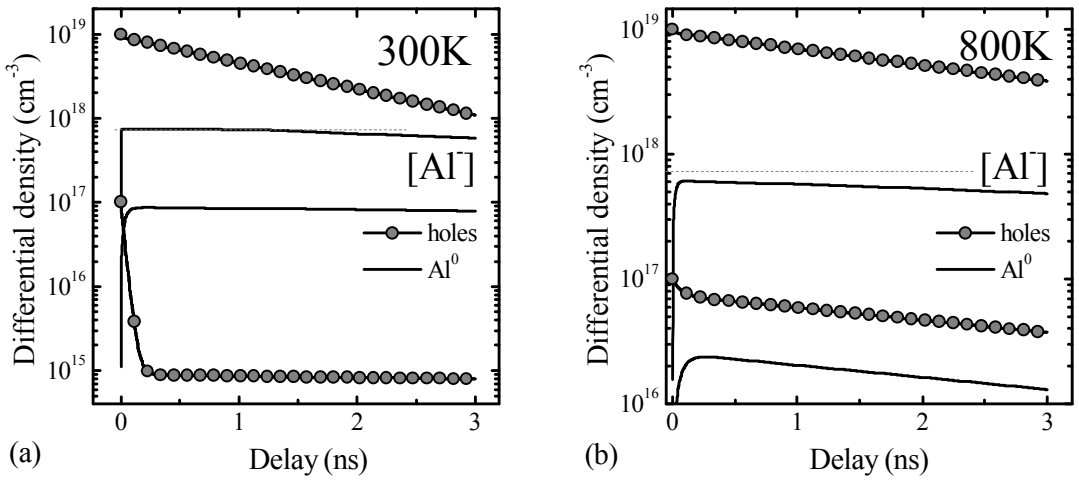

Fig. 6.2. Modeled decay kinetics of the hole and Al^0 concentrations at 300 K (a) and 800 K (b) at $\Delta N_0 = 10^{17}$ and 10^{19} cm^{-3}, according to Eqs. (6.1) and (6.2). The horizontal dashed line at 7.5×10^{17} cm^{-3} marks the concentration of equilibrium compensated aluminum, used in the modeling. [After P29]

At 800 K thermal effects on the decay kinetics can be observed – process (i) becomes significantly longer, due to a temperature-induced reduction of the hole capture cross-section for Al^-, which consequently results in an incomplete photo-recharge of Al^-, even at excess carrier density of 10^{19} cm^{-3}. At 80 K carrier capture by Al was much faster, thus concentration of free holes at low excitations was negligible. It was also observed from the modeling that at high excitations traps are almost saturated and free carrier recombination prevails.

6.2. Compensating Al concentration and activation energy in 3C-SiC

This section is focused on the determination of compensating aluminum concentration and activation energy in 3C-SiC under interband excitation. DT kinetics, measured at 80 K, avoid thermal ionization of the Al^0 impurities which is favorable for precise Al density determination. Fig. 6.3a shows the measured DT decays at different excitation fluences for the *n*-type layer (sample 3C7); similar decay kinetics were also observed in the *p*-type layer (sample 3C8).

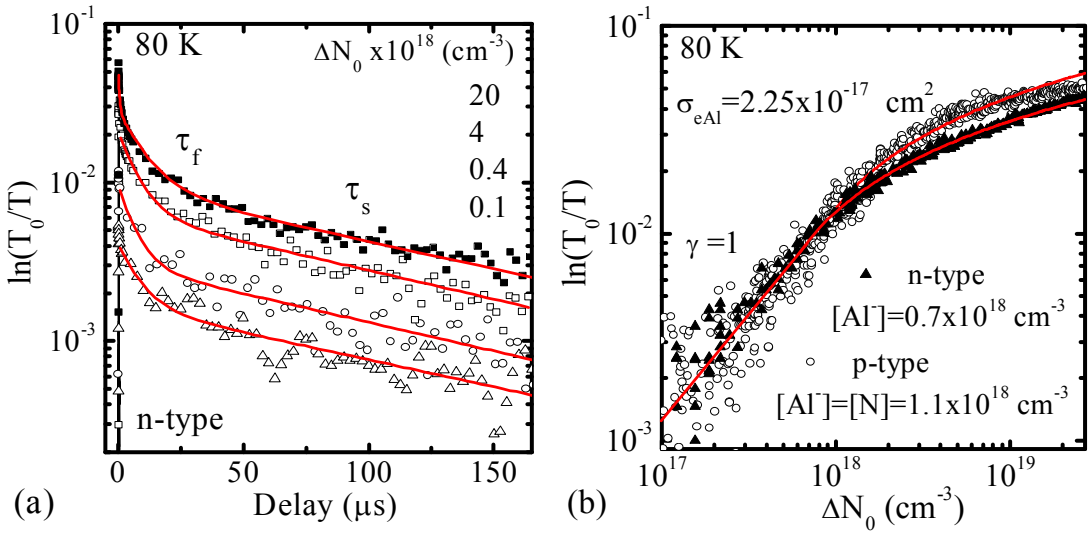

Fig. 6.3. (a) DT decays for the *n*-type layer at 80 K, measured at different excitation fluences. Lines are the two-exponential fits, except for the decays at the highest ΔN_0, for which a three-exponential fit was applied (due to a nonlinear processes). (b) Exposure characteristics for the two layers, measured at 80 K. Lines are the fits by Eqs. (6.4), (6.5). [After P29,P21]

The decay shapes in both samples were non-exponential for all excitation intensities, as expected due to the dominant DAP and eA processes (see section 6.1) that are responsible for the recovery of the initial equilibrium Al^- state at low temperature. The contribution of the fast excess carrier recombination in the trap saturation regime is not resolved in these DT kinetics, since a probe beam with ~2 ns duration was employed. For qualitative analysis the decay curve can approximated with initial τ_f (~ 10 μs) and exponential τ_s (~ 100 μs) time components (their temperature dependences are presented in Fig. 6.4b). Thus, up to $\Delta N_0 \sim 10^{18}$ cm^{-3} the measured DT kinetics reveal the rate of decay of the photo-recharged aluminum state [Al^0]. Consequently, the amplitude of the $\ln(T_0/T)$ signal corresponds to the aluminum-recharge induced absorption. It is seen that upon increasing the excitation intensity the trap-related absorption shows saturating behavior, which is observed more clearly in the exposure characteristics (EC) that are displayed in Fig. 6.3b. The saturation of the $\ln(T_0/T)$ signal arises due to the complete photo-recharge of all Al^- impurities. It allows determination of the total concentration of the minority dopants in the two layers.

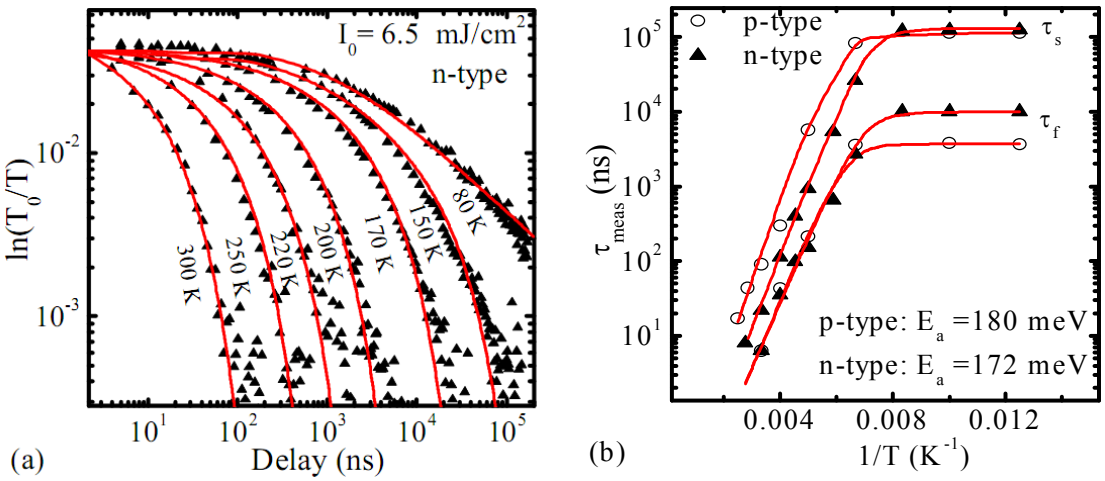

Fig. 6.4. (a) Temperature dependent decays for the *n*-type sample, measured at I_0 = 6.5 mJ/cm^2. (b) Determination of the activation energy in the two layers. Lines were obtained by Eqs. (6.1), (6.2) in (a) and by Eq. (6.3) in (b). [After P29,P21]

In the low excitation regime, when $\Delta N_0 < [Al^-]$, it can assumed that all excited holes are trapped at Al^-, therefore the in-depth distribution of recharged

aluminum P_{Al} follows the excess carrier in-depth profile $\Delta N(z) = \Delta N_0 \exp(-\alpha z)$ within the photoexcited layer of thickness $1/\alpha$. Thus, in the linear region of the measured signal (Fig. 6.3b) the following relationship is valid:

$$\ln(T_0/T) = \sigma_{eAl} \Delta N_0 / \alpha \,. \tag{6.4}$$

Here $\sigma_{eAl} = \sigma_e + \sigma_{Al}$ is the total absorption cross-section that is equal to the sum of the free electron absorption cross-section and the aluminum impurity ionisation cross-section, respectively. In the high excitation regime ($\Delta N_0 >$ [Al^-]), the in-depth profile of P_{Al} no longer follows that of the generated carriers, since within the initial photoexcited layer all available [Al^-] states are recharged (i.e. neutralized), thus P_{Al} = [Al^-]. At some point, within the in-depth profile of the generated carriers, the density of carriers decreases down to the density of Al^-, and so the thickness of this layer is given by $d_1 = \ln(\Delta N_0/[Al^-])/\alpha$. From this point and within a region of thickness $d_2 = 1/\alpha$ the density of recharged Al again follows that of the generated carriers; hence P_{Al} ($z<d_1$) = [Al^-], $P_{Al}(z>d_1) = \Delta N_0 \exp(-\alpha z)$ and the total change of DT is $\ln(T_0/T) = \sigma_{eAl}[Al^-](d_1+d_2)$. Thus, the DT signal measured in the high excitation regime can be described by a relation

$$\ln(T_0/T) = \sigma_{eAl}[Al^-]\{1 + \ln(\Delta N_0/[Al^-])\}/\alpha \tag{6.5}$$

which allows determination of the photo-recharged minority dopant concentration.

For the *n*-type layer, fitting Eq. (6.4) to the linear part of the EC gives $\sigma_{eAl} = 2.2\times10^{-17}$ cm^2. The absorption cross-section for free electrons is already known ($\sigma_e \sim 4.4\times10^{-18}$ cm^2, see section 3.1), thus $\sigma_{Al} = 1.7\times10^{-17}$ cm^2 was found. Thus the photo-ionization of Al^0 at 1064 nm wavelength occurs with a 4 times higher probability than that for the absorption by free electrons, indicating the dominant role of Al^0 in the attenuation of transmission of the probe beam. Fitting of Eq. (6.5) in the trap saturation regime gives [Al^-] = 7.2×10^{17} cm^{-3}, which corresponds to the total aluminum concentration, since in equilibrium all Al is compensated, and so all of it can be photo-recharged.

For the *p*-type layer, the signal also saturates due to a complete photo-recharge of the compensated aluminum, since the absorption cross-section of weakly N bound electrons can be assumed to be the same as that for free electrons. The linear part of the DT gives $\sigma_{Al} = 2.0\times10^{-17}$ cm^2, according to Eq. (6.4), in good agreement with that found in the *n*-type layer. In the trap saturation regime, the data is best fitted with $[Al^-] = 1.1\times10^{18}$ cm^{-3}. At equilibrium, the concentration of the compensated Al is equal to N, thus $[Al^-]$ corresponds to the total concentration of nitrogen in the *p*-type layer.

To determine the activation energy of aluminum, the DT measurements were carried out in the temperature range from 80 K to 300 K. Fig. 6.4a shows the measured DT kinetics at different temperatures and the dependences of the fast and slow decay components (τ_f, τ_s) on the inverse temperature are displayed in Fig. 6.4b. It is seen that from 80 K to 125 K τ_f and τ_s are constant, which indicates that the recombination rates $1/\tau_{DAP}$ and $1/\tau_{eAl}$ are temperature-independent. Decay is nonexponential due to changing with time DAP pair separation. A rapid decrease of τ_f and τ_s is observed at $T > 125$ K, indicating the dominant role of the thermal release of holes from Al^0 and their subsequent capture by E_1 centres in defining the two decay times. They arise due to changing with time $[Al^0]$ concentration. The fits to the measured DT kinetics (Fig. 6.4a) were obtained from numerical modeling using Eqs. (6.1) and (6.2), and so provided the activation energy of Al (E_a) as well as its hole capture cross-section (s_h). $E_a = (176 \pm 4)$ meV and $s_h = (1.0 \pm 0.3)\times10^{-15}$ cm^{-2} for both layers were found. Other samples (3C9-3C12) also exhibited similar activation energies, E_a = 160-210 meV. The obtained values of E_a fall within the (180-220) meV range, reported by other studies [173,174].

6.3. Impact of Al acceptors to carrier diffusion coefficient

Carrier lifetimes (τ_R) and carrier diffusion coefficient (D) were measured using LITG technique in the temperature range from 80 K to 800 K. The latter parameters were determined by monitoring the LITG kinetics at $\Lambda_1 = 1.96$ μm

and Λ_2 = 7.6 μm grating periods. Fig. 6.5 shows representative room temperature kinetics measured at two very different excess carrier densities.

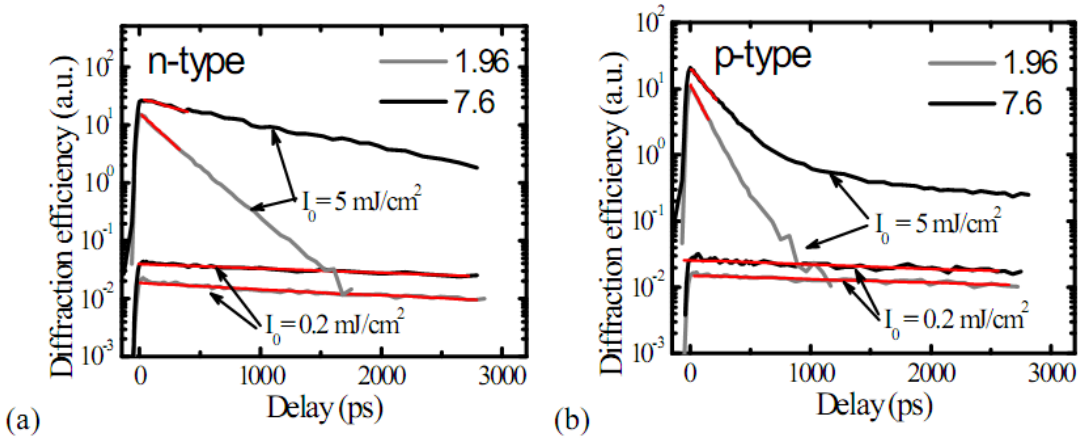

Fig. 6.5. Room temperature LITG kinetics for two grating periods and different excitation levels (0.2 mJ/cm^2 and 5 mJ/cm^2), corresponding to $\Delta N_0 = 0.7\times10^{18}$ cm^{-3} and $\Delta N_0 = 1.8\times10^{19}$ cm^{-3}, respectively. [After P29]

The LITG kinetics, displayed in Fig. 6.5, indicate that at low excitations ($\Delta N_0 < [Al^-]$) the transient gratings (with τ_1 and τ_2 decay times) in both samples are erased with similarly large decay time as in DT measurements. At this excess carrier density all the generated holes are trapped at the Al^- states, so the decay of the transient gratings are predominantly due to thermal release of trapped holes from the Al^0 states, while the carrier diffusion coefficient has negligible impact. At high excitations, when the Al^- states are well saturated, the LITG kinetics exhibit relatively fast and considerably different decay times for different grating periods, which indicates a significant impact of free carrier diffusion coefficient on the erasure of the transient gratings.

The determined values of D at various excitation levels are plotted in Fig. 6.6 for various sample temperatures. The dashed lines in the two plots are the expected $D(\Delta N_e,\Delta N_h)$ trends in a doped semiconductor, estimated according to Eq. (1.21). The D_e values were evaluated from electron mobilities in similarly compensated sample (~10^{18} cm^{-3} of Al) [76-78], where D_e= 2; 7.5 and 4 cm^2/s at 80; 300 and 800 K, respectively. The hole diffusivities D_h were determined from experimental D_a dependences: D_h= 0.9; 1.4 and 0.75 cm^2/s at 80; 300 and 800 K in *n*-type and rather similar of 0.8; 1.5 and 0.85 cm^2/s in *p*-type sample.

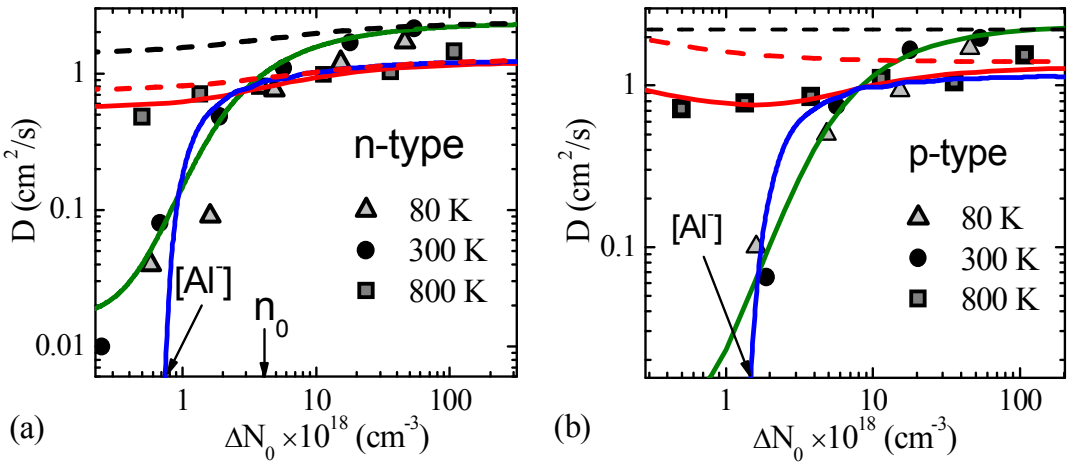

Fig. 6.6. Excitation dependence of the diffusion coefficient in the two layers for different temperatures. Lines are fits according to Eq. (6.6). The dashed lines at 300/800K represent the expected transition from the minority carrier diffusion to the bipolar diffusion, given by Eq. (1.21), when impact of hole capture was disregarded. [After P3,P4,P29]

It is seen that the measured $D(\Delta N)$ dependence at 800 K weakly varies with excitation (Fig. 6.6), while the D obtained at lower temperatures strongly drops at low excitations. The observed trend of $D(\Delta N_0)$ at $T \leq 300$ K was attributed to the high compensation of Al dopants, resulting in hole traps (Al^-) that at low excitations disable the diffusion. For fitting of the measured excitation dependences, in depth average carrier diffusion coefficient D_{av} in a highly compensated semiconductor was calculated:

$$D_{av} = \alpha \times \int D_a\left[\Delta N_e(z), \Delta N_h(z)\right]\chi(z)\exp(-\alpha z)dz,$$
$$\Delta N(z) = \Delta N_0 \exp(-\alpha z) = \Delta N_h(z) + \Delta Al^0(z). \qquad (6.6)$$

Here $\Delta N_e(z) = n_0 + \Delta N(z)$, $\Delta N_h(z) = p_0 + \chi\Delta N(z)$. The factor $\chi(z) = \Delta N_h(z)/\Delta N(z)$ was introduced to take into account the generation of free holes by thermal ionization of Al^0 (equilibrium and photo-recharged). $\Delta N(z)$ and $\Delta N_h(z)$ were obtained from the numerical modeling of the dynamics of hole and Al^0 state densities (Eqs. (6.1), (6.2)). For example, at 800 K at low excitations $\chi = 0.75$ and $\chi = 0.6$ were obtained for *n*- and *p*-type, respectively. The data for the *n*-type layer were fitted using $[Al^-] = 0.75\times10^{18}$ cm^{-3} and for the *p*-type layer $[Al^-] = 1.3\times10^{18}$ cm^{-3}. The $[Al^-]$ values, determined from the excitation dependence of D, are in good agreement with those determined from

the DT data in both layers, as was shown above. Finally, Table 6.1 lists the experimental and modeled parameters of the studied 3C-SiC samples.

Table 6.1. The determined material and aluminum-related parameters.

Sample	$[Al^-]$ $\times 10^{18}$ (cm^{-3})	$E_{a,\,Al}$ (meV)	s_h (Al^-) $(cm^2)^{RT}$	τ_R $(ns)^{RT}$	τ_h $(ns)^{RT}$
***n*-type**	**0.72-0.75**	**172±4**	$(1.0\pm0.3)\times10^{-15}$	**1.5±0.5**	**0.08±0.02**
***p*-type**	**1-1.3**	**180±4**	$(0.9\pm0.3)\times10^{-15}$	**0.38±0.1**	**0.19±0.04**

6.4. Recharged boron acceptor dynamics in diamond

The DT kinetics in diamonds C1 and C2 were used to determine both neutral boron and free carrier lifetime values (τ_B and τ_R), and absorption cross sections (σ_B and σ_{eh}) at various excitations and temperatures implying two photon excitation. In the bulk excitation case, carriers were generated by a Gaussian beam and DT decay was given by a modified relation taking into account the recharged boron absorption:

$$\mathrm{DT}(t)=\left[\sigma_B N_B \exp\left(-t/\tau_B\right)+\sigma_{eh}\left(\Delta N_{02}-N_B\right)\exp\left(-t/\tau_R\right)\right]\times d. \qquad (6.7)$$

Here excitation at 351 nm was used ($h\nu_3$ =3.55 eV), $\Delta N_{02}=bI_0^2/(2h\nu_3)$ is the generated electron-hole pair density, I_0 is the excitation fluence in mJ/cm^2, and b=30 cm/J (as determined in section 3.4). The negatively charged boron concentration N_B, recharged by generated holes, equals to ΔN_{02}, if the condition $N_B > \Delta N_{02}$ is satisfied. Neutral boron density decays with time τ_B. In the opposite case, part of holes are free and recombine via nitrogen defect with much shorter time, $\tau_h \sim \tau_R$.

The FCA signal in some parts of the samples at zero delay was weaker due to a fast initial decay (comparable to system time resolution ~5 ns) in more defective regions. In C1 sample, the average lifetime τ_R in the central part reached 480 ns, while on the edge sides it was of ~300 ns. On the other hand, in C2 lifetime was ~240 ns (see Fig. 6.7) and weakly depended on lateral position. At large delays (~20 μs) free carriers recombined and only recharged boron determined the DT signal. DT value in C2 sample before excitation

pulse indicates residual absorption because of very slow recovery of the recharged boron, exceeding the interval between the laser pulses (0.1 s).

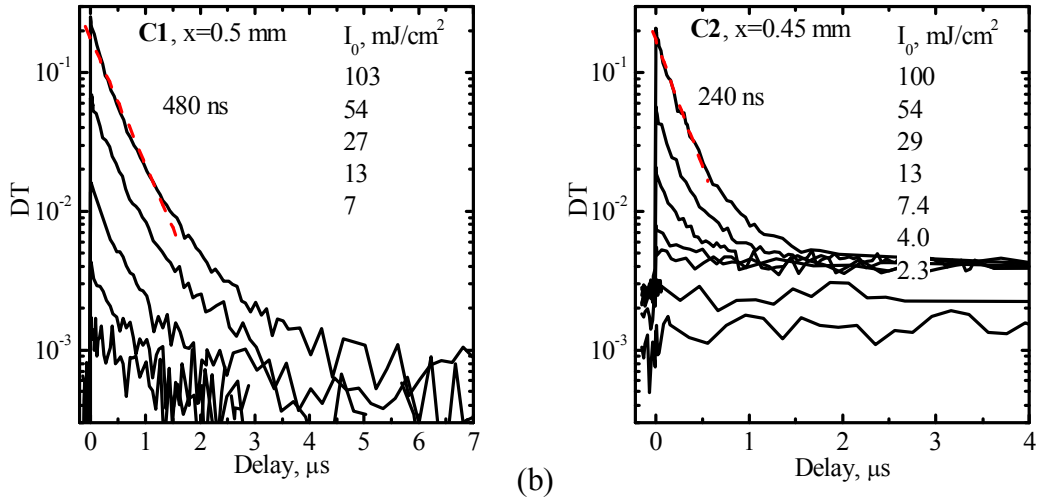

Fig. 6.7. DT decay curves in central parts of the samples C1 (a) and C2 (b). [After P22]

The slow recovery time of recharged boron is shown in Fig. 6.8a. It is observed that the decay becomes much faster with temperature increase. At low temperatures (T <150 K) the decay is slow (about ~500 s in the beginning). In this case the decay is probably dominated by DAP recombination and partly by nonradiative processes. At higher temperatures, boron activates and decay becomes faster, as the thermally generated holes can be easily captured by nitrogen and recombine on it nonradiatively. Therefore the decay shortening can be ascribed to thermal activation of holes and their recombination on nitrogen with τ_{300K} =0.4 s nonradiative time, which coincides with the hole thermal generation time according Eq. (6.3): $\tau_{th} = \exp(E_{B0}/k_BT)/(N_v v_{th\ h}\sigma_0) \approx 0.3$ s. Here density of states in valence band is $N_{vd} = 2\times10^{19}$ cm^{-3}, hole thermal speed is $v_{th\ h} = 1.0\times10^7$ cm/s, and $\sigma_0 = 3\text{-}4\times10^{-20}$ cm^2 is the hole capture cross section to ground state of boron [175].

The blue DAP (peak at 2.5 eV) was observed by PL not to change strongly in intensity up to 800 K. Therefore the observed activation of slow decay (Fig. 6.8b) is probably dominated by nonradiative recombination rate and DAP recombination efficiency should be lower than unity.

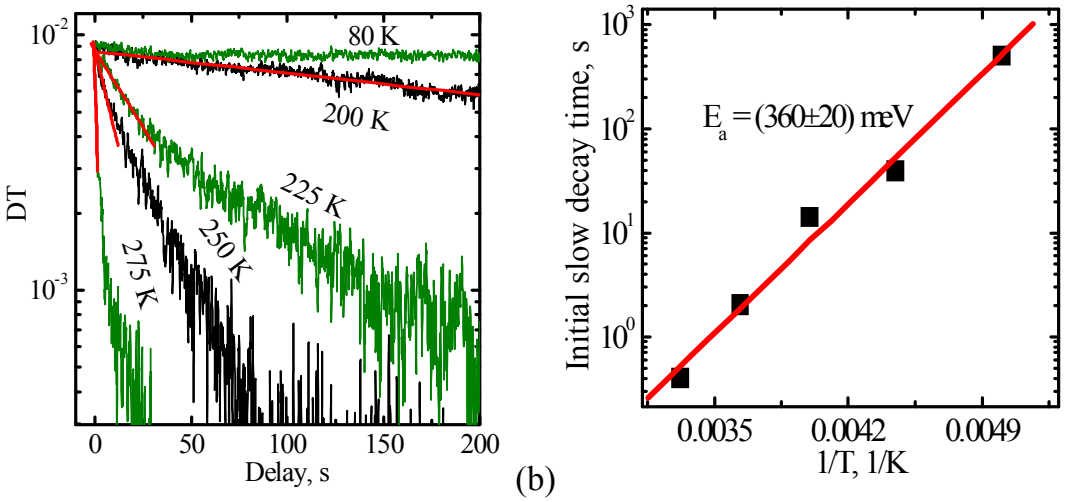

Fig. 6.8. Photoneutralized boron recovery decays (a) and their activation energy (b) in C2 sample. [P22]

It was observed that PL emission saturated with boron trap saturation. This again indicates that free hole to nitrogen transitions are nonradiative, as nitrogen is a nonradiative recombination center [67]. Therefore boron is needed to observe DAP luminescence.

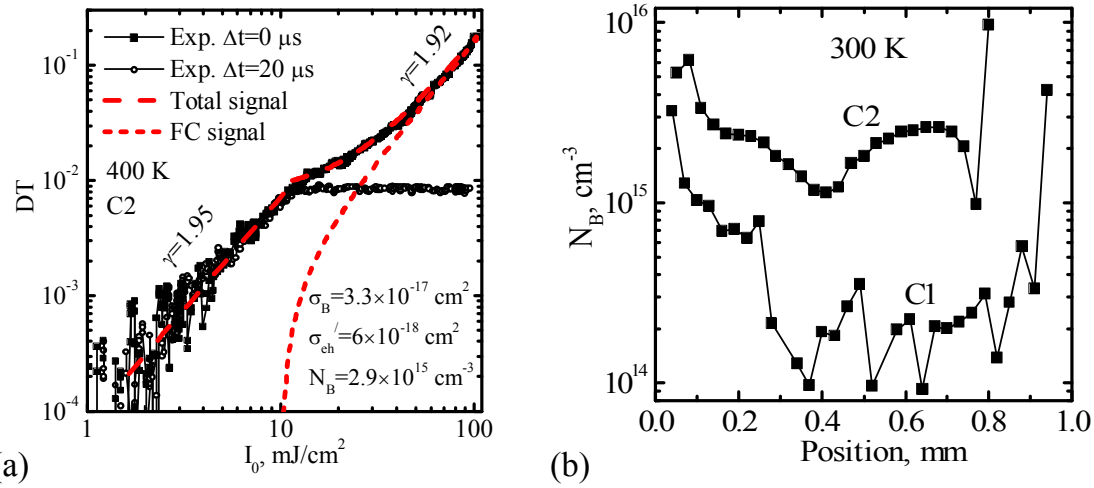

Fig. 6.9. Determination of boron absorption cross section (a) and planar distribution of boron concentration (b) in C1 and C2 samples. [P22]

The boron density was determined varying excitation fluence and applying Eq. (6.7) for approximation of the DT signal in Fig. 6.9a (here, higher temperature was used to avoid accumulation of the slow decay). Clear saturation of boron centers at high photo-excitations was observed, while at low excitations the Eq. (6.7) provided boron absorption cross section at 1064

nm, σ_B =(3.3±0.5)×10^{-17} cm^2, being approximately 4 times larger than σ_{eh}. The determined value is close to literature data, σ_B(for 0.7 eV) =2.3×10^{-17} cm^2 for a sample with 4.4×10^{18} cm^{-3} boron concentration [176]. Probe quantum energy is higher in this work, thus the σ_B value is larger. The saturated DT signal did not change (within error bar) with temperature, indicating that σ_B is temperature independent (as boron is a deep impurity [30]). Using the determined σ_B, the boron lateral distribution in the samples was calculated (Fig. 6.9b). The sample C1 exhibited an order of magnitude lower boron density than the C2 in its central part, thus blue PL intensity was lower. Due to high concentration and more homogeneously distributed B impurity in the sample C2, it revealed the strong luminescence (while in C1, the emission was strong only at its B-rich edges). Therefore, the inhomogeneous distribution of boron impurity can be scanned using the below- bandgap excitation.

6.5. Short summary

1. Photoelectrical parameters were evaluated in compensated *n*-type and *p*-type 3C-SiC layers and "nitrogen-free" HPHT diamonds by a method based on a complete photo-recharge of an acceptor impurity and monitoring of its recovery to the initial charge state.
2. The method provided activation energy of acceptor-type impurities (~200 meV for aluminum in 3C-SiC and 340 meV for boron in diamond) and their concentrations (~10^{16}-10^{18} cm^{-3} and ~10^{14}-10^{16} cm^{-3}, respectively).
3. The DT signal at low fluences provided the photoionization cross-section of Al^0 and B^0 at 1064 nm, which values were found to be about 4 times higher than that of free electron-hole pairs.
4. In a diamond plate, planar scanning of photoneutralized boron absorption provided strongly inhomogeneous spatial variation of B density. Correlation between boron density and its related DAP intensity was proved.

Concluding summary

1. Precise control of photogenerated carrier density was achieved by (i) measuring temperature dependent interband absorption coefficients by novel diffraction based technique and (ii) determining two-photon absorption coefficients from the calibrated value of diffraction efficiency. Surface, bulk and nonlinear recombination rates were separated combining time-resolved DR, DT, LITG and TRPL measurements and numerical modeling.

2. The increase of indirect interband absorption coefficient with temperature in SiC and diamond was approximated using ~60 meV and 160 meV phonon energies and the temperature dependent decrease of bandgaps. Two photon absorption coefficients were found temperature independent and weakly dependent on polarization in GaN.

3. Temperature dependences of free carrier absorption cross section, σ_{eh}, were explained by different carrier scattering by phonons in virtual level. The polarization dependence of σ_{eh} in GaN was rather strong ($\sigma_{\perp}/\sigma_{\parallel}$ = 6.5) at 1053 nm probe wavelength due to the valence band anisotropy, while at 527 nm wavelength the cross section was isotropic and related to electron transitions between the lower and upper conduction bands.

4. Decreasing with excitation ambipolar diffusion coefficient in SiC and GaN is governed by bandgap renormalization at low excitations, while its increase at high carrier densities is determined by carrier plasma degeneracy and screening of carrier-phonon interaction.

5. Strong dependence of carrier diffusion coefficient on nonequilibrium carrier density in diamond was explained by formation of excitons, biexcitons, electron-hole droplets, having lower diffusion coefficient due to higher mass. Additional contribution of electron-hole scattering and exciton-exciton scattering leads to strong decrease of D at 300 K. At very high excitations carrier degeneracy, Coulomb interaction screening and exciton ionization takes place, leading to increase of diffusion coefficient.

6. Bulk carrier lifetime in SiC, mono- and poly-crystalline diamonds is determined by point defects, while in thin GaN layers it is limited by diffusive carrier flow to grain boundaries as confirmed by carrier lifetime microscopy measurements and inverse correlation of lifetime and diffusion coefficient temperature dependences.

7. Saturation of radiative recombination rate in GaN and low light extraction efficiency indicated that the calculated radiative lifetime is by order of magnitude larger than the measured nonradiative one. On the other hand, radiative recombination coefficient in 3C-SiC was determined to be carrier density independent and well agreed with theoretical calculations.

8. Nonradiative nonlinear recombination in SiC is dominated by phonon assisted Auger process, being Coulombically enhanced at low carrier densities and screened at high ones. The unscreened Auger coefficient was almost temperature independent in 4H-SiC.

9. In diamonds, strong decrease of lifetime in T <300 K and T >300 K wings was observed. At low temperatures, it was caused by Auger recombination in exciton, biexciton and electron-hole droplets (with 1.5 ns lifetime). At high temperatures, the decrease of lifetime was explained by trap assisted Auger process (with 560 meV threshold).

10. Compensating acceptor density in cubic SiC and diamond was determined using full recharge of acceptors under interband excitation. Concentrations of aluminum [Al^-] ~10^{16}-10^{18} cm^{-3} and of boron [B^-] ~10^{14}-10^{16} cm^{-3} were determined for 3C-SiC and diamond, respectively. Temperature dependence of recharged trap relaxation provided the trap activation energies (200 and 340 meV for 3C-SiC and diamond, respectively). Four times higher ionization cross sections for acceptors were determined in comparison to free carrier absorption cross sections. Much lower carrier diffusion coefficient at excess carrier density below acceptor concentration was explained by impact of internal space charge field between the immobile recharged acceptors and electrons.

References

[1] S. M. Sze and K. K. Ng, *Physics of Semiconductor Devices*, third ed. (Wiley Interscience, New Jersey, 2007).

[2] A. Dargys and J. Kundrotas, *Handbook on physical properties of Ge, Si, GaAs and InP* (Science and Encyclopedia Publishers, Vilnius, 1994).

[3] S. Adachi, *Properties of Group-IV, III–V and II–VI Semiconductors* (Wiley, New York, 2005).

[4] G. L. Harris, *Properties of Silicon Carbide* (INSPEC, London, 1995).

[5] M. B. J. Wijesundara and R. G. Azevedo, *Silicon Carbide Microsystems for Harsh Environments* (Springer, New York, 2011).

[6] H. Morkoc, S. Strite, G. B. Gao, M. E. Lin, B. Sverdlov and M. Burns, Journal of Applied Physics **76**, 1363 (1994).

[7] K. Takahashi, A. Yoshikawa and A. Sandhu (Eds.), *Wide Bandgap Semiconductors - Fundamental Properties and Modern Photonic and Electronic Devices* (Springer-Verlag, Berlin, 2007).

[8] E. Janzen, A. Gali, A. Henry, I. Ivanov, B. Magnusson and N. Son, Defects in SiC, in *Defects in Microelectronic Materials and Devices* (CRC Press, 2008).

[9] http://www.ioffe.rssi.ru/SVA/NSM/

[10] H. Nagasawa and K. Yagi, Phys. Status Solidi B **202**, 335 (1997).

[11] J. J. Gracio, Q. H. Fan and J. C. Madaleno, J. Phys. D: Appl. Phys. **43**, 374017 (2010).

[12] P. T. Fini and B. A. Haskell, Nonpolar and Semipolar GaN Growth by HVPE in *Technology of Gallium Nitride Crystal Growth* (Springer Series in Materials Science, Vol. 133, 2010).

[13] M. H. Nazaré and A. J. Neves (Eds.), *Properties, Growth, and Applications of Diamond* (Inspec, London, 2001).

[14] R. S. Wagner and W. C. Ellis, Appl. Phys. Lett. **4**, 89 (1964).

[15] W. M. Vetter and M. Dudley, J. Cryst. Growth **260**, 201 (2004).

[16] P. Bhattacharya, R. Fornari and H. Kamimura (Eds.), *Comprehensive Semiconductor Science and Technology*, (Elsevier, 2011).

[17] O. Kordina, Linköping Studies in Science and Technology, A Dissertation: No. 352 (Linköping University, 1994).

[18] A. Belabbes, C. Panse, J. Furthmüller and F. Bechstedt, Phys. Rev. B **86**, 075208 (2012).

[19] C. Raffy, J. Furthmüller and F. Bechstedt, Phys. Rev. B **66**, 075201 (2002).

[20] H. Okumura, S. Misawa and S. Yoshida, Appl. Phys. Lett. **59**, 1058 (1991).

[21] H. J. Leea, H. Ryua, C. -R. Leea and K. Kimb, J. Cryst. Growth **191**, 621 (1998).

[22] F. P. Bundy and J. S. Kasper, J. Chem. Phys. **46**, 4737 (1967).

[23] C. Persson and U. Lindefelt, J. Appl. Phys. **82**, 5496 (1997).

[24] Y. C. Yeo, T. C. Chong and M. F. Li, J. Appl. Phys. **83**, 1429 (1998).

[25] F. Nava, C. Canali, C. Jacoboni, L. Reggiani and S. F. Kozlov, Solid State Commun. **33**, 475 (1980).

[26] C. Y. Fong and B. M. Klein: *Diamond: Electronic Properties and Applications*, eds. L. S. Pan and D. R. Kania (Kluver, Boston, 1995).

[27] M. Dvorak, S. -H. Wei and Z. Wu, Phys. Rev. Lett. **110**, 016402 (2013).

[28] M. Ikeda and H. Matsunami, Phys. Status Solidi A **58**, 657 (1980).

[29] P. J. Dean, E. C. Lightowlers and D. R. Wight, Phys. Rev. **140**, A352 (1965).

[30] B. K. Ridley, *Quantum processes in semiconductors* (Clarendon Press, Oxford, 1999).

[31] R. A. Fisher, *Optical phase conjugation* (Academic Press, London, 1983).

[32] N. Peyghambarian, S. W. Koch and A. Mysyrowicz, *Introduction to semiconductor optics* (Prentice Hall, 1993).

[33] C. Klingshirn, *Semiconductor Optics*, second ed., (Springer-Verlag, Berlin, 2005).

[34] J. F. Muth, J. H. Lee, I. K. Shmagin and R. M. Kolbas, Appl. Phys. Lett. **71** 2572 (1997).

[35] C. D. Clark, P. J. Dean and P. V. Harris, Proc. Roy. Soc. (London) **A277**, 312-329 (1964).

[36] J. S. Im, A. Moritz, F. Steuber, V. Harle, F. Scholtz, and A. Hangleiter, Appl. Phys. Lett. **70**, 631 (1997).

[37] A. Galeckas, P. Grivickas, V. Grivickas, V. Bikbajevas and J. Linnros, Phys. Status Solidi A **191**, 613 (2002).

[38] R. Passler, Phys. Status Solidi B **216**, 975 (1999).

[39] P. Grivickas, V. Grivickas, J. Linnros and A. Galeckas, J. Appl. Phys. **101**, 123521 (2007).

[40] W. J. Choyke, Mater. Res. Bull. **4**, 141 (1969).

[41] P. Ščajev and K. Jarašiūnas, J. Phys. D: Appl. Phys. **42**, 055413 (2009).

[42] G. R. Fowles, *Introduction to Modern Optics* (Dover Publications, New York, 1975).

[43] S. Zollner, J. G. Chen and E. Duda, J. Appl. Phys. **85**, 4419 (1999).

[44] E. Ejder, Phys. Status Solidi A **6**, 445 (1971).

[45] D. F. Edwards and E. Ochoa, J. Opt. Soc. Amer. **71**, 607 (1981).

[46] J. Pernot, W. Zawadzki, S. Contreras, J. L. Robert, E. Neyret and L. Di Cioccio, J. Appl. Phys. **90**, 1869 (2001).

[47] J. D. Wiley, in *Semiconductor and Semimetals*, edited by R. K. Willardson and A. C. Beer (Academic, New York, 1975), Vol 10.

[48] C. Erginsoy, Phys. Rev. **79**, 1013 (1950).

[49] J. R. Meyer and F. J. Bartoli, Phys. Rev. B **24**, 2089 (1981).

[50] M. Costato, G. Gagliani, C. Jacoboni and L. Reggiani, J. Phys. Chem. Solids **35**, 1605 (1974).

[51] J. Pernot, P. N. Volpe, F. Omnes, P. Muret, V. Mortet, K. Haenen and T. Teraji, Phys. Rev. B **81**, 205203 (2010).

[52] E. M. Conwell and M. O. Vassel, Phys. Rev. **166**, 797 (1968).

[53] J. F. Schetzina and J. P. McKelvey, Phys. Rev. B **2**, 1869 (1970).

[54] J. F. Young and H. M. Driel, Phys. Rev. B **26**, 2147 (1982).

[55] N. G. Nilsson, Phys. Status Solidi A **19**, K75 (1973).

[56] C. Persson, U. Lindefelt and B. E. Sernelius, Solid State Electron. **44**, 471 (2000).

[57] N. H. Fletcher, Proceedings of the IRE, 862 (1956).

[58] J. Shumway and D. M. Ceperley, Phys. Rev. B **63**, 165209 (2001).

[59] H. Akiyama, T. Matsusue and H. Sakaki, Phys. Rev. B **49**, 14523 (1994).

[60] D. K. Schroder, *Semiconductor Material and Device Characterization* (Wiley, New York, 1990).

[61] J. Linnros, J. Appl. Phys. **84** , 275 (1998).

[62] W. Shockley and W. T. Read, Phys. Rev. **87**, 835 (1952).

[63] R. N. Hall, Phys. Rev. **87**, 387 (1952).

[64] P. T. Landsberg, Appl. Phys. Lett. **50**, 745 (1987).

[65] A. Hangleiter and R. Hacker, Phys. Rev. Lett. **65**, 215 (1990).

[66] L. Storasta and H. Tsuchida, Appl. Phys. Lett. **90**, 062116 (2007).

[67] L. S. Pan, D. R. Kania, P. Pianetta, J. W. Ager III, M. I. Landstrass and S. Han, J. Appl. Phys. **73**, 2888 (1993).

[68] T. Malinauskas, R. Aleksiejūnas, K. Jarašiūnas, B. Beaumont, P. Gibart, A. Kakanakova-Georgieva, E. Janzen, D. Gogova, B. Monemar and M. Heuken, J. Cryst. Growth **300**, 223 (2007).

[69] T. Trupke, M. A. Green, P. Wurfel, P. P. Altermatt, A. Wang, J. Zhao and R. Corkish, J. Appl. Phys. **64**, 4930 (2003).

[70] A. Dmitriev and A. Oruzheinikov, J. Appl. Phys. **86**, 3241 (1999).

[71] E. F. Schubert, *Physical Foundations of Solid-State Devices* (New York, 2007).

[72] M. Takeshima, Phys. Rev. B **23**, 6625 (1981).

[73] M. Boulou and D. Bois, J. Appl. Phys. **48**, 4713 (1977).

[74] J. Lange, J. Appl. Phys. **35**, 2659 (1964).

[75] M. Nesladek, A. Bogdan, W. Deferme, N. Tranchant and P. Bergonzo, Diam. Relat. Mater. **17**, 1235 (2008).

[76] M. Yamanaka, H. Daimon, E. Sakuma, S. Misawa, K. Endo and S. Yoshida, Jpn. J. Appl. Phys. **26**, L533 (1987).

[77] M. Shinohara, M. Yamanaka, H. Daimon, E. Sakuma, H. Okumura, S. Misawa, K. Endo and S. Yoshida, Jpn. J. Appl. Phys. **27**, L433 (1988).

[78] M. Yamanaka, H. Daimon, E. Sakuma, S. Misawa and S. Yoshida, J. Appl. Phys. **61**, 599 (1987).

[79] J. Pernot, W. Zawadzki, S. Contreras, J. L. Robert, E. Neyret and L. Di Cioccio, J. Appl. Phys. **90**, 1869 (2001).

[80] J. Pernot, S. Contreras and J. Camassel, J. Appl. Phys. **98**, 023706 (2005).

[81] M. Ilegems and H. C. Montgomery, J. Phys. Chem. Solids **34**, 885 (1972).

[82] M. Rubin, N. Newman, J. S. Chan, T. C. Fu and J. T. Ross, Appl. Phys. Lett. **64**, 64 (1994).

[83] J. Walker, Rep. Prog. Phys. **42**, 1606 (1979).

[84] M. Zaitsev, *Optical Properties of Diamond: A Data Handbook* (Springer, Berlin, 2001).

[85] J. Pernot, C. Tavares, E. Gheeraert and E. Bustarret, M. Katagiri and S. Koizumi, Appl. Phys. Lett. **89,** 122111 (2006).

[86] L. Reggiani, D. Waechter and S. Zukotynskii, Phys. Rev. B **28**, 3550 (1983).

[87] J. Isberg, J. Hammersberg, E. Johansson, T. Wikstrom, D. J. Twitchen, A. J. Whitehead, S. E. Coe and G. A. Scarsbrook, Science **297**, 1670 (2002).

[88] J. Isberg, A. Lindblom, A. Tajani and D. Twitchen, Phys. Status Solidi A **202**, 2194 (2005).

[89] C. A. Hoffman, K. Jarašiūnas, H. J. Gerritsen and A. Nurmikko, Appl. Phys. Lett. **33**, 536 (1978).

[90] P. Grivickas, J. Linnros and V. Grivickas, J. Mater. Res. **16**, 524 (2001).

[91] Yu-Chue Fong and S. R. J. Brueck, Appl. Phys. Lett. **61**, 1332 (1992).

[92] K. Neimontas, T. Malinauskas, R. Aleksiejūnas, M. Sūdžius, K. Jarašiūnas, L. Storasta, J. P. Bergman, and E. Janzen, Semicond. Sci. Technol. **21,** 52 (2006).

[93] T. Malinauskas, K. Jarašiūnas, R. Aleksiejūnas, D. Gogova, B. Monemar, B. Beaumont and P. Gibart, Phys. Status Solidi B **243**, 1426 (2006).

[94] T. Malinauskas, K. Jarašiūnas, M. Heuken, F. Scholz, and P. Bruckner, Phys. Status Solidi C **6**, S743 (2009).

[95] T. Malinauskas, K. Jarašiūnas, E. Ivakin, N. Tranchant and M. Nesladek, Phys. Status Solidi A **207**, 2058 (2010).

[96] M. Kozák, F. Trojánek and P. Malý, Opt. Lett. **37**, 2049 (2012).

[97] M. Kunst and G. Beck, J. Appl. Phys. **60**, 3558 (1986).

[98] J. Hassan and J. P. Bergman, J. Appl. Phys. **105**, 123518 (2009).

[99] A. Galeckas, V. Grivickas, J. Linnros, H. Bleichner and C. Hallin, Appl. Phys. Lett. **81**, 3522 (1997).

[100] P. B. Klein, J. Appl. Phys. **103**, 033702 (2008).

[101] R. J. Kumar, J. M. Borrego, R. J. Gutmann, J. R. Jenny, D. P. Malta, H. McD. Hobgood and C. H. Carter, Jr., J. Appl. Phys. **102**, 013704 (2007).

[102] O. Kordina, J. P. Bergman, C. Hallin and E. Janzen, Appl. Phys. Lett. **69**, 679 (1996).

[103] S. Ichikawa, K. Kawahara, J. Suda and T. Kimoto, Appl. Phys. Express **5**, 101301 (2012).

[104] J. Mickevičius and M. S. Shur, R. S. Qhalid Fareed, J. P. Zhang, R. Gaska and G. Tamulaitis, Appl. Phys. Lett. **87**, 241918 (2005).

[105] T. Malinauskas, K. Jarašiūnas, S. Miasojedovas, S. Juršėnas, B. Beaumont and P. Gibart, Appl. Phys. Lett. **88**, 202109 (2006).

[106] Y. Zhong, K. S. Wong, W. Zhang and D. C. Look, Appl. Phys. Lett. **89**, 022108 (2006).

[107] S. Juršėnas, S. Miasojedovas, A. Žukauskas, B. Lucznik, I. Gregory and T. Suski, Appl. Phys. Lett. **89,** 172119 (2007).

[108] T. Malinauskas, K. Jarašiūnas, E. Ivakin, V. Ralchenko, A. Gontar and S. Ivakhnenko, Diam. Relat. Mater. **17**, 1212 (2008).

[109] T. Teraji, S. Yoshizaki, S. Mitani, T. Watanabe and T. Ito, J. Appl. Phys. **96**, 7300 (2004).

[110] J. Hammersberg, J. Isberg, E. Johansson, T. Lundström, O. Hjortstam and H. Bernhoff, Diam. Relat. Mater. **10**, 574 (2001).

[111] R. Ulbricht, S. T. van der Post, J. P. Goss, P. R. Briddon, R. Jones, R. U. A. Khan and M. Bonn, Phys. Rev. B **84**, 165202 (2011).

[112] A. Galeckas, J. Linnros and V. Grivickas, Appl. Phys. Lett. **71** 3269 (1997).

[113] J. -I. Shim, H. Kim, D. -S. Shin and H. -Y. Yoo, J. Korean Phys. Soc. **58**, 503 (2011).

[114] G. Bourdon, I. Robert, I. Sagnes and I. Abram, J. Appl. Phys. **92**, 6595 (2002).

[115] F. Bertazzi, M. Goano and E. Bellotti, Appl. Phys. Lett. **97**, 231118 (2010).

[116] H. Nagasawa, K. Yagi, T. Kawahara, N. Hatta, G. Pensl, W.J. Choyke, T. Yamada, K. M. Itoh and A. Schoner, *Silicon Carbide, Recent Major Advances*, ed. W. J. Choyke, H. Matsunami and G. Pensl (New York: Springer, 2004), pp. 207–228.

[117] H. Nagasawa, T. Kawahara and K. Yagi, Mater. Sci. Forum **389–393**, 319 (2002).

[118] J. Hassan, J. P. Bergman, A. Henry, H. Pedersen, P. J. McNally and E. Janzen, Mater. Sci. Forum **556-557**, 53 (2007).

[119] G. Manolis, M. Beshkova, M. Syväjärvi, R. Yakimova and K. Jarašiūnas, Mater. Sci. Forum **679-680**, 161 (2011).

[120] G. Ferro, Mater. Sci. Forum **645-648**, 49 (2010).

[121] N. Jegenyes**,** G. Manolis, J. Lorenzzi, V. Soulière, D. Dompoint, A. Boulle, G. Ferro and K. Jarašiūnas, Mater. Sci. Forum **679-680**, 153 (2011).

[122] A. A. Lebedev, V. V. Zelenin, P. L. Abramov, E. V. Bogdanova, S. P. Lebedev, D. K. Nel'son, B. S. Razbirin, M. P. Shcheglov, A. S. Tregubova, M. Suvajarvi and R. Yakimova, Semiconductors **41**, 263 (2007).

[123] A. A. Lebedev, P. L. Abramov, N. V. Agrinskaya, V. I. Kozub, S. P. Lebedev, G. A. Oganesyan, A. S. Tregubova, D. V. Shamshur and M. O. Skvortsova, J. Appl. Phys. **105**, 023706 (2009).

[124] A. A. Lebedev, P. L Abramov, E. V Bogdanova, S. P. Lebedev, D. K. Nel'son, G. A. Oganesyan, A. S Tregubova and R. Yakimova, Semicond. Sci. Technol **23**, 075004 (2008).

[125] M. A. Reshchikov, H. Morkoc, S. S. Park and K. Y. Lee, Appl. Phys. Lett. **78**, 3041 (2001); ibid. **81**, 4970 (2002).

[126] T. Paskova, D. A. Hanser and K. R. Evans, Proc. IEEE **98**, 1324 (2010).

[127] N. V. Novikov, T. A. Nachalna, S. Ivakhnenko, O. A. Zanevsky, I. S. Belousov, V. G. Malogolovets, G. A. Podzyarei and L. A. Romanko, Diam. Relat. Mater. **12**, 1990 (2003).

[128] A. Tallaire, A. T. Collins, D. Charles, J. Achard, R. Sussmann, A. Gicquel, M. E. Newton, A. M. Edmonds and R. J. Cruddace, Diam. Relat. Mater. **15**, 1700 (2006).

[129] G. Bogdan, K. De Corte, W. Deferme, K. Haenen and M. Nesládek, Phys. Status Solidi A **203**, 3063 (2006).

[130] N. Habka, J. Barjon, A. Lazea and K. Haenen, J. Appl. Phys. **107**, 103531 (2010).

[131] H. J. Eichler, P. Gunter and D. W. Pohl, *Laser-induced Dynamic Gratings* (Springer, Berlin, 1986).

[132] K. Jarašiūnas, Nonlinear optical characterization of photoelectrical properties of wide bandgap semiconductors by time-resolved four-wave mixing technique, in *Wide Bandgap Materials and New Developments*, Eds. M. Syrjarvi, and R. Yakimova, (Research Singpost, Chapter 5, 117-164, 2006).

[133] K. Jarašiūnas, *Šiuolaikinių puslaidininkinių darinių optinė diagnostika* (Progretus,Vilnius, 2008).

[134] P. B. Klein, R. Myers-Ward, K. -K. Lew, B. L. VanMil, C. R. Eddy, D. K. Gaskill Jr., A. Shrivastava and T. S. Sudarshan, J. Appl. Phys. **108**, 033713 (2010).

[135] K. Jarašiūnas, R. Aleksiejūnas, T. Malinauskas, V. Gudelis, T. Tamulevičius, S. Tamulevičius, A. Guobienė, A. Usikov, V. Dmitriev and H. J. Gerritsen, Rev. Sci. Instrum. **78**, 033901 (2007).

[136] S. G. Sridhara, T. J. Eperjesi, R. P. Devaty and W. J. Choyke, Mater. Sci. Eng. B **61-62**, 229 (1999).

[137] A. Galeckas, P. Grivickas, V. Grivickas, V. Bikbajevas and J. Linnros, Phys. Status Sololidi A **191**, 613 (2002).

[138] A. J. Sabbah and D. M. Riffe, Phys. Rev. B **66**, 165217 (2002).

[139] K. Ramspeck, S. Reissenweber, J. Schmidt, K. Bothe and R. Brendel, Appl. Phys. Lett. **93**, 102104 (2008).

[140] D. Kiliani, G. Micard, B. Steuer, B. Raabe, A. Herguth and G. Hahn, J. Appl. Phys. **110**, 054508 (2011).

[141] J. R. Lakowicz, *Principles of Fluorescence Spectroscopy*, second ed. (Kluwer Academic/Plenum Publishers, New York, 1999).

[142] V. Pačebutas, A. Stalnionis, A. Krotkus, T. Suski, P. Perlin and M. Leszczynski, Appl. Phys. Lett. **78**, 4118 (2001).

[143] S. J. Bepko, Phys. Rev. B **12**, 669 (1975).

[144] E. Kioupakis, P. Rinke, A. Schleife, F. Bechstedt and C. G. Van de Walle, Phys. Rev. B **81**, 241201(R) (2010).

[145] N. Nikogosyan, *Properties of Optical and Laser-Related Materials* (John Wiley & Sons, 1998).

[146] P. Grivickas, A. Martinez, I. Mikulskas, V. Grivickas, R. Tomašiunas, J. Linnros and U. Lindefelt, Mater. Sci. Forum **353-356**, 353 (2001).

[147] D. Huang, F. Yun, M. A. Reshchikov, D. Wang, H. Morkoç, D. L. Rode, L. A. Farina, Ç. Kurdak, K. T. Tsen, S. S. Park and K. Y. Lee, Solid State Electron. **45**, 711 (2001).

[148] J. Pernot, W. Zawadzki, S. Contreras, J. L. Robert, E. Neyret and L. Di Cioccio, J. Appl. Phys. **90**, 1869 (2001).

[149] H. Siegle, G. Kaczmarczyk, L. Filippidis, A. P. Litvinchuk, A. Hoffmann and C. Thomsen, Phys. Rev. B **55,** 7000 (1997).

[150] N. Teofilov, R. Schliesing, K. Thonke, H. Zacharias, R. Sauer, H. Kanda, Diam. Relat. Mater. **12**, 636 (2003).

[151] N. G. Weimann and L. F. Eastman, J. Appl. Phys. **83**, 3656 (1998).

[152] A. B. Sproul, J. Appl. Phys. **76**, 2851 (1994).

[153] A. Yoshida, M. Kato and M. Ichimura, Mater. Sci. Forum **717-720**, 305 (2012).

[154] S. K. Mathis, A. E. Romanov, L. F. Chen, G. E. Beltz, W. Pompe and J. S. Speck, Phys. Status Solidi (a) **179**, 125 (2000).

[155] K. Lee and K. Auh, MRS Internet J. Nitride Semicond. Res. **6**, 9 (2001).

[156] H. Morkoç, Mat. Sci. Eng. R **33**, 135 (2001).

[157] D. Gogova, A. Kasic, H. Larsson, C. Hemingsson, B. Monemar, F. Tuomisto, K. Saarinen, L. Dobos, B. Pecz, P. Gibart and B. Beaumont, J. Appl. Phys. **96**, 799 (2004).

[158] Z. Zhang, C. A. Hurni, A. R. Arehart, J. Yang, R. C. Myers, J. S. Speck and S. A. Ringe, Appl. Phys. Lett. **100**, 052114 (2012).

[159] K. Takiyama, M. I. Abd-Elrahman, T. Fujita and T. Oda, Sol. State Commun. **99**, 793 (1996).

[160] R. Sauer, N. Teofilov and K. Thonke, Diam. Relat. Mater. **13**, 691 (2004).

[161] M. Naamoun, A. Tallaire, F. Silva, J. Achard, P. Doppelt and A. Gicquel, Phys. Status Solidi A **209**, 1715 (2012).

[162] A. A. Lebedev, A. M. Strel'chuk, D. V. Davydov, N. S. Savkina, A. S. Tregubova, A. N. Kuznetsov, V. A. Solov'ev and N. K. Poletaev, Appl. Surf. Science **184**, 419 (2001).

[163] J. Mickevičius, M. S. Shur, R. S. Qhalid Fareed, J. P. Zhang, R. Gaška and G. Tamulaitis, Appl. Phys. Lett. **87**, 241918 (2005).

[164] Y. Lin, E. Flitsyian, L. Chernyak, T. Malinauskas, R. Aleksiejūnas, K. Jarašiūnas, W. Lim, S. J. Pearton and K. Gartsman, Appl. Phys. Lett. **95**, 092101 (2009).

[165] J. Barjon, F. Jomard, A. Tallaire, J. Achard and F. Silva, Appl. Phys. Lett. **100,** 122107 (2012).

[166] E. F. Schubert, *Light-emitting diodes*, second ed. (Cambridge University Press, New York, 2006).

[167] W. L. Wang, M. C. Polo, G. Sánchez, J. Cifre and J. Esteve, J. Appl. Phys. **80**, 1846 (1996).

[168] D. E. Kane and R. M. Swanson, J. Appl. Phys. **73**, 1193 (1993).

[169] C. Persson, U. Lindefelt and B. E. Sernelius, J. Appl. Phys. **86**, 4419 (1999).

[170] Y. Goldberg, M. E. Levinshtein, S. L. Rumyantsev in *Properties of Advanced Semiconductor Materials GaN, AlN, SiC, BN, SiC, SiGe,* Eds. M. E. Levinshtein, S. L. Rumyantsev, M. S. Shur (John Wiley & Sons, Inc., New York, 2001).

[171] B. Monemar, P. P. Paskov, J. P. Bergman, A. A. Toropov, T. V. Shubina, T. Malinauskas and A. Usui, Phys. Status Solidi B **245**, 1723 (2008).

[172] M. Ichimura, Sol. State Electron. **50**, 1761 (2006).

[173] T. Troffer, M. Schadt, T. Frank, H. Itoh, G. Pensl, J. Heindl, H. P. Strunk and M. Maier, Phys. Status Solidi A **162**, 277 (1997).

[174] H. Matsuura, M. Komeda, S. Kagamihara, H. Iwata, R. Ishihara, T. Hatakeyama, T. Watanabe, K. Kojima, T. Shinohe and K. Arai, J. Appl. Phys. **96**, 2708 (2004).

[175] V. I. Polyakov, A. I. Rukovishnikov, V. P. Varnin, I. G. Teremetskaya and V. A. Laptev, Diam. Relat. Mater. **12**, 1783 (2003).

[176] E. Gheeraert, A. Deneuville and J. Mambou, Diam. Relat. Mater. **7**, 1509 (1998).